Edge Effects on the Single Cell Level of Polymer Electrolyte Fuel Cells

Von der Fakultät Energie-, Verfahrens- und Biotechnik
der Universität Stuttgart zur Erlangung der Würde
eines Doktor-Ingenieurs (Dr.-Ing.) genehmigte Abhandlung

Vorgelegt von
Peter Stahl
aus Backnang

Hauptberichter:	Prof. Dr. K. Andreas Friedrich
Mitberichter:	Prof. Dr. Thomas J. Schmidt
Tag der mündlichen Prüfung:	8. Dezember 2017

Institut für Thermodynamik und Wärmetechnik
der Universität Stuttgart

2018

Abstract

Polymer electrolyte fuel cells (PEFC) are about to gain an important role in an energy supply based on renewable energy sources. In order to facilitate the market entry of PEFCs, various targets regarding lifetime, functionality and costs have to be fulfilled. An aspect of PEFCs which has not gathered much attention so far is the outer perimeter of the active cell area. The design of this region is substantially determined by the sealing concept and sealant manufacturing process and can have a considerable influence on the overall cell design. This work aims to illustrate the impact of the configuration of this specific area on operating conditions and degradation effects of the whole cell. The results enable the appropriate design of the sealing solution in order to mitigate unfavorable local operating conditions and degradation effects in the outer cell perimeter.

In Chapter 3 state-of-the-art cell concepts are presented with respect to the design of the cell edge region and the impact on cell design, local operating conditions and manufacturing processes. General impact of the edge region design on the water transport in a cell is discussed in Chapter 5. Five cells with different sealing concepts were operated and the in-plane water distribution was analyzed by means of neutron radiography. It was shown that void volumes in the outer perimeter of a cell favor accumulation of liquid water there, as long as they are not fed by a direct gas flow. As water transport between edge region and flowfield is slow with time constants of $> 1\,\mathrm{h}$ the removal of these water clusters is not possible with the applied cell operation protocols. Cells with a gas feed to the outer cell perimeter are in turn subjected to bypass flows around the flowfield. Particularly for flowfields with high flow resistances – e.g. with serpentine-shaped flowfield channels – this can lead to a significantly reduced stoichiometry in the flowfield and hence to decreased liquid water discharge. As a result the measured water content in the flowfield reached a maximum of twice the water content compared to a cell without a flowfield bypass. In general, local operating conditions were strongly influenced by the cell setup in the outer perimeter.

Startup of PEFCs under freezing conditions is a requirement for many mobile applications. It can be challenging for cell design and operation as electrochemically produced water as well as residual water from a previous operation can freeze and block gas transport pathways, leading to cell failure. In Chapter 6 it is shown by a recently developed *dual spectrum* neutron radiography method that freezing of water over a limited fraction of a cell can occur while water in the rest of the cell remains liquid. At moderate temperatures of $\geq -5\,^{\circ}\mathrm{C}$ this partial freezing occurred simultaneously with the beginning of a cell voltage decline while the final cell failure could be assigned to the freezing of water over the entire cell area. Furthermore it was shown that residual water in the edge region and flowfield of a cell can have a negative influence on cold start capability. Residual water freezes as soon as the cell is cooled below $0\,^{\circ}\mathrm{C}$ and poses a nucleus for a fast phase transition of liquid product water to ice.

Chapter 7 focuses on specific degradation mechanisms occurring in the outer cell perimeter. It is shown that if a catalyst coated membrane (CCM) is sandwiched between gaskets in its outer perimeter and between gas diffusion layers (GDL) in the flowfield, a gap between gasket and GDL can lead to accelerated mechanical deterioration of the membrane. Particularly under oscillating humidification conditions shrinking and swelling of the membrane can induce high local stresses in the membrane at the edges of GDL and gasket. As a result cell failure occurred after $10\,000$ cycles as cracks or pinholes in the membrane led to strong leakages. The experiment showed that a mechanically favorable integration of the CCM with the sealing setup is essential in order to mitigate membrane stress, especially for applications with lifetime requirements of more than $10\,000\,\mathrm{h}$.

Manufacturing and assembling tolerances can lead to a lateral offset of the gaskets or single layers of a sub-gasket on both sides of a CCM. As a result the gas supply to the anode and cathode catalyst layer (CL) can be asymmetric in the outer perimeter of the active area. In Chapter 7 it is shown experimentally that particularly a local interruption of the anode gas supply can cause massive carbon corrosion of the cathode catalyst support. From $1\,\mathrm{mm}$ onwards under the covered area strong thinning of the cathode CL was seen, while the thickness of membrane and anode CL remained unchanged. The results were confirmed by numerical simulation. A specific characteristic of the discussed case was found to be the local electrical isolation between GDL and CL on the anode side by the introduced sub-gasket layer. Thereby a strong negative electrical potential gradient in the anode CL can emerge towards the outer cell perimeter, favoring a low local electrolyte potential since anode overpotentials remain small. As the electrical potential of the cathode CL does not exhibit pronounced potential gradients, the low electrolyte potential leads to high cathode electrode potentials and therefore to significant carbon corrosion rates. It is concluded that cells should intentionally exhibit a lateral offset of gaskets or sub-gasket layers on both sides of the CCM, so that with respect to the assembling tolerances local oxygen starvation occurs on the cathode side rather than hydrogen starvation on the anode side in every case.

Zusammenfassung

Polymer-Elektrolyt-Brennstoffzellen (*polymer electrolyte fuel cell*, PEFC) werden einen wesentlichen Beitrag zu einem zukünftigen Energieversorgungssystem basierend auf erneuerbaren Energieträgern leisten. Um deren Markteintritt zu ermöglichen, müssen verschiedene Anforderungen an Lebensdauer, Funktionalität und Kosten erfüllt sein. Ein bislang nur wenig beachteter Bereich von PEFCs ist der äußere Rand der aktiven Zellfläche. Der Aufbau dieses Bereiches wird im Wesentlichen durch Gestaltung und Fertigungsverfahren der Zelldichtung vorgegeben und bestimmt maßgeblich den Aufbau der gesamten Zelle. Ziel dieser Arbeit ist es darzustellen inwiefern sich die Gestaltung einer Zelle an ihrem äußeren Umfang auf Leistungsfähigkeit und Alterungseffekte der gesamten Zelle auswirkt. Die Ergebnisse dienen als Grundlage für die Entwicklung eines in Bezug auf Leistung, Lebensdauer und Fertigungsaufwand günstigen Zellaufbaus.

Bereits bekannte Zellkonzepte werden in Kapitel 3 bzgl. der Gestaltung des Randbereiches und der Auswirkung auf Zellaufbau, lokale Betriebsbedingungen und Fertigungsaufwand umfassend vorgestellt. Kapitel 5 beschreibt im Wesentlichen die Auswirkungen des Zellaufbaus im Randbereich auf den Wassertransport in der Zelle. Dabei wurde die Wasserverteilung in fünf verschiedenen Zellaufbauten mittels Neutronenradiographie analysiert. Es zeigte sich, dass außerhalb des Flowfields liegende Hohlräume – sofern sie nicht direkt von Gas durchströmt werden – Wasseransammlungen begünstigen. Aufgrund des sehr langsamen Wassertransports zwischen Randbereich und Flowfield, mit Zeitkonstanten von $> 1\,\mathrm{h}$, kann dort akkumuliertes Wasser nur schwer durch entsprechende Betriebsführung entfernt werden. Direkt durchströmte Bereiche außerhalb des Flowfields hingegen begünstigen Bypassströmungen um das Flowfield herum, insbesondere wenn letzteres hohe Strömungswiderstände aufweist, wie beispielsweise durch Mäanderstrukturen. Es wurde gezeigt, dass in diesem Fall die Stöchiometrie im Bereich des Flowfields absinkt. Die daraus folgende Reduzierung des Flüssigwasseraustrages führte zu einer Verdopplung des Wassergehalts in der Zelle im Vergleich zu einer Zelle ohne Bypass. Damit wurde nachgewiesen, dass lokale Betriebsbedingungen massiv durch den Aufbau des Randbereiches einer Zelle beeinflusst werden können.

Für verschiedene Anwendungen von PEFCs wird die Froststartfähigkeit vorausgesetzt, wodurch spezifische Anforderungen an den Betrieb und die Konzeption einer Zelle entstehen. Elektrochemisch produziertes Wasser sowie von einem vorhergehenden Betrieb resultierendes Wasser kann gefrieren und damit Gaswege blockieren, was zum Ausfall der Zelle führen kann.

In Kapitel 6 wird mittels Neutronenradiographie gezeigt, dass im Randbereich einer Zelle akkumuliertes Wasser einen negativen Einfluss auf die Froststartfähigkeit haben kann. Mit einer neuartigen *Dual Spectrum* Methode konnte eindeutig das Gefrieren von Restwasser in einer Zelle bei deren Abkühlung unter $0\,^{\circ}\mathrm{C}$ nachgewiesen werden. Mit dieser Methode konnte ebenfalls erstmals in einer $50\,\mathrm{cm}^2$ Zelle nachgewiesen werden, dass flüssiges Produktwasser bei moderaten Starttemperaturen ($\geq\ -5\,^{\circ}\mathrm{C}$) über einen räumlich begrenzten Bereich der Zellfläche gefriert, während im restlichen Bereich weiterhin flüssiges Wasser vorhanden ist. Der Zeitpunkt des Gefrierens eines ersten Bereiches konnte dabei dem Beginn des Zellspannungseinbruches zugeordnet werden, während der zum Zellausfall führende Einbruch der Zellspannung zeitlich mit dem Gefrieren von Wasser über die gesamte Zellfläche zusammenfiel.

In Kapitel 7 werden spezifische Alterungsmechanismen analysiert, die im Randbereich einer Zelle auftreten können. Es wurde gezeigt, dass in einer katalysatorbeschichteten Membran (*catalyst coated membrane*, CCM) ohne Randverstärkung, die zwischen Gasdiffusionslagen (GDL) und Dichtungsstrukturen verpresst ist, hohe mechanische Spannungen an den äußeren Enden von GDL oder Dichtung auftreten können, sofern sich zwischen GDL und Dichtung ein Spalt befindet. Unter stark schwankender Feuchte und entsprechender Schrumpfung und Schwellung der Membran können so hohe mechanische Spannungen in der Membran auftreten, die in diesem Fall nach $10\,000$ Feuchtezyklen zu einer Perforation der Membran und damit zu einem Zellausfall durch Leckage führten. Die Ergebnisse zeigten, dass eine möglichst vollflächige Verpressung der CCM zwischen GDL und Dichtung insbesondere für Anwendungen mit hohen Lebensdaueranforderungen zu bevorzugen ist.

Bedingt durch Toleranzen in Fertigungs- und Montageprozessen können die Komponenten von Einzelzellen einen lateralen Versatz zueinander aufweisen. Die Begrenzung des mit Reaktionsgasen versorgten aktiven Bereiches einer CCM kann daher auf Anode und Kathode zueinander versetzt sein. In Kapitel 4 wird sowohl experimentell als auch durch numerische Simulation nachgewiesen, dass die lokale Abdeckung der CCM auf der Anodenseite im Randbereich einer Zelle starke Kohlenstoffkorrosion des Katalysatorträgers auf der Kathodenseite hervorrufen kann. Bereits ab $1\,\mathrm{mm}$ unterhalb des anodenseitig abgedeckten Bereiches konnte eine starke Ausdünnung des kathodenseitigen Katalysators nachgewiesen werden, während Membran und Anode keine Veränderungen zeigten. Simulationsergebnisse bestätigen dieses Bild. Ein qualitatives Unterscheidungsmerkmal zu den bisher in der Literatur diskutierten Fällen von lokaler Wasserstoffverarmung ist die elektrisch isolierende Wirkung der auf der Anodenseite zwischen Katalysator und GDL eingebrachten Abdeckfolie. Dadurch wird die Ausbildung eines starken Potentialgradienten in der Festphase des Anodenkatalysators begünstigt, was bedingt durch ein niedriges und relativ konstantes Elektrodenpotential der Anode wiederum einen starken Einbruch des Elektrolytpotentials über eine relativ kurze Distanz zur Folge hat. Das Festphasenpotential auf der Kathodenseite weist durch den elektrischen Kontakt der Katalysatorschicht zur GDL vernachlässigbar kleine Gradienten auf. In Kombination mit einem niedrigen Elektrolytpotential treten dadurch auf der Kathodenseite hohe Elektrodenpotentiale und folglich starke Kohlenstoffkorrosion auf. Konstruktiv sollte daher der mit Gas versorgte Bereich auf der Anodenseite, unter Berücksichtigung aller Fertigungs- und Montagetoleranzen, immer größer ausgeführt sein als der mit Gas versorgte Bereich auf der Kathodenseite.

Acknowledgement

Ich erlaube mir an dieser Stelle einige Worte in meiner Muttersprache abzufassen, um mich außerhalb der engen Grenzen meiner Englischkenntnisse bewegen zu können.

An erster Stelle will ich mich bei meinem Doktorvater, Prof. Dr. K. Andreas Friedrich für die Begleitung während meiner Promotionszeit bedanken. Insbesondere die Bereitschaft, mich als externen Doktoranden auf unkomplizierte und zielgerichtete Weise zu unterstützen weiß ich sehr zu schätzen.

Prof. Dr. Thomas J. Schmidt gilt mein Dank sowohl für die Übernahme des Koreferats als auch für die Möglichkeit innerhalb seiner Abteilung am Paul Scherrer Institut Messungen durchführen zu können. Prof. Dr. Jörg Starflinger danke ich für die Übernahme des Prüfungsvorsitzes.

Die Möglichkeit zur Promotion bei der ElringKlinger AG verdanke ich insbesondere Jürgen Kraft. Ohne ihn würde ich noch heute nichts von heuristischen Prinzipien ahnen und Ockhams Rasiermesser wohl für einen Haushaltsartikel halten.

Ganz besonders hervorheben will ich das Engagement von Johannes Biesdorf, ohne den diese Arbeit wohl nicht in dieser Form entstanden wäre. Sein unermüdlicher Wille zur wissenschaftlichen Wahrheitsfindung und sein unglaubliches Durchhaltevermögen in langen Neutronen-Nächten unter Beibehaltung seines Humors ist meiner Hochachtung gewiss. Auch Pierre Boillat danke ich für die Unterstützung der Messkampagnen mit so manchem magischen Kniff und mit Schweizer Volksliedern.

Sehr profitiert habe ich von der langjährigen Erfahrung von Heiko Knaupp und Matthias Schätzle. Ihre Fähigkeit Leckagen, Kurzschlüsse und widerspenstige Prüflinge auf wundersame Weise zu heilen sowie ihr wunderbarer Humor waren stets wertvolle Hilfe.

Für die Ausbesserung meiner holprigen Englischkenntnisse und für wertvolle Tipps von Doktorand zu Doktorand danke ich besonders Mark Gregory. Die fachgerechte Überprüfung der Eigenheiten von Mitochondrien verdanke ich Dominik Bender.

Besonderer Dank geht an André Diers für heitere Diskussionen rund um die Nernst-Gleichung, Rohmilch und genossenschaftliche Prinzipien. Außerdem an meine Studenten Fabian Haug und Clemens Seeger für die Arbeiten zur Testzelle und Dichtung.

Beim letzten Schliff der Dissertation haben mich Thomas Kiupel, Stefan Hemmer und Michael Götz unterstützt. Gemeinsam mit allen anderen Kolleginnen und Kollegen bei ElringKlinger waren sie wunderbare Begleiter auf diesem langen Weg. Um an dieser Stelle keinen

der zahlreichen Namen zu vergessen will ich allen Mitstreitern im Büro und Labor gemeinsam für Ihre unersetzliche Unterstützung sowohl während der Arbeitszeit als auch abseits davon danken.

Die Idee über PEM-Brennstoffzellen zu promovieren entstand vor allem während der Zeit im gemeinsamen Büro mit Timo Kurz und Dietmar Gerteisen. Auch meine wissenschaftliche Grundausstattung habe ich zu guten Teilen dort erworben, wofür ich beiden herzlich danke.

Meinen Freunden und meiner Familie danke ich für die stetige Unterstützung, für das Zurückholen auf den Boden der Tatsachen, auch wenn es nicht immer so klar war an was ich da eigentlich genau arbeite. Der größte Dank gebührt meinen Eltern, ohne deren bedingungslose Unterstützung in allen Hoch- und Tiefphasen diese Arbeit nicht möglich gewesen wäre.

Table of Contents

Chapter 1

Introduction

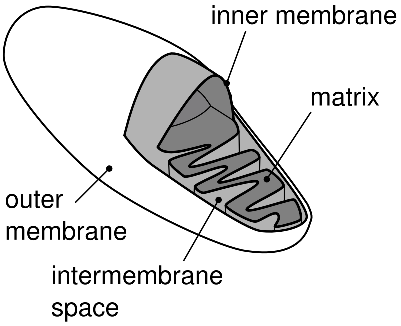

Figure 1.1: Mitochondrion, according to [1].

Life of all organisms composed of nuclei containing somatic cells is based on the conversion of hydrocarbon-containing nutrition into exploitable energy forms. Essentially for the conversion process are the *mitochondria*, known as the power plants of biological cells. They are capable of catalyzing a wide range of different catenated reactions, basically a redox reaction of glucose and oxygen to water, carbon dioxide and adenosine triphosphate (ATP). The latter is an universal energy unit and drives the vital functions of organisms. Oxidation and reduction of the overall reaction are spatially separated by the *cristae*, the inner membrane of the mitochondrion, shown in Figure 1.1, which acts as a proton conducting separator. The life expectancy of a mitochondrium is limited to about $10-20$ days [2]. Its aging process is assumed to be mainly a consequence of oxygen crossover through the cell membrane, a subsequent formation of oxygen radicals in side reactions and the structural decomposition of the mitochondrium [3].

A mitochondrium exhibits an astonishing analogy with a fuel cell. Both accommodate a redox reaction of hydrogen with oxygen, whereby oxidation and reduction are separated by a proton conducting membrane, and both generate utilizable energy forms, electricity or ATP. Fuel cells are a missing link for the conversion of our energy supply into an entirely sustainable system as they enable the direct conversion of hydrogen into electricity. Hydrogen offers the chance to a long-term energy storage by performing electrolysis from fluctuating renewable energy sources. Hydrogen storage is easily scalable to higher capacities as consumption of resources – as noble earths or precious metals – is low compared to secondary cells. The high power density of polymer electrolyte fuel cells (PEFC) facilitates the energy conversion of hydrogen on board of mobile systems and is therefore suitable to enable locally emission-free mobility. Both mitochondria and fuel cells are subject to radical-based degradation processes. But organisms have the advantage of being self-healing, aged mitochondria can be replaced by new ones. Fuel cells are not self-healing and the mitigation of aging processes is a requisite for their successful market entry to replace energy conversing systems based on fossil fuels.

Recent PEFC research has been concentrated on topics around functionality, performance and lifetime. However, actual cell concepts need to be adapted to mass production requirements in order to reduce number and complexity of process steps and to enable reliable and cost efficient component manufacturing and assembly. It is crucial to develop viable concepts for mass production while maintaining or even improving functionality. Particularly the cell sealing concept and its impact on overall cell design and functionality has gained little attention in scientific research, apart from studies about sealant material evaluation.

Edge effects, mentioned in the title of this work, refer to the outer perimeter area of a single cell of a planar PEFC. The design of this area is mainly determined by the cell sealing system and can lead to specific operating conditions there. Water distribution, mechanical stress on the components, gas supply and hence local performance can differ significantly from the conditions in the rest of the cell area. Degradation mechanisms can be more pronounced in the edge region as they are coupled to the local operating conditions. Locally enhanced degradation effects can be a limiting factor for the lifetime of the whole PEFC stack, so that understanding and mitigation of these edge effects is essential. This work aims to give a comprehensive analysis of the impact of PEFC sealing solutions and the according design of a cell on local operating conditions and lifetime. The main scientific achievements are:

- Water management and gas transport in the outer perimeter of the active cell area was assessed by neutron radiography. Void peripheral areas around the active area were shown to either favor accumulation of liquid water or act as a flowfield bypass, both significantly changing operating conditions in the cell.
- In-situ neutron imaging of PEFCs during cold starts from sub-zero temperatures with a novel dual spectrum method revealed that a limited fraction of a cell can freeze while the electrochemical water production in the remaining areas continues. Phase transitions of supercooled water to ice could be verified directly in a cell.
- Residual water, remaining in a cell prior to a cold start, was shown to initiate freezing of a limited adjacent cell area and lead to a significantly reduced local water production.
- Mechanical protection of the membrane in its outer perimeter was found out to be crucial in order to avoid membrane deterioration caused by mechanical stress, e.g. induced by humidity cycling.
- Experiments as well as numerical simulation showed that a slight lateral offset of gaskets in the cell edge region can lead to local hydrogen starvation resulting in a strong carbon corrosion of the cathode catalyst layer.

Chapter 2

PEFC Fundamentals

Electrochemical systems as PEFCs are multiphase systems, comprising ionic and electrical conducting material phases and porous gas networks. At the interfaces between the different phase domains – the *electrodes* – oxidation and reduction reactions, facilitated by catalysts, can take place. Basically a species s adsorbs at an active catalytic site of an electrode in reduced (s_{red}) or oxidized (s_{ox}) form [4]. z electrons are transferred during the oxidation or reduction reaction respectively

$$s_{red} \rightleftharpoons s_{ox} + z e^{-}. \tag{2.1}$$

Fuel cells are galvanic cells, accommodating a redox reaction of oxygen with a hydrogen containing fluid, in case of a PEFC with pure hydrogen. The overall redox reaction of a PEFC

$$2\,H_2 + O_2 \longrightarrow 2\,H_2O \tag{2.2}$$

is spatially separated into the oxidation and the reduction part of the reaction by an electrical isolating but proton conducting electrolyte. On each side of the electrolyte, a porous gas electrode accommodates electrochemical reactions. On the anode side, a hydrogen oxidation reaction (HOR) of molecular hydrogen takes place

$$H_2 + 2\,H_2O \rightleftharpoons 2\,H_3O^{+} + 2\,e^{-}, \tag{2.3}$$

whereas the formed protons do not persist alone but bonded to water molecules located in the electrolyte. In an idealized model, oxonium ions (H_3O^+) represent the wide spectrum of possible hydration states. Generated electrons are transferred to the solid phase of the electrodes. Hydrogen ions are transported through the electrolyte membrane, facilitating an oxygen reduction reaction (ORR) on the cathode side with electrons conducted from the anode side over an external electronic circuit where they perform electrical work

$$O_2 + 4\,H_3O^{+} + 4\,e^{-} \rightleftharpoons 6\,H_2O. \tag{2.4}$$

2.1 Electrolyte

Liquid water is a suitable electrolytic conductor for PEFCs as it can form weak bonds with dissociated hydrogen ions (H^+). In a simplified view oxonium ions (H_3O^+) are formed. They are surrounded by a hydrating solvate shell of associated water molecules which are themselves hydrated but with lower binding forces. The hydrated oxonium ions can be transported through the aqueous solution driven by a concentration gradient or an external electrical field. Theodor von Grotthuß found a mechanism, which gives rise to a significantly increased electrolytic conductivity for the couple H_2O/H^+ compared to other electrolytes. Due to similar binding forces of the hydrogen bonds and fast structural reorganization of the aqueous network, protons can easily migrate in the solvent bounded network [1, 4–6].

In addition to its function as a proton conductor, the electrolyte has to separate anode and cathode gas compartments and ensure electrical isolation. Therefore thin polymer membranes (typically $15 - 50\,\mu\mathrm{m}$ thick) with a high capability to retain the aqueous electrolyte (water) are employed. The field of PEFCs is prevailed by perfluorinated sulfonic acids (PFSA), mostly a polytetrafluoroethylene (PTFE) backbone with side chains consisting of vinyl ether groups and a sulfonic acid (SO_3H), as depicted in Figure 2.1. As the terminating hydrogen proton can dissociate easily, additional ion exchange sites are provided thereby. The proton conductivity of a PFSA *ionomer* is typically some magnitudes higher compared to pure water.

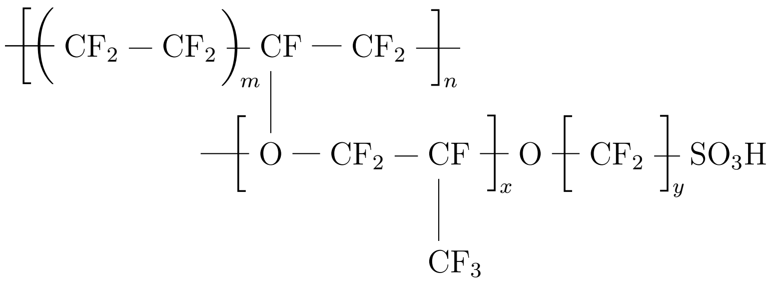

Figure 2.1: Chemical structure of PFSA membranes, for DuPont's Nafion®: $m = 5 - 13.5$, $x \geq 1$, $y = 2$, values can vary for other PFSA membrane types [7–9].

Resulting from the properties of PTFE and sulfonic acid, PFSA ionomers have hydrophobic and hydrophilic regions. Following the location of the SO_3^- end groups, aqueous network structures in the scale of a few ångström are formed inside the membrane as verified in the early 1980s by x-ray studies [10–13]. The pore network builds continuous water pathways between anode and cathode side of the ionomer, therein protons can be transported by

- molecular diffusion of H_3O^+
- molecular transport of H_3O^+ driven by an electrical field and

- structural diffusion in the hydrogen aqueous network (Grotthuß mechanism).

The stored water content in a PFSA ionomer is essential for its conductivity and is described by λ_{mem}, which is the relation between the amount of substance of water in the membrane and of the SO_3^- end groups n_{H2O} and $n_{\mathrm{SO}_3^-}$, respectively

$$\lambda_{\mathrm{mem}} = \frac{n_{\mathrm{H2O}}}{n_{\mathrm{SO}_3^-}}. \tag{2.5}$$

Strong dehydration can cause a collapse of the capillary pore network inside an ionomer. The process is reversible, recovering is possible by boiling a membrane in water. As a result the maximum water uptake capability and hence the conductivity at full humidification can vary due to the thermal history of an ionomer. A maximum water content of $\lambda_{\mathrm{mem}} = 14$ for a pre-dried membrane and $\lambda_{\mathrm{mem}} = 23$ for a boiled membrane was reported (at $30\,^{\circ}\mathrm{C}$) [14].

2.2 Electrodes

Electrodes are the coupling interfaces between the different phases of an electrochemical system and accommodate and catalyze electrochemical reactions, involving species from the ion and electron conducting phases and from the gas phase. The electrolyte, sandwiched between two electrodes, acts as a transport phase for protons, produced in the HOR at the anode electrode and consumed in the ORR on the cathode side. Electrons from the HOR are conducted to the cathode side via an external electrical circuit where they can perform electrical work. Both electrodes are porous structures so that the reactants can permeate to the catalytically active sites. PEFC electrodes are mostly based on carbon black as an electron conducting support. Catalyst particles, usually platinum or platinum alloys, are dispersed on the carbon spheres as shown in Figure 2.2. The porous electrode is infiltrated with ionomer in order to join the electrolytic phase of the membrane ionomer to the active reaction sites of the catalyst. Hydrogen or oxygen molecules diffuse through the thin ionomer layer and are adsorbed at the catalyst surface. Both, oxidation and reduction reactions involve an electron transfer step from an adsorbed atom to the solid phase or vice versa. In case of the anode, the covalent bond of catalytically adsorbed molecular hydrogen is broken and hydrogen is oxidized while the emerging electron is transferred to the solid electrode phase [15]. The resulting protons are then immediately hydrated in the solvent network which can be represented by oxonium ions (H_3O^+).

The driving force for an electrode reaction is a difference in the *electrochemical potential* of reactants and products. The electrochemical potential μ_i^* of a component is the sum of

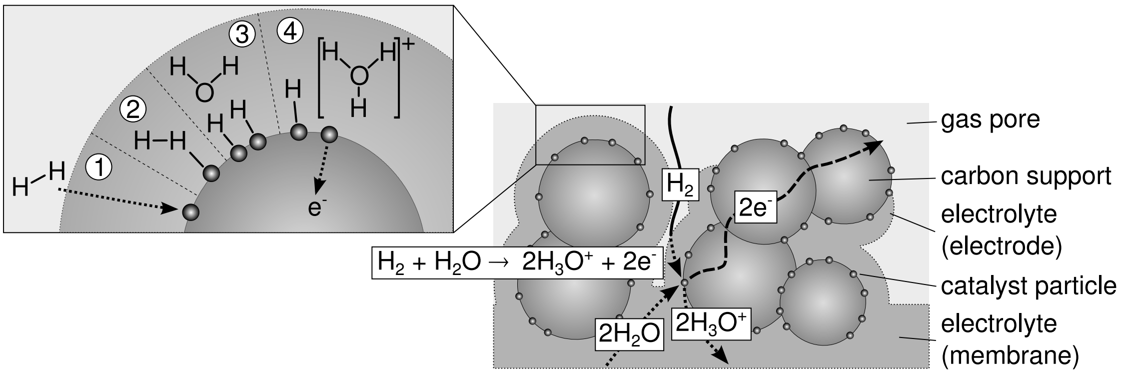

Figure 2.2: 3-phase boundary of a porous anode electrode and reaction steps of the HOR.

the electrical or electrolytic potential φ and the chemical potential μ_i. As charged species in concentrated solutions interfere themselves, the standard chemical potential $\mu_i^{\ominus}$[1] has to be corrected by the activity a_i [4]

$$\mu_i^* = \mu_i + z_i F \varphi = \mu_i^{\ominus} + \Re T ln(a_i) + z_i F \varphi. \tag{2.6}$$

$\Re$ denotes the ideal gas constant, T the temperature, F the Faraday constant and z_i the valency of the charge carrier. An electrode reaction will proceed until an electrochemical equilibrium is reached between the reduced ($\mu^*_{i,\mathrm{red}}$) and the oxidized ($\mu^*_{i,\mathrm{ox}}$) state [16]

$$\sum_{i,\mathrm{ox}} \upsilon_{i,\mathrm{ox}} \mu^*_{i,\mathrm{ox}} = \sum_{i,\mathrm{red}} \upsilon_{i,\mathrm{red}} \mu^*_{i,\mathrm{red}}. \tag{2.7}$$

For a PEFC cathode with the stoichiometry factors $\upsilon_{i,\mathrm{ox}}$ and $\upsilon_{i,\mathrm{red}}$ from Equation 2.4

$$\mu^*_{\mathrm{O_2}} + 4\mu^*_{\mathrm{H_3O^+}} + 4\mu^*_{\mathrm{sol}} = 6\mu^*_{\mathrm{H_2O}} \tag{2.8}$$

is obtained, with the electrochemical potentials of gaseous oxygen $\mu^*_{\mathrm{O_2}}$, of H_3O^+ in aqueous solution $\mu^*_{\mathrm{H_3O+}}$, the solid electron conducting solid phase μ^*_{sol} and liquid water $\mu^*_{\mathrm{H_2O}}$. Using Equation 2.6 in Equation 2.8 results in

$$\begin{aligned} \left(\mu^{\ominus}_{\mathrm{O_2}} + \Re T \ln\left(a_{\mathrm{O_2}}\right)\right) + 4\left(\mu^{\ominus}_{\mathrm{H_3O^+}} + \Re T \ln\left(a_{\mathrm{H_3O^+}}\right) + z_{\mathrm{H_3O^+}} F \varphi^0_{\mathrm{ely}}\right) \\ + 4\left(\mu_{\mathrm{e^-}} + z_{\mathrm{e^-}} F \varphi^0_{\mathrm{sol,ca}}\right) = 6\left(\mu^{\ominus}_{\mathrm{H_2O}} + \Re T \ln\left(a_{\mathrm{H_2O}}\right)\right) \end{aligned} \tag{2.9}$$

---

[1] Standard conditions: $T^{\ominus} = 298.15\,\mathrm{K}$ and $p^{\ominus} = 101\,325\,\mathrm{Pa}$.

with the activities a_{O_2}, $a_{H_3O^+}$ and a_{H_2O} and the standard chemical potentials $\mu^{\ominus}_{O_2}$, $\mu^{\ominus}_{H_3O^+}$ and $\mu^{\ominus}_{H_2O}$ of molecular oxygen, oxonium ions and water, respectively. φ^0_{ely} and $\varphi^0_{\mathrm{sol,ca}}$ are the ionic and electrical potentials of the phases. μ_{e^-} describes the chemical potential of the solid electrode phase. $z_{H_3O^+} = +1$ and $z_{e^-} = -1$ are the valencies of oxonium ions and electrons, respectively. Rearranging Equation 2.9 results in the theoretical potential difference between electrolyte (φ^0_{ely}) and the electron conducting phase ($\varphi^0_{\mathrm{sol,ca}}$), also called *Galvani potential* $\Delta\varphi^0_{\mathrm{ca}}$, in the form of the *Nernst equation* for the electrochemical equilibrium

$$\Delta\varphi^0_{\mathrm{ca}} = \varphi^0_{\mathrm{sol,ca}} - \varphi^0_{\mathrm{ely}} = \frac{\mu^{\ominus}_{O_2} + 4\mu^{\ominus}_{H_3O^+} - 6\mu^{\ominus}_{H_2O}}{4F} + \frac{\mu_{e^-}}{F} + \frac{\Re T}{4F} \ln\left(\frac{a_{O_2}\left(a_{H_3O^+}\right)^4}{\left(a_{H_2O}\right)^6}\right). \quad (2.10)$$

$\Delta\varphi^0_{\mathrm{ca}}$ has a theoretical character, as it is not directly measurable. For its determination a further *reference electrode* with a defined electrode potential is required. Hydrogen electrodes with platinum catalysts are widely used as reference electrodes as they exhibit stable and reproducible electrode potentials. As the anode in a PEFC is a hydrogen electrode, it can be used as a reference electrode in the case of electrochemical equilibrium for convenience. The Galvani potential of the anode $\Delta\varphi^0_{\mathrm{an}}$ in analogy to Equation 2.10 is

$$\Delta\varphi^0_{\mathrm{an}} = \varphi^0_{\mathrm{sol,an}} - \varphi^0_{\mathrm{ely}} = \frac{2\mu^{\ominus}_{H_3O^+} - \mu^{\ominus}_{H_2} - 2\mu^{\ominus}_{H_2O}}{2F} + \frac{\mu_{e^-}}{F} + \frac{\Re T}{2F} \ln\left(\frac{\left(a_{H_3O^+}\right)^2}{a_{H_2}\left(a_{H_2O}\right)^2}\right) \quad (2.11)$$

with the electron potential of the anode electrode $\varphi^0_{\mathrm{sol,an}}$, the electrochemical potential of molecular hydrogen $\mu^{\ominus}_{H_2}$ and the activity of hydrogen in the gas phase a_{H_2}. By definition the Galvani potential for a *standard hydrogen electrode* (SHE) $\Delta\varphi^{\ominus}_{\mathrm{an}}$ without the influence of phase activities ($a_i = 1$) as the standard case is

$$\Delta\varphi^{\ominus}_{\mathrm{an}} := 0\,\mathrm{V_{SHE}}. \quad (2.12)$$

For pure substances, the standard chemical potential $\mu^{\ominus}_i$ is equal to the standard Gibbs free energy of formation $\Delta g^{\ominus}_{\mathrm{f},i}$ [17]. With literature values from [18] ($\Delta g^{\ominus}_{\mathrm{f},H_2} = 0\,\mathrm{kJ\,mol^{-1}}$, $\Delta g^{\ominus}_{\mathrm{f},H_3O^+} = \Delta g^{\ominus}_{\mathrm{f},H_2O} = -237.19\,\mathrm{kJ\,mol^{-1}}$) it results $\mu_{e^-} = 0$ from Equations 2.11 and 2.12. Inserting into Equation 2.10 leads to the standard cathode electrode potential $\Delta\varphi^{\ominus}_{\mathrm{ca}}$ at 25 °C

$$\Delta\varphi^{\ominus}_{\mathrm{ca}} = \frac{\Delta g^{\ominus}_{\mathrm{f},O_2} + 4\Delta g^{\ominus}_{\mathrm{f},H_3O^+} - 6\Delta g^{\ominus}_{\mathrm{f},H_2O}}{4F} = 1.228\,\mathrm{V_{SHE}}. \quad (2.13)$$

In order to account for temperature influences on the electrode potentials under electrochemical equilibrium, the temperature corrected Gibbs free energy of formation $\Delta g_{\mathrm{f},i}$

$$\Delta g_{\mathrm{f},i} = \Delta h_{\mathrm{f},i} - T \Delta s_{\mathrm{f},i} \tag{2.14}$$

has to be applied to Equation 2.13, with the temperature corrected enthalpy and entropy of formation $\Delta h_{\mathrm{f},i}$ and $\Delta s_{\mathrm{f},i}$. Usually the overall cell voltage $\Delta\varphi^0_{\mathrm{cell}}$ is measured experimentally between the solid phase of anode ($\varphi^0_{\mathrm{sol,ca}}$) and cathode ($\varphi^0_{\mathrm{sol,an}}$) electrode. With Equations 2.10 and 2.11 we get the cell voltage depending on both electrode potentials $\Delta\varphi^0_{\mathrm{ca}}$ and $\Delta\varphi^0_{\mathrm{an}}$

$$\Delta\varphi^0_{\mathrm{cell}} = \varphi^0_{\mathrm{sol,ca}} - \varphi^0_{\mathrm{sol,an}} = \Delta\varphi^0_{\mathrm{ca}} - \Delta\varphi^0_{\mathrm{an}}. \tag{2.15}$$

Using Equations 2.10, 2.11 and 2.15, the temperature corrected theoretical *open circuit voltage* (OCV) of the cell $\Delta\varphi^0_{\mathrm{cell}}$ is given by

$$\Delta\varphi^0_{\mathrm{cell}} = \frac{\Delta g_{\mathrm{f,O_2}} + 2\Delta g_{\mathrm{f,H_2}} - 2\Delta g_{\mathrm{f,H_2O}}}{4F} + \frac{\Re T}{4F} \ln\left(\frac{a_{\mathrm{O_2}} \left(a_{\mathrm{H_2}}\right)^2}{\left(a_{\mathrm{H_2O}}\right)^2}\right). \tag{2.16}$$

2.3 Reaction Kinetics

As soon as the electrode potential is deflected from its equilibrium potential, oxidation and reduction reactions occur, forcing the recovery of the electrochemical equilibrium. The resulting charge transfer gives rise to an external electrode current. The difference between actual electrode potential $\Delta\varphi_i$ and equilibrium potential $\Delta\varphi_i^0$ is called the *overpotential* η[1] [4]

$$\eta = \Delta\varphi_i - \Delta\varphi_i^0. \tag{2.17}$$

The reaction at both electrodes consists of sequential reaction steps such as adsorption, splitting or forming of a molecular bond, electron transfer and dissociation. According to the models of *Tafel*, *Heyrovsky* and *Volmer* for the HOR at the anode, two different reaction pathways are conceivable, Tafel-Volmer and Heyrovsky-Volmer [4, 19, 20]. Figure 2.3 shows the free energy characteristics of a Volmer reaction

$$\mathrm{Pt}\cdots\mathrm{H_{(ad)}} \rightleftharpoons \mathrm{Pt} + \mathrm{H^+} + \mathrm{e^-} \tag{2.18}$$

---

[1] η for an anode or cathode electrode of a PEFC under normal operation is positive or negative, respectively.

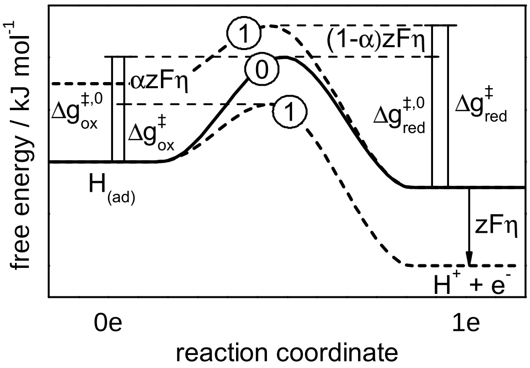

Figure 2.3: Activation energy for the Volmer reaction under equilibrium of the entire HOR ⓪ and under the influence of an electrode overpotential η ①. Both curves ① show the same activation characteristics but are shifted vertically. [4]

which is the rate-limiting step in a Tafel-Volmer reaction pathway [21, 22]. Between initial and final reaction state an activation barrier has to be overcome. The reaction is reversible and can proceed in both reaction coordinates. Under electrochemical equilibrium, oxidation and reduction reactions are in balance and the overall net current density is zero. The activation energies for the oxidation and reduction reaction $\Delta g^{\ddagger}_{\mathrm{ox}}$ and $\Delta g^{\ddagger}_{\mathrm{red}}$ have to be provided in order to reach the activated state (*activated complex*, denoted with ‡). Statistically defined fractions of the activated complex will reach the final state or return to the initial state, respectively. Under electrochemical equilibrium, the free energy of the oxidized equals the reduced state of the *entire* HOR, according to Equation 2.7. For the particular Volmer step, the free energy in the reduced state $(150\,\mathrm{meV})$ is higher than in the oxidized state $(75\,\mathrm{meV})$ [19, 21]. An overpotential lowers the free energy of the oxidized state by $ze\eta$ (in meV) or $zF\eta$ (in $\mathrm{J\,mol^{-1}}$)[1], with $z = 1$ for a single Volmer step. The activation energies for oxidation and reduction $\Delta g^{\ddagger}_{\mathrm{ox}}$ and $\Delta g^{\ddagger}_{\mathrm{red}}$ do not necessarily change equally with the overpotential, the transfer coefficient α describes the asymmetry

$$\Delta g^{\ddagger}_{\mathrm{ox}} = \Delta g^{\ddagger,0}_{\mathrm{ox}} - \alpha z F \eta \tag{2.19}$$

$$\Delta g^{\ddagger}_{\mathrm{red}} = \Delta g^{\ddagger,0}_{\mathrm{red}} + (1-\alpha)\, z F \eta. \tag{2.20}$$

$\Delta g^{\ddagger,0}_{\mathrm{ox}}$ and $\Delta g^{\ddagger,0}_{\mathrm{red}}$ are the activation energies for oxidation and reduction under equilibrium conditions. The external current density of the electrode i results from the sum of anodic and cathodic current densities i_{ox} and i_{red}, whereby the latter is negative and the anodic current

---

[1] In case of the HOR, the positive overpotential results from a positive shift of the solid electrode potential and/or a negative shift of the electrolyte potential from the equilibrium, the HOR is facilitated thereby.

density is positive by definition

$$i = i_{\mathrm{ox}} + i_{\mathrm{red}} = zFk_{\mathrm{ox}} - zFk_{\mathrm{red}}. \tag{2.21}$$

According to the model of Svante Arrhenius, the reaction rate of oxidation and reduction k_{ox} and k_{red} can be described as a function of the activation energy and the temperature T [23]

$$k_{\mathrm{ox}} = K_{\mathrm{ox}} c_{\mathrm{red}} \exp\left(-\frac{\Delta g^{\ddagger}_{\mathrm{ox}}}{\Re T}\right) \quad \text{and} \quad k_{\mathrm{red}} = K_{\mathrm{red}} c_{\mathrm{ox}} \exp\left(-\frac{\Delta g^{\ddagger}_{\mathrm{red}}}{\Re T}\right) \tag{2.22}$$

with empiric rate constants K_{ox} and K_{red} and the concentrations of the reduced and oxidized species c_{red} and c_{ox}. The *Butler-Volmer* equation is constructed with Equations 2.19 to 2.22

$$i = zFK_{\mathrm{ox}} c_{\mathrm{red}} \exp\left(-\frac{\Delta g^{\ddagger,0}_{\mathrm{ox}} - \alpha zF\eta}{\Re T}\right) - zFK_{\mathrm{red}} c_{\mathrm{ox}} \exp\left(-\frac{\Delta g^{\ddagger,0}_{\mathrm{red}} + (1-\alpha)\, zF\eta}{\Re T}\right). \tag{2.23}$$

Without an external electrode current ($i = 0$, $\eta = 0$), both oxidation and reduction currents are equal and denoted as the *exchange current density* i_0

$$i_0 = i_{\mathrm{ox}}(\eta = 0) = -i_{\mathrm{red}}(\eta = 0) = zFK_{\mathrm{ox}} c^{\mathrm{ref}}_{\mathrm{red}} \exp\left(-\frac{\Delta g^{\ddagger,0}_{\mathrm{ox}}}{\Re T}\right) \tag{2.24}$$

$$= zFK_{\mathrm{red}} c^{\mathrm{ref}}_{\mathrm{ox}} \exp\left(-\frac{\Delta g^{\ddagger,0}_{\mathrm{red}}}{\Re T}\right). \tag{2.25}$$

$c^{\mathrm{ref}}_{\mathrm{ox}}$ and $c^{\mathrm{ref}}_{\mathrm{red}}$ are the reference concentrations of oxidized and reduced species, respectively. i_0 is a characteristic value for the catalyst activity. Besides intrinsic material parameters and morphology of the catalyst it also depends on the electrolyte and operating conditions such as temperature. With i_0 the Butler-Volmer equation can be simplified to

$$i = i_0 \left[\left(\frac{c_{\mathrm{red}}}{c^{\mathrm{ref}}_{\mathrm{red}}}\right) \exp\left(\frac{\alpha zF\eta}{\Re T}\right) - \left(\frac{c_{\mathrm{ox}}}{c^{\mathrm{ref}}_{\mathrm{ox}}}\right) \exp\left(\frac{-(1-\alpha)\, zF\eta}{\Re T}\right)\right]. \tag{2.26}$$

The overpotential η refers to the *activation overpotential* of one electrode, without other contributions such as ohmic resistance or transport overpotential, and is denoted in the following as $\eta_{\mathrm{act,an}}$ and $\eta_{\mathrm{act,ca}}$ for anode and cathode, respectively.

2.4 Typical Cell Design

For scientific or experimental purposes, PEFCs are often realized as *single cells*, while for technical applications multiple single cells are assembled to *stacks*. A cell typically comprises planar components, being assembled in a multilayer setup, as shown in Figure 2.4. The electrochemically active components are compressed between *bipolar plates (BPP)* with *flowfields* (FF), which act as anode and cathode of two adjacent cells in a stack.

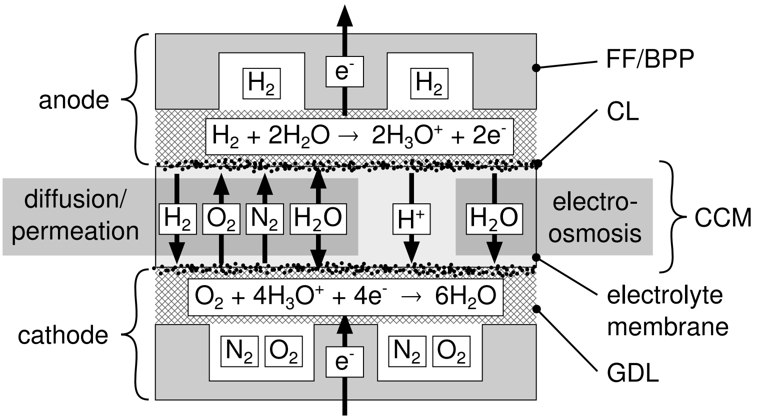

Figure 2.4: Typical single cell setup, electrode reactions and main species transport mechanisms.

2.4.1 Catalyst Coated Membrane

The core component of a cell is the electrolyte membrane, sandwiched between the anode and cathode catalyst layer (CL). The unit is referred to as *catalyst coated membrane* (CCM). The membrane is about $15 - 50\,\mu\mathrm{m}$ thick, whereby the tendency goes to a further thickness reduction in order to reduce ohmic losses, as long as the influence of gas crossover effects can be controlled. To maintain mechanical integrity of thin membranes, they are mostly mechanically reinforced with a porous PTFE core. The CLs are usually between 5 and $15\,\mu\mathrm{m}$ thick agglomerates of carbon black, with dispersed platinum or platinum alloys on it and infiltrated with ionomer. The membrane is ideally gas tight, so hydrogen and air in the anode and cathode gas compartment, on either side of the membrane, should not mix. However, small gas crossover cannot be prevented, especially thin membranes allow a certain crossover flow.

2.4.2 Gas Diffusion Layer

Between CL and BPP a porous gas diffusion layer (GDL) is employed. It is based on nonwoven carbon papers, woven carbon cloth or other substrates based on carbon such as foams or felts with a thickness of about 130 to $250\,\mu\mathrm{m}$ [24]. Its primary functions are

- mechanical protection of the sensitive CCM
- electrical contacting of the CL with low contact resistances
- heat transfer of the waste heat from the cell reaction
- drainage of product water while the membrane remains sufficiently humidified and
- enabling a homogeneous gas supply to the CL.

Particularly the balance between water drainage and gas supply is subject of wide research activities as both targets are contradictory. In order to enhance water drainage from the GDL and ensure water-free pores for gas transport, hydrophobic coatings are applied to the GDL, usually based on PTFE. These increase the capillary pressure in the pores, so the GDL acts as a barrier for water from the CL and increases liquid water pressure in the CL. In order to enhance the electrical and thermal contact between GDL and CL and to reduce mechanical stress to the membrane, a *micro porous layer* (MPL), is applied on the CL facing side of the GDL, made of carbon black powder. The MPL has a significantly lower porosity and often a higher PTFE loading compared to the rest of the GDL. As a result of the higher capillary pressure, the MPL was observed to be almost dry under normal operating conditions [25]. It has an essential function as it keeps the gas pathways to the CL free of water. Without a MPL, the GDL tends to be flooded at its interface to the CL and cell performance is significantly reduced due to gas transport inhibition [26].

2.4.3 Flowfield and Bipolar Plates

Figure 2.4 indicates that the CCM and the GDLs are sandwiched between two BPPs, one on the anode and one on the cathode side. They act as current and heat collectors, as gas distribution elements and help to remove the product water from the cell. For gas and water transport they exhibit a FF, consisting of channel and land structures, which aim to distribute gases – air or oxygen and hydrogen – homogeneously over the active cell area.

A BPP has an anode FF on one side and a cathode FF on the opposite side in the stacking direction. In case of liquid cooled PEFC, a coolant FF is situated between both FF, inside the BPP. The BPP is then composed of two single plates, one with the cathode FF and one with the anode FF.

Table 2.1: Comparison of the characteristics between molded graphitic and stamped metallic BPPs.

	molded graphite composite BPPs	stamped metallic BPPs	
typical cell pitch[†]	$3 - 5$	$1.2 - 1.5$	mm
typical material density	$1600 - 2100$	$7800 - 8000$	$\mathrm{kg\,m^{-3}}$
process time	$> 30^{\bullet}$	$1.5^{\star}$	s
joining method	adhesive bonding	laser welding	
contact resistance	very good	coating required	
forming restrictions	independent design of coolant and gas FF	coolant FF is negative of gas FF	
minimum forming radii	0.1	0.2	mm
minimum mold release slopes	5	20	deg

[†] The *cell pitch* describes the periodicity between cells in a stack, in the direction of stacking.

• For molding only.

⋆ For stamping only.

BPPs for mass production are manufactured either from graphite composite material or from sheet metal. The former are molded from a mixture of binder and graphite filler in powder form. The mass is cured in the cavity into its final geometry. Anode and cathode plate are joined together to a BPP assembly by bonding, whereby the adhesive is applied in a dispensing or screen printing process. Graphitic BPPs are widely used as they exhibit a good chemical stability, but for mass production the high process times of $> 30\,\mathrm{s}$ are critical.

Metallic BPPs are particularly interesting for high volume production as the processing time is at least one order of magnitude lower than for graphitic BPPs in case of progressive die stamping, as indicated in Table 2.1. Substrates most commonly used are stainless steels, often 316L or 304L [27, 28]. The sheets are usually $0.075 - 0.1\,\mathrm{mm}$ thick, with a clear trend to thinner materials in order to reduce the cell pitch, weight and material cost. Also titanium alloys are employed for their outstanding chemical stability even though the raw material is expensive. The mentioned stainless steels exhibit a good corrosion stability, but no good conductivity due to passivation layers formed on their surface. Conductive coatings are required in order to ensure low ohmic resistances over the lifetime of a BPP.

2.5 Mass Transport

Proton conductivity of the ionomer membrane essentially depends on the mobility of water molecules, so that it is also permeable for liquid water. Water transport between anode and cathode side is possible driven by concentration gradients in both directions, which can be approximated by Fick's law of diffusion[1]. Furthermore the conducted protons in the electrolyte are dragging water molecules in their solvation shell towards the cathode side. This effect, called *electroosmotic drag*, is quantified by the electroosmotic drag coefficient K_{drag}

$$K_{\mathrm{drag}} = \frac{\dot{n}^{\mathrm{mem}}_{\mathrm{H_2O,eo}} F}{i_{\mathrm{ely}}} \tag{2.27}$$

as the relation between molar water flux in the membrane $\dot{n}^{\mathrm{mem}}_{\mathrm{H_2O,eo}}$ and the protonic current i_{ely}. K_{drag} can reach values up to $1-3$ under typical PEFC conditions[2] [29–32].

Although the membrane has the function of a *gas separator*, it is not ideally gas tight. Gases – oxygen, hydrogen and nitrogen – can be exchanged via the liquid water phase of the electrolyte membrane. Beside partial pressures of the species on both sides of the membrane, the humidification state of the ionomer essentially determines the gas crossover rates, a higher water content generally favors gas crossover [33–35]. In particular nitrogen crossover plays an important role for PEFC operation as its accumulation on the anode side in combination with a recirculation loop requires purging strategies to limit the inert gas fraction. Under common operation conditions the nitrogen fraction can exceed $50\,\mathrm{vol.}\,\%$ [33].

Hydrogen or oxygen has to be transported from the FF channels through the porous GDL and MPL to the CL by diffusive and hydraulic transport, while generated product water has to be removed from the cell. A pressure and concentration gradient emerges from FF to CL as soon as current is drawn and reactants are consumed. The scalar molecular diffusion flux $\dot{n}$ is described by Fick's first law [1]

$$\dot{n} = -D_{i,j} \nabla c \tag{2.28}$$

with the binary diffusion coefficient $D_{i,j}$ and the species concentration c. For the diffusion of more than two components, as it can be the case in fuel cells, Fick's law is expanded to the Stefan-Maxwell Equations in a matrix form, as done in Section 7.2.3. The hydraulic transport in the porous structures is described by the Darcy equation with the scalar fluid velocity u, the permeability of the porosity κ, the dynamic viscosity μ_{f} and the pressure p [36]

$$u = \frac{-\kappa}{\mu_{\mathrm{f}}} \nabla p. \tag{2.29}$$

On the cathode side, the reactant is diluted with at least $79\,\mathrm{vol.}\,\%$ of nitrogen[3]. As only oxygen is consumed in the ORR, diffusion is a dominating transport mechanism in the porous layers.

---

[1] See Equation 7.10.

[2] Cell temperature $T_{\mathrm{cell}} < 80\,°\mathrm{C}$ and membrane water content $\lambda_{\mathrm{mem}} = 10 - 22$.

[3] Disregarding the water content in the gas feed.

Water removal from the cell and reactant supply to the electrodes are contradictory objectives. Therefore the water distribution in the GDL plays an important role and essentially determines the cell efficiency. Due to the wide range of different pore sizes and morphologies, water transport was shown to take place via discrete percolation pathways instead of a homogeneous flooding of the porosity [37, 38]. In some experinents it could be observed that these pathways do not change during cell operation [39, 40]. Some groups aim to intentionally arrange water transport pathways in patterns by GDL modification in order to enhance cell performance [41, 42].

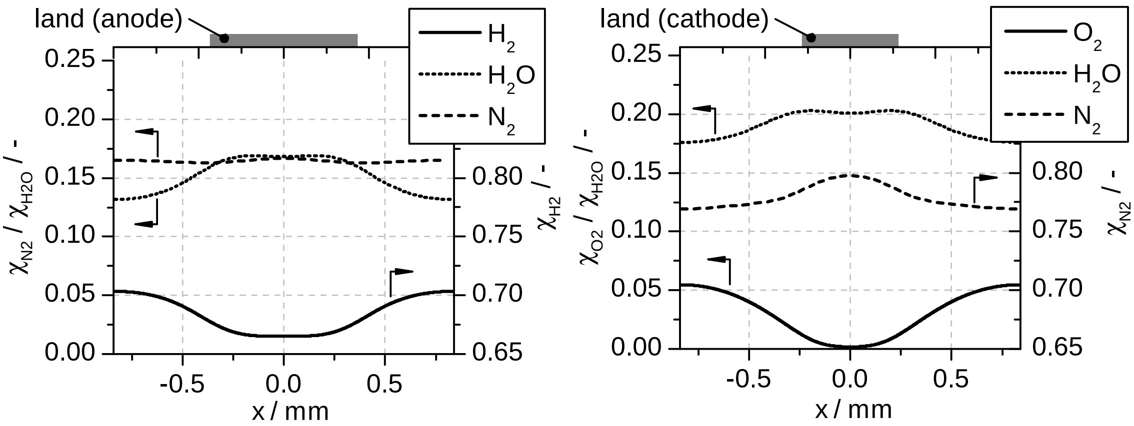

Figure 2.5: Molar fraction χ of species on the anode (left) and cathode (right) CL over one channel-land pitch of the FF at a current density of $1.6\,\mathrm{A\,cm^{-2}}$. Values were calculated with the model described in Section 7.2.

Particular attention is paid to the channel-land structure of the FF, as transport pathways between the FF channels and the electrode areas below the lands are obviously longer than to the areas below the channels. Figure 2.5 shows the molar fractions χ of the involved species in the CL on anode and cathode side over the width of one FF pitch extracted from the model in Section 7.2. In the area under the land significant reactant depletion is seen on anode and cathode side. On the cathode side oxygen concentration drops down to almost 0, which emphasizes that air cathodes are a bottleneck in PEFC operation. Water, which is present only in gaseous form in this model, is accumulated mainly under the lands, as also verified by neutron radiography elsewhere [26].

On anode and cathode side, usually more than the stochiometrically required gas flows are supplied in order to ensure a sufficient reactant concentration in the CL as well as to improve liquid water discharge by an appropriate differential pressure. The stoichiometry λ is defined as the relation between supplied and stoichiometric gas flows $\dot{V}$ and $\dot{V}_{\mathrm{stoich}}$

$$\lambda = \frac{\dot{V}}{\dot{V}_{\mathrm{stoich}}} \tag{2.30}$$

whereby $\dot{V}_{\mathrm{stoich}}$ depends on the actual cell current I, cell temperature T, and the partial pressure of the reactant p

$$\dot{V}_{\mathrm{stoich}} = \frac{I\Re T}{pzF} \tag{2.31}$$

with the number of transferred electrons per gas molecule z (HOR: $z = 2$, ORR: $z = 4$).

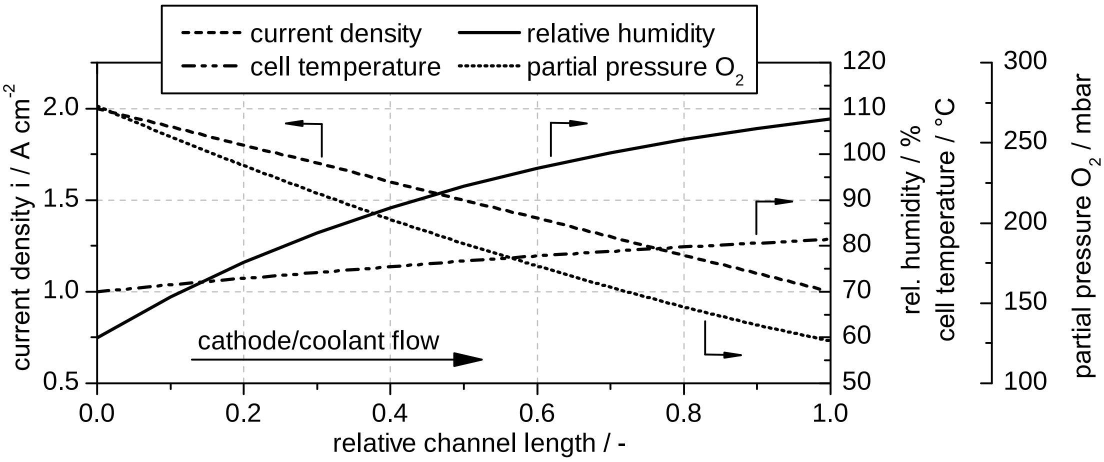

Figure 2.6: Schematic illustration of the gradients of coolant/cell temperature, current density, oxygen partial pressure and relative humidity over the length of a cathode FF channel. Air and coolant are streaming in co-flow. No liquid water discharge is taken into account. Stoichiometry is set to 1.8.

Due to reactant consumption, oxygen partial pressure on the cathode side exhibits a negative gradient over the channel length, entailing a decrease in local current density towards the cathode outlet [43], indicated in Figure 2.6. Product water is mainly discharged via the cathode due the high gas volume flow compared to the anode. Water accumulation leads to an increasing humidity towards the cathode outlet. A configuration where cathode gas and coolant are streaming in the same direction is advantageous as the temperature increases towards the outlet and enhances water discharge by evaporation. In the shown example the relative humidity exceeds $100\,\%$, illustrating the importance of liquid water discharge from the FF. The situation on the anode side differs from the cathode as flow velocities are lower due to the higher reactant concentration and low stoichiometries. As a result water uptake capacity of the gas and the pressure drop over the flowfield are lower, so that liquid water removal on the anode side is less effective compared to the cathode. Liquid water transport is driven by the pressure drop over the flowfield, which can be influenced by the FF geometry.

2.6 Cell Characteristics

Under real conditions, one will notice that the calculated Nernst potential cannot be reached. An OCV of only about $0.9 - 1.05$ V can be measured instead of the 1.23 V (at 25 °C) according to Equation 2.16. Gas crossover of hydrogen to the cathode and oxygen to the anode give rise to this difference. HOR is facilitated on the cathode side, ORR on the anode side, leading to an *electrical load* without an external current being measured [34]. As a consequence, the cell voltage drops down by the crossover overpotential η_{xo}.

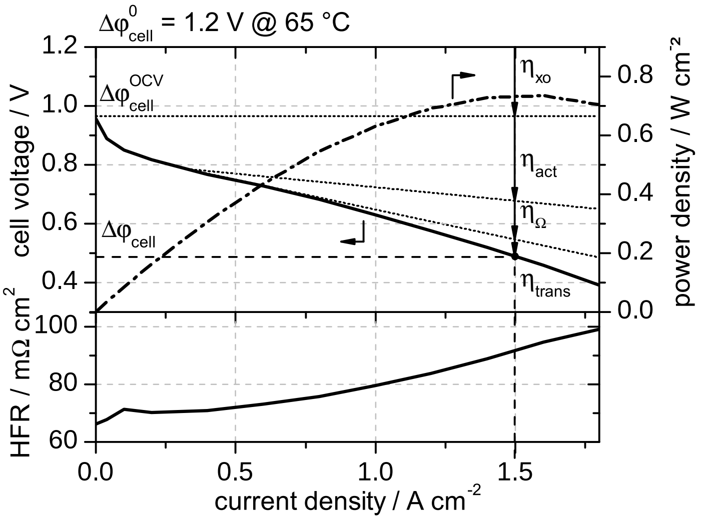

Figure 2.7: IV-curve[1] of a PEFC and the according power density. Overpotentials due to loss mechanisms are indicated schematically. The bottom diagram shows the high frequency resistance (HFR), measured with a milliohmmeter at 1 kHz.

Under external load, the cell voltage drops down steadily as a consequence of loss mechanisms, depicted in an *IV-curve*, as exemplarily shown in Figure 2.7. The losses are quantified by the overpotential η (see Equation 2.17). The total activation overpotential η_{act} is calculated from the activation overpotentials of anode and cathode $\eta_{\mathrm{act,ca}}$ and $\eta_{\mathrm{act,an}}$

$$\eta_{\mathrm{act}} = \eta_{\mathrm{act,ca}} - \eta_{\mathrm{act,an}}. \tag{2.32}$$

---

[1] Measurement conditions: Stoichiometry $\lambda = 2.5$ on anode and cathode side, cell temperature $T = 65$ °C, atmospheric operation.

Activation prevails especially in the lower load range over the other loss mechanisms. η_{act} is negative in a PEFC as $\eta_{\text{act,ca}} < 0$ and $\eta_{\text{act,an}} > 0$. The cathode activation overpotential is dominant as anode activation overpotentials are small, usually below $100\,\text{mV}$ [44]. Activation overpotentials can be calculated from the current density by the Butler-Volmer equation (Equation 2.26) with numerical methods. For overpotentials $|\eta_{\text{act,i}}| >> \frac{RT}{zF}$ one part of the Butler-Volmer equation (the reduction term in case of the anode, the oxidation term in case of the cathode) becomes negligible small [4] and the activation overpotentials can be calculated directly by the *Tafel equation*

$$\eta_{\text{act,an}} = \frac{\Re T}{\alpha z F} \ln\left(\frac{|i|}{i_0}\frac{c_{\text{red}}^{\text{ref}}}{c_{\text{red}}}\right) \quad \text{and} \quad \eta_{\text{act,ca}} = \frac{-\Re T}{(1-\alpha)\,zF} \ln\left(\frac{|i|}{i_0}\frac{c_{\text{ox}}^{\text{ref}}}{c_{\text{ox}}}\right). \tag{2.33}$$

All current conducting components in a fuel cell are ohmic resistors. The main absolute contribution to ohmic losses arises from the ionic resistance of the electrolyte membrane and the electrolyte in the CL. Both fluctuate in the range of several magnitudes as operating conditions, especially temperature and humidification, vary. Particularly under low temperature and humidification the electrolyte conductivity decreases dramatically [45, 46]. The bulk resistances of CL, GDL, BPP and endplates and contact resistances are relatively constant and low. The ohmic overpotential η_Ω results from Ohm's law with all component resistances $R_{c,\Omega}$ being connected in series and with the active cell area A_{cell}

$$\eta_\Omega = i \cdot A_{\text{cell}} \sum_i R_{c,\Omega}. \tag{2.34}$$

The total ohmic resistance of a cell is measured by a milliohmmeter at $1\,\text{kHz}$ (see Section 4.1.3), here referred to as *high frequency resistance* (HFR). Figure 2.7 shows that the HFR rises with current density, likely due to membrane dehydration at high gas flows and electroosmotic drag.

Due to diffusive and hydraulic mass transport losses in the cell, especially in the porous layers GDL, MPL and CL, the partial pressure of the reactants in the electrodes will be reduced under high current densities, as the consumed gas flows are high and also the generated product water blocks the pores of the diffusion layers. This mass transport losses lead to a transport overpotential η_{trans} as the Galvani potential as well as reaction kinetics strongly depend on the reactant concentration.

2.7 Degradation Mechanisms

PEFCs underlie various degradation mechanisms, leading to a performance loss over the lifetime. The ionomer membrane and the CL were identified as the main contributors and though are subject of extensive research activities.

Platinum Dissolution and Agglomeration

Platinum or platinum alloys, dispersed on porous carbon black supports, are commonly used as PEFC catalysts. Basically platinum can be dissolved in the aqueous solution of PEFCs

$$\mathrm{Pt} \longrightarrow \mathrm{Pt}^{2+} + 2\,\mathrm{e}^{-} \tag{2.35}$$

whereby the solubility strongly depends on the environmental conditions such as pH, humidity, temperature and electrode potential. Dissolved platinum can migrate into the ionomer membrane and precipitate by reduction with hydrogen permeating the membrane, resulting in a platinum deposition in the membrane (*Pt band*). Platinum oxide layers can be formed on the catalyst surface with chemisorbed oxygen or oxygen from water molecules, leading to a deceleration of platinum dissolution. As oxide formation depends on the electrode potential, potential cycling can lead to reduction and re-establishment of the oxide layer, and as a consequence to the enhancement of platinum dissolution. Dissolved platinum can precipitate on other crystalline platinum particles on the CL (*Ostwald ripening*), leading to particle growth and a reduction of the active surface area. A third discussed mechanism is the migration and agglomeration of crystalline platinum, as the formation of bigger particles is energetically favored. It also results in bigger agglomerates with a reduced active surface area. [47, 48]

Carbon Support Oxidation

Carbon of the CL support can be oxidized to carbon dioxide or monoxide under the presence of water according to the following reactions [47, 49]

$$\mathrm{C} + 2\,\mathrm{H_2O} \longrightarrow \mathrm{CO_2} + 4\,\mathrm{H^+} + 4\,\mathrm{e^-} \qquad \Delta\varphi^0_{\mathrm{COR,CO_2}} = 0.207\,\mathrm{V_{SHE}} \tag{2.36}$$

$$\mathrm{C} + \mathrm{H_2O} \longrightarrow \mathrm{CO} + 2\,\mathrm{H^+} + 2\,\mathrm{e^-} \qquad \Delta\varphi^0_{\mathrm{COR,CO}} = 0.518\,\mathrm{V_{SHE}} \tag{2.37}$$

with the according equilibrium potentials $\Delta\varphi^0_{\mathrm{COR,CO_2}}$ and $\Delta\varphi^0_{\mathrm{COR,CO}}$ for the carbon oxidation reaction (COR). Both reactions – catalyzed by platinum [50] – lead to an irreversible loss of carbon support including the supported platinum catalyst particles. The reaction mechanism requires the presence of water and therefore depends on local operating conditions. Below $0.8\,\mathrm{V}$, carbon corrosion rates are low, but under higher electrode potentials, such as OCV conditions, significant carbon loss rates occur [49]. Particularly a local starvation of hydrogen on the anode, caused by unfavorable cell design, operating conditions or an air/fuel boundary during cell startup/shutdown, was identified as a main cause for carbon corrosion as it can lead to high cathode potentials [51–57]. Basically the HOR drops down in the hydrogen starved area and as a result from the reduced proton generation the electrolyte potential decreases locally. As the solid potential on the cathode side stays constant due to electrical in-plane conductivity of CL and GDL, the cathode electrode potential rises up. Cathode electrode potentials of $> 1.4\,\mathrm{V}$ were measured, leading to a fast deterioration of the CL [53, 57].

Membrane deterioration

Especially under transient humidity conditions, the electrolyte membrane can be subject to serious mechanical stress due to swelling and shrinking under water uptake and discharge. The polymer tends to creep until (micro-)cracks are formed, leading to an increased gas crossover rate. Once a crack occurred, gas crossover and combustion reaction of hydrogen and oxygen lead to an increase in local temperature and further acceleration of the local decomposition of the membrane [48, 58–61]. Different groups identified the edges of the active area as the main affected region as clamping leads to point loads (cf. Section 3.2.2 and 7.1).

More attention was paid to chemical decomposition of the ionomer membrane in the last years. The involvement of hydrogen peroxide (H_2O_2) in the degradation was proven by various groups [8, 62, 63]. H_2O_2 can be generated by an incomplete reduction of hydrogen [62]

$$O_2 + 2\,H^+ + 2\,e^- \longrightarrow H_2O_2 \qquad \Delta\varphi^0_{\mathrm{H_2O_2}} = 0.67\,\mathrm{V_{SHE}} \tag{2.38}$$

whereby the reaction is favored by low electrode potentials. Therefore peroxide formation is believed to occur mainly on the anode side with oxygen permeated from the cathode [64]. Peroxide itself does not attack the ionomer, but as it is chemically unstable, it can easily be decomposed to radicals ($\cdot$OH or $\cdot$OOH), e.g. under the presence of metal ions or platinum particles in the membrane. Radicals can lead to an unzipping of the PFSA structure, beginning with the weak side chains up to the backbone structure [8, 64]. The decomposition results in a reduction of the membrane thickness and therefore in a further increase of gas crossover and to an acceleration of the decomposition process.

Chapter 3

On the Fringes of the Active Area

Regarding degradation effects of PEFCs, much attention has been paid to mechanisms such as carbon corrosion [50, 65–67], platinum agglomeration and dissolution [47, 66, 68–70] or mechanical and chemical membrane deterioration [71–74]. Their occurrence and intensity is tightly coupled to local operating conditions such as humidity, temperature or reactant concentration. As these can vary on temporal as well as on spatial scales as a result of operating parameters and cell design implications, degradation effects are also likely to occur inhomogeneously [51, 53–55, 75–81]. Concerning this matter, the outer perimeter of the active area in a single cell is of particular interest. A specific design of this area is required since CCM and GDL have to be integrated in a mechanically favorable way, while anode and cathode gas compartments have to be sealed against each other and towards the environment. Also the media are supplied and discharged at the edges of the active area FF.

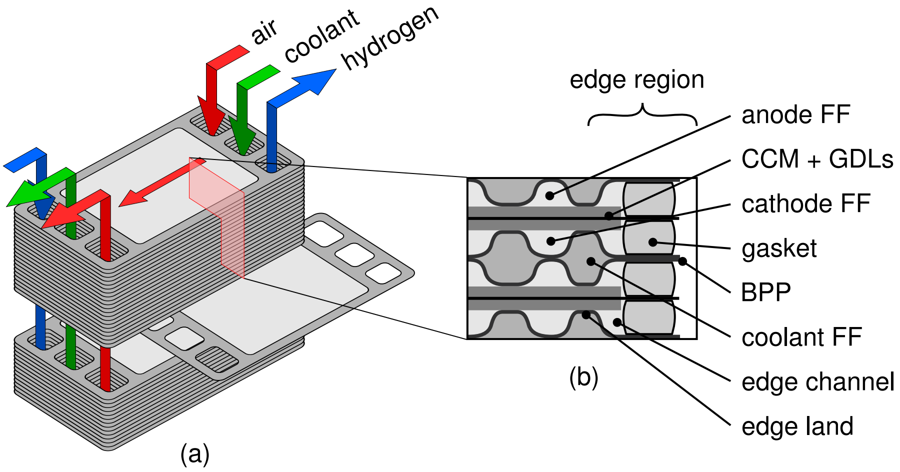

Figure 3.1: (a) A plurality of planar single cells is assembled to a stack. The reactants and the coolant are supplied and discharged via manifold openings in the BPP in a direction perpendicular to the cell plane. (b) Each cell is composed out of a CCM, two GDLs, gaskets and BPPs with FFs for anode and cathode reactants and for a coolant.

As a result of the different design parameters in the outer perimeter of the active area, local conditions, such as reactant distribution, liquid water fraction, mechanical load onto the membrane or contact to a sealant material, may vary. Hence also degradation mechanisms and performance may be different compared to the rest of the active area. The influence of this specific area has yet not been fully understood, only a few publications are dedicated to this topic. This work aims to comprehensively investigate the outer perimeter of the active area, regarding cell design, local operating conditions and degradation mechanisms, in order to understand the interrelation between cell design and both performance and degradation in this specific area.

In the following, the outer perimeter of the active area is referred to as *edge region*, as indicated in Figure 3.1, comprising the sealant, the outermost channel of the FF (*edge channel*) and the outermost land of the FF (*edge land*).

3.1 Cell Concepts

Overall cell layout, FF design and component selection are always in strong interrelation with the concept of media supply and the sealing solution of a cell. In the following an overview is given over different prevalent cell designs regarding their impact on the configuration of the edge region. Also references to relevant patents, disclosing different types of edge region designs, will be provided.

3.1.1 Review of Stack and Cell Designs

A PEFC stack is composed of a plurality of planar single cells. A BPP, a CCM and two GDLs are stacked alternatingly onto each other in a direction perpendicular to the cell plane as shown in Figure 3.1. On either side of a BPP is a FF, one for the anode fuel gas for a first cell and one for the cathode oxidant on the opposing side for a second neighboring cell. Both single plates of a BPP encase a coolant FF which is discharging the reaction waste heat. The supply of all media is realized via openings in each BPP (*manifolds*), in the example at a longitudinal end of the BPP, and are then distributed over the active area and discharged over further manifold openings.

Figure 3.2 (a) shows a view on the cathode side of a BPP, including sealing and welding lines, of an exemplary cell layout. It can be divided into the manifold regions at both longitudinal ends of the BPP and the active area in the middle part. A gasket surrounds each manifold and the active area on the anode and cathode side of the CCM in order to seal them against the environment and against the other media compartments. The coolant FF between both single plates of a BPP is sealed against the environment and against the gas manifolds by welding of

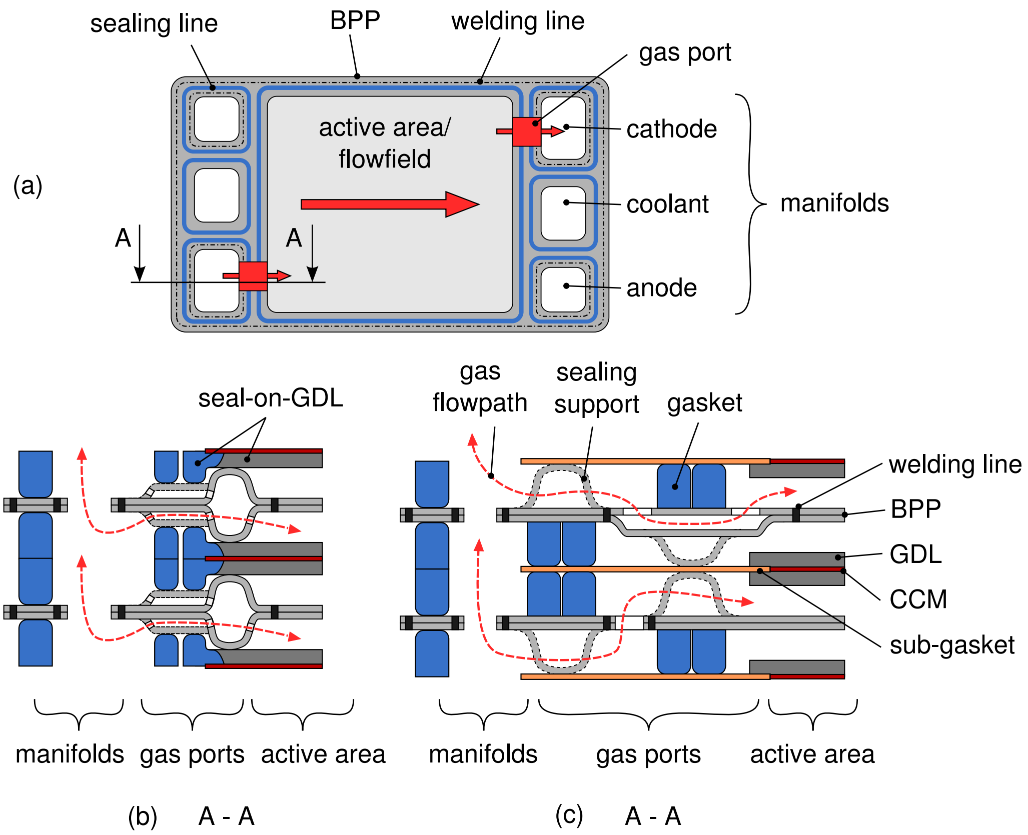

Figure 3.2: (a) View on the cathode side of a BPP, with the gas pathways indicated in red. Gas port regions connect the manifolds with the correlating FF. (b) Exemplary solution for the design of the gas port, whereby both single plates of the BPP are raised up locally to create a passage volume in between [82]. (c) An offset of the sealing lines on both sides of the BPP enable the gas feed between manifold and FF [83]. A SG is required to mechanically stabilize the CCM in its outer perimeter.

both plates around the gas manifolds and around the whole BPP, as shown in Figure 3.2 (a) by the dot-dashed line.

Both gases are interchanged between manifold and the corresponding FF via a *gas port* structure, as depicted schematically in Figure 3.2 (a). The gas ports aim to lead the media streams across the sealing lines of manifold and active area and across the welding line of the manifold. A wide variety of gas port concepts exist. Three prominent ones will be explained here.

Figure 3.2 (b) shows a gas port solution, disclosed in a patent application [82]. In the gas port region, both plates of the BPP are raised locally, forming a volume between each other, through which gases are conducted. The gaskets superimposed to the raised area are reduced in their thickness to compensate the reduced sealing gap. The concept enables all sealing lines to be congruent in the stacking direction which is mechanically advantageous.

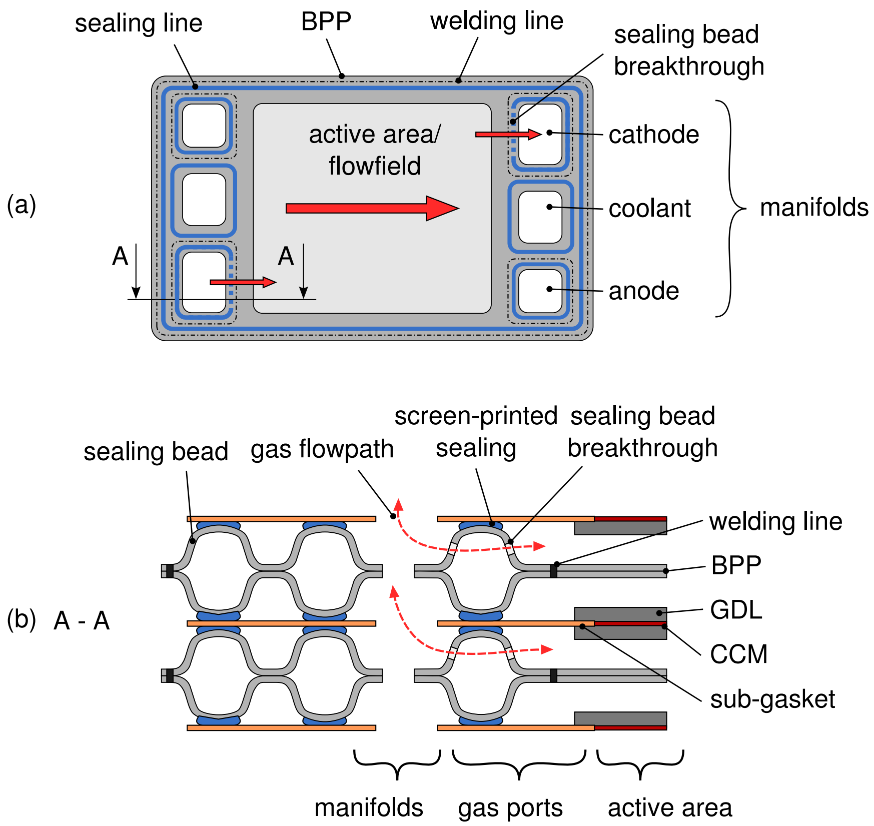

Figure 3.3: (a) View on the cathode side of a BPP with indicated sealing and welding lines. The solution requires a CCM with a SG, in order to protect the CCM from mechanical damage. (b) The sealing structure comprises a metallic bead with a screen-printed sealing on it. Gas supply and discharge is performed via breakthroughs in the bead.

As gases are locally conducted in between both plates of the BPP, the gas port region has to be sealed against the coolant FF by welding lines around it (not shown in Figure 3.2). Another design concept for the gas ports is shown in Figure 3.2 (c), according to a patent of Rock et al. [83]. It is based on the lateral offset of two gaskets from each other on both sides of a BPP in the gas port region. In between the two gaskets, the media flow tunnels the BPP and so crosses the sealing lines into the FF or vice versa. As the drawing indicates, different structures are required in two neighboring BPP. This can be achieved by using identical BPPs and rotating every second BPP by 180° around the stacking axis. As the sealing lines are locally incongruent in the gas port region, support features are required on the BPP to ensure mechanical stability. They are in direct contact with the CCM and induce high stresses. In order to avoid mechanical deterioration, a reinforcing frame around the CCM is required. This *sub-gasket* (SG), made from polymer foils such as polyethylene terephthalate (PET), polyethylene naphthalate (PEN) or Kapton [84] (single sheet thickness $30 - 80\,\mu\mathrm{m}$), is adhered to the CCM, for instance by laminating, and withstands high mechanical loads [85–89]. It can be on only one side of the CCM (one layer SG) or on both (two layer SG).

According to Figure 3.3 (a), the sealing line for the active area can also be routed all around the manifold sealings. In contrast to the setups shown in Figure 3.2, one sealing line instead of two separates two adjacent media compartments from each other. The sealing itself is implemented as a combination out of a metal bead, integrally formed with the BPP, and a screen-printed sealing on it (Figure 3.3 (b)), according to various patents [90–92], whereby the required elasticity comes from the elastomer as well as from the bead. The gas ports are just openings in the sealing beads [93]. Welding lines surround the gas manifold sealing beads. Metallic sealing beads require very high compression forces in order to reach gas tightness, so the employment of a SG is indispensable due to high mechanical loads onto the CCM.

3.1.2 Sealant Application

Loose gaskets are often used in laboratory cells (Figure 3.4 (a)), but are not suitable for mass production of PEFC stacks as their low stiffness impedes both automated handling and geometric measurements for quality assurance issues. Therefore sealants are usually formed on a stiff component of a cell, such as the BPP, GDL or a SG, to create a subassembly of reproducible and stable geometry. Forming technologies employed for the sealing structure are cured-in-place (CIP), injection molding (IM) or screen printing. The latter is only viable to print thin elastomer layers up to $200\,\mu\mathrm{m}$. They are employed in combination with a metallic bead, so that manufacturing and assembly tolerances can be compensated by plastic deformation of the bead (see Figure 3.3). CIP techniques are elastomer dispensing processes with subsequent curing by UV-light or heat. Scalability to high volume production is not feasible due to long process times. Also the required compression forces are relatively high for CIP sealings. IM gains more and more interest, as the formed sealing structures exhibit low geometric tolerances and structured sealings can be formed. But further process time reduction is required for mass volume production, which is an issue mainly attributed to sealant material development.

Application of the sealant to the BPP is of increasing interest, mainly due to the high dimensional stability of the BPP and the simplicity in handling and cell assembly. Figure 3.4 (b) shows an exemplary cell setup with a sealing structure applied on a BPP, with two GDLs and a CCM including a SG. The sealant can generally be applied onto a BPP or a single plate. Beside the sealing structure for both gas compartments also the coolant FF sealing can be formed with an elastomer, so that the welding process of the BPP drops out. The robustness

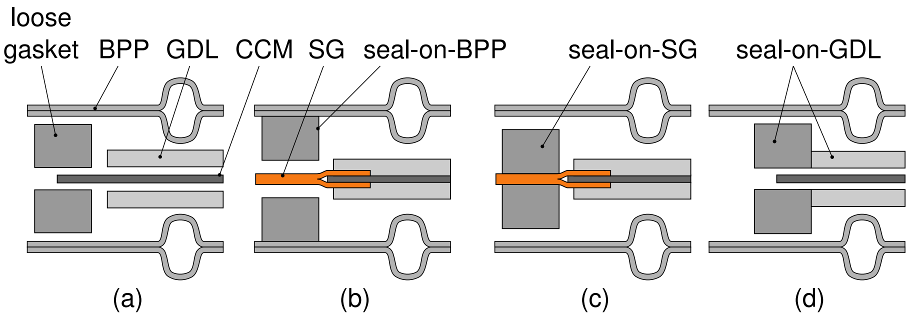

Figure 3.4: Cell components before cell assembly with different kinds of sealant application. (a) Loose gaskets for experimental cells. (b) Seal-on-BPP, sealing structure adhered to the BPP in an injection molding or screen-printing-process. (c) Seal-on-SG, sealing structure applied on the SG in an injection molding or screen-printing process. (d) Seal-on-GDL, sealing structure mechanically adhered to the GDL. Two seal-on-GDLs and a CCM are pre-assembled and then assembled with the BPP.

of the SG also allows a direct application of a sealant to it (seal-on-SG, Figure 3.4 (c)), e.g. by an IM process. It has to be considered that in this configuration the expensive and sensitive CCM is involved in a further manufacturing step, giving rise to higher reject cost and to longer process times due to lower allowed process temperatures. The last solution, seen in Figure 3.4 (d), depicts a seal-on-GDL whereby the sealant is adhered to one or two GDLs in an IM process and is then assembled to a subassembly with the CCM. In this case the use of a SG can be avoided with an appropriate cell design as the CCM is mechanically favorable attached to the sealant at its outer edge without significant peak stresses.

PEFC stacks with metallic BPPs exhibit cell pitches of $1.2 - 1.5\,\mathrm{mm}$. With sheet metal thicknesses of $0.075 - 0.1\,\mathrm{mm}$ the sealing gap remains small with $1 - 1.35\,\mathrm{mm}$. Manufacturing and assembling tolerances, thermal expansion and shrinkage of the components and sealant material deterioration require a compensation by the gasket in order to maintain the minimal contact pressure for gas tightness. Flat gaskets as schematically depicted in Figure 3.4 are relatively stiff. Small thickness deflections result in high force changes and can lead to failure after several thousand hours of operation. Whereas structured sealings, with narrow sealing lips, exhibit high local contact pressures[1] and a higher elasticity compared to flat sealings [94, 95]. Hence structured sealings are more robust against thickness changes and maintain gas tightness over a wide range of compression thicknesses. For redundancy, often two or more parallel sealing lips are employed.

---

[1] Gas tightness of a sealing system in terms of a maximal tolerable pressure difference until a distinct leakage occurs is determined by the highest local contact pressure of the contact partners.

3.1.3 Flowfield Bypass

Homogeneous distribution of the reactants over the active area of a cell is a main task of the FF structure. Its boundary is defined by the outermost land (edge land). Between edge land and the gasket of the active area a gap (edge channel) is inevitable due to manufacturing and assembly tolerances of the sealing component and of the BPP. The edge land can be structured in order to increase mechanical stability of metallic BPP, as disclosed in a patent of Miller et al. [96]. The according design elements are often referred to as *piano structures*.

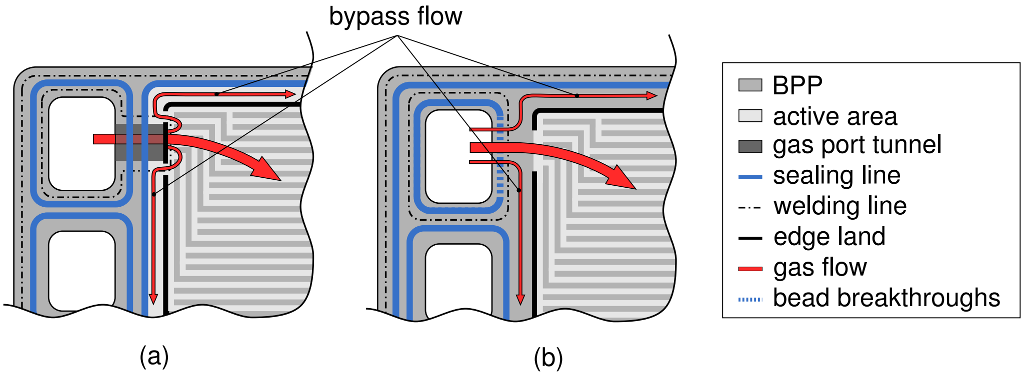

Figure 3.5: A bypass gas flow can emerge around the FF structure of a cell. (a) In case of a seal-on-GDL design, according to Figure 3.2 (a) and (b). (b) For a SG based design, as shown in Figure 3.3.

Figure 3.5 (a) shows an exemplary cell setup for a seal-on-GDL solution (referring to the solution from Figure 3.2 (a) and (b)). The gap between edge land and sealing structure can be reduced to less than $1\,\mathrm{mm}$ with some effort so that the edge channel is narrow. The electrochemically active region extends to the sealing structure. The edge land is interrupted in this case, as welding lines cross the edge land in order to surround the whole gas port region. Gas can pass through the interruptions into the edge channel, forming a bypass stream around the FF.

When a SG is employed according to a solution as shown in Figure 3.3, a fraction of the CCM at its outer perimeter is electrochemically inactive due to the coverage by the SG (Figure 3.5 (b)). A bypass around the FF can also occur, as interruptions in the edge land are required close to the gas port region. The edge region is wider compared to the seal-on-GDL design, as the overlap region of SG and CCM, which can be up to $4\,\mathrm{mm}$ wide, must not be overcompressed.

In both presented solutions, gas can also be exchanged between FF and edge channel by transport through the GDL, besides hydraulic transport through gaps in the edge land. In BPP based on graphite composite material, the edge land can be formed continuously around the FF, whereby only gas transport via the GDL is possible into the edge channel.

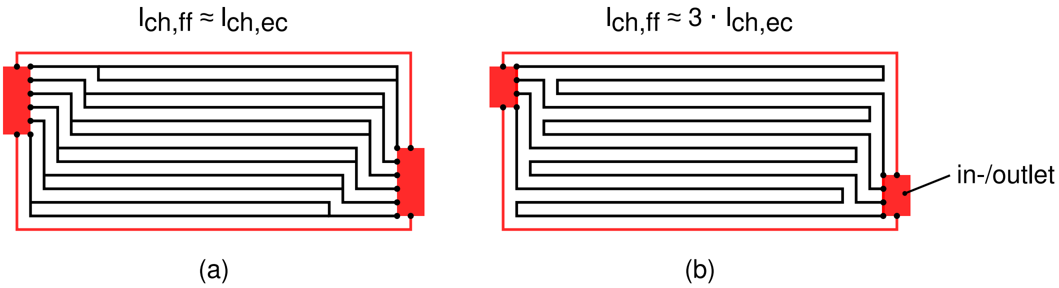

Figure 3.6: The length and geometry of edge channels and FF channels is crucial for the influence of a FF bypass. (a) edge channel and FF channel lengths $l_{\text{ch,ec}}$ and $l_{\text{ch,ff}}$ are approximately equal with straight FF channels. (b) The FF channel is around three times longer in a multiple serpentine FF.

The impact of a bypass flow around the FF can be different depending on the cell design. Particularly the cross section and length of the bypass/edge channel compared to the geometry of a regular FF channel is crucial. Figure 3.6 shows two common FF layouts, in (a) with straight channels where one channel of the feed area supplies two FF channels. The length of a FF channel $l_{\text{ch,ff}}$ and of an edge channel $l_{\text{ch,ec}}$ is approximately the same, whereas a FF channel is around three times longer than the edge channel in case of a multiple serpentine FF as shown in Figure 3.6 (b).

In order to estimate the influence of a bypass, gas flow distribution is calculated for different, technically relevant cell designs with a simple numerical approach. The assumptions made are

- the GDL is not included, cross flow over the FF lands is not possible
- only reactants, air on the cathode side and pure hydrogen on the anode side, are considered, product and humidification water are not taken into account
- current density and hence reactant consumption is homogeneously distributed over the active area[1].

The pressure drop $\frac{\partial p}{\partial x}$ of a FF channel and of an edge channel is given by their length l_{ch}, the fluid density ρ, the pressure loss coefficient ζ and the hydraulic diameter of the channel d_{H} [97]

$$\frac{\partial p}{\partial x} = \zeta \frac{l_{\text{ch}} \rho u^2(x)}{2 d_{\text{H}}}, \tag{3.1}$$

---

[1] In case of an employed SG, the edge region of the CCM is inactive. This effect is not taken into account here as it was found to have a negligible influence on the gas flows.

whereby only straight channels are assumed, bends are neglected as their influence is considered insignificant in this case. The local gas velocity over the length of a channel $u(x)$ is

$$u(x) = \frac{\dot{n}_{\mathrm{ch}}(x)\Re T}{p(x) d_{\mathrm{ch}} w_{\mathrm{ch}}}. \tag{3.2}$$

$\dot{n}_{\mathrm{ch}}(x)$ denotes the local molar gas flow, d_{ch} is the channel depth and w_{ch} the channel width. In the edge channel as well as in the FF, gas consumption drags down gas velocity over the length of a channel. The local molar gas flow is given by

$$\dot{n}_{\mathrm{ch}}(x) = \frac{i l_{\mathrm{ch}} w_{\mathrm{act}} \lambda}{zF} - \int\limits_{0}^{x} \frac{i \cdot w_{\mathrm{act}}}{zF}\, dx \tag{3.3}$$

with the cell current density i, the stoichiometry λ and the width of the electrochemically active area per channel w_{act}[1]. ζ is calculated by [97]

$$\zeta = \iota \frac{64}{Re} \quad \text{with} \quad Re = \frac{u(x) \rho d_{\mathrm{H}}}{\eta_{\mathrm{f}}} \tag{3.4}$$

with a coefficient for the channel geometry ι, the Reynolds number Re and the dynamic viscosity η_{f}. The channel geometry is approximated as a rectangular cross section. Fitting the empirical values for ι from Gnielinski et al. [97] with a cubic approach leads to

$$\iota = -0,769 \left(\frac{d_{\mathrm{ch}}}{w_{\mathrm{ch}}}\right)^3 + 2,035 \left(\frac{d_{\mathrm{ch}}}{w_{\mathrm{ch}}}\right)^2 - 1,885 \left(\frac{d_{\mathrm{ch}}}{w_{\mathrm{ch}}}\right) + 1,5. \tag{3.5}$$

In small cells serpentine channels can be realized, while in large-scale cells pressure drop becomes relevant and straight channels are preferred. The calculated setups (see Table 3.1) reflect this requirement, so that a $50\,\mathrm{cm}^2$ cell with serpentine FFs on anode and cathode, a $200\,\mathrm{cm}^2$ cell with straight channels on the cathode and serpentines at the anode and a $400\,\mathrm{cm}^2$ cell with straight channels on both sides are simulated.

Numerical iterations are performed with *Matlab/Simulink*. Pressure drop over both, edge channel and FF channel are calculated separately. The molar gas flow fraction through the bypass related to the total flow x_{bp} is adjusted until the pressure drop difference between FF and edge channel is below $0.05\,\mathrm{Pa}$ with a simple linear optimization scheme. The edge channel width $w_{\mathrm{ch,ec}}$ is varied while all other parameters are kept constant.

---

[1] In the FF w_{act} is equal to the *FF pitch*, which denotes the periodicity of the channel-land structure, the sum of channel and land width $w_{\mathrm{pitch}} = w_{\mathrm{ch}} + w_{\mathrm{l}}$. In case of the edge region, w_{act} is equal to the edge channel width plus half the width of the (edge) land $w_{\mathrm{pitch}} = w_{\mathrm{ch}} + \frac{1}{2} w_{\mathrm{l}}$.

Table 3.1: Parameter sets for calculation of FF bypass flows.

case	1	2	3	unit
active area	50	200	400	cm^2
FF type anode	serpentine	serpentine	straight	-
FF type cathode	serpentine	straight	straight	-
number of FF channels	42†	60†	80†	-
active area size ($l \times w$)	71.3×70.1	199.6×100.2	299.4×133.6	$\mathrm{mm} \times \mathrm{mm}$
FF channel geometry ($w \times d$)	anode: 0.6×0.5 cathode: 0.9×0.5			$\mathrm{mm} \times \mathrm{mm}$
FF pitch	1.67			mm
cell temperature	70			°C
inlet pressure	1.3			$\mathrm{bar_a}$
inlet stoichiometry	anode: 1.4 cathode: 1.7			-
current density	1			$\mathrm{A\,cm^{-2}}$

† The number denotes the parallel FF channels. In case of a serpentine FF, one continuously formed channel line includes three parallel channels.

The results in Figure 3.7 show that serpentine FFs exhibit a significantly higher bypass flow compared to straight FFs. x_{bp} exceeds $10\,\%$ for an edge channel width of $> 0.7\,\mathrm{mm}$ for all serpentine FFs without respect to the cell size. Whereby for straight channel FFs x_{bp} remains below $10\,\%$ for $w_{\mathrm{ch,ec}} < 2.5\,\mathrm{mm}$. Comparing the cathode side of the cells with 200 and $400\,\mathrm{cm}^2$ reveals that bypass effects are mitigated with the number of FF channels. Figure 3.7 also shows that serpentine FFs exhibit a significant drop of the stoichiometry in the FF λ_{ff} for raising edge channel widths, while straight FFs show a slight and linear stoichiometry drop. Due to a low inlet stoichiometry at the anode, in the 50 and $200\,\mathrm{cm}^2$ cell, λ_{ff} drops below 1 for $w_{\mathrm{ch,ec}} > 1.5\,\mathrm{mm}$, probably leading to a considerable cell performance break-in or degradation effects in a real cell.

Figure 3.8 shows the pressure drops over anode and cathode FF of the $200\,\mathrm{cm}^2$ cell. The cathode pressure drop does not show a significant sensitivity to the edge channel width, as the FF channels are straight and in the same length scale as the edge channel. The anode pressure drop decreases clearly, even more pronounced for higher current densities. This can have a significant influence on cell performance as liquid water removal relies on a sufficiently high FF pressure drop. For $w_{\mathrm{ch,ec}} > 1.5\,\mathrm{mm}$ anode FF stoichiometry drops below 1. Results are truncated at $\lambda_{\mathrm{ff}} = 1$ as the model does not account for that case.

Bypass effects can be minimized by inserting bypass breaking structures [98]. But depending on the cell design, an entire closure of the bypass is not always possible without inserting additional parts, e.g. due to assembly tolerances. Furthermore, if bypass breaking structures are formed, void volumes without a direct gas feed can arise. Water can easily accumulate

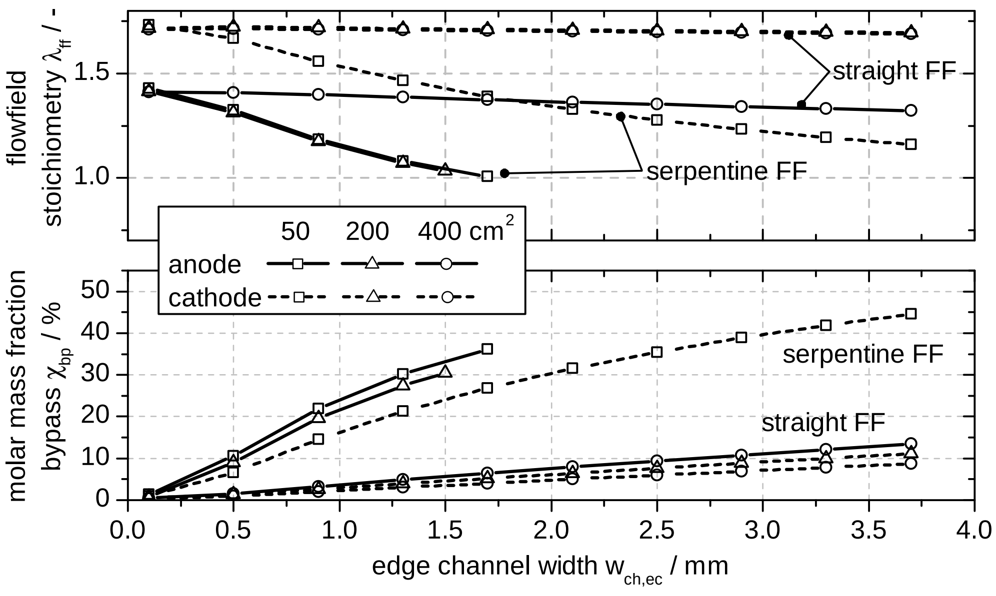

Figure 3.7: Top: Stoichiometry in the FF λ_{ff} in various cell designs for different edge channel/bypass widths $w_{\text{ch,ec}}$. Particularly in cells with a serpentine FF, a bypass can lead to a significant reduction of the stoichiometry in the FF, while the active cell area does not have a significant influence. Bottom: According molar gas flow fractions through the FF bypass x_{bp} on anode and cathode side.

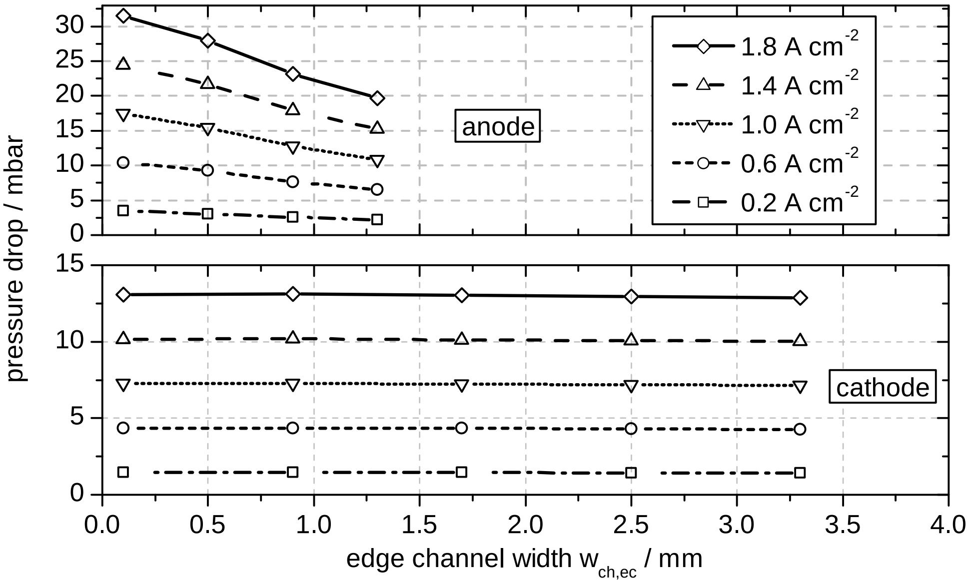

Figure 3.8: Impact of the edge channel width $w_{\text{ch,ec}}$ in a $200\,\text{cm}^2$ cell according to Table 3.1 on the FF pressure drop at different current densities. The anode pressure drop decreases significantly with an increasing bypass cross section. On the cathode side the influence of the bypass is negligible as FF and bypass channels exhibit a similar length.

there, which can be crucial for cell functionality, e.g. in case of a startup from freezing conditions.

3.1.4 Tolerances

Each manufacturing and assembly step is afflicted with tolerances. Forming of a gasket on another component comprises positioning tolerances of the substrate as well as tooling tolerances. The latter can be shifted towards a few $\mu\mathrm{m}$ but positioning tolerances can hardly be reduced below $0.1\,\mathrm{mm}$. Particularly positioning of flexible components, such as the CCM, GDLs or SG layers is subject to higher tolerances since they do not exhibit stiff reference elements.

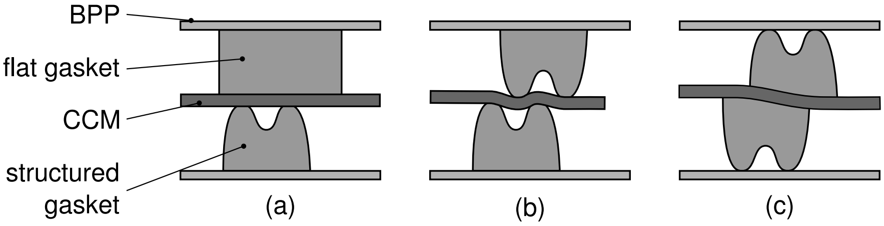

Figure 3.9: Impact of lateral assembling and manufacturing tolerances on the functionality of different sealing configurations. (a) Seal-on-BPP with combination of flat and structured sealing. (b) Seal-on-BPP with two structured sealings. A lateral offset causes high mechanical stresses in the CCM. (c) Seal-on-GDL or seal-on-SG solution, lateral offset can cause inhomogeneous pressure distribution, but only moderate stress onto the CCM/SG.

A differentiated sealing structure can only be formed by IM on the far side of a carrier element. In case of a seal-on-BPP design (Figure 3.9 (b)), the sealing lips are facing the CCM. A lateral shift between two BPPs reduces the pressure at the contact lines in absence of an opposing mechanical support. Also high mechanical strains can be induced into the CCM, increasing the risk of mechanical damage of the sensitive CCM in setups without a reinforcing SG [61, 99, 100]. Whereas a combination of flat and structured sealing features high tolerance against lateral offset of the BPP (Figure 3.9 (a)).

For designs with a sealing adhered to GDL or SG the sealing lips face the BPP as shown in Figure 3.9 (c). Lateral shift of the sealing carrying elements can cause a reduced contact pressure between lips and BPP, but with less impact on sealant functionality compared to (b). Also the mechanical load onto the CCM is reduced compared to (b).

In PEFCs the height adjustment between the cell components is crucial in order to ensure an ideal compression of every single component. Especially the functionality of GDL and gaskets

Table 3.2: Tolerance chain for different sealing concepts. Values refer to a full cell with a two layer BPP, two GDLs, a CCM and – if employed – a two-layer SG.

process	seal-on-GDL (Figure 3.4 (d))	seal-on-BPP/-SG (Figure 3.4 (b) and (c))
BPP stamping[†]	$\pm(2 \cdot 5\,\mu\mathrm{m})$	$\pm(2 \cdot 5\,\mu\mathrm{m})$
IM sealing height	$\pm(2 \cdot 10\,\mu\mathrm{m})$	$\pm(2 \cdot 10\,\mu\mathrm{m})$
GDL thickness[•]	$\pm(2 \cdot 10\,\mu\mathrm{m})$	$\pm(2 \cdot 10\,\mu\mathrm{m})$
SG thickness	-	$\pm(2 \cdot 5\,\mu\mathrm{m})$
CCM thickness	-	$\pm 5\,\mu\mathrm{m}$
sum	$\pm 50\,\mu\mathrm{m}$	$\pm 65\,\mu\mathrm{m}$

[†] Value applies to tolerances over a single plate as well as over different production batches. See [101].

[•] For the uncompressed GDL. For simplicity it is assumed that the same tolerance is valid for the compressed state.

strongly depends on their compression state. Regarding the cell designs, depicted in Figure 3.4, compression of the components in both main force paths – via sealing structures and via GDLs and CCM – is coupled. Hence thickness variations of the components can lead to varying compression states and therefore to an influence on the component functionality, particularly tightness of the gaskets and electrical and thermal contacting in the active area. An estimation of the thickness tolerances of single components for two exemplary sealing designs is given in Table 3.2. For the seal-on-GDL concept, CCM thickness variations can be neglected as the CCM is extended under the FF as well as under the gaskets. Tolerances of a seal-on-BPP or seal-on-SG sum up to about $15\,\mu\mathrm{m}$ more compared to seal-on-GDL. However both tolerances of ± 50 and $\pm 65\,\mu\mathrm{m}$ emphasize that sealing design can be challenging, considering sealing gaps of $< 1.3\,\mathrm{mm}$.

3.1.5 Sealing Materials

Although a wide variety of sealing materials for PEFCs has been investigated in the past, the focus currently lies on two main material categories, ethylene propylene diene monomer rubber (EPDM) [102–106] and silicone based materials [103–105, 107, 108]. The former is known for its low gas permeability, good stability against inorganic acids, aqueous solutions and coolant media with glycol additives. In addition decisive mechanical properties for reliable functionality, such as compression set or hardness over several thousands of hours are superior for EPDM [102, 103, 105, 106]. Particularly under bending load and increased temperatures, silicone gaskets are subject to crack formation and high mass losses. By-products of silicone are likely to cause catalyst poisoning [109, 110], while EPDM remains stable, as shown by Tan et al. [105, 106] and Lin et al. [103]. Also own measurements indicate that under exposure to deionized water (Figure 3.10 (a)) or a water-glycol mixture (BASF Glysantin® FC G 20-00/50, Figure 3.10 (b)) at 90 °C, EPDM exhibits lower mass loss compared to liquid silicone rubber (LSR) after more than $5000\,\mathrm{h}$ and even reaches an equilibrium state at a mass loss of about $2-3\,\%$. LSR showed a constant mass loss, leading to a significant loss of sealing force.

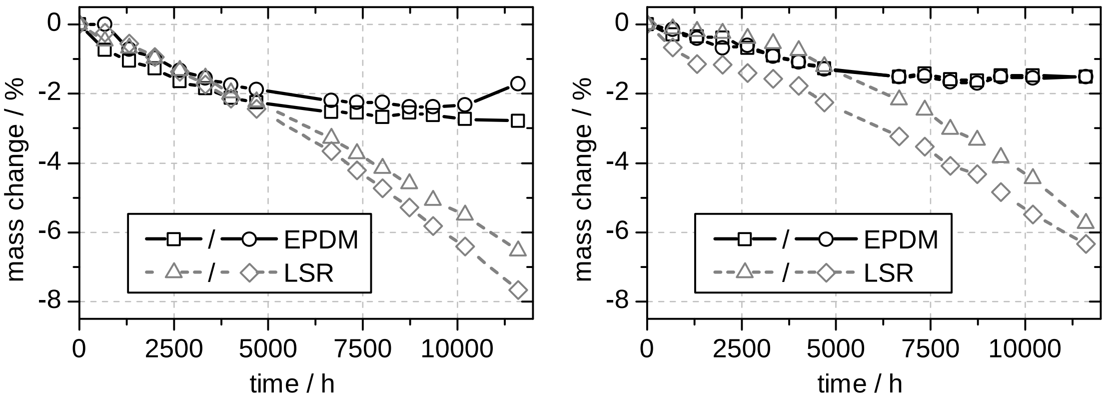

(a) Deionized Water.

(b) Water-glycol coolant medium.

Figure 3.10: Mass change of various EPDM and LSR samples under exposure to different media at 90 °C.

Most EPDM compounds are cross-linked by peroxide-initiated radical mechanisms [111]. Although allowing for relatively short process times, the process is not viable for PEFC applications as by-products can harm cell components or block active sites of the catalyst or the ionomer. By-products can be reduced or avoided by addition or condensation cross-linking, but reaction kinetics are significantly slower resulting in higher process times. Attention to silicone based materials has been paid mainly due to short polymerization times and a simple processability, especially in case of LSR. Two-component LSR materials for addition cross-linking are available and can be processed in IM tools. Still an issue for both, EPDM and silicones is the adhesion on the substrate, particularly on coated stainless steel alloys. Adhesive agent or primers are intended to be avoided, but plasma pre-treatment with or without additives could be a promising alternative.

3.2 Literature Review

In the previous sections, the main focus was on the interrelation of the cell concept with the design of the outer cell perimeter. The sealing solution as an essential part of the cell design dictates the design of the edge region and hence the resulting predominant operating conditions in the outer perimeter of the active area. As a result of the local conditions, degradation effects can differ from the active area and require a comprehensive analysis. Several groups already analyzed some aspects of the matter. In the following some of their results will be summarized, with a focus on degradation effects in the edge region of a PEFC as well as the investigation of prevailing operating conditions in this specific area.

3.2.1 Operating Conditions in the Edge Region

Only a few publications are dedicated to the operation parameters in the outer fringes of a cell. Freunberger et al. measured the local voltage drop between the current collector and the interface of GDL and CL in a small differential cell and calculated the local current density from a conductivity map of the GDL in sub-millimeter resolution [112, 113]. The small differential cell exhibited two channels of $2\,\mathrm{mm}$ width and three ribs of the same size. Under the outer rib the current density was significantly lower than under the inner rib, and about $1.3\,\mathrm{mm}$ under the outer rib even dropped to zero. It was concluded that the section under the outer rib was only fed with gas from one side and water accumulation blocked the GDL pores there. Li et al. aimed to model the experimental setup of Freunberger [114] in a 2D approach. Their results contradict the experimental findings as the difference in current density between inner and outer rib was not significant. But they concluded that the experimental results of Freunberger were not consistent due to inhomogeneous GDL compression or general shortcomings of the method, while they failed to consider the one-sided gas supply of the active area under the outer rib.

Lee et al. measured the local potential drop between current collector and the interface between cathode GDL and BPP in a 3-channel FF [115]. Under the outer rib, which was only fed by gas from one side, even under H_2/O_2 operation, the voltage drop was up to $10\,\mathrm{mV}$ lower compared to the inner rib, indicating a lower local current density. But it remains doubtful how the voltage drop could also be measured under the channel area with the described experimental setup.

Employing a CCM with a reinforcing SG at its outer perimeter requires an overlap between both layers for mechanical connection. Hence active area is covered partially by the SG. Zhao et al. compared a cell with a Pt/C catalyst under the SG to one without a CL in this area. They revealed from the comparison of cyclovoltammetry (CV) measurements of the different setups, that even under the SG, until about $1.2\,\mathrm{mm}$ from its edge, the CL contributes to the cell activity [84]. It was also shown that the porous CL under the SG contributes to gas crossover between anode and cathode gas compartment as gas can bypass the membrane around its edge.

3.2.2 Specific Degradation Effects

PFSA membranes are subject to swelling and shrinkage as a result of water uptake and release. The deformation induces stresses to the membrane, mostly pronounced in in-plane direction. In the active area, stresses are expected to be homogeneously distributed due to plane clamping between GDLs, assuming that channel-land variations can be neglected. In case of direct clamping of the membrane by gaskets in its outer perimeter, local load maxima can occur at the inner sealant border, as Huang et al. showed with a numerical model [58]. Also in some experimental works, mechanical membrane failure was observed to occur at the edges of the active area [59, 116, 117]. Others just suppose that the maximal mechanical deterioration occurs on the membrane edges [60, 118]. Employment of a SG can mitigate the effect, as it stabilizes the membrane/CCM on the fringes [84], and inhibit microcrack propagation [48], also load maxima are diminished. Wu et al. operated cells under humidity and load cycling and found cracks at the membrane edges in a cell without SG, while a SG prevented a second cell from mechanical membrane failure [59]. But on the other hand, employment of a SG can enhance gas crossover around the edge of a CCM, as gas can permeate through the porous CL [84], leading to the formation of H_2O_2 and radical species which results in an increase of chemical membrane deterioration [63, 64].

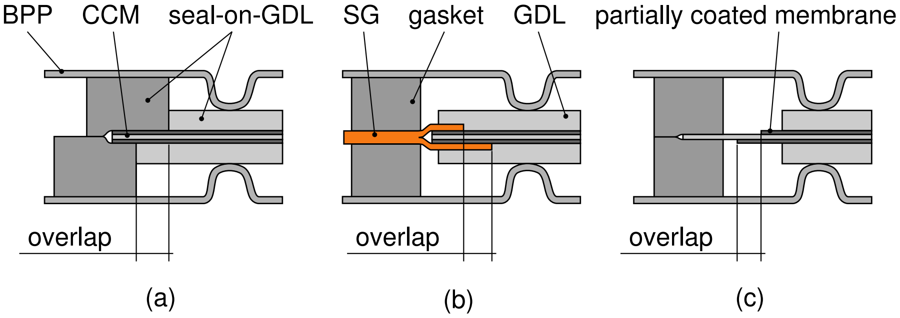

Figure 3.11: Effect of lateral assembly tolerances on the overlap between anode and cathode active area for different cell setups. (a) Offset between two seal-on-GDLs. (b) Offset between two layers of a SG. (c) In case of a partially catalyst coated membrane, the offset between the outer edges of both CL gives rise to an overlap of both active areas.

In case of a CCM with the catalyst coated area extending to the membrane edges, the active area on anode and cathode side is geometrically limited by coverage of the CCM by a SG or a sealing structure in the outer perimeter, schematically depicted in Figure 3.11 (a) and (b). Assembly tolerances of both, SG or gasket (e.g. in form of a seal-on-GDL) under industrial production conditions typically lie in the range of $\pm 0.1 - 0.4\,\mathrm{mm}$, so that the outer edge of the active area at anode and cathode side can exhibit an offset. Assuming that the cathode extends over the anode active area, the cell is locally supplied with oxidant on the cathode while the anode is subject to fuel starvation conditions. As a consequence, the hydrogen ion generation in the HOR and hence the membrane potential decrease, leading to a high cathode electrode potential. Many groups generally verified this effect, caused by flooding, insufficient gas supply or heterogeneities in reactant distribution by numerical modeling [51–54] or observation of cathode electrode thinning due to the high cathode potential and subsequent carbon corrosion [53–55]. So the intentional oversizing of the anode active area, so that even under consideration of large tolerances no fuel gas starvation occurs, could be advantageous [119].

Instead of a full area catalyst coating, catalysts can be applied partially onto the membrane on the anode and cathode side in order to reduce material costs. The coating process is subject to tolerances, so that anode and cathode CL are positioned with an offset to each other on their edges, as schematically depicted in Figure 3.11 (c). The impact of overlapping electrodes on membrane and electrode potentials in the outer perimeter is well known from the implementation of reference electrodes [120–123]. In case of an overlapping cathode, the membrane potential decreases outside the anode electrode edge due to a lack of protons emerging from the HOR. In contrast an anode overlap causes a raising membrane potential. The former case can cause a high cathode electrode potential as the solid electrode potential remains almost constant in the edge region while the electrolyte potential drops[1]. As a result, carbon corrosion of the cathode electrode support can occur. Sompalli et al. showed that, apart from catalyst support degradation, the membrane can be subject to significant thinning under a cathode overlap [124]. The effect was found to be more pronounced under low humidity conditions ($25\,\%\,\mathrm{RH}$) due to reduced proton conductivity of the electrolyte. An anode overlap eliminated the problem under full humidification, but under low humidification also inexplicable membrane thinning was found.

A group around J. Kawaji found out, that low local cathode potentials in the outer perimeter of direct methanol fuel cells correlate with high membrane degradation [125]. It was concluded that the low potentials could enhance peroxide formation in the ORR, leading to chemical membrane attack, but no explanation for the origin of the low local potentials was given.

---

[1] This assumption applies only if the solid electrode conductivity is high compared to the proton conductivity of the electrolyte, so that a potential gradient can only emerge in the electrolyte but not in the solid electrode.

3.3 Conclusions

In this chapter it was shown that the cell design on the fringes of a PEFC is strongly coupled to the entire cell and even to the stack design. The sealing solution determines the design of manifolds, gas ports and FF. Also the effort for component manufacturing and stack assembly can differ significantly with the sealing solution.

- A seal-on-GDL solution (Figure 3.4 (d)) enables a setup without the employment of an additional SG and for relatively small space requirements in the edge region of the cell. The space between sealing and edge land can be small and is only limited by positioning tolerances in the assembly process.
- Whereas a design using a SG (Figure 3.4 (b) and (c)) requires additional process steps and implies high space requirements in the outer perimeter of a cell. The overlap between SG and CCM can sum up to $0.5 - 20\,\%$ of the active area [85].
- Depending on the cell design the influence of a FF bypass can be enhanced and FF stoichiometry can suffer from significant reductions, especially for FFs with serpentine-like channels.
- A literature review revealed that specific degradation mechanisms can occur in the edge region. Without SG, the membrane runs the risk of fast thinning and failure due to high mechanical stresses. Also a setup with the cathode electrode exceeding over the anode electrode can cause membrane deterioration and oxidation of the CL carbon support on the cathode side.

Chapter 4

Experimental[*]

In-situ experiments in this work were carried out with a single test cell by means of classical electrochemical characterization techniques and post-mortem analysis. Static and dynamic water distribution inside the cell was visualized by neutron radiography (NR). In the following the cell design and the deployed experimental procedures are highlighted.

4.1 Experimental Setup

In the frame of this work a $50\,\mathrm{cm}^2$ single PEFC was developed, in particular fitted to the requirements of NR. The cell is designed as a technical cell, meaning that operating stoichiometries are comparable to full size cells and considerable reactant concentration gradients occur over the FF. However, the thermal concept does not allow for pronounced temperature gradients over the cell area. Predominantly experiments were performed with graphitic BPP, however, for the sake of completeness a metallic BPP design is presented as it was developed in the frame of this work in order to evaluate a novel sealing concept which is based on the present results.

4.1.1 Test Cell

Both, anode and cathode FFs consist of a distribution area with parallel channels, connecting the gas in- and outlets to a multiple serpentine channel FF as exemplarily shown for the anode in Figure 4.1. Two serpentines are supplied by one distribution channel. Compared to a straight FF, serpentines approximately triple the pressure drop over the FF, so that liquid water removal is facilitated. The cell plane is orientated vertically, so that both gas inlets are on top, the outlets on the bottom of the FF, facilitating liquid water discharge by the influence of gravitation. Geometries of the channel-land structure of the milled graphitic and stamped metallic BPP are shown in Table 4.1. Metallic BPPs are coated with gold to maintain low contact resistances. Used GDLs are nonwoven types with a MPL (Freudenberg H23C8). Their

---

[*] Parts of this chapter were published in [126], [127] and [128].

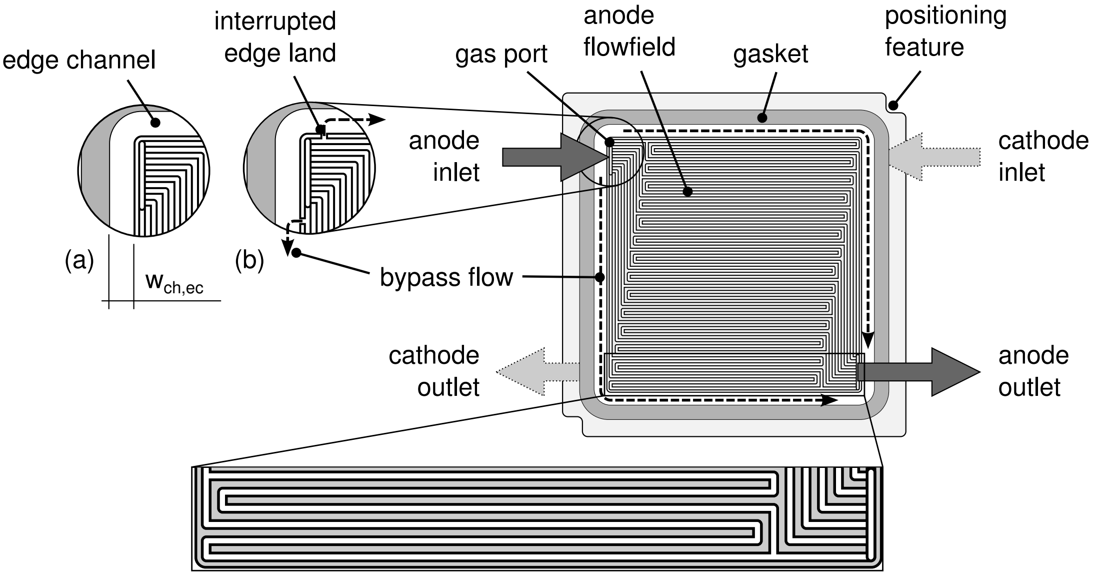

Figure 4.1: View on the FF of the anode BPP with multiple serpentine channels. Parallel single channels connect the main FF area to the gas in- and outlets. (a) With a continuously formed edge land, the edge channel is only accessible for gas by permeation through the GDL. (b) With gaps in the edge land, as found in many metallic FF designs, a bypass flow can occur around the FF.

Table 4.1: Details about the geometry of channel-land structures of the anode and cathode FF.

			graphitic BPP		metallic BPP		
			anode	cathode	anode	cathode	
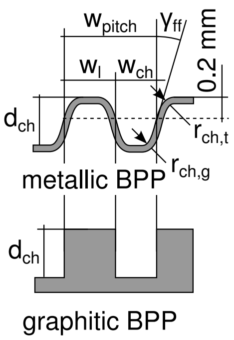	channel width	w_{ch}	0.81	1.11	$0.5^{\star}$	$0.77^{\star}$	mm
	land width	w_l	0.86	0.56	$0.95^{\star}$	$0.68^{\star}$	mm
	FF pitch	w_{pitch}	1.67	1.67	1.45	1.45	mm
	channel depth	d_{ch}	0.5	0.6	0.4	0.4	mm
	channel wall slope	γ_{ff}	0	0	20	20	°
	radius channel ground	$r_{ch,g}$	-	-	0.2	0.25	mm
	radius channel top	$r_{ch,t}$	-	-	0.3	0.25	mm
	no. of parallel channels		42	42	48	48	-

* Widths of channel-land structures with a channel wall slope $\neq 0°$ are measured at a channel depth of $0.2\,\mathrm{mm}$, as shown in the figure.

porosity is $70\,\%$ and their compressed thickness $200\,\mu\mathrm{m}$. The PTFE content amounts to $4\,\%$. State-of-the-art CCMs are used with a $15\,\mu\mathrm{m}$ thick PFSA membrane and a platinum catalyst loading of 0.1 and $0.4\,\mathrm{mg\,cm^{-2}}$ on anode and cathode side, respectively (Greenerity Concept MEA).

As explained in Figure 3.5, metallic BPPs can exhibit gaps in the edge land in some designs. This case is reproduced in the test cell by two small gaps of $0.8\,\mathrm{mm}$ in the edge land close to the in- and outlets (Figure 4.1 (b)). If not mentioned otherwise, the edge land is continuously formed around the FF (Figure 4.1 (a)) in the following experiments.

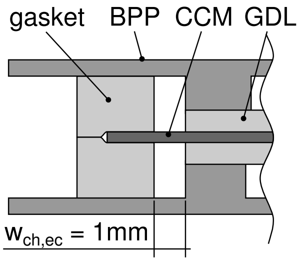

Figure 4.2: Standard sealing solution with flat gaskets.

As a cell sealing two flat gaskets made from EPDM are compressed with about $1\,\mathrm{N\,mm^{-1}}$ between the BPPs to a thickness of $0.7\,\mathrm{mm}$ each, as depicted in Figure 4.2. The CCM is in direct contact with the sealant. Both GDLs are aligned with the outer perimeter of the edge land. The width of the edge channel is adjusted to $1\,\mathrm{mm}$. Both, sealing setup and edge channel width are varied from the described solution in various experiments.

BPPs, CCM and gaskets are compressed between two endplates with a nominal compression force of $4050\,\mathrm{N}$. Thereby the GDL is compressed with $2650\,\mathrm{N}$ or $0.53\,\mathrm{N\,mm^{-2}}$ and the gaskets with $1400\,\mathrm{N}$. The endplates are $20\,\mathrm{mm}$ thick and made from aluminum, coated with nickel and silver, in order to ensure electrical conductivity as they also act as current collectors. Serpentine shaped cooling channels are integrated into each endplate. The coolant outlet is on the top side in order to facilitate gas bubble discharge. Venting of the cooling system is particularly relevant for NR as the cooling channels are in the field of view and bubbles cause image fragments. Therefore additional vents on top of the cooling channels are employed as shown in Figure 4.3. Deionized water is used as a standard coolant. For NR experiments it is replaced by heavy water (^2H_2O). The latter exhibits a low attenuation to neutrons [129, 130]. The coolant inlet temperature is generally adjusted to $1\,^{\circ}\mathrm{C}$ below the setpoint, additional heating pads (Minco Polyimide Thermofoil Heaters) on both endplates allow a precise temperature control to the setpoint.

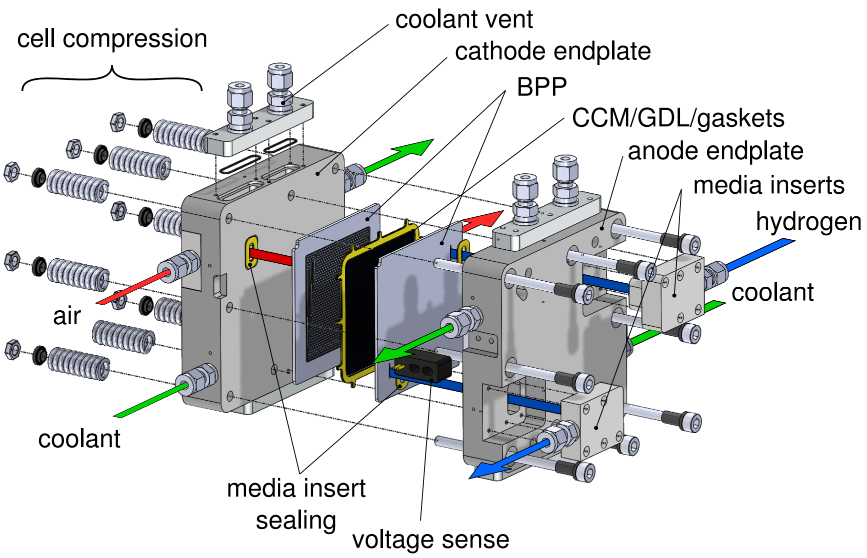

Figure 4.3: Assembly of the developed isothermal single cell.

Due to the single cell conception, both FFs can be supplied with gas from their backside without the need for manifolds which generally facilitates the cell design. The gases are supplied via media inserts, in order to avoid contamination of the gases by ions from the endplate substrate or coating. They are made of PTFE as it has a high transparency to neutrons [131]. Anode and cathode gas flows are configured in counter-flow mode (Figure 4.1). The coolant flow of each endplate is in co-flow with the gas flow on its side[1]. Emerging temperature differences between all coolant in- and outlets do not exceed $1.5\,\mathrm{K}$ due to the massive endplates, a good thermal contact between BPP and endplates and a high coolant flow of $1\,\mathrm{l}\,\mathrm{min}^{-1}$.

4.1.2 Setup for Sub-Zero Startups

For startup from sub-zero temperatures, the cells are cooled down to the start temperature by the coolant medium. A water-glycol mixture ($50/50\,\%$) is employed as a standard coolant medium. For experiments with NR a hydrogen-free fluid (Fluorinert$^{\mathrm{TM}}$ FC-770, 3M) is deployed due to its low attenuation to neutrons.

Cold starts from sub-zero temperatures are performed without an environmental chamber. To avoid fragments in NR experiments, condensation and freezing of water on the cell surface has to be prevented in the field of view. As Figure 4.4 shows, an additional hood is placed on both, anode and cathode endplate and is purged with dry nitrogen to keep the cell surface dry.

---

[1] The coolant FFs of both endplates are connected in series with a short, thermally isolated piping.

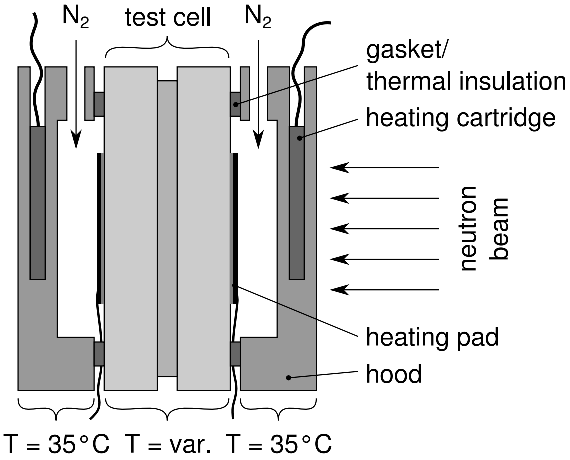

Figure 4.4: Cross section of the test cell with heated hoods, purged with dry nitrogen, to prevent condensation or freezing of water on the cell surface for NR experiments.

The hood itself is heated with cartridges to $35\,^{\circ}\mathrm{C}$ to prevent condensation on its outer surface. $2\,\mathrm{mm}$ thick silicon foam gaskets thermally isolate the hood from the test cell.

4.1.3 Test Bench

For cell conditioning and all experiments described in Chapter 7, a commercial test bench (GreenLight G100) is employed, the according schematic diagram is shown in Figure 4.5 (a). Gases are pre-humidified with a bubbler, the cell inlet pressure is controlled with a valve at the outlets, cascaded mass flow controllers in front of the humidifiers regulate air, nitrogen and hydrogen flows. All inlet pipes are heated to $5\,^{\circ}\mathrm{C}$ above the cell temperature. The ohmic cell resistance (high frequency resistance, HFR) is measured with a Tsuruga 3566 milliohmmeter at $1\,\mathrm{kHz}$.

For all experiments in Chapter 5 and 6 a self-made test bench (Figure 4.5 (b)) is used. High mass flows on anode and cathode $\dot{V}_{\mathrm{rec,an}} = \dot{V}_{\mathrm{rec,ca}} = 3\,\mathrm{l\,min^{-1}}$ are recirculated in front of the cell to improve dynamic behavior and stability of the humidification. Gas pressure is controlled by a proportional valve in the recirculation system. Gases are humidified with liquid water injectors. Mass flow controllers at the outlets of the cell control the mass flows through anode and cathode compartments. Droplets are separated in front of the mass flow controllers in order to mitigate measurement errors. The HFR is measured at $5\,\mathrm{kHz}$ by a direct modulation of the electrical load.

In all experiments, the cell temperature T_{cell} is measured with a thermocouple introduced in a hole in one of the endplates. T_{cell} is employed to control the coolant temperature and heating pads.

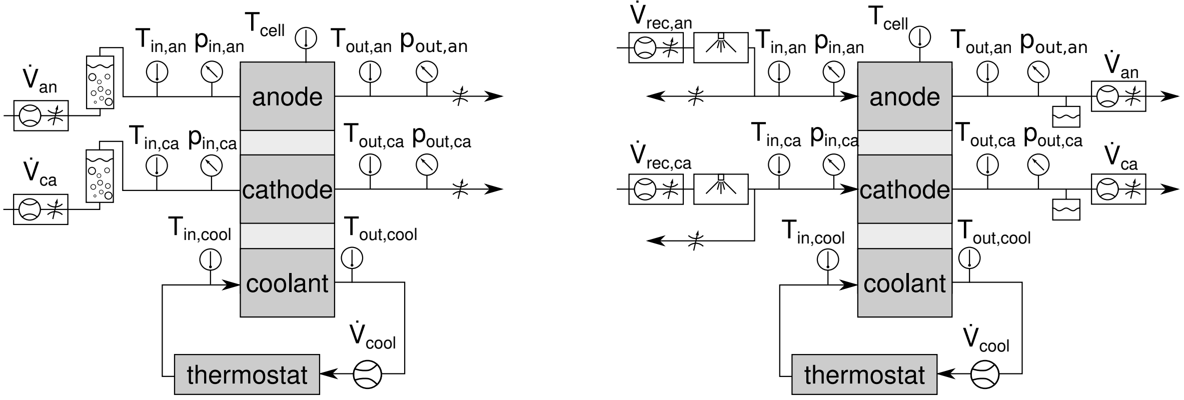

(a) Standard test bench.

(b) Test bench for NR and sub-zero startup experiments.

Figure 4.5: Schematic setup of test benches for operation of the test cell.

4.1.4 Cell Operation

Cells are operated in galvanostatic mode. Supplied gases are hydrogen on the anode and air on the cathode side. In some cases $30\,\%$ nitrogen is added on the anode, to simulate a hydrogen recirculation and nitrogen accumulation by crossover from the cathode side. Gases were humidified to 30 and $80\,\%$ RH, as listed in Table 4.2. Gas inlet pressures are close to atmospheric operation, the anode is constantly set to $100\,\mathrm{mbar}$ above the cathode. All cells undergo a conditioning procedure by potentiostatic cycling between OCV, $0.6\,\mathrm{V}$ and $0.4\,\mathrm{V}$ until steady state voltages do not change anymore.

Table 4.2: Standard operation parameters for the test cell.

parameter	symbol	value	unit
stoichiometry anode	λ_{an}	1.4	-
stoichiometry cathode	λ_{ca}	2.3	-
coolant volume flow	$\dot{V}_{\mathrm{coolant}}$	1	$\mathrm{l\,min^{-1}}$
cell temperature	T_{cell}	65	°C
gas inlet humidification anode	RH_{an}	30	%
gas inlet humidification cathode	RH_{ca}	80	%
anode inlet pressure	$p_{\mathrm{an,in}}$	1.3	$\mathrm{bar_a}$
cathode inlet pressure	$p_{\mathrm{ca,in}}$	1.2	$\mathrm{bar_a}$

An IV-curve of the test cell with graphitic BPPs in Figure 4.6 (a) shows a good performance with about $0.6\,\mathrm{V}$ at $1.3\,\mathrm{A\,cm^{-2}}$ and only slight mass transport losses at higher current densities. The HFR shows a slight trend to higher values at higher current densities. The metallic test cell exhibits a considerably lower performance with $0.6\,\mathrm{V}$ at $1.1\,\mathrm{A\,cm^{-2}}$ (Figure 4.6 (b)), likely an effect of the increased thermal and electrical contact resistances between BPP and GDL as a result of channel wall slopes and hence reduced contact areas. It emphasizes the challenging development of PEFCs with metallic BPPs. For the metallic BPPs, the cell performance reveals a low sensitivity to a temperature variation from 60 to $70\,°\mathrm{C}$, as seen in Figure 4.6 (b). The small voltage deviation of $45\,\mathrm{mV}$ at $1.8\,\mathrm{A\,cm^{-2}}$ can be explained by a reduced membrane humidification at $70\,°\mathrm{C}$, as the HFR is about $25\,\mathrm{m\Omega\,cm^2}$ higher at $70\,°\mathrm{C}$.

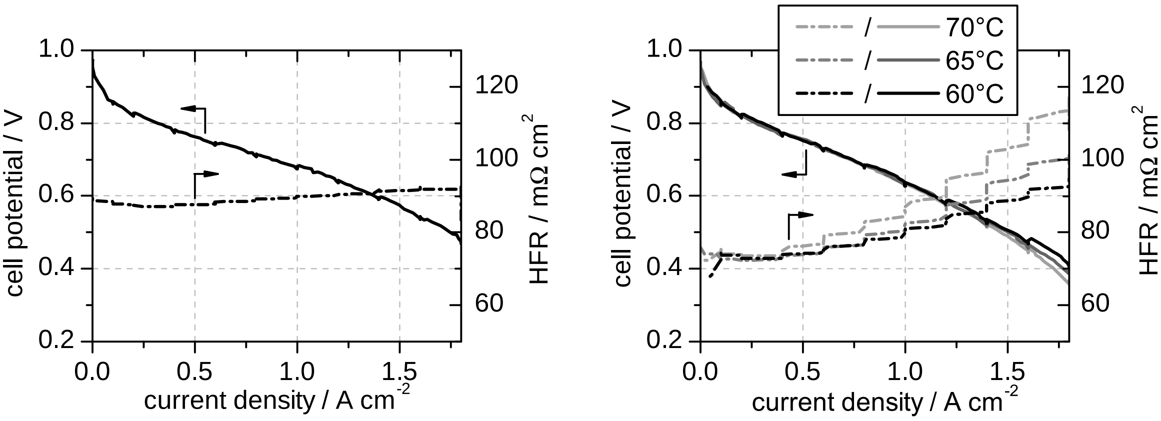

(a) Test cell based on graphitic BPPs, at a cell temperature of $65\,°\mathrm{C}$.

(b) Test cell based on metallic BPPs at different cell temperatures.

Figure 4.6: IV-curves and HFR for different test cells, with a stoichiometry of $\lambda = 2.5$ on anode and cathode. The cell current was decreasing from higher to lower values.

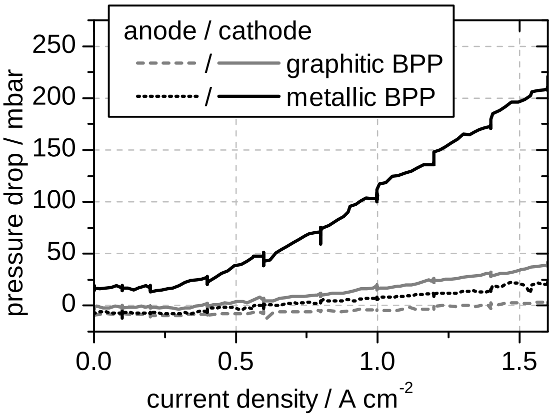

Figure 4.7: Pressure drop over the anode and cathode compartment for graphitic and metallic BPPs for $\lambda = 2.5$ on anode and cathode.

Pressure drop over the FF differs significantly between graphitic and metallic FF, especially for higher current densities and hence higher gas flows, indicated in Figure 4.7. The significantly reduced FF channel cross section of the metallic BPP gives rise to this effect. The generally higher pressure drop on the cathode side mainly originates from the higher gas flow on this side, as the reactant – oxygen – is diluted with nitrogen in air.

4.2 Basic Methods

For the experiments performed in the frame of this work a wide range of different electrochemical characterization techniques were applied. They are described in the following.

4.2.1 Linear Sweep Voltammetry

Gas crossover effects over the electrolyte membrane strongly depend on the structural composition of the membrane. Both, gradual membrane thinning due to chemical polymer decomposition and local mechanical membrane damage e.g. by GDL fiber penetration, can lead to an increase in gas crossover. Hence measurement of the latter can be an indicator for the mechanical membrane integrity. Here, linear sweep voltammetry (LSV) is performed in order to enable a precise determination of the gas crossover flow [34, 132].

The cell is conditioned with $3\,\mathrm{l\,min^{-1}}$ nitrogen on the cathode and $3\,\mathrm{l\,min^{-1}}$ hydrogen on the anode for $20\,\mathrm{min}$. Both gas flows are humidified to $80\,\%\,\mathrm{RH}$, the cell temperature is set to $65\,°\mathrm{C}$. The anode serves as a reference electrode, the cathode as a working electrode. The anode inlet pressure is kept constantly at $300\,\mathrm{mbar}$, the cathode inlet pressure at $200\,\mathrm{mbar}$, so hydrogen can permeate to the cathode. A positive voltage is applied from working to reference electrode by an external potentiostat (Zahner Zennium). The emerging external current from oxidation of hydrogen (HOR) on the working electrode i_{xo} can be measured and the molar hydrogen crossover flow $\dot{n}_{\mathrm{xo}}$ can be quantified with

$$\dot{n}_{\mathrm{xo}} = \frac{i_{\mathrm{xo}}}{zF}. \tag{4.1}$$

The cell voltage is gradually swept from 0.2 to $0.6\,\mathrm{V}$. Figure 4.8 (a) depicts the crossover current density over the cell potential. The finite internal short resistance of the membrane gives rise to a slight curve slope as the linear fits in Figure 4.8 (a) show. Therefore the y-axis intercept at $0\,\mathrm{V}$ is taken as the crossover current density. As Figure 4.8 (a) shows, the curve slope slightly rises up with the pressure difference between both gas compartments. An incomplete oxidation of the crossed over hydrogen particularly under low cell potentials at high pressure differences could be the reason for that. However, LSV enables an exact quantification of the crossover compared to methods based on pressure drop measurements,

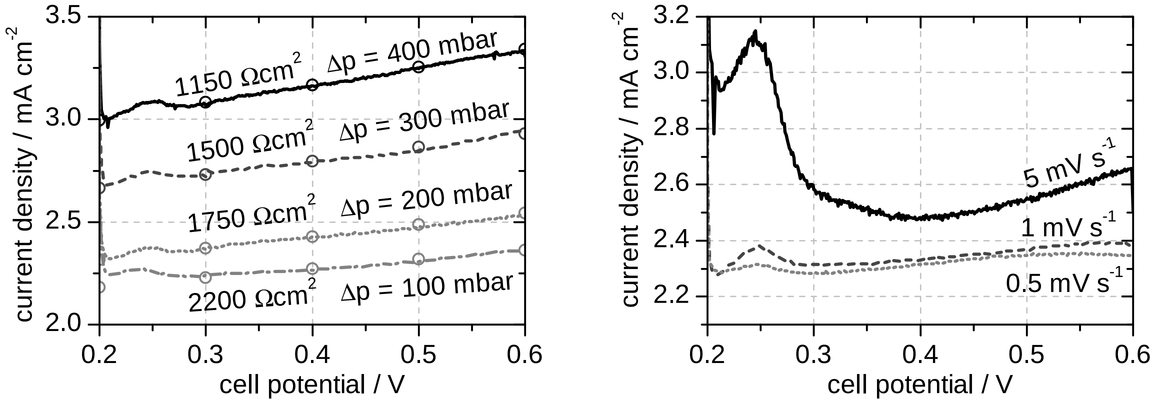

(a) Variation of the pressure difference between anode and cathode compartment with a voltage sweep rate of $1\,\mathrm{mV\,s^{-1}}$. Circles show the best linear fit for the internal short resistance.

(b) Variation of the voltage sweep rate at a pressure difference of $100\,\mathrm{mbar}$.

Figure 4.8: LSV measurement curves with the anode as a reference electrode at $65\,°\mathrm{C}$.

as long as no pinholes or such lead to excessively high crossover flows [133]. The pressure difference is set to $100\,\mathrm{mbar}$ in the experiments as low crossover flows can be quantified more precisely. A variation of the voltage sweep rate, shown in Figure 4.8 (b), revealed stable values for $\leq 1\,\mathrm{mV\,s^{-1}}$ so that all measurements are carried out with $1\,\mathrm{mV\,s^{-1}}$. The internal short resistance was calculated as the slope of a linear fit of the crossover current density between 0.3 and $0.55\,\mathrm{V}$.

4.2.2 Cyclovoltammetry

A meaningful indicator for degradation of the CL is its electrochemically active area (ECA), as platinum dissolution and agglomeration and also carbon support corrosion give rise to a decrease in available active reaction sites. Cyclovoltammetry (CV) is performed since it enables the determination of the ECA with an electrochemical method [134, 135].

As the CL is a porous high surface agglomerate, the ECA is magnitudes higher than the geometrical cell area A_{cell}

$$ECA = \Omega_{\mathrm{cl}} \left(\frac{m_{\mathrm{Pt}}}{A_{\mathrm{cell}}} \right)^{-1} \quad \left[\mathrm{cm^2_{Pt}\,mg^{-1}_{Pt}}\right] \tag{4.2}$$

with the catalyst loading $m_{\mathrm{Pt}} \cdot {A_{\mathrm{cell}}}^{-1}$ in $\mathrm{mg\,cm^{-2}}$. The surface area factor Ω_{cl} is in the order of $10^2 - 10^5$ for carbon black supported platinum or platinum alloy electrodes in PEFCs [136, 137].

ECA determination by CV is based on the cyclic chemisorption and desorption of a monolayer of hydrogen on the active catalyst sites under potential cycling. Oxidation and reduction reactions cause external currents and are analyzed to quantify the available reaction sites. One of both PEFC electrodes is used as a reference electrode and hence purged with hydrogen while the working electrode is charged with nitrogen. The cell potential is swept continuously from 0.08 to $0.9\,\mathrm{V}$ and vice versa in a triangle-like shape over time. In the lower voltage range of about 0.08 to $0.35\,\mathrm{V}$ hydrogen is oxidized or reduced

$$\mathrm{Pt\cdots H_{ad}} \rightleftharpoons \mathrm{Pt + H^+ + e^-} \tag{4.3}$$

resulting in an anodic (positive) or cathodic (negative) current, as Figure 4.9 shows for a cathode as a working electrode. In the upper voltage range ($> 0.7\,\mathrm{V}$) platinum is oxidized or reduced in a two step reaction via PtOH [138]. The lower and upper voltage limits are set in order to inhibit hydrogen and oxygen evolution, as gas evolution can damage the CL.

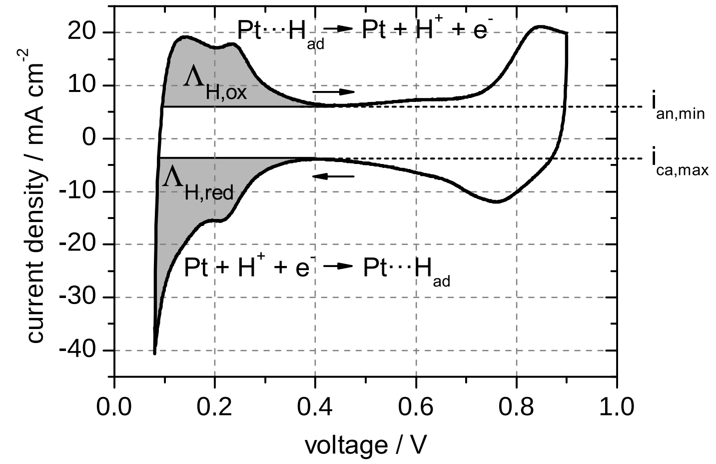

Figure 4.9: Exemplary cyclovoltammogram of a PEFC cathode with a sweep rate of $\gamma_{\mathrm{CV}} = 100\,\mathrm{mV\,s^{-1}}$ with indicated integration areas for hydrogen oxidation and reduction.

The current density is integrated over the hydrogen adsorption and desorption peaks less the double layer capacitance[1], as indicated in Figure 4.9, revealing the areas $\Lambda_{\mathrm{H,ox}}$ and $\Lambda_{\mathrm{H,red}}$. The according transferred specific charge of the reactions $q_{\mathrm{H,ox}}$ and $q_{\mathrm{H,red}}$ in $\mathrm{C\,cm^{-2}}$ can be calculated with the sweep rate γ_{CV} in $\mathrm{mV\,s^{-1}}$

$$q_{\mathrm{H,ox}} = \frac{\Lambda_{\mathrm{H,ox}}}{\gamma_{\mathrm{CV}}} \quad \text{and} \quad q_{\mathrm{H,red}} = \frac{\Lambda_{\mathrm{H,red}}}{\gamma_{\mathrm{CV}}}. \tag{4.4}$$

For electrodes based on solid and planar polycrystalline platinum, the area specific number of reaction sites Γ_{Pt} is well known with $210\,\mathrm{\mu C\,cm_{Pt}^{-2}}$ [139]. So the ECA can be calculated to

$$ECA_{\mathrm{ox/red}} = \frac{q_{\mathrm{H,ox/red}}}{\Gamma_{\mathrm{Pt}}} \left(\frac{m_{\mathrm{Pt}}}{A_{\mathrm{cell}}}\right)^{-1} \quad \left[\mathrm{cm_{Pt}^{2}\,mg_{Pt}^{-1}}\right]. \tag{4.5}$$

For the CV the cell is conditioned as for the LSV with $3\,\mathrm{l\,min^{-1}}$ of humidified hydrogen and nitrogen on the reference and working electrode side, respectively. Five subsequent linear voltage sweeps are performed from 0.08 to $0.9\,\mathrm{V}$ and vice versa with an external potentiostat (Zahner Zennium). The ECA is calculated from the average of the last three cycles. As the gas pressure on the reference electrode side is set to $100\,\mathrm{mbar}$ above the working electrode side, hydrogen crossover and its oxidation on the working electrode causes a shift of the cyclovoltammogram to higher current densities. Under the assumption that in the intermediate voltage range (at about $0.4 - 0.5\,\mathrm{V}$) neither oxidation nor reduction reactions occur and only double layer capacitance charging/discharging contributes to the measurement current, the crossover current density i_{xo} can be calculated with the minimum current density of the anodic sweep $i_{\mathrm{an,min}}$ and the maximum current density of the cathodic sweep $i_{\mathrm{ca,max}}$

$$i_{\mathrm{xo}} = \frac{i_{\mathrm{an,min}} + i_{\mathrm{ca,max}}}{2}. \tag{4.6}$$

The sweep rate γ_{CV} was varied over a wide range for both the anode and cathode as a working electrode, presented in Figure 4.10 (a) and 4.10 (b). ECA_{red} in case of the anode and ECA_{ox} in case of the cathode decrease with the sweep rate, likely an effect of limiting diffusion processes at the phase boundaries. ECA_{ox} for the anode and ECA_{red} for the cathode are stable over the sweep rate and therefore are used for the evaluation of CL degradation

---

[1] The double layer capacitance of the CL is charged/discharged with a changing electrode potential. Between anodic and cathodic sweep of the CV, the polarity of the double layer changes. As a result from charging/discharging currents, anodic and cathodic currents have an additional offset to each other ($i_{\mathrm{an,min}} > i_{\mathrm{ca,max}}$).

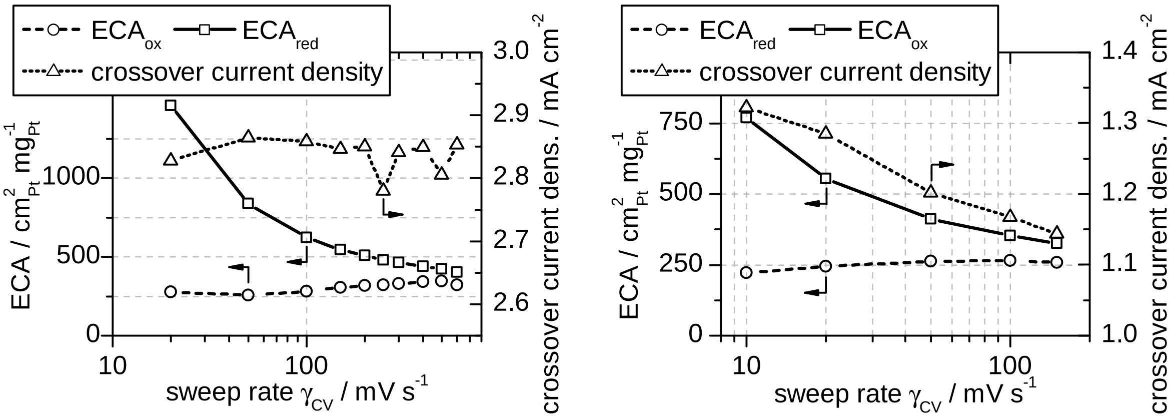

(a) Anode as a working electrode.

(b) Cathode as a working electrode.

Figure 4.10: Influence of the CV sweep rate γ_{CV} on the ECA calculated from the hydrogen adsorption and desorption peaks ECA_{red} and ECA_{ox}, respectively and on the measured hydrogen crossover current density.

in the following. Sweep rates of $\gamma_{\mathrm{CV}} = 200\,\mathrm{mV\,s^{-1}}$ for the anode and $\gamma_{\mathrm{CV}} = 100\,\mathrm{mV\,s^{-1}}$ for the cathode as a working electrode are chosen. The crossover current density is stable over the sweep rate for the anode but decreases for the cathode. For the latter, the crossover current density is lower by about a factor of 2 compared to the anode. It emphasizes that for the cathode as a working electrode not the gas crossover but other processes such as the HOR are rate-limiting.

4.2.3 Fluoride Measurement

Degradation effects relating to the electrolyte membrane mainly result in a decomposition of the polymer structure. Byproducts of the degradation process consist of fluorine to a substantial part, as it makes the main fraction of the polymer backbone [64]. The verification and quantification of fluoride (F^-) in the product water of a PEFC is hence a viable method to characterize membrane degradation mechanisms.

An ion selective electrode [140] (Mettler Toledo perfectION™ comb F) was employed in order to quantify fluoride ions in the product water from droplet separators in the anode and cathode outlets. The samples are diluted 1:1 with a total ionic strength adjustment buffer (TISAB) solution to raise the ionic strength of the solution to a maximum which will diminish the influence of the ionic composition of the sample [141]. TISAB solution also adjusts the pH value of the sample so that interferences from OH^- ions are reduced. A self-made TISAB solution is used without complexing agents as those would induce measurement

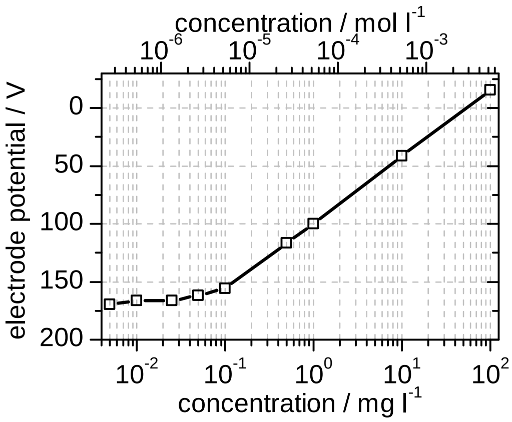

Figure 4.11: Calibration curve of a fluoride ion selective electrode with standard samples, 1:1 diluted with low level TISAB.

errors especially for low fluoride concentrations ($< 2 \cdot 10^{-5}\,\mathrm{mol\,l^{-1}}$). The composition of the used TISAB is described in [142]. Figure 4.11 shows the calibration curve for the ion selective electrode with standard samples at $25\,°\mathrm{C}$, 1:1 diluted with low level TISAB. The decreasing slope in the lower concentration range illustrates the challenge of low concentration measurements. The detection limit is set to a concentration of $0.02\,\mathrm{mg\,l^{-1}}$ as the measurement error is unacceptably high for lower concentrations. The measured voltage of the ion selective electrode is linearly interpolated between the calibration points to a fluoride concentration. Although the higher amount of fluoride ions is expected to be found on the cathode side [143], fluoride concentration is measured for both, anode and cathode product water.

4.2.4 Infrared Membrane Defect Detection

Mechanical deterioration of PEFC membranes can arise locally intensified as a result of varying operation parameters as well as by discrete mechanical damage. Accordingly, gas crossover can locally rise up dramatically, leading to a reduction in cell performance as well as to severe damage of cell components by the exothermic reaction of hydrogen and oxygen, catalyzed by the CL. In order to localize membrane defects the latter can be exploited. The cathode endplate and BPP are replaced by a $3\,\mathrm{mm}$ thick steel grid to compress the CCM including both GDLs, as shown in Figure 4.12. The anode FF is purged with hydrogen with a pressure of $70\,\mathrm{mbar_g}$. The reaction of crossed over hydrogen with oxygen on the cathode CL can be localized easily by an infrared (IR) camera (Goratec TVS 200EX) due to the exothermic reaction heat. IR images qualitatively show the position of membrane defects, but do not enable a quantification of crossover flows. The method can also be applied with diluted

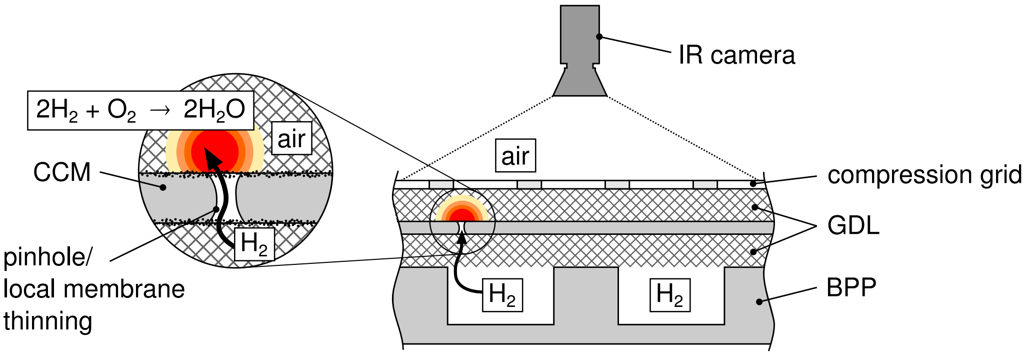

Figure 4.12: Experimental setup for membrane defect localization. Hydrogen crossover leads to direct combustion with ambient air, whereby the reaction heat is detected with an IR camera.

hydrogen in nitrogen to mitigate the invasiveness of the method by excessive reaction heat, as Yuan et al. showed [73].

4.2.5 CCM Post-Mortem Analysis

Cross sections of the CCM, including both GDLs, are analyzed by means of scanning electron microscopy (SEM). Mainly the thickness of the membrane and both CLs is determined as both can be reduced in thickness when they are subject to degradation effects. Samples of about $8\text{x}20\,\mathrm{mm}$ are cut out from the CCM plane with the GDLs. The sample is embedded in epoxy resin (2 component Bühler EpoThin™ 2 Epoxy System) and put into a vacuum chamber at $400\,\mathrm{mbar_a}$ to remove gas bubbles before curing. Mechanical compression of the CCM was avoided for precise thickness measurements. Samples are grinded with a Bühler Phoenix 4000 Sample Preparation System (1200 and 4000 grinding paper) and afterwards sputtered with a thin gold layer (Quorum Q 150 TS) for SEM analysis with a Zeiss Sigma Gemini.

As an alternative, microtome cutting of the samples as well as cracking of samples frozen with liquid nitrogen was tried but did not reveal satisfying results. Also infiltration of the GDL with ethanol before embedding into epoxy resin was tried in order to improve resin infiltration of the hydrophobic GDL, but swelling of the membrane due to ethanol uptake inhibited reproducible measurements of the membrane thickness.

4.3 Neutron Radiography

Since distribution and transport of liquid water plays a decisive role in PEFCs, its investigation is highly desirable. Conventional methods such as transparent cells [144–146] or freezing and disassembling of cells [25, 147] come to their limitations since they are highly invasive. For that reason imaging methods were applied to PEFCs for more than one decade, in particular magnetic resonance imaging [148, 149], x-ray radiography and tomography [37, 150–152] and neutron radiography (NR) [26, 131, 153–167]. Major drawback of magnetic resonance imaging is the strong interaction of the magnetic field with electronic circuits and the according restrictions relating to the cell design. X-ray imaging is capable of high spatial resolutions but limited to a small field of view (FOV). An unfavorable low attenuation coefficient for water compared to other structural materials of a cell (aluminum, carbon, PTFE)[1] requires cell modifications to obtain sufficient transparency. Also exposure times are limited due to the harming effect of x-ray radiation on PEFC components [168].

In contrast, required adaption of the cell design for NR is minimal since the attenuation coefficients for aluminum, carbon and PTFE are at least one magnitude below that of water for cold neutrons[2]. The FOV for NR is big enough to image a full size cell. The relative low neutron energy allows for imaging of a cell over days without significant impact on component deterioration. However, materials are activated in the neutron beam. Beside the difficult access to NR facilities the main disadvantage of the method is a relatively low spatial resolution compared to x-ray imaging.

4.3.1 Basic Principle

A neutron beam led through a structure is attenuated by neutron scattering or capture. The probability of an interaction with an element is characterized by its microscopic cross section σ_n in barn ($1\,\mathrm{b} = 10^{-28}\,\mathrm{m}^2$). The macroscopic cross section or attenuation coefficient $\Sigma = \sigma_\mathrm{n} N$ accounts for the atomic density N of the structure. The attenuation of the incident beam intensity I_0 can be described with the *Lambert-Beer law* [131, 169]

$$I_\mathrm{n} = I_0 \cdot e^{-\Sigma\delta} = I_0 \cdot e^{-\sigma_\mathrm{n} N \delta}. \tag{4.7}$$

I_n is the remaining beam intensity behind the structure and δ the thickness of the sample. In case of PEFC imaging, only the *difference* between attenuation of a dry cell and of an operating cell is of interest as it describes the actual water thickness. With Equation 4.7 the water thickness $\delta_{\mathrm{H_2O}}$ can be calculated with the intensity of the dry reference image I_ref and

---

[1] See [131], p. 29.

[2] Cold neutron energy range is defined by $0.12 - 12\,\mathrm{meV}$, see [131], p. 29.

the experimentally determined attenuation coefficient of water $\Sigma_{\mathrm{H_2O}}$

$$\delta_{\mathrm{H_2O}} = -\frac{1}{\Sigma_{\mathrm{H_2O}}} ln\left(\frac{I_{\mathrm{n}}}{I_{\mathrm{ref}}}\right). \tag{4.8}$$

4.3.2 Experimental Setup

All NR experiments were performed at the beamline for *Imaging with COld Neutrons* (ICON) of the *Swiss Spallation Neutron Source* (SINQ) at Paul Scherrer Institute, Switzerland. The mean energy of the neutrons amounts to $8.53\,\mathrm{meV}$ ($3.097\,\text{Å}$) [170], characterizing them as *cold neutrons*.

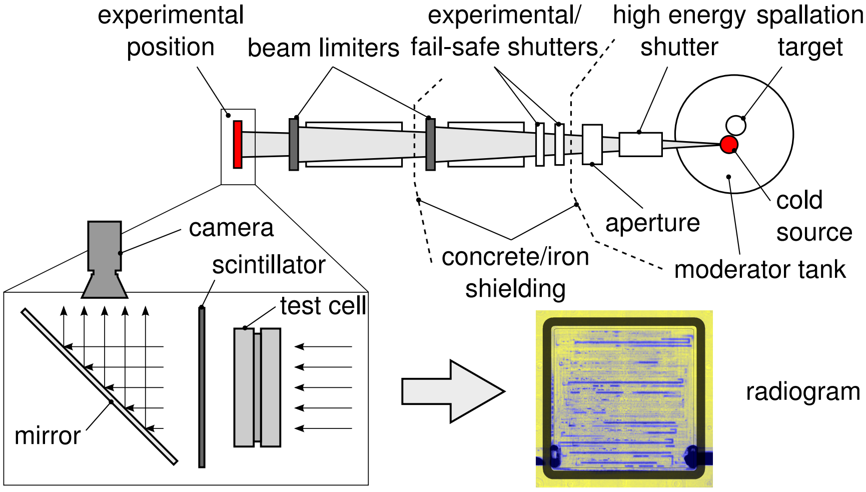

Figure 4.13: Experimental setup of the ICON beamline according to [170] and [171]. The test cell is imaged *through-plane*, the resulting radiogram shows the *in-plane* water distribution.

In front of the cold neutron source, a diaphragm with different circular apertures is inserted into the beam besides three different shutter systems, as shown in Figure 4.13. Two beam limiters restrict the beam to the FOV in order to generally reduce the neutron flux on the testing equipment. The cell plane of the PEFC is orientated perpendicular to the neutron beam, the experimental setup is denoted as *through-plane* imaging, although the *in-plane* water distribution is investigated. The neutron flux behind the sample is absorbed and converted into photons by a scintillator. A high sensitivity CMOS camera records the emitted light reflected from a $45°$ mirror, images are merged over the exposure time. General imaging parameters are listed in Table 4.3.

Experimental position 2 of the ICON beamline was chosen for all experiments, with a distance to the aperture $L = 6864\,\mathrm{mm}$ and an aperture diameter $D = 40\,\mathrm{mm}$ [170].

Table 4.3: Experimental parameters for the NR imaging setup.

parameter	normal setup (Chapter 5)	cold start setup (Chapter 6)	unit
aperture	40		mm
L/D ratio	172		-
optical setup	Midi		-
camera	Andor iKon-L, 2048x2048 px^2		-
pixel size	45	115	µm
resolution $r_{\mathrm{ESF}}^{\star}$	80	520	µm
resolution $r_{\mathrm{FWHM}}^{\star}$	95	440	µm
exposure time	10	3	s

* Effective resolution, calculation see Section 4.3.4.

Figure 4.14 shows the geometrical dependency of the effective resolution r from L, D and the distance between sample and scintillator/detector L_{S}. The L/D ratio has a major influence on the resolution, it causes a sharp edge of the specimen being imaged as blurred edge. The response of the imaging setup to a sharp edge is called *edge spread function* (ESF), the derivative of the ESF is the *line spread function* (LSF). As indicated in Figure 4.14, the effective resolution r_{ESF} can be calculated from ESF, based on the width between 10 and $90\,\%$ of the step response. Alternatively the width of the LSF at $50\,\%$ of the peak function (*full width at half maximum*, FWHM) can be taken as the effective resolution r_{FWHM}. [131]

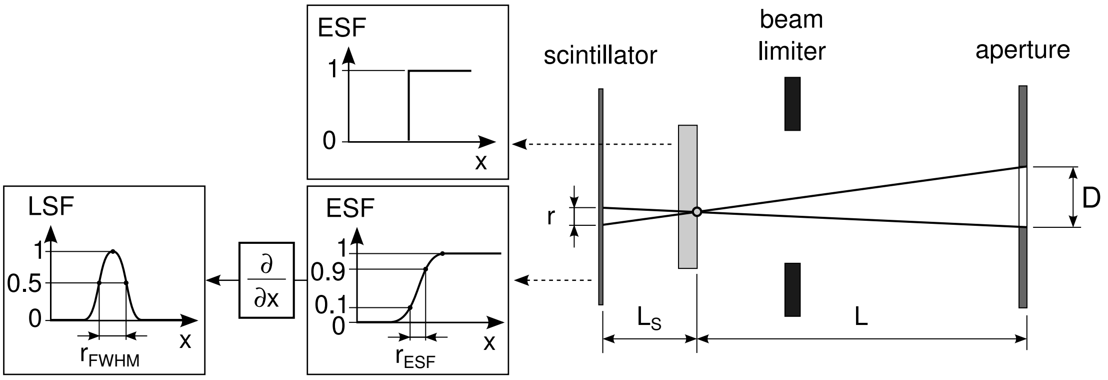

Figure 4.14: Geometrical relations of NR imaging setup and calculation methods for the resolution, based on the edge spread function (ESF) or line spread function (LSF). According to [131].

4.3.3 Data Processing

All images pass a flat-field correction and a median filter treatment over 5x5 pixels and over three subsequent images. The spatial intensity distribution of the incident beam is analyzed and accounted for by a correction field. Open beam images without the test cell serve as reference images in order to remove measurement artifacts from scattering effects. According to Equation 4.8, every image is referenced to a dry image of the cell. The latter is obtained after purging the cell with dry nitrogen for $30\,\mathrm{min}$. Figure 4.15 shows an exemplary reference image. The local water thickness $\delta_{\mathrm{H_2O}}$, measured perpendicular to the cell plane is calculated with Equation 4.8 in mm with $\Sigma_{\mathrm{H_2O}} = 0.45\,\mathrm{mm}^{-1}$. Figure 4.16 exemplarily shows the water distribution over the cell plane, with the position of the gasket schematically drawn. In- and outlets are frequently flooded with water and therefore excluded from data analysis. The water thickness is averaged over the FF area ($\delta_{\mathrm{H_2O,FF}}$) and over the edge channels ($\delta_{\mathrm{H_2O,EC}}$), the according areas are indicated in Figure 4.16.

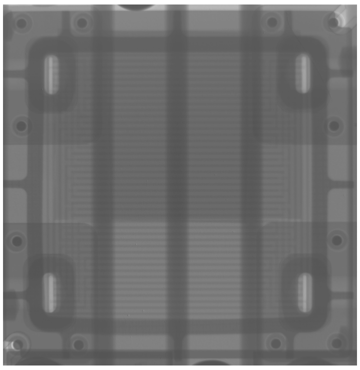

Figure 4.15: Reference image of a dry cell. Three cooling channels are crossing the image vertically.

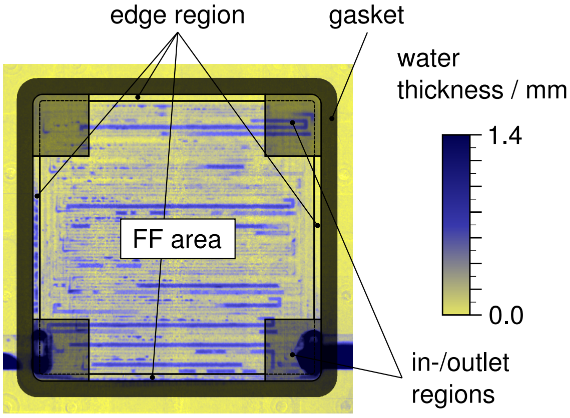

Figure 4.16: Exemplary neutron radiogram with water colored in blue, void areas in yellow. Gas in- and outlet regions are excluded from the analysis. Water content in the FF and edge region is analyzed separately.

In the following, the static and dynamic water content is analyzed in different cell areas, mainly the edge region and FF. Particularly in Chapter 5, both areas may be different in its composition, such as free volume space or porosity, and comparison of the water mass or average water thickness between the different regions may be of limited expressiveness. Therefore the volumetric water filling grade or water volume fraction $\Theta_{\mathrm{H_2O}}$ is introduced for each cell region

$$\Theta_{\mathrm{H_2O}} = \frac{\delta_{\mathrm{H_2O}}}{\sum\limits_{c} \Psi_c \delta_c \varepsilon_c}. \tag{4.9}$$

All free volumes in the gas compartments of the cell are FF channels or GDL pores. Each single component c has a thickness of δ_c perpendicular to the cell plane, the porosity ε_c and covers a relative area fraction of the cell area of Ψ_c[1].

In some cases, the absolute water mass m_{H_2O} is calculated from the mean water thickness $\delta_{\mathrm{H_2O}}$

$$m_{\mathrm{H_2O}} = \delta_{\mathrm{H_2O}} \cdot A_{\mathrm{seg}} \cdot \rho_{\mathrm{H_2O}} \tag{4.10}$$

with the segment area A_{seg} and the volumetric mass density of water $\rho_{\mathrm{H_2O}}$.

4.3.4 Method Validation

For the NR measurements the effective resolution is determined according to the method explained in Section 4.3.2. For the measurements described in Chapter 5, a grid made of gadolinium on a silicon layer ([172], shown in Figure 4.17 (a)) is adhered to the scintillator and one of the grid edges is used to determine the effective resolution based on the ESF and LSF, indicated in Figure 4.17 (c). With $r_{\mathrm{ESF}} = 80\,\mu\mathrm{m}$ and $r_{\mathrm{FWHM}} = 95\,\mu\mathrm{m}$, deviations between both methods are small. Considering the pixel size of $42\,\mu\mathrm{m}$, the resolution is fairly good and sufficiently high to image water accumulations on the channel-land scale which is about a magnitude bigger.

For imaging of cold starts, presented in Chapter 6, the resolution is measured at the edge of a gasket, indicated in Figure 4.17 (b). Both calculation methods reveal significantly higher values for the resolution, with $r_{\mathrm{ESF}} = 520\,\mu\mathrm{m}$ and $r_{\mathrm{FWHM}} = 440\,\mu\mathrm{m}$, seen in Figure 4.17 (d). The high values originate on the one hand from the camera resolution, as in the setup for cold starts the pixel size amounts to $115\,\mu\mathrm{m}$. Also the additional parts for the cold start setup (see Section 4.1.2), a thicker employed scintillator and the low exposure time of $3\,\mathrm{s}$ have a main influence on stronger blurring effects and give rise to the low effective resolution.

A viable method to validate the measurement accuracy of the water thickness in a cell by NR is the so called *double-dead-end* mode [160]. The cell is pre-dried and then operated with oxygen and hydrogen while both outlets are closed with valves for a defined time t. All product water remains in the cell and its theoretical mean thickness over the cell plane $\delta_{\mathrm{H_2O,th}}$

---

[1] In the FF area, Ψ_c is 1 for all components. Solely for the case that the GDL does not extend over the whole edge region, Ψ_c can be smaller than 1 in the edge region.

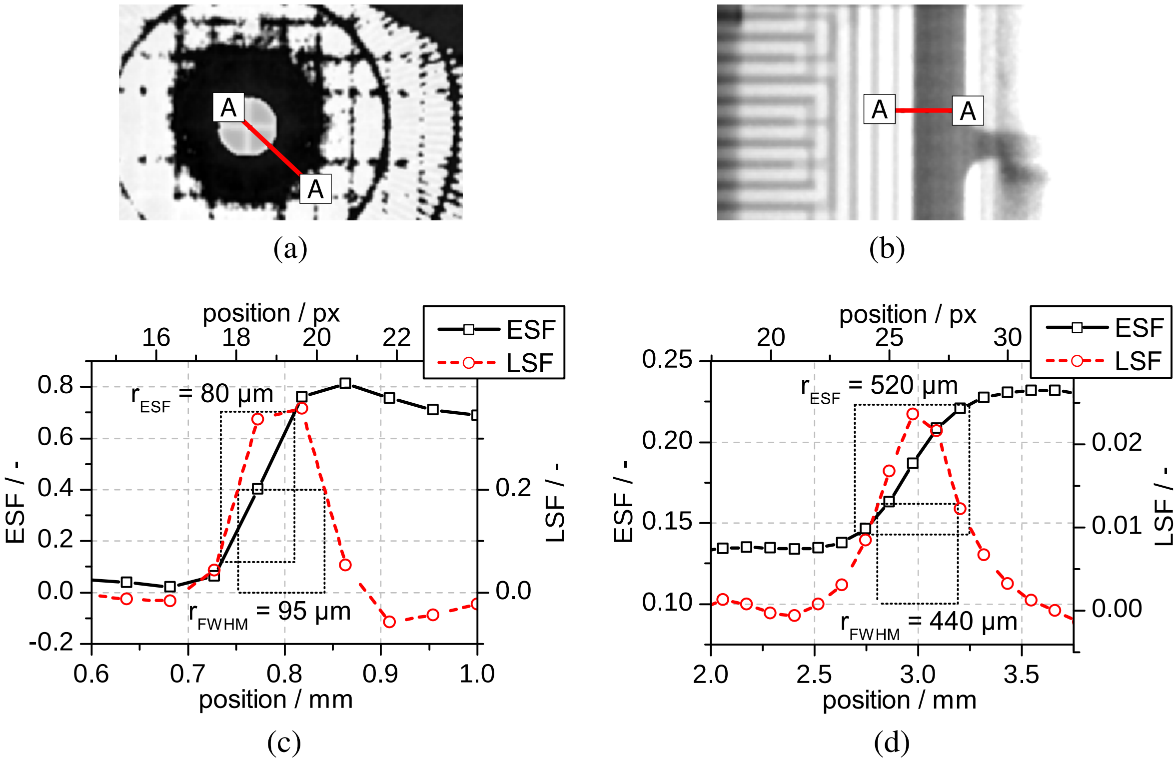

(a) (b) (c) (d)

Figure 4.17: Measurement of the effective resolution, based on the method explained in Section 4.3.2. (a) and (b) Detail with the scanning line in the NR images for the measurement campaign of Chapter 5 and 6, respectively. (c) and (d) show the according ESF and LSF with the measured resolution values.

can be calculated from the applied cell current $I(t)$

$$\delta_{\mathrm{H_2O,th}} = \int_0^t \frac{I(t) \cdot M_{\mathrm{H_2O}}}{z \cdot F \cdot \rho_{\mathrm{H_2O}} \cdot A_{\mathrm{cell}}}\, dt \tag{4.11}$$

with the molar mass of water $M_{\mathrm{H_2O}} = 18.015\,\mathrm{g\,mol^{-1}}$. By comparing $\delta_{\mathrm{H_2O,th}}$ with the measured value $\delta_{\mathrm{H_2O}}$, the accuracy of the NR measurement can be determined. Figure 4.18 (a) and 4.18 (b) show the measured water thickness $\delta_{\mathrm{H_2O}}$ for five different NR measurements compared to the theoretical value $\delta_{\mathrm{H_2O,th}}$. By choosing the operation time t from 46.5 to $442\,\mathrm{s}$ at a cell current of $I = 10\,\mathrm{A}$[1], the generated water mass per active cell area was varied from 1.1 to $8.4\,\mathrm{mg\,cm^{-2}}$. For the experiments with 4.2, 4.3 and $8.3\,\mathrm{mg\,cm^{-2}}$ the measurement error remains below $15\,\%$. For the lower generated water masses (2.1 and $1.1\,\mathrm{mg\,cm^{-2}}$) the relative error is significantly higher due to the low absolute values but the absolute error is

---

[1] The cell current of $I = 10\,\mathrm{A}$ was applied with an initial ramp of $0.5\,\mathrm{A\,s^{-1}}$ over $20\,\mathrm{s}$.

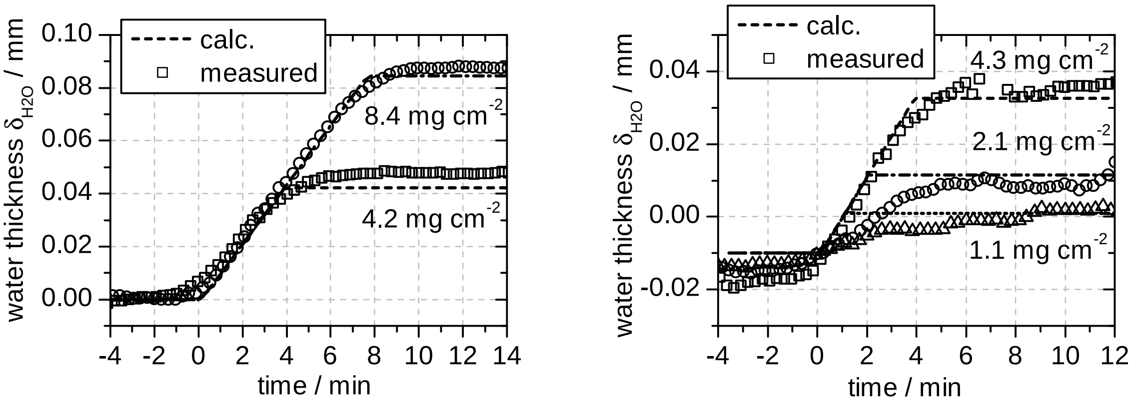

(a)

(b)

Figure 4.18: Measured water thickness by NR $\delta_{\mathrm{H_2O}}$ during double-dead end operation compared to the calculated theoretical value $\delta_{\mathrm{H_2O,th}}$ for different generated water masses.

comparable. Thereby it has to be considered, that water thickness is only analyzed in the FF area (as indicated in Figure 4.16) and unequal water distribution between FF and in- and outlet regions can lead to measurement uncertainties. Also water accumulation in the short in- and outlet pipings can lead to measurement errors. Nevertheless, NR was verified to be capable of performing high accuracy measurements with low measurement errors under static as well as transient conditions.

4.3.5 Isotope Labeling

Apart from observing the actual water distribution in a cell, neutron imaging has the potential to provide more information about species transport, based on its isotopic sensitivity. Species can be marked and retraced by replacing them by an isotope with a differing cross section. In fuel cells, particularly isotopes of hydrogen are predestined to be used for *isotope labeling* due to the 10 times higher cross section of protium (^{1}H, $\sigma_{\mathrm{n}} = 82.03\,\mathrm{b}$) compared to deuterium (^{2}H, $\sigma_{\mathrm{n}} = 7.64\,\mathrm{b}$), while the physical properties remain nearly constant [130]. The reactant gases can be labeled as well as the humidification water on anode or cathode side as described in [161]. In this work, the anodic reactant hydrogen is labeled in order to investigate gas pathways on the anode side of a cell. Particularly the accessibility of the edge region for gas is of high interest.

If the anode reactant is switched from commonly used $^1H_2$ to $^2H_2$, unlabeled ^{1}H atoms can be replaced by ^{2}H in all present species in the cell as there are H_2O, H_3O^+ and H_2, schematically depicted in Figure 4.19. Due to its high exchange current density, the HOR on the anode side pushes $^2H_3O^+$ ions into the electrolyte phase and ^2H_2O can be produced in the cathode sided ORR. Intermolecular exchange of $^1H^+$ and $^2H^+$ in the membrane is possible between H_3O^+ and H_2O. As revealed in [161], the exchange of water located in the membrane and unlabeled H_2O vapor is also believed to contribute to isotope exchange.

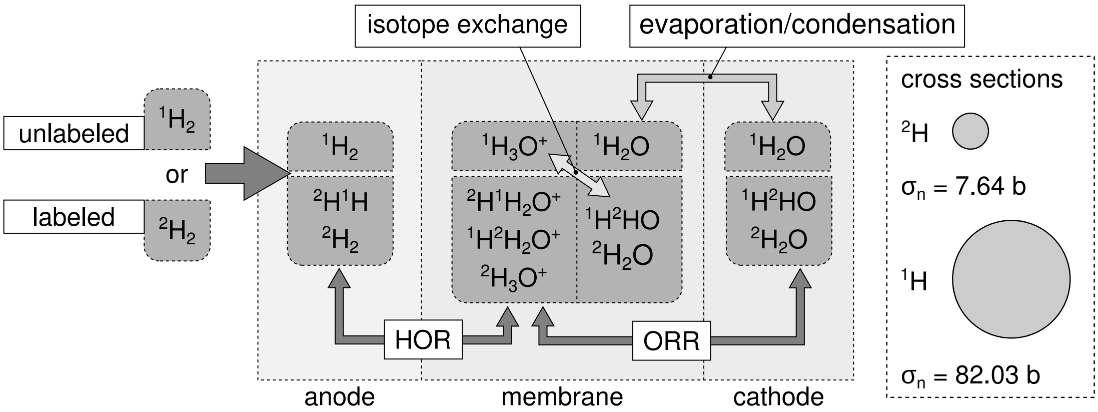

Figure 4.19: General reaction mechanisms for isotope labeling of the anode reactant with $^2H_2$ and cross sections of ^1H and ^2H. Only hydrogen containing species are shown for convenience.

Assuming that the water distribution remains constant for a short time interval under static operating conditions, changes in measured water thickness can be attributed to a change of the present isotopes. In this work (Chapter 5), cells were operated with $^1H_2$ for $60\,\mathrm{min}$, then the reactant is switched to $^2H_2$ for $5\,\mathrm{min}$ and again to $^1H_2$. During operation with labeled hydrogen, neutron attenuation will be reduced firstly in areas with a good hydrogen supply. Hence the method can be used to qualitatively verify the accessibility of a specific cell area for hydrogen. However, an exact quantification is impeded as a wide range of side reactions can occur. Mainly the high exchange current density of the HOR leads to a fast exchange of labeled and unlabeled H atoms without respect to the overall cell current density. Also the transport path of H_3O^+ in the membrane is not straight forward due to exchange of H^+ between solvated H_2O and H_3O^+ molecules respectively as detailed in [161].

Although there is ^1H_2O as well as ^2H_2O present in the cell, the water volume fraction for data analysis is still calculated with the cross section of ^1H_2O for convenience, here called *equivalent ^1H_2O volume fraction*.

4.3.6 Dual Spectrum Imaging

Liquid water can freeze in PEFCs during startups from sub-zero temperatures. Time and location of these phase transitions are of high interest for the understanding of the occurring mechanisms and for the mitigation of cell designs and operation strategies with respect to sub-zero startups. Classical neutron imaging does not allow for a direct differentiation of water and ice. Neither the fraction of both, water and ice, nor their thickness and molar density is known *a priori*. The cross sections of liquid water and ice are almost identical in a wide energy range but differ from each other for a wavelength $\lambda_\mathrm{n} > 2.86\,\text{Å}$ ($< 10\,\mathrm{meV}$), as measured by Torres et al. [173] and Josic et al. [129]. The relation between the microscopic cross sections of a sample in two suitable energy domains therefore changes with the liquid/ice composition, as schematically depicted in Figure 4.20. The effect is exploited with a *Dual Spectrum Imaging* method, based on an alternating measurement with the white beam spectrum and with a beryllium filter introduced into the beam, proposed by Biesdorf et al. [162].

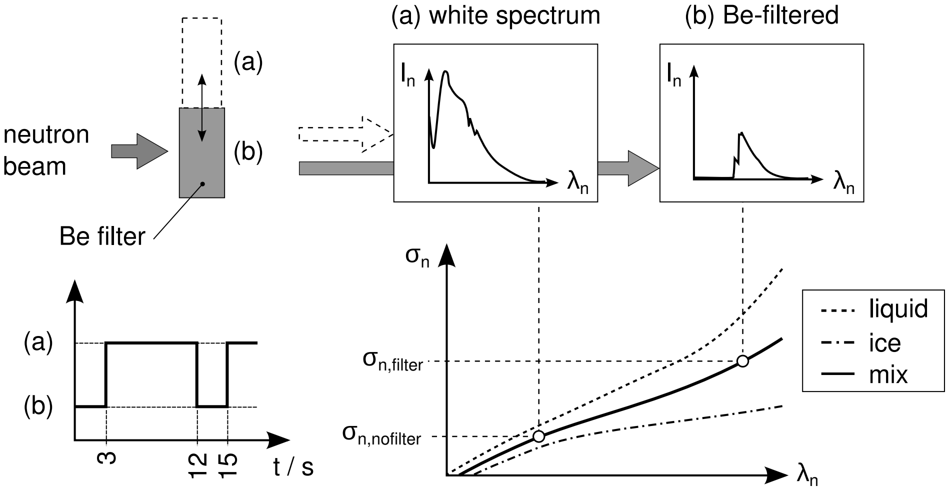

Figure 4.20: Principle of Dual Spectrum Imaging with a Beryllium filter periodically introduced into the beam. Water phase transitions can be detected by evaluating the relation between filtered and full white beam cross sections $\sigma_{\mathrm{n,filter}}$ and $\sigma_{\mathrm{n,nofilter}}$. According to [162] with data from [170] and [173].

The white spectrum of the ICON beamline provides cold neutrons with a mean energy of $8.53\,\mathrm{meV}$, while a low-pass beryllium filter cuts the spectrum above $5.25\,\mathrm{meV}$ (wavelengths below $3.95\,\text{Å}$ are removed) [170]. By motorizing the filter, it is possible to periodically introduce it into the beam for $9\,\mathrm{s}$, followed by a $3\,\mathrm{s}$ period without filter. For constant characteristics the filter is maintained at $35\,°\mathrm{C}$ by heating pads.

The optical density Δ is introduced in the Lambert-Beer law (Equation 4.7)

$$\Delta = -\ln\left(\frac{I_{\mathrm{n}}}{I_0}\right) = \delta N \sigma_{\mathrm{n}}. \tag{4.12}$$

Sample thickness δ and molar density N are assumed to be constant during one complete measurement cycle of $12\,\mathrm{s}$, so that the relation between the microscopic sample cross section with filter $\sigma_{\mathrm{n,filter}}$ and without filter $\sigma_{\mathrm{n,nofilter}}$ can be calculated from the relation of the according optical densities Δ_{filter} and $\Delta_{\mathrm{nofilter}}$ [162]

$$\sigma_{\mathrm{rel}} = \frac{\Delta_{\mathrm{filter}}}{\Delta_{\mathrm{nofilter}}} = \frac{\sigma_{\mathrm{n,filter}} N \delta}{\sigma_{\mathrm{n,nofilter}} N \delta} = \frac{\sigma_{\mathrm{n,filter}}}{\sigma_{\mathrm{n,nofilter}}}. \tag{4.13}$$

σ_{rel} is the *relative attenuation* and serves as an indicator for the aggregate state of water in the cell. Considering Figure 4.20, frozen water exhibits a lower σ_{rel} compared to liquid water. The contrast between the phases was found to be low with about $1.6\,\%$. It can also be affected by the water thickness and beam hardening effects [162]. The method has only been applied to date on static, time-invariant systems [162], therefore it has to be applied with care. To improve image quality, filtered and non-filtered images are merged over acquisition periods of $120\,\mathrm{s}$. Although ice and liquid water can be present at the same time in a cell, the water thickness is calculated from $\Delta_{\mathrm{nofilter}}$ with the attenuation coefficient of liquid water ($\Sigma_{\mathrm{H_2O}} = 0.45\,\mathrm{mm}^{-1}$). As the interpretation of the revealed data of Dual Spectrum Imaging can be challenging, the method will be combined with the ordinary observation of volumetric expansions of droplets due to freezing and with electrochemical measurement values.

Chapter 5

Water Transport in the Outer Cell Perimeter[*]

In Chapter 3 it was elaborately explained that the cell design is strongly dominated by the sealing solution in the outer cell perimeter. Wide spaces can be required outside the FF, in particular when a SG is employed. Most cell designs based on metallic BPPs exhibit gaps in the edge land, leading to considerable bypass flows around the FF, while graphitic BPPs can have continuously formed edge lands around the FF. In the latter case, void volumes in the cells are formed without being fed by a gas flow. Water accumulation is likely to occur there.

In this chapter the effect of the cell design in its outer perimeter on water distribution and transport in both, edge channel and FF, is investigated by means of NR measurements. Thereby the design restrictions given by different sealing solutions were taken into account and five distinct cell setups were employed accordingly. The cells were subjected to a wide variation of operating parameters such as temperature, gas pressure, gas humidification and electrical load. Static as well as dynamic characterization of the water distribution over the cell plane was performed. Also isotope labeling was employed to obtain information about the accessibility of the edge region of the cells for gas.

5.1 Employed Cell Setups

Five different cells with variations in the outer cell perimeter design were operated and imaged consecutively in a NR measurement campaign. The basic experimental setup is described in Section 4.3, whereby graphitic BPPs were used. As the overviews in Figure 5.1 and Table 5.1 exhibit, the cells differ from each other in

- the employment of a SG in contrast to a direct sealing on the CCM,
- the width of the edge channel $w_{\text{ch,ec}}$, as it is a requirement for SG based setups to account for the overlap between SG and CCM. Cells with $w_{\text{ch,ec}} = 3.5\,\text{mm}$ as well as $w_{\text{ch,ec}} = 0.7\,\text{mm}$ were employed,

---

[*] Parts of this chapter were published in [126].

- the accessibility of the edge channel for gas, the edge land is interrupted or continuously formed around the FF (cf. Figure 4.1), the former case is indicated by a hatched edge land in Figure 5.1 and
- the sealant manufacturing method. Flat gaskets are employed as well as a seal-on-GDL with a structured gasket in one case (cell 5).

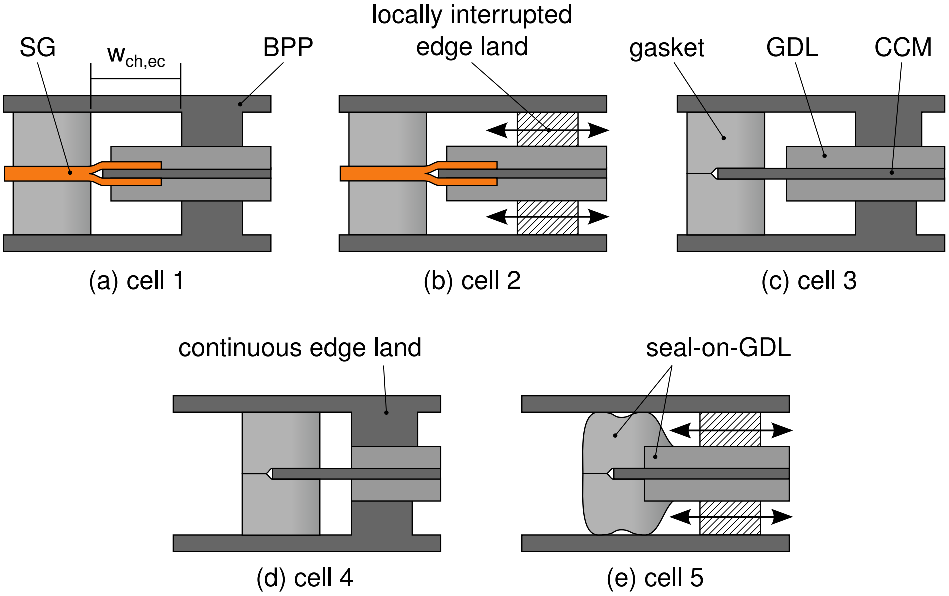

(a) cell 1 (b) cell 2 (c) cell 3

(d) cell 4 (e) cell 5

Figure 5.1: Cross section of the test cell showing the different employed sealing setups. (a) and (b) CCM stabilized with a two-part SG, sealed with flat gaskets, with closed and opened edge channel, respectively. (c) and (d) Direct sealing of the CCM with flat gaskets and different edge channel widths. (e) Seal-on-GDL concept, with a sealing structure integrally formed on the GDL.

Table 5.1: Cell configurations used for neutron imaging measurements.

experiment/ cell no. -	active area cm^2	edge land* -	edge channel width mm	sealing concept -	sub-gasket -
1	52.7	continuous (a)	3.5	single flat gasket	yes
2	52.7	interrupted (b)	3.5	single flat gasket	yes
3	57.0	continuous (a)	3.5	single flat gasket	no
4	49.8	continuous (a)	0.7	single flat gasket	no
5	51.8	interrupted (b)	0.7	seal-on-GDL	no

* See Figure 4.1.

The cell configurations enable for the comparison of individual characteristics, such as the employment of a SG, the edge channel width or the edge land type (interrupted or continuous) between two cells with all other features being identical. In case of cell 5, the used GDL (Freudenberg H2315 I3 C1[1]) has a higher PTFE content of $7\,\%$ compared to $4\,\%$ in cells 1-4 (Freudenberg H23C8), while GDL porosity and thickness are the same for all cells with $70\,\%$ and $200\,\mu\mathrm{m}$, respectively. All other components do not differ from the explanation in Chapter 4.

Employed SGs are made of two $40\,\mu\mathrm{m}$ thick PEN films in a frame-like shape. They are laminated onto each other with the CCM sandwiched in between. The frame has a width of $11\,\mathrm{mm}$ and the overlap between SG and CCM amounts to $7.5\,\mathrm{mm}$.

5.2 Operating Conditions and Data Analysis

To account for the influence of gas humidification on the static water distribution in the cell, inlet humidification on anode and cathode side were varied individually over a wide range in so called *RH-maps* [163]. Also load, stoichiometry, gas inlet pressure and cell temperature were varied individually while keeping all other parameters at the standard values (cf. Section 4.1.4). Each state was held for $30\,\mathrm{min}$, ended by purging anode and cathode side sequentially by abruptly releasing the gas pressure to remove residual water from the cell. Anode and cathode purges were executed with a time shift of $30\,\mathrm{s}$. The procedure was repeated four times. For analysis of the steady state, the arithmetic average of the water volume fraction $\overline{\Theta}_{\mathrm{H_2O}}$ between 9 and $2\,\mathrm{min}$ before the first gas purge was calculated. The stability of the operation state was assessed with a linear regression of $\Theta_{\mathrm{H_2O}}$ over the analyzed interval as pointed out by Figure 5.2. The regression coefficient β – the slope of the regression function – is employed as a measure for the stability of the water content in the cell. The standard deviation of $\Theta_{\mathrm{H_2O}}$ was calculated referring to the linear regression function. $\Theta_{\mathrm{H_2O}}$ is also averaged over a period of $90\,\mathrm{s}$ after the first two gas purges, to evaluate the efficiency of the purges, which can be an indicator for the gas accessibility of certain cell areas.

The shutdown procedure of a technical cell aims to prevent the components from degradation as well as to condition the cell for the next start. Especially in systems which are subject to freezing conditions, residual water has to be removed from the FF since it can freeze and block gas pathways during the start [164]. The importance of the ability to remove liquid water from the cell is taken into account in a specific experiment (*dynamic water transport*), where the gas inlet humidification on anode and cathode side was switched sequentially from 80 to $30\,\%$ and back to $80\,\%$. Water transport processes are expected to occur on long time scales, as the following experiments will show, so here each humidification step was held for $1\,\mathrm{h}$.

---

[1] Name according to a former notation.

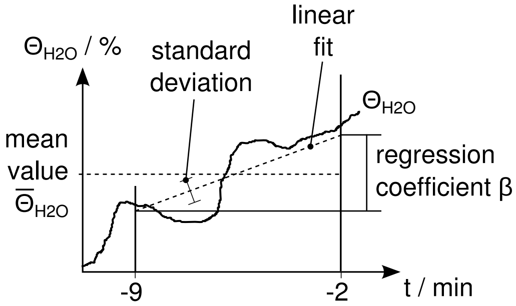

Figure 5.2: Method to analyze the water volume fraction $\Theta_{\mathrm{H_2O}}$ by calculating the mean value $\overline{\Theta}_{\mathrm{H_2O}}$, a regression coefficient β and the standard deviation from the linear fit over a period from 9 to $2\,\mathrm{min}$ before purging the cell.

Note: In this work the water volume fraction $\Theta_{\mathrm{H_2O}}$ will be separately analyzed in the edge region and the FF, according to Figure 4.16. Thereby the edge region comprises the edge channel as well as the outer half of the edge land. The FF area accordingly comprises also the inner edge land area.

In this chapter the relative gas humidity at the cell inlets will be depicted in the order *anode/cathode*.

5.3 Results

In the following the results from NR including electrochemical operating parameters are presented. The results showing the influence of an opened or closed edge channel and of the edge channel width are highlighted. Also the aspects of a seal-on-GDL concept relating to the water transport are presented. Finally the pressure drop over the FFs is correlated with the measured water content in the cell.

5.3.1 Opened and Closed Edge Channels

Figure 5.3 shows the mean water volume fraction in cell 1 and 2, with closed and opened edge channels, respectively. In cell 1 the edge channel permanently contained more than $15\,\%$ of water, even at dry conditions as $20/40\,\%\,\mathrm{RH}$, with a dry cathode at $80/0\,\%\,\mathrm{RH}$ or without anode humidification at $0/80\,\%\,\mathrm{RH}$. Increasing humidification generally entailed higher water content in the edge channel. In the FF the water content followed the cathode gas humidification. The anode did not seem to have a significant influence on the FF water content as the point $80/0\,\%\,\mathrm{RH}$ indicates where the FF was almost dry and the HFR rises up considerably. The regression coefficients indicate a stable operation in the FF but a slow

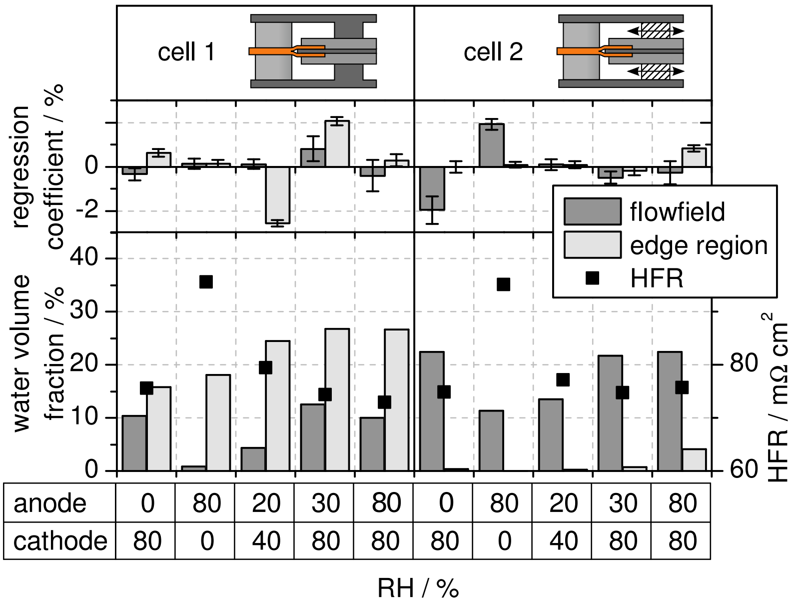

Figure 5.3: RH-map of cell 1 and 2, showing the relative water volume fraction $\overline{\Theta}_{\mathrm{H_2O}}$ in the FF as well as in the edge region and the HFR value at different gas inlet humidification. Regression coefficients indicate the stability of the measurement point. The edge channels of cell 1 and 2 are closed and opened, respectively.

equilibration in the edge channel at $20/40\,\%\,\mathrm{RH}$ and $30/80\,\%\,\mathrm{RH}$. The HFR generally shows a good consistence in cell 1 as a low FF water content correlates with a high HFR and vice versa.

Cell 2 exhibited a relatively dry edge region. Even with both gases humidified at $80\,\%\,\mathrm{RH}$, only $4\,\%$ of the edge region volume was filled with water which is low compared to cell 1. It is obvious that a bypass flow constantly dried out the edge region of cell 2 by water uptake, also indicated by the pressure drop over the cell which was around $4\,\mathrm{mbar}$ lower for cell 2 compared to cell 1 on both, anode and cathode side. In the FF the stoichiometry decreased due to the bypass and the water removal was hindered leading to a constantly higher water content. The regression coefficient shows a higher instability of $\Theta_{\mathrm{H_2O}}$ in the FF at $0/80\,\%\,\mathrm{RH}$ and $80/0\,\%\,\mathrm{RH}$, what is likely to be an effect of the low stoichiometry and therefore slow or unstable water removal. Even though the FF water content in cell 2 is significantly higher than in cell 1, the HFR in both cells is similar.

Figure 5.4 shows that the edge region water content in cell 1 increased with a raising pressure, from $27\,\%$ at $1.3\,\mathrm{bar_a}$ up to about $41\,\%$ at $2\,\mathrm{bar_a}$. In contrast, the water content in the FF was relatively unaffected by pressure. Although the volumetric gas flow and hence the pressure drop over the cell was lowered with a higher overall gas pressure, water removal

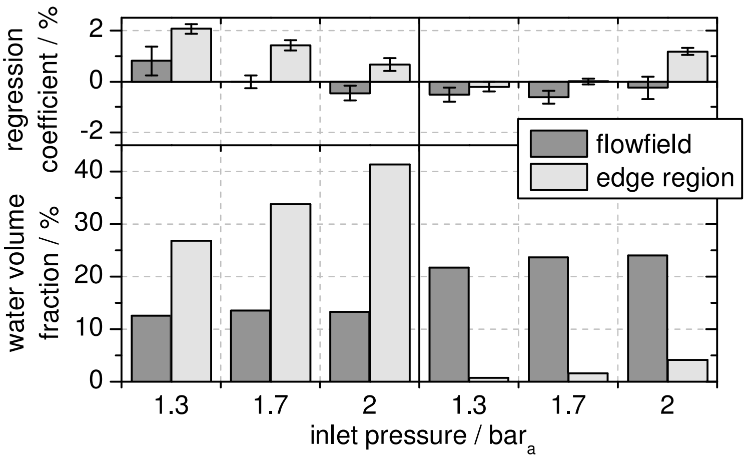

Figure 5.4: Water volume fraction $\overline{\Theta}_{\mathrm{H_2O}}$ of cell 1 (left) and 2 (right) under variation of the gas inlet pressure.

seemed to be still effective due to a sufficient pressure drop of 8 and $15\,\mathrm{mbar}$ on anode and cathode side, respectively at a gas inlet pressure of $2\,\mathrm{bar_a}$.

In cell 2 the edge region was almost dry, the water volume fraction rose up only marginally from 0.7 to $4\,\%$ when changing the gas inlet pressure from 1.3 to $2.0\,\mathrm{bar_a}$. The overall water content in the FF was significantly higher than in cell 1, resulting from a lower pressure drop, as already seen in the RH-map in Figure 5.3 and rose up by about $2\,\%$ from 1.3 to $2.0\,\mathrm{bar_a}$.

Figure 5.5 shows the water content for cell 1 and 2 when varying the electrical load under a constant gas stoichiometry. The FF water content in cell 1 decreased with an increasing load although more water is electrochemically produced. Therefore, improved liquid water removal at a higher gas velocity and pressure drop is likely to be the reason. However, no correlation between load and water could be seen in the edge region, indicating that the liquid water removal driven by pressure drop has no major influence. In cell 2, the edge channel stayed dry, independent of the applied load, resulting from a high bypass flow in the edge channel, as described before. In the FF the water content decreased with increasing load, whereas at a low current of $20\,\mathrm{A}$ the regression coefficient reveals that the operation state was not in equilibrium, therefore slow water removal from the FF due to low gas flows could be a reason.

A variation of the cell temperature was performed with cell 1, while maintaining the relative gas inlet humidity at $30/80\,\%\,\mathrm{RH}$, shown in Figure 5.6. The HFR slightly decreased with increasing temperature, in line with literature findings [174, 175]. The water volume fraction in the edge region rose up marginally from 55 to $65\,°\mathrm{C}$ and dropped down at $75\,°\mathrm{C}$. The regression coefficient values indicate, that the edge region water content at $65\,°\mathrm{C}$ was falling

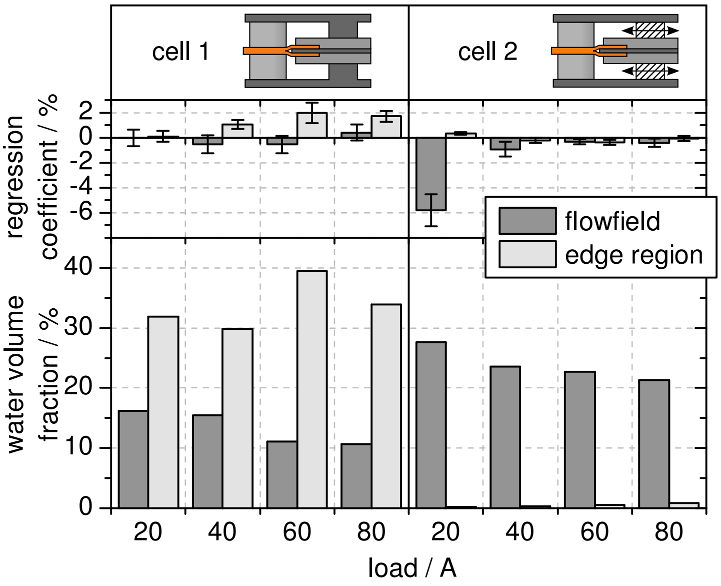

Figure 5.5: Water volume fraction of cell 1 and 2 under the influence of the electrical load, while maintaining a constant stoichiometry.

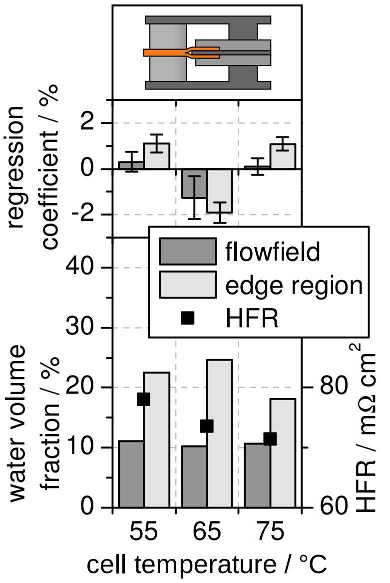

Figure 5.6: Water volume fraction and HFR in cell 1 under variation of the cell temperature.

down and did not reach an equilibrated state. A more pronounced decrease of the edge region water content with the temperature would have been expected as water uptake capability increases with the temperature. But it has to be considered that temperature gradients can occur over the FF and particularly the temperature in the edge region might be different to the FF due to convection and less current production there [176]. Also the measurement values were not observed to be stable after holding the temperature for 30 min. The water content of the FF did not show any sensitivity for the cell temperature.

Isotope labeling experiments were performed with cell 1 and 2 where they were operated with $^2H_2$ for 5 min instead of $^1H_2$. While running the cell on $^2H_2$, ^2H_2O is produced electrochemically in the ORR but also via a wide range of different reaction paths, as described in Section 4.3.5. Residual ^1H_2O is partially substituted by ^2H_2O where $^2H_2$ has access to the electrode.

In Figure 5.7 it is once more obvious that the FF of cell 2 constantly contained a significantly higher water content than in cell 1 as a result of the FF bypass. A slight decrease of the apparent water content in the edge region of cell 1 during the isotope exchange shows that this area is accessible for hydrogen gas. Gas exchange between FF and edge region has to take place even though it is a closed edge channel. In the edge region of cell 2 no changes could be

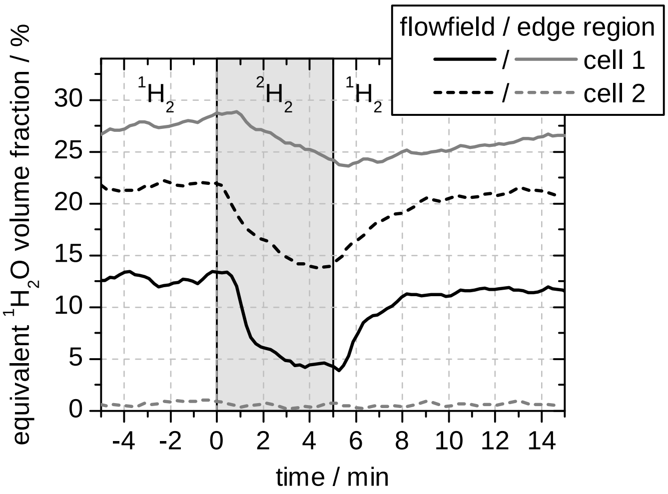

Figure 5.7: Isotope labeling of cell 1 and 2: Fuel gas was temporarily switched from $^1H_2$ to $^2H_2$. The water volume fraction was calculated using the cross section of ^1H_2O.

observed, the edge channel was constantly kept dry by the bypass gas flow, so that isotope exchange cannot be verified.

5.3.2 Influence of the Edge Channel Cross Section

As the test cell used in this work is just a model and geometrical and operational parameters in commercial cells can differ considerably, the impact of the edge region on water distribution and cell performance can also vary over a wide range. The major influence factor is the geometrical relation between the cross sections of edge channel and FF and the type of the FF – serpentine or straight (cf. Section 3.1.3). To qualitatively investigate this effect, the edge channel width was varied between 3.5 and $0.7\,\mathrm{mm}$ in cell 3 and 4, respectively. Both have continuous edge lands, entirely surrounding the FF and no SG.

As seen in the RH-map in Figure 5.8, the water content in the FF was fairly reproducible between both setups. Obviously it follows the cathode gas humidification, as also seen in cell 1 and 2 before. The anode humidification does not have a strong influence on the FF water content. The HFR also shows a coincident behavior, being inversely proportional to the FF water content. The HFR of cell 4 generally exhibits the same characteristic, but with a negative offset. A variation of the ohmic resistances between the cell assemblies could be the reason for that. The edge region of cell 3 generally contained a higher fraction of water and a higher absolute water mass over all operation points compared to cell 4. High regression coefficients for the edge region in cell 3 indicate a slow stabilization of the water content. Figure 5.8 also shows the water content after purging both gas compartments as hatched bars.

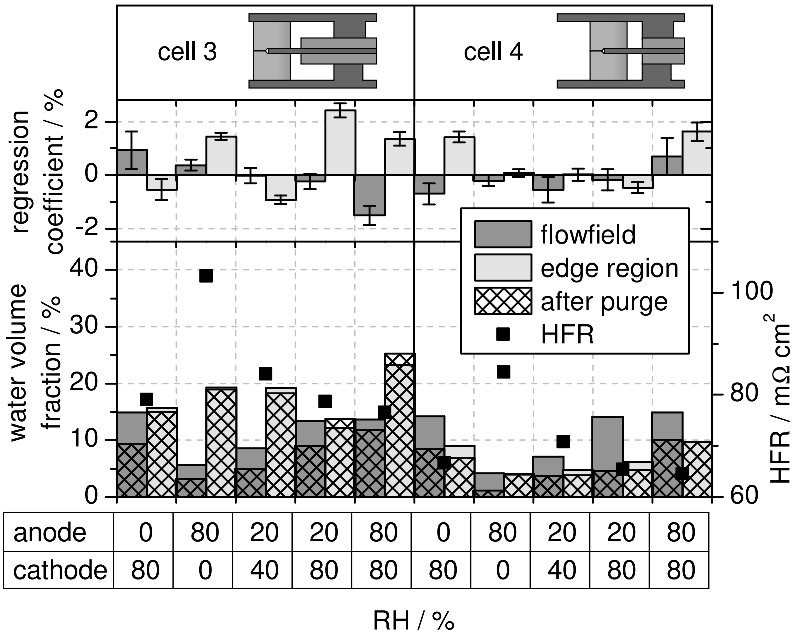

Figure 5.8: Water volume fraction in cell 3 and 4 with an edge channel width of 3.5 and $0.7\,\mathrm{mm}$ respectively under variation of the gas inlet humidification.

Even in the FF area, water could be removed only partially by repeated purges. In both cells no water could be removed from the edge region by purging, changes in water volume fraction were in the range of measurement inaccuracy. Under humid operation as $80/80\,\%\,\mathrm{RH}$ discrete droplets were observed in the NR images, blocking the edge channel with a thickness of up to 1.0 and $0.8\,\mathrm{mm}$ in cell 3 and 4, respectively. As the channel depth is $0.5\,\mathrm{mm}$ on either side, it is evident that there cannot be a continuous bypass flow in the edge channel.

However, results of the *dynamic water transport* experiment in Figure 5.9 show, that water can be exchanged between FF and edge region, driven by diffusion of humidified gas. The inlet gas humidification was switched from $80/80$ to $30/30\,\%\,\mathrm{RH}$ and vice versa. Each point was held for $1\,\mathrm{h}$. The time constants for water transport to the edge region are high, even after $1\,\mathrm{h}$ of dry operation no equilibrium was reached for the water content in the edge region. During the dry operation 0.16 and $0.17\,\mathrm{g}$ of water were removed from the FF of cell 3 and 4 respectively, while 0.06 and $0.03\,\mathrm{g}$ were removed from the edge region of cell 3 and 4. But it has to be considered, that the initial water content in the edge region at the beginning of the dry phase was $0.3\,\mathrm{g}$ in cell 3 compared to only $0.06\,\mathrm{g}$ in cell 4. Dynamic water transport properties of cell 3 and 4 in the FF area obviously are the same, but in the wide edge region of cell 3, the removed water mass was higher than in cell 4, apparently correlating with a generally higher water mass in the edge channel.

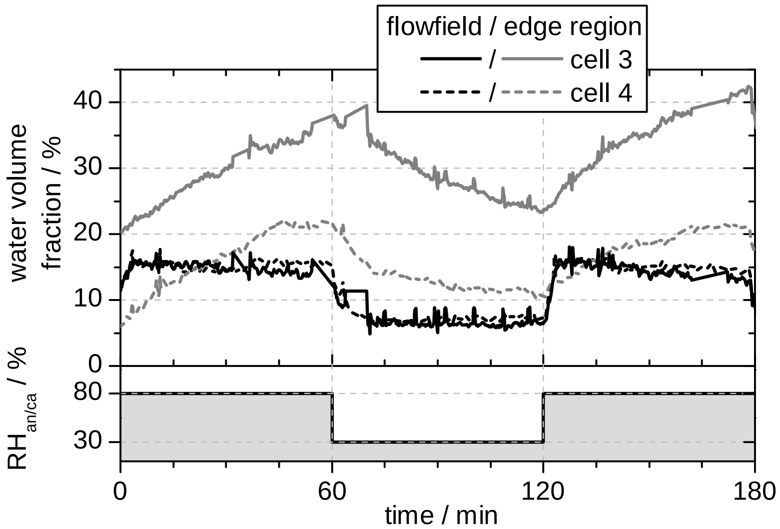

Figure 5.9: Water volume fraction of cell 3 and 4 when instantly changing the gas inlet humidification from $80/80$ to $30/30\,\%\,\mathrm{RH}$ and vice versa.

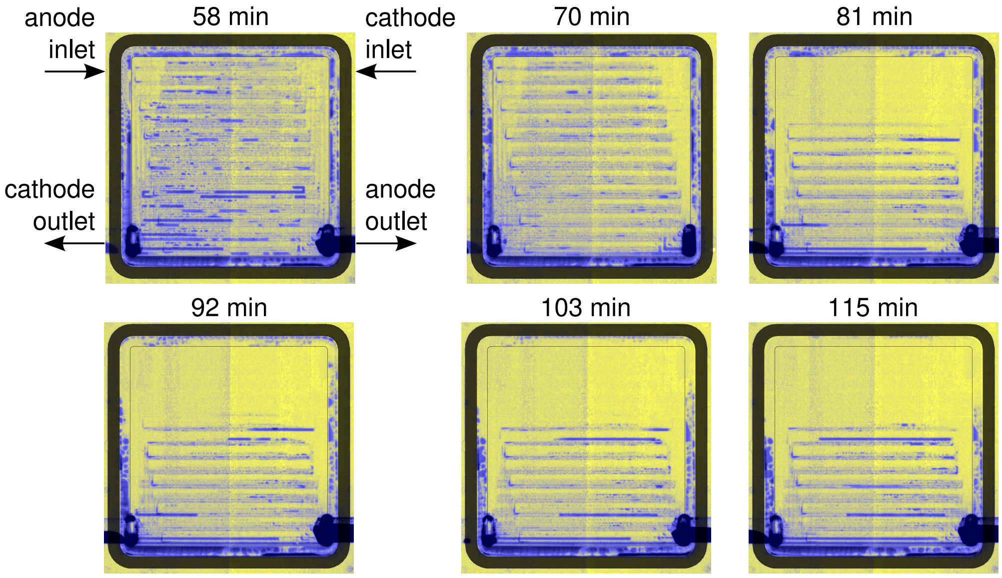

Figure 5.10: Water distribution in cell 3 during dry operation with $30/30\,\%\,\mathrm{RH}$. Times refer to the x-axis of Figure 5.9.

Figure 5.10 depicts the in-plane water distribution over cell 3 during the dry-out phase. The FF was dried out in the top section of the cell where the dry gas comes in and reached an equilibrium state after about $15\,\mathrm{min}$. From the edge region, water was also removed from the top section of the cell and especially from the inner side of the edge channel which is orientated to the FF. Water in the bottom region of the edge channel remained nearly unchanged.

Examining the results of the isotope exchange experiment, as shown in Figure 5.11, reveals that the water content in the edge region of cell 3 decreased significantly during the $^2H_2$ operation, proving that hydrogen can reach the electrode surface there. As seen in the radiograms in Figure 5.12, water was widely distributed over the edge channel, before the $^2H_2$ operation, proving a large surface for isotope exchange. Particularly droplets in the anode inlet region were disappearing due to the isotope exchange. The bottom part of the edge channel stayed almost unchanged. In contrast to this behavior in cell 4 a marginal decrease of water

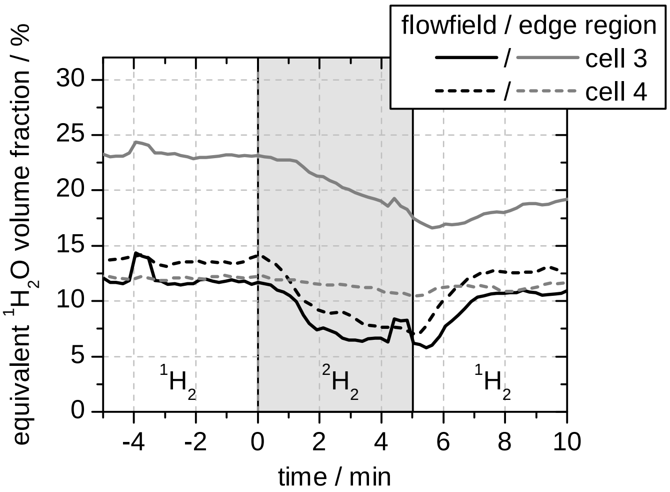

Figure 5.11: Equivalent water volume fraction during isotope labeling of cell 3 and 4. Fuel gas was temporarily switched from $^1H_2$ to $^2H_2$.

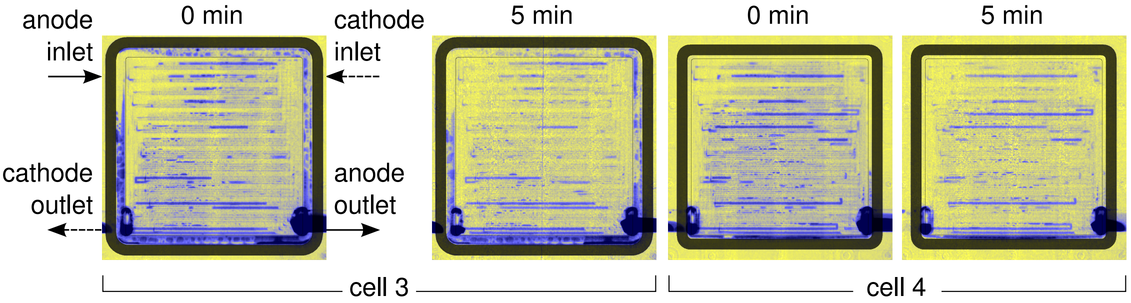

Figure 5.12: In-plane water distribution in cell 3 and 4 before $(0\,\mathrm{min})$ and after $(5\,\mathrm{min})$ operating the cell with $^2H_2$ for $5\,\mathrm{min}$.

content in the edge region attributed to the isotope exchange could be observed. All water in the edge channel stayed accumulated in its bottom part during the isotope exchange, blocking the pathway for H_2. In the FF, the behavior is similar to cell 3.

5.3.3 Seal-on-GDL Solution

Cell 5 has a seal-on-GDL based setup, which is a viable solution for mass production as described in detail in Section 3.1.2. It has the decisive advantage of a low space requirement in the edge region. So the edge channel can be designed quite narrow, $0.7\,\mathrm{mm}$ in this case. It has to be taken into consideration that a different GDL as in all other cells was used. It has a higher PTFE content of $7\,\%$ instead of $4\,\%$. The edge channel is opened (cf. Figure 4.1), which is characteristic for many commercial metallic based BPP as there are welding lines crossing the edge land. Drying-out of the edge channel is forced by a bypass stream. But generally more water than in cell 2 stayed in the edge channel. Especially in humid operation states from $60/80\,\%\,\mathrm{RH}$ upwards, up to $10\,\%$ of the edge region was filled with water, as depicted in Figure 5.13. As already seen in cells 1-4, the HFR shows an inversely proportional behavior to the FF water content. Due to the open edge channel water removal by purging both gas compartments was effective, around $1/3$ of the present water volume in the edge region was removed as long as a critical water mass is exceeded prior to purging. Below $5\,\%$ water volume, no water was drained out by purging, it is likely that the residual water mass was located in the GDLs in these cases. The water volume in the FF area was clearly higher than in cell 4 which has a closed edge channel. The difference can arise from the different GDL types but also from the lessened gas flow in the FF due to the bypass flow around the FF.

The steady state point at a humidification of $80/80\,\%\,\mathrm{RH}$ was measured two times to validate experimental reproducibility. Both points had identical water contents in the FF. In the edge region the regression coefficient indicates that the difference between both points is a result of an unbalanced state.

Cell 5 was also subjected to dynamic changes of the gas inlet humidification, shown in Figure 5.14. The results reveal a faster response of the water mass located in the edge region compared to cell 3 and 4. The direct gas feed of the edge channel is likely to be responsible for shorter water transport pathways. But it still took about 10 and $30\,\mathrm{min}$ until equilibration of the edge region when drying or humidifying respectively.

To overcome the restrictions caused by through-plane imaging, namely the difficulties in differentiating anode and cathode sided water, both gas compartments were purged sequentially [165]. Figure 5.15 exemplarily shows the water content and distribution in FF and edge region

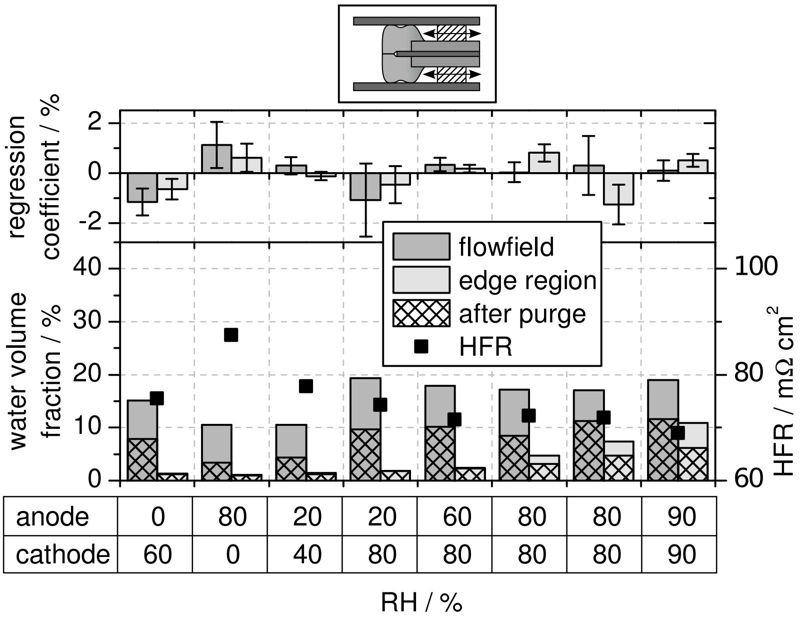

Figure 5.13: RH-map of cell 5 under variation of the gas inlet humidification and drift values indicating the stability of the operating state.

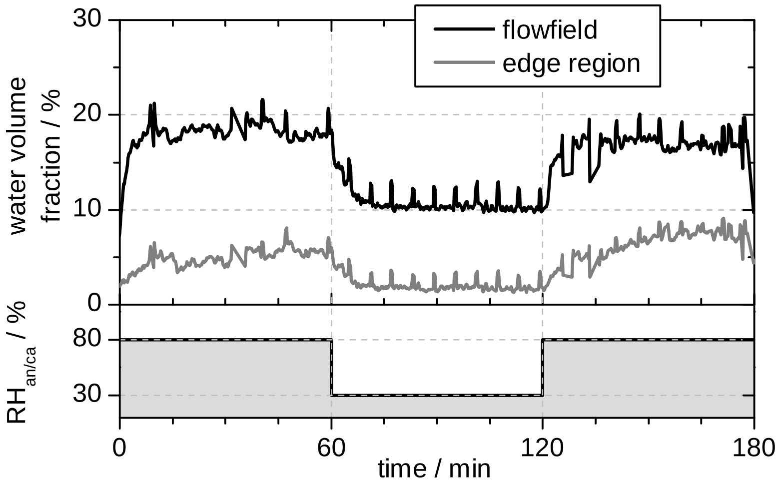

Figure 5.14: Dynamic water transport of cell 5 when changing the gas inlet humidity for one hour from $80/80$ to $30/30\,\%\,\mathrm{RH}$ and vice versa.

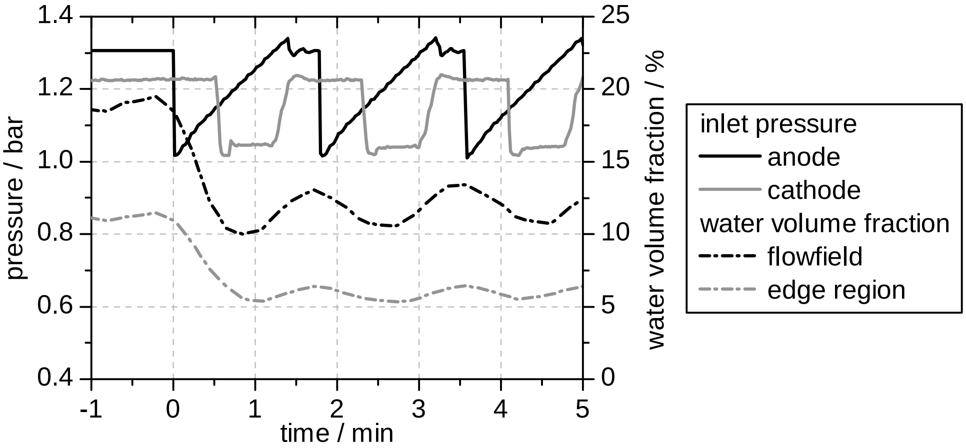

Figure 5.15: Water volume fraction in FF and edge region of cell 5 during 6 subsequent gas purges, 3 on the anode and 3 on the cathode side.

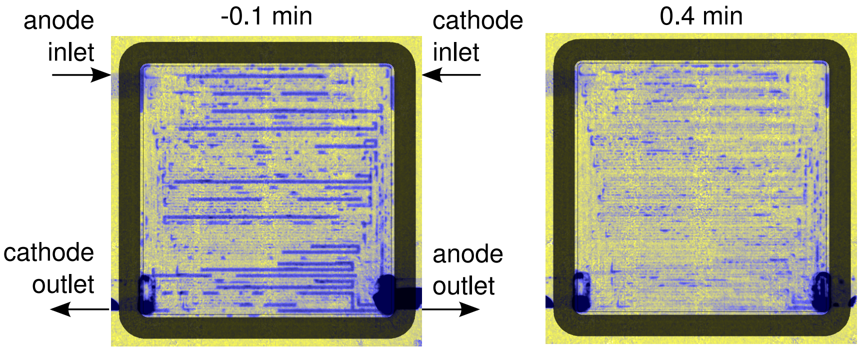

Figure 5.16: Water volume fraction in cell 5 before purging ($-0.1\,\mathrm{min}$) and after purging the anode ($0.4\,\mathrm{min}$). The water mass is indicated in blue. Time refers to Figure 5.15.

during a series of purges in cell 5. It is obvious that mainly anode channels were filled with water, as after the first anode purge a major part of residual water in the FF as well as in the edge region was removed. Also the local inconsistency of the FF channels at the bend positions of the serpentines enables a rough differentiation of anode and cathode sided water in the FF.

Before the purges residual water in the edge region was mainly located behind both gas inlets on top of the cell, exactly between the both breakthroughs of the edge land where no significant gas flow takes place as the radiograms in Figure 5.16 show. An anode sided purge drained out water located around the anode inlet area. A subsequent cathode purge had the same effect on the cathode inlet side. The residual water after both purges is expected to remain in the GDL and CCM and could not be drained out by further purges.

5.3.4 Pressure Drop

Liquid water, located in the FF as droplets or as a film, leads to an increase of the pressure drop over the cell. Therefore the pressure drop can be employed as an indicator of the water content in the cell [177–179]. The model from Section 3.1.3, based on Bernoulli's equation, is employed to calculate the FF pressure drop with consideration of the water content in the cell measured by NR. Thereby the measured water content in the cell is assumed to be located on the ground of the FF channels as a film of constant thickness, equally distributed between anode and cathode. It has to be considered, that the model neither accounts for the pressure drop between pressure sensors and the cell gas ports, nor for gas flow through the GDLs. In order to account for these contributions to the pressure drop and also for inhomogeneous water distribution over the cell, the calculated results for the pressure drop are multiplied with a constant factor on anode and cathode side to fit the measurement data. The factor is known as *two phase pressure drop multiplier* in the literature [178], here denoted as $k_{\mathrm{dp,an}}$ and $k_{\mathrm{dp,ca}}$ for anode and cathode, respectively.

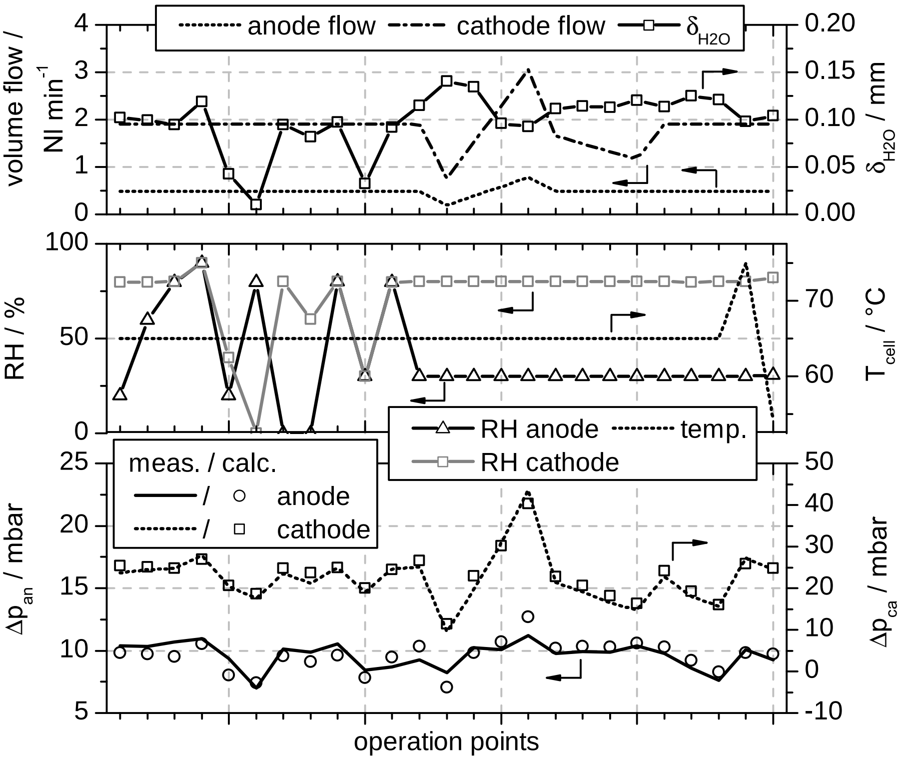

Figure 5.17: Top/middle: Operating parameters including the measured mean water thickness in the cell $\delta_{\mathrm{H_2O}}$. Bottom: Pressure drop over anode and cathode FF for different static operation points. Experimental data compared with results from calculation based on the simple model from Section 3.1.3.

Figure 5.17 shows the experimental data compared to the calculated pressure drops for the best fit with $k_{\mathrm{dp,an}} = 1.2$ and $k_{\mathrm{dp,ca}} = 2.2$ for a wide range of different static operation states. The top part of Figure 5.17 shows the according operation parameters, cell temperature, water thickness measured by NR $\delta_{\mathrm{H_2O}}$, gas volume flows and gas inlet humidification. The volume flow variations indicate changing electrical loads and stoichiometries. Each point was held over $30\,\mathrm{min}$ and all parameters were averaged over the last $7\,\mathrm{min}$. For constant volume flows and cell temperature the pressure drops basically follow the water thickness in the flowfield. The deviations between model and experiment are acceptable with a mean error of $6.2\,\%$ $(0.6\,\mathrm{mbar})$ on the anode and $6.1\,\%$ $(1.2\,\mathrm{mbar})$ on the cathode side. Also under variation of volume flows and cell temperature the agreement is good. It reveals that the pressure drop can be a viable measure for the rough estimation of the overall water content in the cell by means of a very simple model approach.

5.4 Discussion

Even though the test cell exhibits less FF channels, a smaller active area and also another relation between FF width and length compared to common full size cells, the effect of a FF bypass between both systems is comparable. The theoretical calculation of the remaining FF stoichiometry and of the flow distribution between FF and edge channel caused by a bypass in Section 3.1.3 showed a negligible influence of the cell size and number of channels, while the FF type (serpentine or straight channels) was shown to have a major impact. But it has to be considered that the absolute volume flow in a bypass generally scales with the cell area, having an influence on local water transport. This effect also occurs in the FF when scaling up the active cell area, since the number of channels related to the cell area determines the local volume flow in one channel. Nevertheless the test cell is employed as a model here, since the results are transferable to industrial full size PEFC systems with few restrictions.

It was seen, that in general gas humidification on the anode side has a minor influence on the overall water content in the cell. Comparing all points with $80\,\%\,\mathrm{RH}$ humidification at the cathode side in the rh-maps in Figure 5.3, 5.8 and 5.13 reveals a variation of $\Theta_{\mathrm{H_2O}}$ in the range of measurement uncertainty although the anode humidification varied from 0 to $80\,\%\,\mathrm{RH}$.

In all experiments a clear trend to an increased water accumulation in the bottom part of the cell could be observed. Both, gravitation and accumulation of product water close to the gas outlets can be the reasons for that, but both effects cannot be examined separately.

Opened and Closed Edge Channels

It was found that if the edge region of a cell is not charged with a direct gas feed, water is permanently accumulated there, especially in its bottom part as Figure 5.9 shows. In cell 3 and 4 for example, water volume fractions in the edge channel reached up to $24\,\%$ and $10\,\%$, respectively. Water removal from this area was hardly possible by purging (Figure 5.8), indicating a minor influence of pressure drop driven liquid water transport there. However, dynamic changes of the gas inlet humidification proved that water transport between the FF and the edge region is possible, but on quite long time scales. In cell 3 it was observed that the drying process does not reach an equilibrium even after one hour of drying (Figure 5.9). That can be a critical issue in fuel cells exposed to freezing conditions, as residual water in the cell is expected to exacerbate cold starts and long drying processes are not viable for system routines.

During the drying procedure, water was removed from the inner border of the edge channel in cell 3 first, possibly driven by water uptake of the FF gas stream. Also isotope exchange experiments confirmed that gas can diffuse through the GDL into the edge region. The results concur with the effect of a dominant water transport via evaporation and diffusion between closed edge channel and FF. The dominance of water vapor diffusion compared to transport in liquid form is likely to originate from the high capillary pressure of the GDL, caused by small pores and the hydrophobic PTFE coating.

In certain metallic BPP designs considerable bypass streams around the FF can be established if the edge land exhibits gaps. In cells 2 and 5, both with an opened edge channel, 3.5 and $0.7\,\mathrm{mm}$ wide, the edge region contained only small amounts of water compared to the FF, pointing out that high volumetric gas flows cause strong water removal by pressure differences and water uptake. The FF was thereby also affected as the gas flow was lowered there and a lower pressure drop entails reduced droplet removal, as it is the case in cell 2. Figure 5.3, 5.4 and 5.5 definitely show that cells with a strong bypass flow like cell 2 can have twice the FF water content over a wide range of operating conditions compared to a cell without a bypass like cell 1.

The significance of the bypass in technical cells, particularly with straight FFs, can be lower than in the test cell used in this work, depending on the cell geometry (cf. Section 3.1.3). For serpentine-like shaped FFs, the impact can be considerable and bypass flows should be minimized by globally reducing the edge channel cross section or by inserting a plurality of discrete bypass breaking structures. In general it is inevitable to consider the influence of the edge region geometry in cell design and development.

Influence of the Edge Channel Cross Section

Further investigations proved that the edge channel width can have a significant influence on the water transport in cells with a closed edge region under dynamic conditions. In wide edge channels a higher water mass was accumulated and also the relative volume filling grade was higher compared to cells with narrow edge channels, as results in Figure 5.8 reveal. Under dynamic variation of the gas inlet humidity a cell with wide edge channels exhibited considerably higher equilibration times as higher water masses have to be transported and transport pathways are longer (Figure 5.9). But in contrast to the described cells with a FF bypass, no evidence for an influence of the edge channel width on the FF water content could be found, emphasizing that no significant gas flows pass the edge region in this case.

Influence of the Operating Conditions

It was found that the operation temperature has a slight influence on the water distribution in the range between 55 and $75\,^{\circ}\mathrm{C}$, shown in Figure 5.6 for cell 1. One would expect that if diffusion processes dominate the water transport in the edge channel, this effect would be stronger, but it has to be considered that the measured operating points were not stable as temperature changes had a slow effect on the water distribution.

Under a raising inlet gas pressure, the water volume in a closed edge channel increased significantly. In cell 1 the edge region was filled with about $41\,\%$ of water at $2\,\mathrm{bar_a}$ compared to $27\,\%$ at $1.3\,\mathrm{bar_a}$ (Figure 5.4). This concurs with the assumption of a dominant gaseous water transport in the edge region as the decreasing water uptake capability of gas with raising pressure results in a worsened water removal. In contrast, the water content in the FF was relatively unaffected by pressure, although volumetric gas flow and hence the pressure drop over the cell is lowered with a raising inlet pressure.

A direct influence of the current density on the water distribution could not be proven. But as cells were operated in stoichiometric mode, an increasing gas velocity improves liquid and vapor water removal. A corresponding decrease of the water content in the FF was observed (Figure 5.5). The edge region water content did not show a consistent dependency from the electrical load.

The bigger part of water was observed to be located in the bottom part of the cell in all operating states, in the FF as well as in the edge region. As all cells were operated with a vertically orientated cell plane, gravity influences can be the reason for that. However, it has to be considered that both gas outlets are in the bottom part of the cell and electrochemically produced water accumulates preferably towards the cell outlets.

In each cell a good agreement between FF water content and the measured HFR value could be found. High water contents result in good membrane humidification and a low HFR, which is in line with the findings of Owejan et al. [166]. The edge region water content did not seem to have an influence on the HFR. Observed variations between different cells can be assigned to variations in the cell assembly.

Comparison of Sealing Solutions

All investigated sealing setups differ in the mechanical implementation of the CCM in its outer perimeter. In solutions based on a SG, the CCM is partially covered and inactive in the area superimposed to the edge channel. However, no influence of the SG on the water distribution was seen in the comparison of cell 1 (with SG) and 3 (without SG) in Figure 5.3 and 5.8 under consideration of the drift values.

But as a SG requires a wide edge region to accommodate the overlap between CCM and GDL, a large free volume is formed, leading to the described disadvantages as intensified water accumulation or a FF bypass. Whereas a cell setup based on a seal-on-GDL, as shown in cell 5, enables to design a narrow edge channel, posing a small reservoir for water accumulation, short water transport pathways and a fast dynamic behavior. And the CCM has a good mechanical attachment to the sealing since it is entirely covered by the GDL. Also the utilization of the active area is very good in seal-on-GDL setups, as the covered CCM area under the sealing is small.

5.5 Conclusions

It was found that the structure of a PEFC in its outer perimeter, which mainly depends on the implemented sealing solution, can strongly affect the water transport mechanisms of a cell. The following results were revealed from NR measurements:

- Free volumes in the edge region tend to be flooded with water if they are not supplied by a direct gas feed. Time constants for water transport between FF and edge region can then be in the range of hours. For operation under higher pressure the accumulated water mass increases in the edge region, whereas temperature and electric load do not have a significant influence. In edge channels with a higher cross section, a higher volume fraction remained filled with water, likely an effect of extended water transport pathways.

- Even though water transport in the edge region is slow if there is no supply by a direct gas stream, it was proven by isotope exchange experiments that it is accessible for gas, diffusing from the FF through the GDL into the edge channel.
- In cell setups where an open edge region is directly accessible for gas flows, a bypass stream around the FF can emerge and lowers the stoichiometry in the active area. As a result, the edge channel is dried out and the integral water content in the FF increases as water removal strongly depends on the gas volume flow.

Chapter 6

Sub-Zero Startup of PEFCs*

Startup capability under freezing conditions is required for PEFC systems operated under outdoor conditions. Self-startup without any external heating is a prerequisite for state-of-the-art systems with reduced complexity. Starting PEFCs from sub-zero temperatures can be challenging as generated product water risks to freeze, causing cell failure by blocking gas pathways for reactant gases in the porous layers. Hence a fundamental understanding of the cell failure mechanisms is essential in order to enable robust system functionalities even at temperatures far below $0\,°\mathrm{C}$. In this work a focus was set on analysis of water transport processes during isothermal startups at temperatures between -10 and $-2.5\,°\mathrm{C}$. NR was applied in order to analyze spatial heterogeneities of water production during a cold start[1] and also to verify phase transitions from water to ice. The latter was facilitated by a recently developed dual spectrum NR method, which was applied for the first time to a $50\,\mathrm{cm}^2$ test cell. The results reveal that at $-5\,°\mathrm{C}$ and above freezing can occur in a limited region while the rest of the cell continues to generate liquid product water. But as temperature is shifted downwards, water production tends to be more uniform and freezing mechanisms seem to proceed more homogeneously over the cell plane.

A second focus was laid on the impact of the initial membrane water content and of liquid residual water in the FF on cold start capability. Both can be influenced by the cell shutdown procedure and are hence a viable starting-point to improve the cold start capability. It was proven that residual water generally has a negative influence on cold start capability. This work is based on results from NR experiments as well as on classical electrochemical parameters.

6.1 Literature Review

Actual research focuses on understanding the influence of individual parameters or components on the cold start capability of PEFCs in order to deduce mitigation strategies. A widely applied method is to perform isothermal cold starts [25, 147, 152, 164, 180–196]. Thereby temperature

---

[1] In the following the term *cold start* is used as a synonym for a fuel cell startup under freezing conditions.

*Parts of this chapter were published in [127] and [128].

is held constant during the startup by an external cooling circuit [147, 152, 164, 180–184, 196–199] a climate chamber [25, 185, 186, 189, 190, 193–195, 197, 200–205], or by Peltier elements [192, 206]. Isothermal cold starts are performed as they facilitate the understanding of single parameter influences. Beside the measurement of standard electrochemical parameters also spatial current distribution measurements [202, 203], CVs [191, 201], electrochemical impedance spectroscopy [181, 188, 191, 195], transparent cells [192, 198, 206], NR [164, 167, 180–182, 185, 199], X-Ray tomography [152] or ex-situ cryo-SEM [25, 147, 187, 188, 204] analysis were reportedly used for the evaluation of cold starts.

There is still an ongoing debate about the influence of water located in the membrane on the cold start capability. Membrane water can be generally distinguished into freezable and non-freezable water. Strong binding forces of water molecules to the sulfonic acid end groups of the membrane (SO_3^-) prevent a limited fraction from freezing. Up to $\lambda_{\mathrm{mem}} = 14$ of non-freezable water was reported [45], which maintains ionic conductivity even at temperatures far below $0\,^{\circ}\mathrm{C}$. Thompson et al. proposed that the remaining free water can be frozen [46]. These results were contradicted by another group reporting that ice formation in the membrane could only be observed at very high swelling states such as $\lambda_{\mathrm{mem}} = 50$ [207]. During a cold start, water uptake by the membrane is desirable as it preserves a part of product water from freezing. Therefore, the membrane's initial humidification state is crucial for the operation time as a dry membrane can absorb a higher amount of product water [187, 188]. However, Chacko et al. additionally showed, that an excessively dry membrane inhibits a successful cold start as its poor ionic conductivity does not allow for drawing any current from the cell [189].

Water can be drained into the GDL as well as into the FF during a cold start [152, 164, 182, 192]. Ge et al. observed water evolving from the CL in a transparent cell at cell temperatures down to $-3\,^{\circ}\mathrm{C}$ [198]. They concluded that the freezing point was depressed in the CL by $2\,^{\circ}\mathrm{C}$ due to the high capillary pressure of the CL (also see [183, 208]). The lack of water in the FF after a cold start at $-5\,^{\circ}\mathrm{C}$ was then attributed to freezing in the GDL or CL. Another group concluded from their experiments, that a temperature gradient from the CL to the FF appears and water begins to freeze at the point where the temperature reaches $0\,^{\circ}\mathrm{C}$ [205]. Using the pressure drop in the cathode FF as an indicator, they concluded that even at $-7\,^{\circ}\mathrm{C}$ water reached the FF channels. Mukundan et al. showed NR measurements where for cold starts at $-10\,^{\circ}\mathrm{C}$ and below water was accumulated mainly at the interface between cathode CL and cathode GDL, while for a cold start at $-8.5\,^{\circ}\mathrm{C}$ the water was shifted to the cathode GDL volume [182].

In the absence of an initiating nucleation, liquid water can persist in a PEFC under sub-zero temperatures as *supercooled water*. This was unambiguously revealed for the first time by Ishikawa et al. [192, 206, 208] and recently confirmed by Biesdorf et al. [162]. It is evident that low cell temperatures give rise to a higher probability for an initial freezing event as the activation barrier for the phase transfer decreases with the temperature [209]. Hence, operating time is generally observed to reduce with a decreasing temperature in numerous experiments [164, 182, 183, 190, 193, 196, 198, 201–203]. The freezing of water under sub-zero temperatures can either be triggered by activation of the phase change, e.g. in form of a mechanical shock or due to a nucleation site [164]. Freezing can be initiated in the CL, MPL, GDL or even in the FF. It is still unclear if water in the membrane can also act as a initiator for freezing as relevant publications are contradictory [45, 46, 187, 207].

The freezing mechanism mainly depends on the startup temperature. At low temperatures as $-20\,^{\circ}\mathrm{C}$, all product water was observed to freeze immediately in the CL [187, 188, 193, 204], while some results show that at $-10\,^{\circ}\mathrm{C}$ water reaches the interface between CL and MPL [193, 204]. At higher temperatures, water can reach the GDL and even the FF before freezing [152, 206, 208]. This behavior can be shifted to lower temperatures in small cells as they statistically accommodate less nuclei where freezing can be initiated and supercooled water can thus persist for longer times [196].

As soon as freezing is initiated by a nucleus, the blockage of the gas pathways is a function of local water production and hence of local current density. An inhomogeneous freezing behavior over the cell plane can be expected as the current density exhibits a strong gradient as known from experiments above $0\,^{\circ}\mathrm{C}$ [43, 210]. Lin et al. showed in non-isothermal cold starts of a segmented cell, that shortly before the cell failure, current production close to the gas outlets breaks down [202]. As the cell is operated in galvanostatic mode, current density in the inlet region rises up before the entire cell breaks down. Also measurements from Jiao et al. showed, that the current production close to the cell outlets is low and generally limits the cold start capability [203].

As has been reported in literature, residual water can be present in a cell prior to a cold start originating from previous cell operation. Residual water may be located in the membrane, CL, MPL, GDL and in the FF. Its amount and distribution strongly depends on the applied shutdown procedure, such as cell cooling profile and purging of the gas compartments after cell operation. In Chapter 5 it was shown that in certain cell designs, water can remain in the outer perimeter of the FF, if this region is not accessible for a direct gas feed. Even after purging with dry gas for up to an hour, liquid water droplets can remain in the cell. After a cell shutdown, its temperature can fall below $0\,^{\circ}\mathrm{C}$ under the influence of environmental conditions.

As system downtime can easily exceed several hours, residual water is most likely to be frozen at an upcoming cold start, accelerating the freezing of additional product water and hence lowering the cold start capability.

6.2 Experimental Protocol and Data Analysis

For the experiments a test cell as described in Section 4.1.1, with an opened edge channel, was employed. For the experiment in Section 6.3.4 it was replaced with a cell with a closed edge channel. An automated conditioning and start protocol, listed in Table 6.1, is applied to ensure constant conditions for each cold start. In order to force water accumulation in the edge region of the cell for certain experiments, the conditioning step was replaced by cell operation under load until sufficient product water was generated. In Table 6.1 $\dot{V}_{\mathrm{an}}$ and $\dot{V}_{\mathrm{ca}}$ denote the volume flow on anode and cathode side and T_{cs} the cold start temperature.

Table 6.1: Standard experimental protocol for cold starts.

no.	step name	operating conditions	duration/condition for next step
1	drying	$T_{\mathrm{cell}} = 25\,^{\circ}\mathrm{C}$, $\dot{V}_{\mathrm{ca}} = 1.5\,\mathrm{l\,min^{-1}}$, $\dot{V}_{\mathrm{an}} = 0.6\,\mathrm{l\,min^{-1}}$, dry N_2	HFR $\geq 0.5\,\Omega\,\mathrm{cm}^2$
2	conditioning	$\dot{V}_{\mathrm{an/ca}} = 0.5\,\mathrm{l\,min^{-1}}$, N_2, $50\,\%\,\mathrm{RH}$	$10\,\mathrm{min}$
3	pipe blow	$\dot{V}_{\mathrm{an/ca}} = 0.2\,\mathrm{l\,min^{-1}}$, dry N_2	$15\,\mathrm{s}$
4	subcooling	$T_{\mathrm{cell}} = -15\,^{\circ}\mathrm{C}$	$T_{\mathrm{cell}} = -15 \pm 0.5\,^{\circ}\mathrm{C}$
5	heating	$T_{\mathrm{cell}} = T_{\mathrm{cs}}$	$T_{\mathrm{cell}} = T_{\mathrm{cs}} \pm 0.5\,^{\circ}\mathrm{C}$
6	gas flows	$\lambda_{\mathrm{an/ca}} = 8.5$ (ref. to current of step 7) $T_{\mathrm{cell}} = T_{\mathrm{cs}}$	$\Delta\varphi_{\mathrm{cell}} > 0.8\,\mathrm{V}$
7	operation	current ramp $0.01\,\mathrm{A\,cm^{-2}\,s^{-1}}$ current density see Table 6.2, $\lambda_{\mathrm{an/ca}} = 8.5$ $T_{\mathrm{cell}} = T_{\mathrm{cs}}$	$\Delta\varphi_{\mathrm{cell}} < 0.2\,\mathrm{V}$
8	imaging	no gas flows, $T_{\mathrm{cell}} = T_{\mathrm{cs}}$	$10\,\mathrm{min}$
9	heating up	$T_{\mathrm{cell}} = 25\,^{\circ}\mathrm{C}$	$T_{\mathrm{cell}} = 25 \pm 0.5\,^{\circ}\mathrm{C}$

One of the main influencing factors on the cold start capability and particularly on the operation time until cell failure is the current density i during a cold start. In order to compare cold starts with different current densities, the accumulated charge current density q is introduced as the integrated cell current density over the operating time t

$$q = \int_{t} i\,dt. \tag{6.1}$$

Figure 6.1 shows the electrochemical data for an exemplary cold start at $-5\,^\circ\mathrm{C}$. It can be divided into three sequential phases. In phase I water uptake by the membrane gives rise to a falling HFR and an increasing cell voltage. In phase II water is accumulated in CL, GDL and FF, while cell voltage and HFR remain stable. In phase III the membrane resistance begins to rise up – likely a result of membrane dehydration caused by a prevailing electroosmotic drag over back diffusion [211] or a change in vapor saturation pressure – and the cell voltage decreases until final cell failure. Cold starts are often observed to directly pass from phase I to III as no stable cell operation can be achieved. In Figure 6.1 the accumulated charge current densities q_uptake, q_stable, q_failure, q_cs and q_acc assigned to the individual phases are shown. Note that the time on the x-axis in the following graphs refers to the beginning of cell operation in step 7 of a cold start.

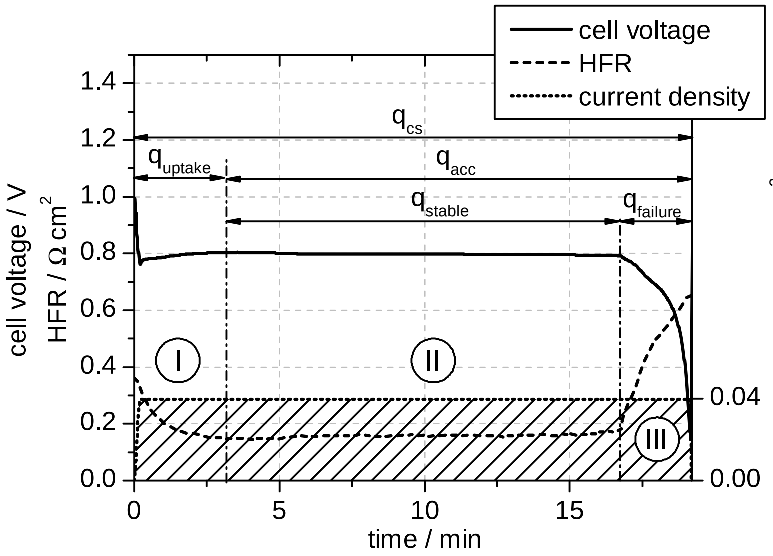

Figure 6.1: Data of an exemplary isothermal cold start at $-5\,^\circ\mathrm{C}$ and $0.04\,\mathrm{A\,cm^{-2}}$ and the accumulated charge current densities q assigned to the different phases I-III.

Figure 6.2 shows an exemplary neutron radiogram during a cold start at $-2.5\,^\circ\mathrm{C}$. The gas inlets are both on top, the outlets on the bottom of the cell plane as indicated. For data analysis the cell plane is divided into 9 areas, labeled with letters A to I. The water thickness is averaged in each region. The areas close to the in- and outlets are excluded as accumulated water on the outer cell surface superimposed the measurements there. The indicated droplets in Figure 6.2 (A1-E5) are analyzed by dual spectrum NR in one experiment (cf. Figure 6.4). Table 6.2 shows the number of performed cold starts with and without the use of NR with the according startup temperature and current density.

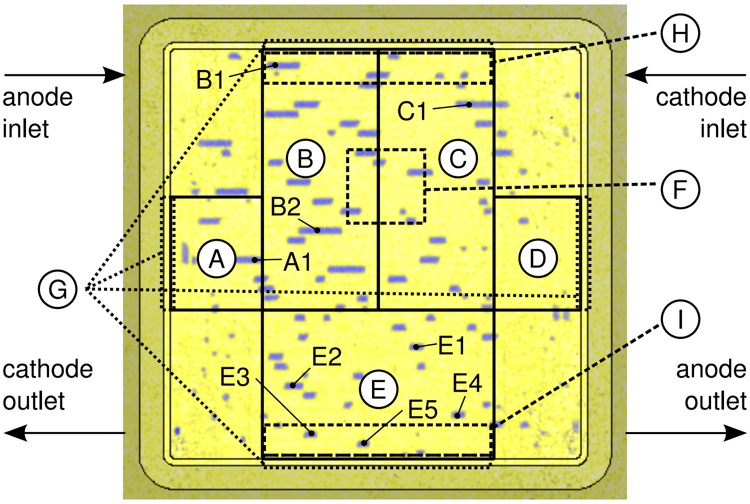

Figure 6.2: In-plane water distribution during an isothermal cold start at $-2.5\,°\mathrm{C}$ and $0.04\,\mathrm{A\,cm^{-2}}$, $28\,\mathrm{min}$ after startup. Labels indicate averaging areas and monitored droplets. Water filled areas are colored in blue, void areas are yellow.

Table 6.2: Number of isothermal cold starts performed at different start temperatures and current densities with and without the use of NR.

current density /	Temperature / °C				
$\mathrm{A\,cm^{-2}}$	-2.5	-5	-7.5	-10	
0.02	-	1	-	-	with NR
		3	1	-	w/o NR
0.04	3	22	3	2	with NR
	2	11	2	2	w/o NR
0.1	-	-	-	-	with NR
	-	4	1	-	w/o NR
0.2	-	-	-	-	with NR
	-	1	-	-	w/o NR

6.3 Results

6.3.1 Dual Spectrum Neutron Radiography

Crucial startup temperatures for non-isothermal cold starts of full size cells lie at $-20\,^{\circ}\mathrm{C}$ and below. However, at negative temperatures close to $0\,^{\circ}\mathrm{C}$ freezing mechanisms are believed to proceed slower, facilitating a basic understanding of PEFC cold starts. Also liquid water percolation through the GDL into the FF is more likely. Amongst others isothermal cold starts at $-2.5\,^{\circ}\mathrm{C}$ at a current density of $0.04\,\mathrm{A\,cm^{-2}}$ were performed. Droplets formed in the FF and their aggregate state transition was studied by dual spectrum NR combined with the simultaneous observation of volume changes resulting from phase changes. Single droplets were picked out in order to monitor the relative attenuation σ_{rel} over a part of their projected area. Calculating σ_{rel} of droplets is promising as their high water thickness provides stable values and reduces the influence of interferences.

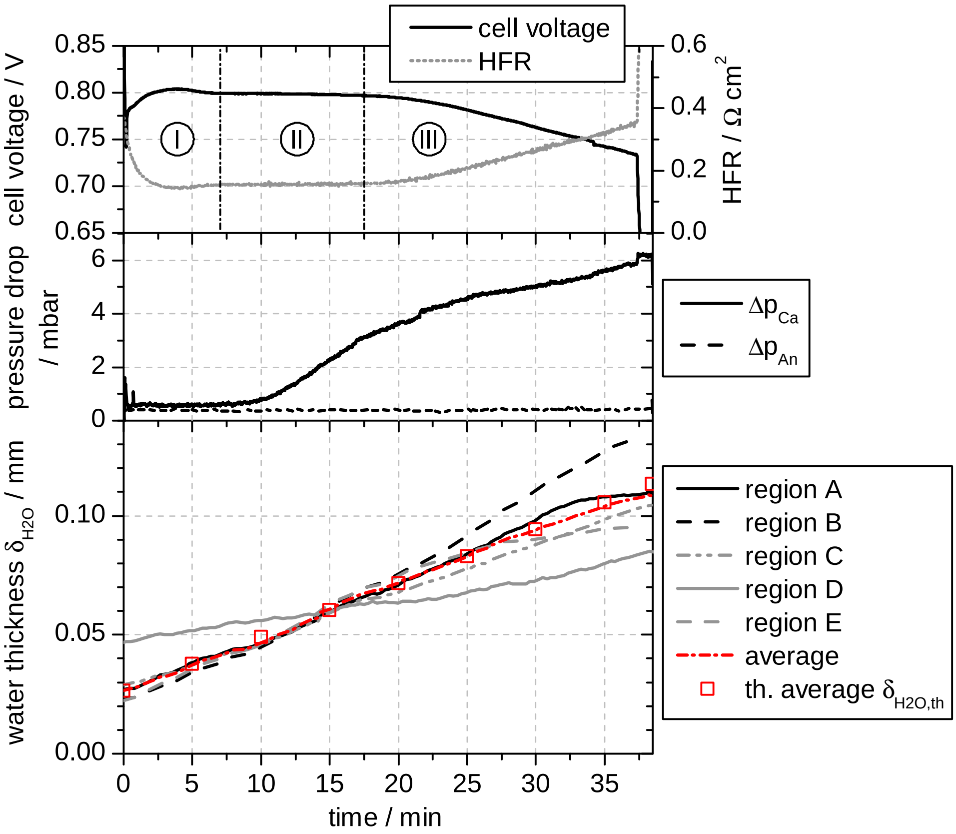

Figure 6.3: Voltage, HFR and pressure drops during an isothermal cold start at $-2.5\,^{\circ}\mathrm{C}$. Water thickness in different regions of the cell (labels refer to Figure 6.2) and calculated theoretical average water thickness for the entire cell under the assumption that all product water remains in the cell.

Water droplets were observed to percolate into the FF about $11\,\mathrm{min}$ after startup ($q = 26\,\mathrm{C\,cm^{-2}}$), supposing that water is present in liquid phase. The major part emerges into the cathode FF, as indicated by the raising pressure drop in the cathode compartment in Figure 6.3, while the anode pressure drop remains constant. This behavior was also identified elsewhere [205]. Droplets located in the FF were not observed to move during the cold start, likely caused by the low pressure drop of $< 6\,\mathrm{mbar}$ on the cathode side and negligible water uptake of the gases at low temperatures. At about $18\,\mathrm{min}$ after startup the characteristic bend in voltage and HFR is seen, interpreted as the initiation of ice formation in one of the cell components [189]. Simultaneously, droplets in region E stopped to grow while droplets in region A-D continued to grow. The pressure drop rose up slower from that point. Except in region D, the water accumulation rates were constant and almost identical in all regions until they diverged after the bend in cell voltage, ending up with the lowest final water thickness in region E and with the maximum in region B, around $40\,\%$ above region E. Region D differed significantly from the rest of the cell, it exhibited the highest initial water thickness but the lowest increase in water thickness.

The average water production of the entire cell remained constant, consistently with the galvanostatic operation mode. Assuming that all electrochemically produced water remains in the cell the theoretical water thickness in the cell $\delta_{\mathrm{H_2O,th}}$ can be calculated with

$$\delta_{\mathrm{H_2O,th}} = \frac{q \cdot M_{\mathrm{H_2O}}}{2F \cdot \rho_{\mathrm{H_2O}} \cdot A_{\mathrm{cell}}}. \tag{6.2}$$

The calculated values for $\delta_{\mathrm{H_2O,th}}$, shown in Figure 6.3, are in good accordance with the measured average water thickness, indicating that water uptake of the gases has a negligible influence. At $-2.5\,^{\circ}\mathrm{C}$ and a volume flow of 97 and $233\,\mathrm{ml\,min^{-1}}$ at anode and cathode, respectively, a maximum of $40\,\mathrm{mg}$ of water can be discharged by the gases over the duration of the cold start of $38\,\mathrm{min}$ according to Arden Buck equation [212]. This corresponds to a water thickness of only $8\,\mu\mathrm{m}$.

Figure 6.4 shows the relative attenuation σ_{rel} of selected droplets, marked in Figure 6.2, and cell voltage and HFR during the cold start. As droplets are growing slowly in the FF, a sufficient droplet size to analyze the relative attenuation with acceptable noise is reached from about $20\,\mathrm{min}$ after the start of current. Before, droplets do not fill the analyzing areas, so σ_{rel} neither shows a reasonable value nor is stable. All droplets close to the gas outlets in region E (E1-E5) steadily grew up until about $18\,\mathrm{min}$ and then stopped to expand just at the same time as cell voltage begins to decrease. An abrupt volume expansion at that point is seen but cannot be clearly distinguished from the droplet growing process resulting from water

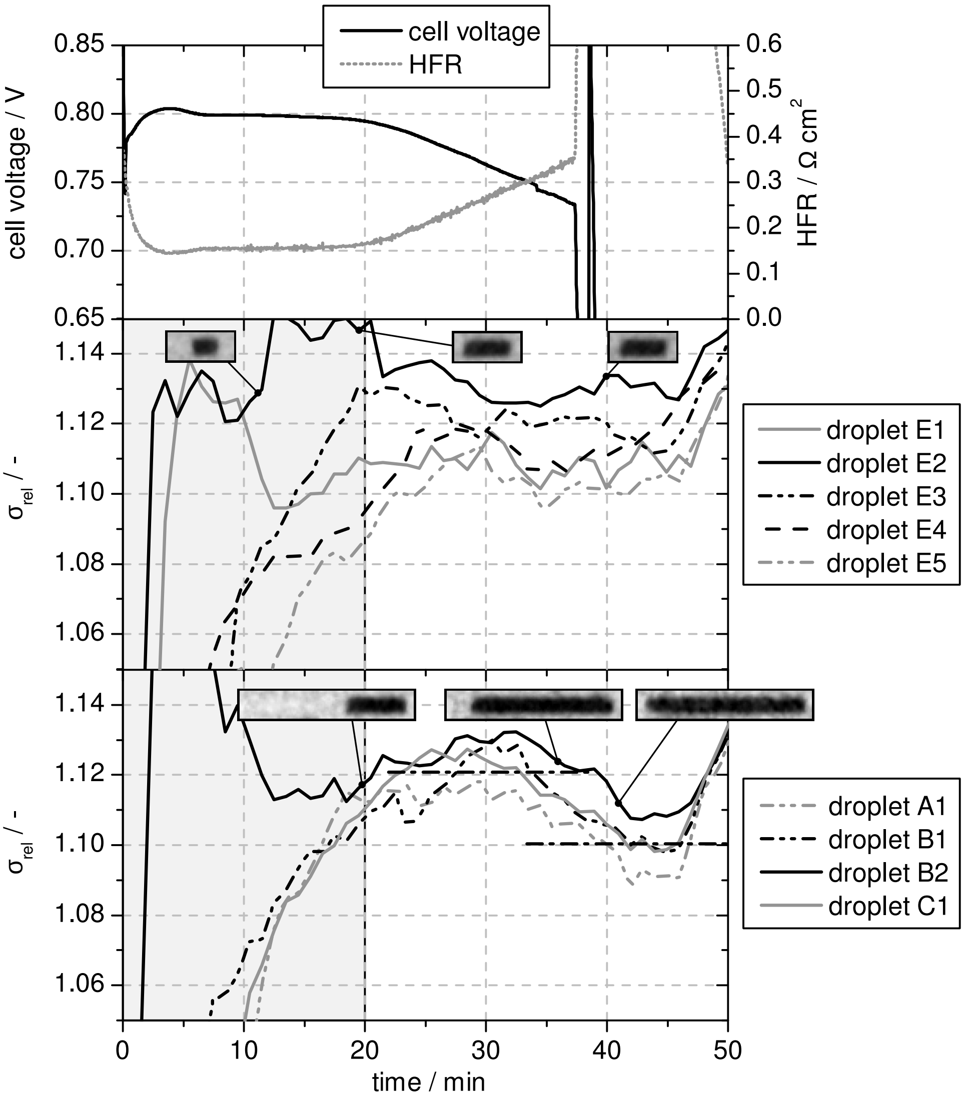

Figure 6.4: Cell voltage and HFR for an isothermal cold start at $-2.5\,^{\circ}\mathrm{C}$ and relative attenuation of individual droplets (labels refer to Figure 6.2). Small images show the shapes of droplet E2 and B2 in different states. Freezing of droplets in region A-C is seen simultaneously to the cell failure while droplets in region E seem to be already frozen from about $20\,\mathrm{min}$.

accumulation. The values for σ_{rel} are generally not stable at $18\,\mathrm{min}$, meaning that no phase change of droplets in region E can be identified by the dual spectrum method. Around the final cell failure ($38\,\mathrm{min}$) neither a significant change of σ_{rel} nor any further droplet volume expansion can be seen in region E, which indicates that these droplets were already frozen. The analyzed droplets A1, B1, B2 and C1 all lie in the top part of the cell. They grew steadily until $38\,\mathrm{min}$ after startup and even continued to grow when droplets in region E stopped to expand, indicating that water in a liquid state still must be present there. Simultaneously with the cell failure at $38\,\mathrm{min}$ a prompt volume expansion of all droplets in region A-D is seen and the meniscus of some droplets changed from a concave to a convex shape. The phase change from water to ice can be confirmed unambiguously by the negative step of σ_{rel} over a period of about $7\,\mathrm{min}$ simultaneously with the cell failure. The average change of the droplets A1-C1 amounts to $1.8\,\%$ and coincides well with the experimental results in [162] where a contrast of $1.6\,\%$ was measured. The discrepancy can arise from general measurement uncertainties, an error in the background correction or sample scattering effects.

6.3.2 Spatial Heterogeneities during Cold Starts

In the experiments monitored by NR no stable operation with respect to cell voltage and HFR could be observed for cold starts at $-5\,^{\circ}\mathrm{C}$ and below. As soon as a minimum HFR is reached by membrane water uptake, HFR increases and the cell voltage begins to decrease. Figure 6.5 shows an exemplary cold start at $-5\,^{\circ}\mathrm{C}$. The minimum HFR was reached after $2\,\mathrm{min}$, followed by an increase over almost $10\,\mathrm{min}$ ($23.5\,\mathrm{C\,cm^{-2}}$). Concomitantly the voltage decreases to $0.2\,\mathrm{V}$. In neutron radiograms, no droplets were seen in the FF channels. The image is confirmed by the pressure drop in both gas compartments, which remained constant. The water thickness in the cell rose up constantly in the cell regions A-E with only slight differences. However, a discrepancy of up to $25\,\%$ between the measured average water thickness for the entire cell and the theoretically calculated value $\delta_{\mathrm{H_2O,th}}$ is seen. A small part of it can be explained by water uptake capacity by the gases. For a volume flow of 97 and $233\,\mathrm{ml\,min^{-1}}$ on anode and cathode side, respectively, maximum water uptake at $-5\,^{\circ}\mathrm{C}$ over $11.8\,\mathrm{min}$ equals around $6.8\,\mathrm{mg}$ according to Arden Buck equation [212]. This corresponds to a mean water thickness of $\delta_{\mathrm{H_2O}} = 1.4\,\mu\mathrm{m}$ over the $50\,\mathrm{cm^2}$ cell plane, explaining $5\,\%$ of the $25\,\%$ discrepancy. The rest is assumed to be an error in the background calculation already observed in previous studies [160].

As averaging over regions A-E may not be sensible to local deviations on small scales, the entire cell plane was scanned with smaller averaging areas. Region F, with a size of $1.6\,\mathrm{cm^2}$, was found to be the only area showing a significantly differing trend. Simultaneously with

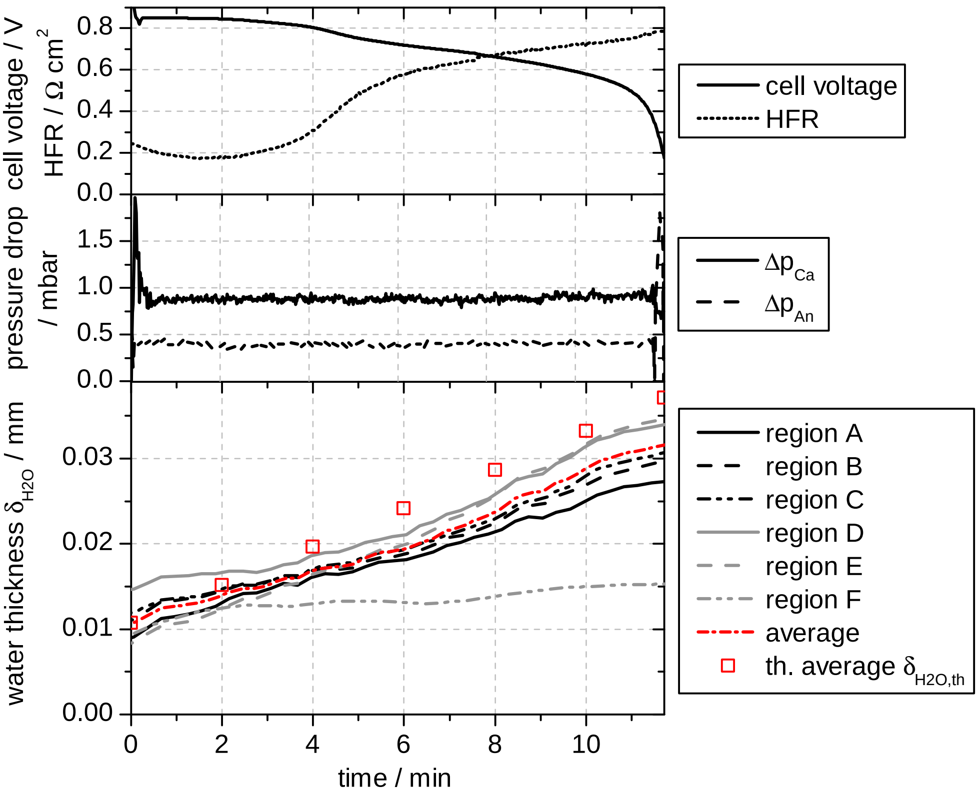

Figure 6.5: Electrochemical data and water thicknesses during an isothermal cold start at $-5\,^{\circ}\mathrm{C}$ and calculated theoretical water thickness for the entire cell under the assumption that all product water remains in the cell.

the bend in cell voltage and the beginning of HFR increase water accumulation stopped there and a stagnation until cell failure is seen. Note that region F is superimposed to regions B and C and hence is included in the results for the water thickness in these regions. A decreasing or interrupted water production within a local dead spot, as described here, could be proven in 2 of 5 investigated cold starts at $-5\,^{\circ}\mathrm{C}$. During all cold starts at $-5\,^{\circ}\mathrm{C}$ and below, neither emerging droplets in the FF were observed by NR nor an increasing pressure drop over one of the gas compartments was measured.

Cold starts at $-10\,^{\circ}\mathrm{C}$ generally exhibit a lower mean operation time than at $-5\,^{\circ}\mathrm{C}$, which is in good agreement with literature [164, 182, 183, 190, 193, 196, 198, 201–203]. The initial phase I of a selected cold start in Figure 6.6 lasts for around $2\,\mathrm{min}$ ($4.7\,\mathrm{C\,cm^{-2}}$). No stable operation (phase II) was observed. Phase III, indicated by an increasing HFR and a decreasing cell voltage, took around $7\,\mathrm{min}$ ($18\,\mathrm{C\,cm^{-2}}$) until cell failure. The constant pressure drop over the anode and cathode FF and also the neutron radiograms confirm that no water was drained into the FF channels. The water thickness in the different regions evolved approximately

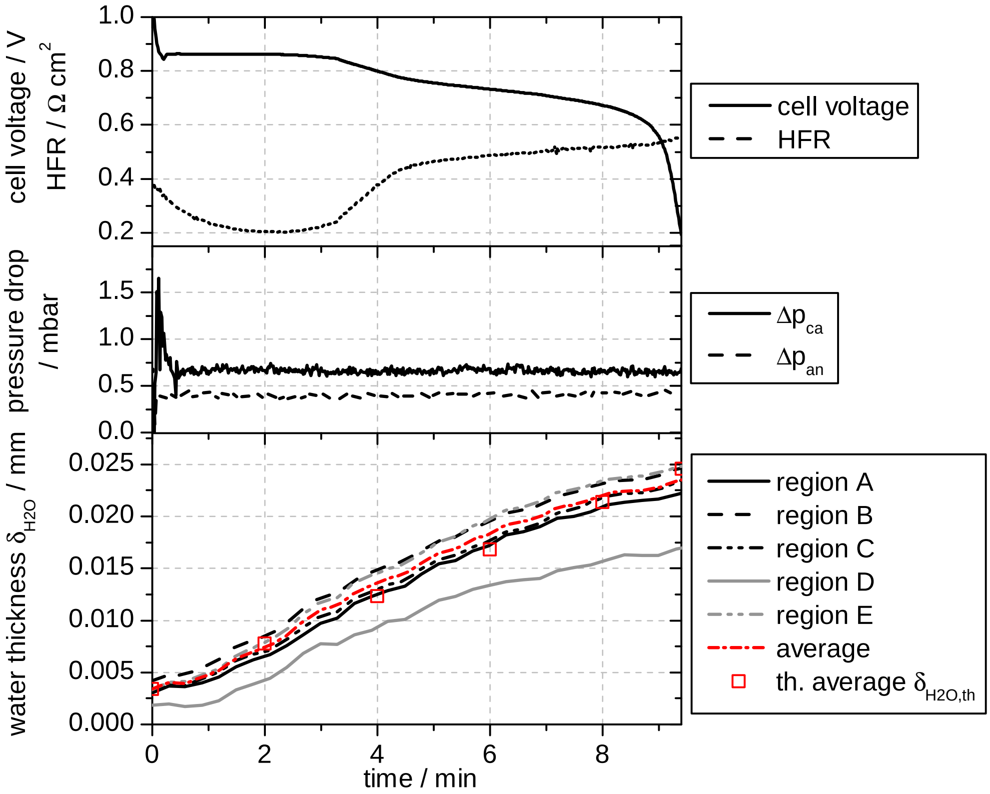

Figure 6.6: Electrochemical data and water thicknesses in a cell during an isothermal cold start at $-10\,^{\circ}\mathrm{C}$ and calculated theoretical water thickness.

linear during the cold start. The segments do not differ significantly among themselves, except region D, where the water accumulation rate and the absolute water thickness permanently remain below the other segments. In region D the water thickness permanently stays at around $30\,\%$ below the average value for the entire cell. Disregarding region D the highest water mass was accumulated in region E, the lowest in A, by the time of cell failure. The difference between both amounts to about $10\,\%$. Although the entire FF was scanned with an averaging area of $1\,\mathrm{cm}^2$ no areas with an appreciably differing water thickness evolution were found as it was the case for cold starts at $-5\,^{\circ}\mathrm{C}$. The calculated theoretical water thickness in Figure 6.6 remains slightly below the measured mean water thickness, but the difference does not exceed $10\,\%$, which is in good accordance with common measurement uncertainties [160].

In order to obtain an impression of water distribution on a smaller scale, the water thickness was averaged in region E along the horizontal direction[1] in order to obtain a mean water distribution over the channel-land structure. Figure 6.7 shows a cutout of the averaged water

---

[1] The cell plane is orientated vertically in the experiments, the main FF channels are than horizontally orientated (cf. Figure 4.1). Water distribution was averaged over the length of a FF channel.

thickness before a cold start at $-5\,°\mathrm{C}$ and averaged between 0 and 5 and between 5 and $10\,\mathrm{min}$ of operation. Water is initially mainly accumulated under the ribs. During the operation this qualitative distribution does not change and even more water accumulates under the ribs between the $0-5$ and $5-10\,\mathrm{min}$ point while changes under the channels are lower. Locally slightly negative water thicknesses are obtained. It is likely to be a measurement artifact as result of residual water in the reference images, or of a water film on the outer surface of the cell.

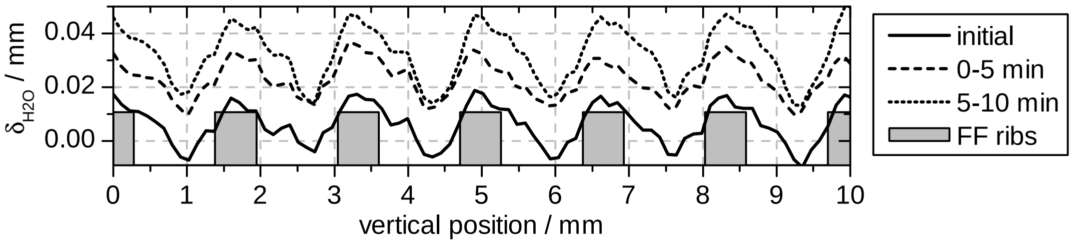

Figure 6.7: In-plane water distribution in the cell over channels and lands, obtained by averaging in the flow direction of region E at different phases of a cold start at $-5\,°\mathrm{C}$. The image shows an extract over 6 channels. The gray scheme indicates the position of the FF ribs.

6.3.3 Influence of the Initial HFR on Cold Start Capability

42 cold starts were performed at $-5\,°\mathrm{C}$, at current densities between 0.02 and $0.2\,\mathrm{A\,cm^{-2}}$ under different conditioning procedures. Cells were started up with residual water in certain cell areas, as well as without any visible water in the FF. The HFR at $25\,°\mathrm{C}$ before cold starts varied between 0.069 and $0.182\,\Omega\,\mathrm{cm^2}$ as Figure 6.8 indicates. The difference arises from different conditioning procedures. Particularly for some cold starts, residual water was forced to remain in the cell and caused low HFR values. q_{cs} ranges from 6.6 to $72.9\,\mathrm{C\,cm^{-2}}$ without any obvious correlation to the initial HFR. The mean value of the HFR is $0.13\,\Omega\,\mathrm{cm^2}$ with a standard deviation of $0.027\,\Omega\,\mathrm{cm^2}$ while q_{cs} has a mean value of $29.3\,\mathrm{C\,cm^{-2}}$ and a standard deviation of $12.2\,\mathrm{C\,cm^{-2}}$. Two outliers reached more than twice the mean value with 68 and $72.9\,\mathrm{C\,cm^{-2}}$.

Theoretically, the accumulated charge current density of phase I, q_{uptake} should increase with the initial HFR due to an increased water uptake capability of the membrane. As the latter is limited physically, q_{uptake} should converge to a maximum value with an increasing initial HFR. Assuming that in the initial phase no water is transported to the CL or GDL (as done in [189]), q_{uptake} corresponds to the amount of water absorbed by the membrane. In

Figure 6.8 a trend is seen where q_{uptake} rises with the initial HFR, which confirms this theory, but an exact correlation cannot be verified due to statistically insufficient data.

The residual water mass in the cell before all cold starts could not be quantified as only a part of the experiments were performed with imaging.

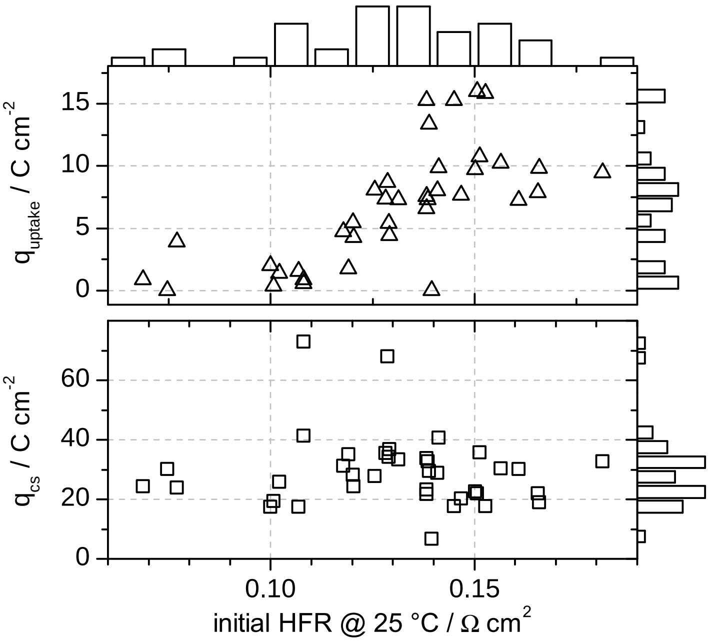

Figure 6.8: Dependency of q_{cs} and q_{uptake} from the initial HFR before cooling down the cell. Each data point represents a single cold start, performed at $-5\,^{\circ}\mathrm{C}$ at current densities between 0.02 and $0.2\,\mathrm{A\,cm^{-2}}$.

6.3.4 Influence of Residual Water on Cold Start Capability

Viable sealing solutions for mass production of PEFC require an adapted cell design, particularly in the outer perimeter of the active area. Especially sealing solutions based on a SG require large free volumes between the gasket and FF. In Chapter 5 it was shown that if these free volumes are exposed to a direct gas flow, they can act as a bypass around the FF, lowering the stoichiometry in the active area. Otherwise, if they are isolated from a direct gas feed, they are susceptible to flooding. In the latter case, residual water can remain in the cell even after prolonged purging with dry gas as time constants for water transport can be shifted to hours in the isolated areas. Two different negative influences of residual water on the cold start capability are conceivable:

- Residual water freezes in the cell and can act as a nucleus for frost initiation of electrochemically produced water during a cold start. Hence, the cold start capability can be reduced as the formation of supercooled water is impeded.
- Residual water clusters, e.g. in the outer perimeter of the cell, can be redistributed during cell downtime by in-plane diffusion over the membrane plane and thus lower the membrane water uptake capacity during cold starts.

The latter case was not described in literature relating to cold starts so far. But indirectly it can be concluded that humidification of the membrane by in-plane diffusion has a negative influence on the cold start capability as water uptake capacity of the membrane is lowered and product water transport is shifted towards the CL and GDL pores where it is susceptible to freezing [188, 209]. It has to be considered that in-plane diffusion in the membrane is a very slow process. Equilibration can take days or weeks, as indicated by a falling HFR after shutting down a cell after operation.

The influence of residual water clusters on the cold start capability was investigated with an adapted cell setup. Between sealing structure and FF an edge channel of $1\,\mathrm{mm}$ width is left (cf. Figure 4.2) which leads to an accumulation of water as shown in Chapter 5. An edge land continuously surrounds the FF, which impedes convective flow in the edge channel. Water can only be exchanged between FF and edge channel by lateral permeation through the GDL. Product water was generated by operating the cell under load and the cell was then subjected to the standard conditioning protocol from Table 6.1. As water can hardly be removed from the edge channel, it remained there at least partially during the subsequent multiple cold starts.

Before the cold start the major part of water remains in the bottom part of the edge channel (bottom part of region G), which is possibly an effect of gravitation and of a humidity gradient from in- to outlet during conditioning. The outlet regions are filled up with water, they act as a water trap and can hardly been dried out. In some cases, water droplets were also located on the left and right hand sided edge channel, but they vanished after few cold starts. The top part of the edge channel was permanently free of droplets. Figure 6.9 shows the relative attenuation σ_{rel} of a water cluster located in the bottom part of region G during cooling down the cell from 25 to $-15\,^{\circ}\mathrm{C}$. The cluster has an area of around $35\,\mathrm{mm}^2$ and a mean water thickness of $0.63\,\mathrm{mm}$. Neither current was drawn nor the cell was fed with gases during cool down.

A negative step of the relative attenuation σ_{rel} is seen at a cell temperature between 2.5 and $-8\,^{\circ}\mathrm{C}$ as it is characteristic for a phase transition from liquid water to ice. The step amounts to about $2\,\%$, which agrees quite well with the previous results in this chapter and the data from Biesdorf et al. [162]. In the FF, no phase transitions could be observed. The mean water thickness was small compared to that in the edge channel which resulted in σ_{rel} being impacted by a large noise.

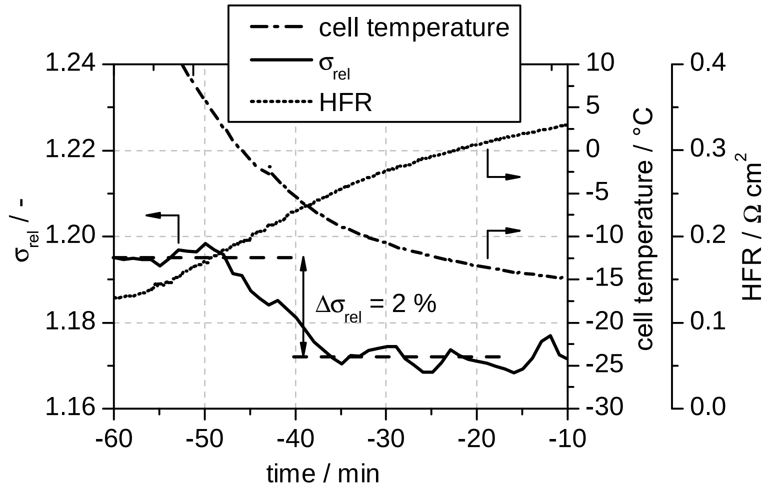

Figure 6.9: Relative attenuation σ_{rel} of a residual water cluster in the edge channel during cool down as a measure for phase transitions. A negative step of σ_{rel} by $2\,\%$ clearly proves a phase transition from water to ice. Time on the x-axis refers to the beginning of the following cold start.

In the following phase II and III of a cold start will be emphasized since all processes beside membrane water uptake are expected to have a strong influence here. The residual water in the cell – apart from water located in the membrane – is expected to mainly affect phase II and III of a cold start. For that reason, the membrane humidification phase I was excluded from the subsequent considerations and in the following it is referred to the accumulated charge density of phase II and III, q_{acc} .

16 subsequent cold starts were performed, where the water content in the cell and particularly in the edge channel varied. Figure 6.10 shows the initial water thickness for each of the cold starts in both, the edge channel ($\delta_{\mathrm{H_2O,ec}}$) and the FF ($\delta_{\mathrm{H_2O,ff}}$) over q_{acc} as well as the HFR at 25 °C before cooling down the cell. Although the cell is dried until HFR exceeds $0.5\,\Omega\,\mathrm{cm}^2$ followed by a conditioning phase of $10\,\mathrm{min}$ with humidified gas ($50\,\%\,\mathrm{RH}$) at 25 °C before each cold start, neither constant FF water content nor a constant HFR could be reproduced over all cold starts. The drying phase seems to be too short to establish an equilibrium condition.

$\delta_{\mathrm{H_2O,ec}}$ was averaged over region G ($1.4\,\mathrm{cm}^2$) and $\delta_{\mathrm{H_2O,ff}}$ over region A-E ($34\,\mathrm{cm}^2$). Negative values for the water thickness are obtained in some cases. A conceivable reason is that residual water in the reference image falsifies the neutron radiograms as the images for all cold starts are referenced to one global reference image for which the cell was dried extensively.

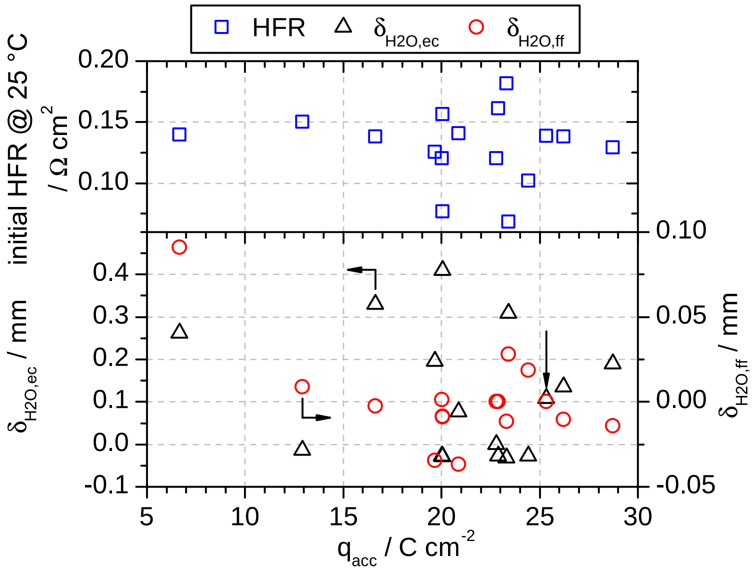

Figure 6.10: Initial HFR at 25 °C before a cold start and water thickness in the FF $\delta_{\mathrm{H_2O,ff}}$ and in the edge channel $\delta_{\mathrm{H_2O,ec}}$ for different cold starts over the accumulated charge current density of phase II and III q_{acc}. All cold starts were performed at $-5\,°\mathrm{C}$ and $0.04\,\mathrm{A\,cm^{-2}}$. The vertical arrow indicates the investigated cold start in Figure 6.11.

For the temporal evolution of phase II and III, no influence of the initial HFR is expected as a full membrane humidification is supposed. The assumption is confirmed by the absence of any correlation between q_{acc} and the HFR (top part of Figure 6.10).

All cold starts reached values for q_{acc} between 6.6 and $28.7\,\mathrm{C\,cm^{-2}}$. Thereby the water thickness in the edge channel $\delta_{\mathrm{H_2O,ec}}$ shows a very slight correlation to q_{acc}. Even cold starts with more than $0.3\,\mathrm{mm}$ of water in the edge channel reached values of 16.5 to $23.5\,\mathrm{C\,cm^{-2}}$ for q_{acc}. However, the cold start with the lowest value for q_{acc} also exhibited the highest FF water thickness with more than $0.4\,\mathrm{mm}$, indicating a negative influence of the residual water in the FF. Also the three cold starts with highest values for q_{acc} have relatively low initial water thicknesses in both, edge channel and FF.

One of the cold starts with $q_{\mathrm{cs}} = 25.3\,\mathrm{C\,cm^{-2}}$ (marked with an arrow in Figure 6.10) with initial values for the water thickness of $\delta_{\mathrm{H_2O,ec}} = 0.11\,\mathrm{mm}$ and $\delta_{\mathrm{H_2O,ff}} = 0\,\mathrm{mm}$ is selected for further analysis. A long operation time was reached in spite of residual water in the edge channel. The major part of residual water was located in the bottom part of the edge channel. The mean water thickness before the cold start in the right, left and top side of the edge channel amounts to only $0.06\,\mathrm{mm}$ compared to $0.31\,\mathrm{mm}$ in the bottom part. Figure 6.11 shows the evolution of cell voltage, HFR over the operation time. Also the increase of water thickness relative to the beginning of the cold start $\Delta\delta_{\mathrm{H_2O}}$ is shown. Both, cell voltage and

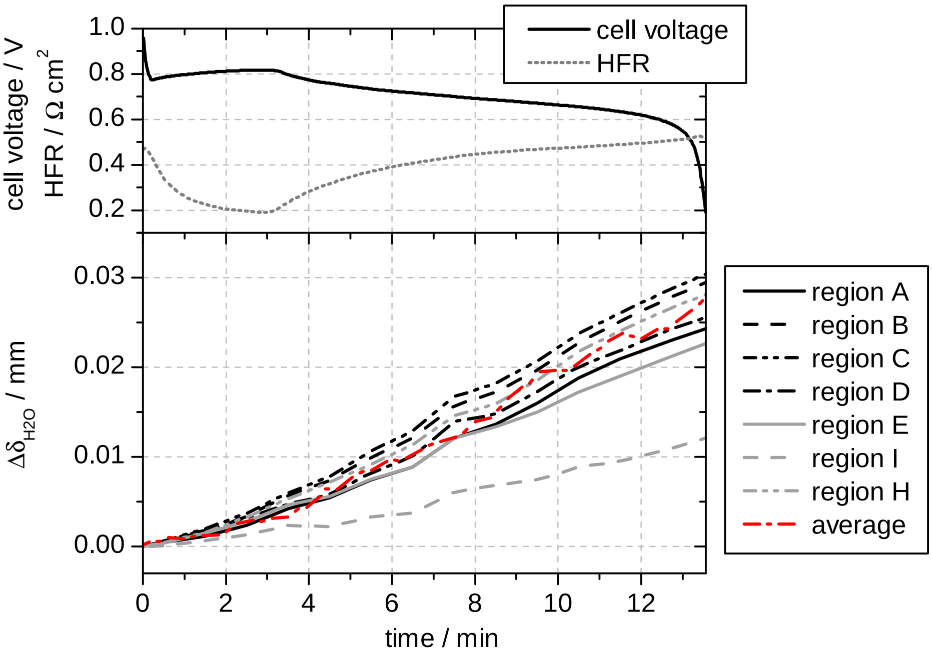

Figure 6.11: Electrochemical data and change of water thicknesses from the beginning of the cold start $\Delta\delta_{\mathrm{H_2O}}$ in a cell during a cold start at $-5\,°\mathrm{C}$ with residual water in the bottom part of the edge channel.

HFR exhibit a sharp bend at $3.1\,\mathrm{min}$ or $7.3\,\mathrm{C\,cm^{-2}}$ after startup. Subsequently HFR rises up from 0.2 to $0.5\,\Omega\,\mathrm{cm^{-2}}$ and cell voltage decreases from 0.8 to $0.2\,\mathrm{V}$. The water layer grows up almost equally distributed over the cell plane in regions A-D, without respect to the different initial water thicknesses. Region E exhibits a slightly reduced water accumulation rate. By scanning the whole FF, it was found that in the most bottom part of region E, here denoted as region I (cf. Figure 6.2), with an area of $2.4\,\mathrm{cm^2}$, less than half the water mass accumulated compared to the cell average. In contrast to the bottom part, the top part of the edge channel accommodates almost no residual water, the mean initial water thickness amounts to only $0.02\,\mathrm{mm}$. In the adjacent segment in the FF, region H (cf. Figure 6.2) with an area of $2.4\,\mathrm{cm^2}$, no differing water accumulation rate can be found compared to the average value.

All cold starts with a considerable initial amount of water in the edge channel were analyzed regarding a similar behavior as described before. In 3 of 9 cases, a region was found close to the flooded edge channel on the bottom part of the cell where water accumulation rate was significantly reduced compared to the rest of the cell. The relevant area never exceeded $3\,\mathrm{cm^2}$.

6.3.5 Preferential Water Pathways in Porous Layers

In all cold starts at $\leq -5\,^{\circ}\mathrm{C}$ not a single droplet was seen to be drained into the FF in the neutron radiograms. All water seems to be retained in one of the porous layers. However, as soon as the cell was heated up after a failed cold start, droplets emerged into the FF over the whole cell plane at about $2.5\,^{\circ}\mathrm{C}$. Figure 6.12 shows the water distribution in the cell during heat up after three different cold starts at $-5\,^{\circ}\mathrm{C}$. The accumulated charge current density over the whole cold starts q_{cs} was in the range from 30 to $33\,\mathrm{C\,cm^{-2}}$ for all three cases. Note that the cell was dried and re-conditioned before each start according to the standard protocol. The comparison of the images reveals an almost exact match of position and shape of the droplets in the FF.

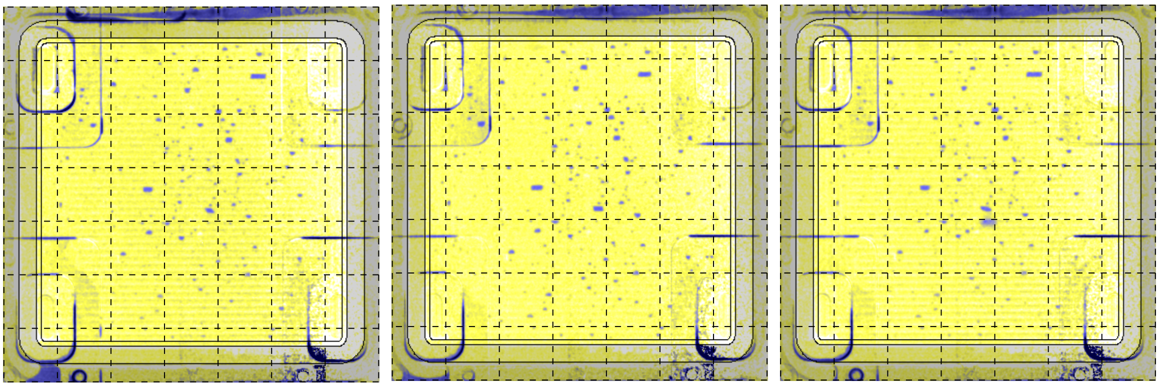

Figure 6.12: Water distribution in the cell during heating up at $5\,^{\circ}\mathrm{C}$, after three different cold starts. Grids are drawn to facilitate comparison of the images.

6.4 Discussion

Dual Spectrum Neutron Radiography

Under cold start conditions at moderate subfreezing temperatures ($-2.5\,^{\circ}\mathrm{C}$) and a current density of $0.04\,\mathrm{A\,cm^{-2}}$, NR revealed that liquid water can be drained into the GDL and also into the FF, where droplets grow up permanently during the cold start. All droplets located in the bottom part of the cell close to the gas outlets (region E), stopped to grow about $18\,\mathrm{min}$ after startup. Subsequently the water production rate began to slightly decrease in this region until final cell failure, indicating filling of CL and GDL pores with ice after an initial freezing event. As a consequence diffusion losses increased, bringing down local current density and water production. The rest of the cell continued to produce water, even with a higher rate, as the galvanostatic operation mode forces the total current to remain constant. Just at the final voltage breakdown of the cell, a distinct negative step of σ_{rel} and a simultaneous volume expansion of droplets prove that the top part of the cell (region A-D) immediately freezes, leading to cell failure terminating operation. At this point, droplets in region E do not show any changes, neither in volume nor in relative attenuation, confirming the early freezing point at 18 min.

Coinciding with the present results, the outlet region of a cell was already identified as the bottleneck for cold starts in other works as it generally exhibits the lowest current density and hence the lowest waste heat production [202, 203, 213]. The spatially limited ice formation in the outlet region could be explained by thermal gradients due to inhomogeneous waste heat production, so that temperatures can reach $0\,^{\circ}\mathrm{C}$ in the area adjacent to the gas inlets. However, the long and stable operation of the cell without significant changes of HFR and cell voltage for about $18\,\mathrm{min}$ without any evidence for a freezing event strongly indicates the presence of supercooled water in the cell until frost initiation occurs, which has already been identified by various groups [162, 192, 206, 208]. In general, it can be concluded that spatially limited freezing is possible in a PEFC, possibly caused by the fact that freezing – once initiated by a local nucleus – cannot spread out over the whole cell as water clusters in the cell are not continuous.

Spatial Heterogeneities during Cold Starts

In total, 42 isothermal cold starts were performed at $-5\,^{\circ}\mathrm{C}$. In 4 cases, a stable cell voltage and HFR were established (phase II) before the cell performance began to decrease (phase III), but none of them were analyzed by means of NR. In the remaining cases, the breakdown phase immediately followed on the initial phase of membrane humidification, indicating that a freezing event immediately occurs as soon as water is drained into the MPL and/or GDL. In none of these cold starts water was observed to reach the FF channels, which was confirmed by the stable pressure drop over both anode and cathode FF. Hence product water has to accumulate in the CL, MPL and/or in the GDL apart from membrane water uptake. The product water was found to be accumulated homogeneously distributed over the FF, except in a small area of $1.6\,\mathrm{cm}^2$ in the middle of the FF, where water production stopped simultaneously with the start of cell voltage breakdown. It is believed that in this area, local freezing occurs, without spreading out over the whole cell area. Once more it can be concluded that the water clusters in the cell which are frozen initially are not connected to accumulated water in the rest of the cell.

However, over a period of $6\,\mathrm{min}$ after the initial freezing event the cell power decreased by about $25\,\%$. It is unlikely that this change arises just from increased transport losses in a tiny cell area of less than $2\,\mathrm{cm}^2$, so the phenomena resulting in this power loss must occur over a substantial part of the cell area. Even after the freezing event, water production rates in the rest of the cell do not diverge or change significantly. So one can conclude that if any freezing occurs outside region F, it has to occur homogeneously over the cell plane.

In contrast, no areas with an immediate interruption in water production were found for cold starts at $-10\,°\mathrm{C}$. Water production rates were widely homogeneous over the cell area. Just one area in the cell (region D in Figure 6.6), with an area of about $10\,\mathrm{cm}^2$, was observed to produce around $30\,\%$ less water compared to the whole cell. The cell voltage breaks in immediately after the HFR reaches its minimum value, even before a stable cell voltage is reached. A possible explanation is that after an initial phase of membrane humidification, water is drained into the CL where it immediately begins to freeze. This coincides well with the results from other works, where an immediate freezing of water in the CL or MPL after the membrane humidification phase is propagated for temperatures of $-10\,°\mathrm{C}$ and below [187, 188, 193, 204]. It also elucidates the homogeneous water production over the cell area – except in region D – as ice formation leads to a uniform increase of gas transport losses.

Nevertheless it should still be taken into account, that the water distribution – and as a result the processes leading to ice formation – can be highly inhomogeneous on a smaller scale, caused by the channel-land structure of a FF. A detailed view into the NR data disclosed that prior to a cold start a major part of product water is located below the ribs (Figure 6.7) as a result of previous operation and conditioning at temperatures above $0\,°\mathrm{C}$. During the cold start, further water accumulation takes place under the ribs as well as under the channels. It is obvious that the water clusters under the ribs dominate the mass transport losses and are subject to a higher risk to freeze as the probability to encounter a nucleus is higher there.

In general, the results reveal, that a partial freezing of a cell plane is possible. After an initial freezing event, cell power decreases, indicating a subsequent expansion of freezing. This is supported by the fact that cells of a higher active area size exhibit a longer time between initial freezing event and cell failure than small cells for temperatures of $-10\,°\mathrm{C}$ and above, as elaborated in Section 6.4.

Influence of the Initial HFR on Cold Start Capability

Independent from the start temperature, the initial phase of a cold start is characterized by the water uptake of the electrolyte phase and hence a decreasing HFR. A high initial membrane humidification before the cold start has a negative influence on the water uptake capacity and hence also on the length of the humidification phase (phase I). It was found that q_{uptake}

increases with an increasing initial HFR (Figure 6.8), which coincides well with the theory and with literature [191].

Previous publications mainly related their argumentation to the duration of a cold start or the produced water mass during an entire cold start. Both parameters are comparable to q_{cs} in this work. Chacko et al. did not find a direct influence of the initial HFR on the produced water mass as long as the HFR is below $0.5\,\Omega\,\mathrm{cm}^{-2}$ [189]. Also Oberholzer et al. did not find a strong correlation between HFR and the entire operating time while humidification during conditioning was varied from 10 to $80\,\%\,\mathrm{RH}$ [164]. Both works conducted isothermal cold starts at $-10\,°\mathrm{C}$. At lower temperatures as $-30\,°\mathrm{C}$ Tajiri et al. discovered that membrane humidification and the subsequent freezing in the CL seem to be overlaid, as the cell voltage already falls down significantly before the HFR could even reach its minimum [186]. The results of this work at $-5\,°\mathrm{C}$ are in line with these findings. q_{cs} did not show any correlation to the initial HFR, which was varied between 0.069 and $0.182\,\Omega\,\mathrm{cm}^{-2}$ (Figure 6.8). Other effects than the initial membrane humidification seem to dominate the overall cold start capability at these temperatures.

Influence of Residual Water on Cold Start Capability

In Chapter 5 it was elaborated that depending on the cell design and particularly on the sealing concept, a considerable amount of water can be accumulated in an edge channel outside the FF, on the fringes of the active area. In this work, the influence of residual water clusters on the internal behavior of a cell during cold starts was investigated in order to verify if it has an influence on cold start capability. To quantify the cold start capability, the accumulated charge current density from the end of the initial membrane humidification until cell failure q_{acc}, was used. It enables to investigate cold starts disregarding the initial membrane water content, which can vary due to the conditioning procedure.

A residual water cluster, located in the bottom part of the cell edge channel, with a mean thickness of $0.63\,\mathrm{mm}$ and an area of $35\,\mathrm{mm}^2$ was monitored during cell cool down. The dual spectrum parameter σ_{rel} generally revealed stable values, but decreased by about $2\,\%$ at a cell temperature between 2.5 and $-8\,°\mathrm{C}$. This coincides well with the results from Biesdorf et al., where a contrast for σ_{rel} of $1.6\,\%$ was found for a phase transition from water to ice [162]. So it is verified unambiguously that residual water clusters in PEFCs immediately freeze when cooling down the cell to $< 0\,°\mathrm{C}$.

By deviating from the standard conditioning procedure the residual water mass in the cell before a cold start was varied. It was observed that the water content in edge channel and FF could hardly been varied independently, hence a separate investigation of the influence of residual water in both regions was not possible. However, it could be shown that residual water generally has a slight negative influence on q_{acc}. Nevertheless, the present data is not sufficiently supported by statistics to quantify a correlation.

A detailed observation of cold starts with residual water, particularly in the bottom part of the edge region was performed. 3 of 9 investigated cold starts revealed that in a small area in the FF, adjacent to the water clusters, the water production rate was reduced during the cold starts from the point where the cell voltage showed a bend and the HFR began to rise up. In the case shown in Figure 6.11, the produced water amount was reduced by about $50\,\%$ in the area close to the residual water cluster in the edge channel (region I) compared to the average over the whole cell. In the rest of the cell, no significant deviation from the mean water production was found.

One theory for the reduced water production rate in region I is, that in that area residual water is already frozen when starting the cell from sub-zero temperatures, posing a nucleus for further freezing of generated product water. As the initial water thickness in region I lies in the same range as in the other areas, the rest of the cell would be expected to show the same behavior. A possible explanation for that inconsistency is that in the rest of the cell, water is located in the membrane as non-freezable water or in the CL where the freezing point is depressed, while in region I it is located in the GDL or FF, caused by diffusive transport from the adjacent water cluster in the edge channel. Another possible explanation is that the frozen residual water cluster in the edge channel poses a nucleus for freezing of the generated product water only in a limited area around it and discontinuously formed water clusters inhibit the frost propagation over the whole cell. So the rest of the product water around that area remains in a non-frozen or supercooled state.

The results reveal that residual water in a cell has a generally negative influence on the cold start capability. This can be a crucial issue. Apart from the described mechanisms, residual water in the edge region of a cell can also be redistributed over the whole cell area by diffusion in the membrane or porous layers during system downtime, leading to a reduced water uptake capacity of the membrane.

Preferential Water Pathways in Porous Layers

Imaging cold starts with NR provides a further insight into water transport processes in porous layers as water is frozen in the place of its main percolation pathways in the CL and GDL. When a cell is thawed after a failed cold start, water drains out right at its recent position in the pores and gives an indication of the main transport pathways. After subsequent cold starts of the same cell with consistent operating conditions, an astonishing coinciding image of water droplet distribution and even droplet shape was found. It proves that preferential water percolation paths in the porous layers of a PEFC exist, as already found out by means of other methods [40, 214].

Influence of the Active Cell Area on Cold Start Capability

Apart from the entire operation time during a cold start, the sequence between initiation of freezing and end of operation (phase III) is of special interest, as its duration could give an information about the frost propagation over the cell area. Therefore, recent publications on isothermal, galvanostatic cold starts were reviewed regarding the accumulated charge current density from the point where a stable voltage plateau is left until cell failure, q_{failure}. Figure 6.13 and Table 6.3 show q_{failure} for different cell sizes, for cold starts at -5, -10 and $-20\,°\text{C}$. Despite no attention was paid to operating conditions and employed cell components and apart from uncertainties in the determination of the end of the stable voltage plateau, at $-10\,°\text{C}$ an increase of q_{failure} with the active area size is seen. At $-5\,°\text{C}$ a similar trend was found but the few literature values do not allow for a further evaluation. At a lower temperature as $-20\,°\text{C}$ q_{failure} does not vary significantly with a range from 2 to $8\,\text{C}\,\text{cm}^{-2}$ over all reviewed publications. The latter concurs with the finding, that at $-20\,°\text{C}$ generated product water immediately freezes in the CL of the whole cell without reaching a supercooled state [188, 193, 204]. The active area size of the cells does not have any impact on this mechanism

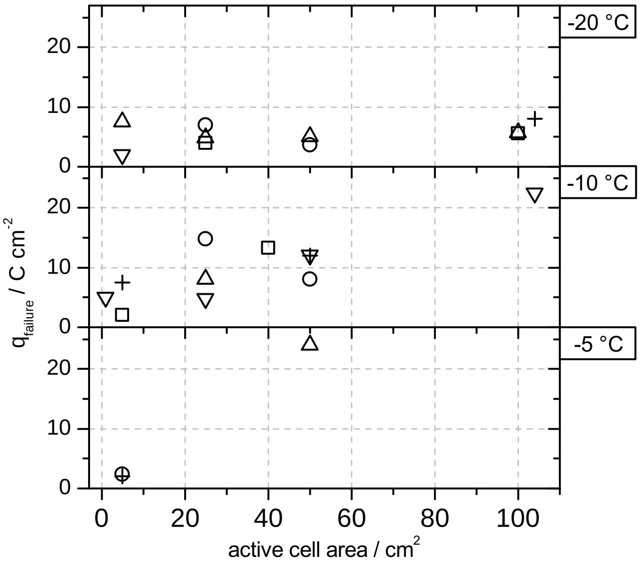

Figure 6.13: Literature values for the accumulated charge current density between end of the stable voltage plateau and cell failure q_{failure} (phase III) against the active cell area at different cold start temperatures.

as freezing occurs homogeneously over the cell plane, disregarding general temperature or concentration gradients over the cell plane.

Table 6.3: Literature values for q_{failure}, describing the accumulated charge current density between end of a stable voltage plateau and cell failure (phase III). q_{failure} is the product of current density and failure time.

cell size cm^2	current density $\mathrm{A\,cm^{-2}}$	failure time s	q_{failure} $\mathrm{C\,cm^{-2}}$	Ref. -
		$-5\,°\mathrm{C}$		
5	0.02	120	2.4	Ge 2006 [198]
5	0.1	20	2	Ge 2007 [183]
50	0.04	600	24	this work
		$-10\,°\mathrm{C}$		
1	0.1	50	5	Ishikawa 2007 [206]
5	0.05	150	7.5	Chacko 2008 [189]
5	0.1	20	2	Ge 2007 [183]
25	0.04	120	4.8	Lin 2014 [202]
25	0.04	200	8	Tabe 2012 [193]
25	0.04	370	14.8	Tajiri 2007 [190]
40	0.07	190	13.3	Jiao 2011 [205]
50	0.02	600	12	Mishler 2012 [184]
50	0.02	400	8	Mukundan 2009 [182]
50	0.04	300	12	this work
104	0.015	1500	22.5	Hishinuma 2004 [194]
		$-20\,°\mathrm{C}$		
5	0.05	150	7.5	Ge 2007 [183]
5	0.1	20	2	Ge 2007 [183]
25	0.01	700	7	Tabe 2012 [204]
25	0.04	120	4.8	Tajiri 2007 [190]
25	0.04	100	4	Tabe 2012 [193]
50	0.01	500	5	Thompson 2008 [187]
50	0.02	180	3.6	Mukundan 2009 [182]
100	0.02	280	5.6	Du 2014 [215]
100	0.02	280	5.6	Zhou 2014 [216]
100	0.02	280	5.6	Luo 2014 [217]
104	0.01	800	8	Hishinuma 2004 [194]

A general dependency of the total operation time during a cold start from the active area size was demonstrated in [196]. It was concluded that generated supercooled water in a cell segment of a defined area size runs the risk to freeze to a certain probability. As soon as freezing is initiated in one segment of a cell – consisting out of a multitude of single segments – ice propagates throughout the whole cell. The bigger the cell area, the more segments are present and the higher the probability that in one of them freezing is initiated. Lower startup temperatures reduce the required activation barrier for freezing and therefore generally increase the probability for a transition from supercooled water to ice. As a result, the operation time until cell failure decreases with a decreasing temperature.

In the frame of this work it was shown that local freezing of a fraction of a cell is possible at moderate startup temperatures as $-2.5\,^{\circ}\mathrm{C}$ and to some extent at $-5\,^{\circ}\mathrm{C}$, while water remains – at least partially – liquid in the rest of the cell. The non-frozen areas can proceed to generate product water, supported by a locally increased current density and hence increased waste heat production. The results indicate, that in the $50\,\mathrm{cm}^2$ cell, continuous water clusters over a significant area of several cm^2 can exist. They can freeze without affecting other water clusters in the cell due to the lack of a connection between the different clusters. The assumption, that continuous water clusters over a significant area of several cm^2 exist coincides well with the work of Biesdorf et al., where the cold start capability was found to decrease with an increasing active cell area [196]. The proposed theory was based on the fact that freezing – once initiated in one place in the cell – can propagate throughout a significant fraction of the active cell area. Therefore the existence of continuous water clusters of a relevant size is a requirement.

Considering the found dependency of the time for the frost propagation over the cell in phase III from the cell size from the literature review (in form of q_{failure} at $-10\,^{\circ}\mathrm{C}$) and with the theory of isolated water clusters covering a significant fraction of the cell area, the voltage decrease after an initial freezing event could be attributed to the subsequent freezing of further isolated water clusters in the cell.

At $-2.5\,^{\circ}\mathrm{C}$ one segment was found to initially freeze during the cold start, while at lower temperatures freezing seemed to proceed more homogeneously over the cell area. This behavior can be explained by the increased probability of having a freezing event in every segment of the cell to a defined time at lower startup temperatures.

Since certain areas of a cell seemed to remain unfrozen during a cold start, the results support the theory of supercooled water, as observed by many other groups [152, 162, 164, 192, 198, 205, 206, 208].

6.5 Conclusions

In this work isothermal cold starts were performed with a PEFC test cell with an active area of $50\,\mathrm{cm}^2$ at temperatures between -10 and $-2.5\,^{\circ}\mathrm{C}$ and the in-plane water distribution in the cell was analyzed by means of NR. In contrast to previous works, the total charge drawn during the cold start was separated in different phases (membrane water uptake, stable operation, failure). A further particularity of this work is that realistic sealing solutions were taken into account and the effect of residual water was assessed not only in the FF but also in the edge region of the cell. The key findings are the following:

- During a cold start at $-2.5\,^{\circ}\mathrm{C}$ water droplets were observed to be drained into the cathode FF, where they constantly grew but did not move. Freezing of droplets in a part of the cell, located close to the gas outlets, was proven by dual spectrum NR, while the rest of the droplets remained unfrozen.
- At temperatures from $-5\,^{\circ}\mathrm{C}$ and below, water production was seen to be more homogeneously distributed over the cell plane. Water did not percolate into the FF but remained in CL and GDL. However, local spots with a significantly reduced water production were found, likely areas which are subject to local ice formation.
- It was found out, that the initial membrane humidification state, measured by the HFR at room temperature, shows a strong correlation to the duration of the first phase of a cold start, characterized by a falling HFR due to membrane humidification. The initial HFR variation results from different conditioning and shutdown procedures. Therefore, the initial membrane humidification phase at the beginning of a cold start was excluded for further investigations.
- Freezing of residual water clusters in a cell during cool down below $0\,^{\circ}\mathrm{C}$ was directly verified by dual spectrum NR.
- Residual water (e.g. in porous media of FFs) was proven to have a slightly negative influence on the cold start capability. However, the conditioning procedure did not allow to vary the residual water in the edge region and FF independently.
- Residual water in the bottom edge channel of a cell caused an adjacent cell segment of up to $3\,\mathrm{cm}^2$ to produce less water compared to the rest of the cell in 3 of 9 investigated cold starts. It is believed that residual water in the edge channel freezes before starting the cell from sub-zero temperatures, causing the generated product water in the surrounding cell area to freeze faster during a cold start.
- Water pathways through CL and GDL during a cold start were identified to be consistent between different cold starts, supporting the theory of preferential water transport pathways in the porous layers.
- After a first freezing event the duration of the breakdown until cell failure was found to be dependent on the active area size of a cell for cold start temperatures $\geq 10\,^{\circ}\mathrm{C}$ in a literature review. This coincides well with the results of this work, as it was seen that local ice formation in a cell is possible before frost propagates over the whole cell.
- The results are also in good accordance with the theory of supercooled water and the finding that operation time during a cold start generally decreases with the cell size, as

the initiation of freezing is more probable in bigger cells due to the presence of more freezing nuclei [196]. Two outliers with an operation time of more than twice than the mean value confirmed this image. It is likely that no freezing occurred in these cases in the absence of a nucleus.

Chapter 7

Degradation Mechanisms in the Outer Cell Perimeter

In Chapter 5 it was seen that operating conditions in the edge region of a cell can deviate from the FF. Since occurrence and impact of degradation mechanisms are strongly coupled to local conditions such as temperature, humidity, reactant concentration and mechanical stress on the components, cell aging in the edge region may exhibit specific characteristics. A separate assessment of the area is required in order to determine if effects which limit the overall cell lifetime can occur there.

In this chapter a focus is laid on two specific degradation mechanisms occurring in the edge region, mechanical membrane damage and carbon support oxidation of the cathode CL caused by hydrogen starvation on the anode side. Both are generally known from the literature, but to the authors best knowledge they have not been investigated with respect to the specific boundary conditions in the outer perimeter of PEFCs.

7.1 Mechanical Membrane Deterioration

Depending on the sealing solution, the membrane can be clamped between gaskets or the single layers of a SG in its outer perimeter. Compared to the FF – where compression forces on the membrane are homogenized by the flexible GDLs – mechanical load on the membrane can be unfavorable in the edge region as point loads are likely to occur at the edges of gaskets or SG layers. As described in Section 3.2.2, different groups observed or assumed mechanical membrane failure at the edges of the active area [59, 60, 116–118], Huang et al. also found a load maximum there by numerical simulation [58]. The present experiment aims to determine if under unfavorable implementation of the membrane in its outer perimeter mechanical failure of the membrane can limit the lifetime of a cell.

7.1.1 Experimental Description

For this experiment, the test cell, described in Chapter 4 was used. By the employment of a CCM without PTFE reinforcement (Greenerity Concept MEA with a $25\,\mu\mathrm{m}$ thick *Nafion 211CS* membrane) and the application of an accelerated stress test protocol, mechanical stress on the membrane over several thousand hours of operation is simulated in a short period. A flat gasket in direct contact to the CCM, without the employment of a SG, was used, as shown in Figure 7.1. The edge channel width $w_{\mathrm{ch,ec}} = 3.5\,\mathrm{mm}$ was chosen in order to enlarge the area of the CCM without any mechanical support from the GDL. It is expected that the design favors high mechanical point loads on the membrane at the edges of gaskets and GDLs.

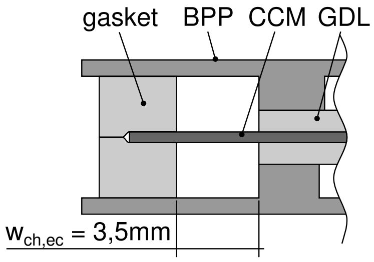

Figure 7.1: Sealing setup for RH-cycling.

The cell was subjected to alternating gas humidification, known as *RH-cycling* [61, 71, 218]. After a conditioning procedure (cf. Section 4.1.4), the cell was purged with $3\,\mathrm{l\,min^{-1}}$ of nitrogen on anode and cathode side at a cell temperature of $80\,^{\circ}\mathrm{C}$ with an inlet overpressure of $300\,\mathrm{mbar}$. The dewpoint of the gas inlet humidification on both sides was switched from 80 to $2\,^{\circ}\mathrm{C}$ (100 and $1.5\,\%\,\mathrm{RH}$) every $5\,\mathrm{min}$ with a humidifier bypass. After 6000 cycles, the dry phase was extended to $9\,\mathrm{min}$ in order to accelerate the degradation process. LSV measurements were performed periodically in order to determine the gas crossover over the membrane. Product water was taken from condensate separators directly at both gas outlets and its fluoride content was analyzed with an ion selective electrode.

7.1.2 Results

As the gas inlet humidification alternated between 1.5 and $100\,\%\,\mathrm{RH}$, the membrane resistance also followed a cyclic profile. Figure 7.2 shows the HFR oscillation between 0.07 and $300\,\Omega\,\mathrm{cm^2}$ for humid/dry intervals of 5 and $5\,\mathrm{min}$, and to a maximum of $600\,\Omega\,\mathrm{cm^2}$ for an extended drying interval of $9\,\mathrm{min}$.

The initial values for the crossover current density of $1.8\,\mathrm{mA\,cm^{-2}}$, shown in Figure 7.3 (a), are in good accordance with literature findings, where values around $2\,\mathrm{mA\,cm^{-2}}$ and below

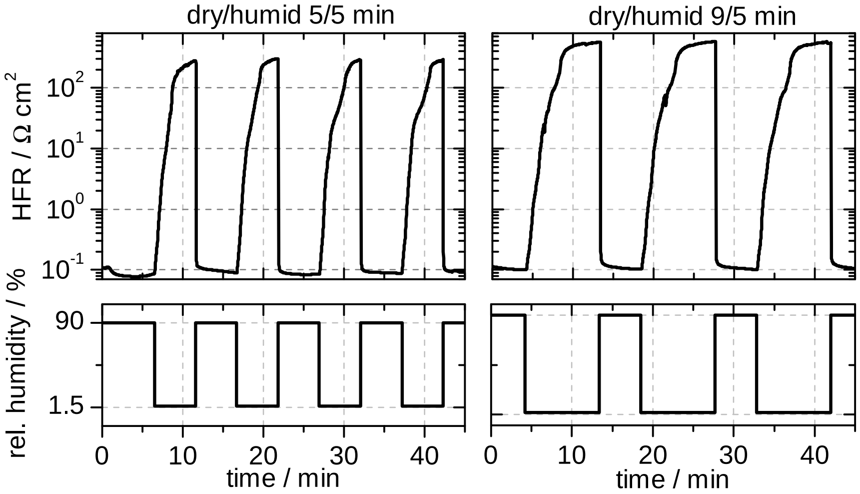

Figure 7.2: Specific HFR during RH cycling where gas inlet humidification was varied from 1.5 to $100\,\%\,\mathrm{RH}$ for drying phases of $5\,\mathrm{min}$ (left) and $9\,\mathrm{min}$ (right).

were reported for new membranes [34, 132, 219]. At about 8000 cycles, the crossover current density started to increase, reaching $4.5\,\mathrm{mA\,cm^{-2}}$ at about $10\,000$ cycles. The internal short resistance increased over the first 1000 cycles, likely an effect of conditioning mechanisms, and significantly decreased from 2.6 to $0.1\,\Omega\,\mathrm{cm^2}$ between 6000 and $10\,000$ cycles.

In the product water, fluoride ion concentration varied from below the detection limit $(0.02\,\mathrm{mg\,l^{-1}})$ to a maximum of $0.32\,\mathrm{mg\,l^{-1}}$ at the cathode side as seen in Figure 7.3 (b). In

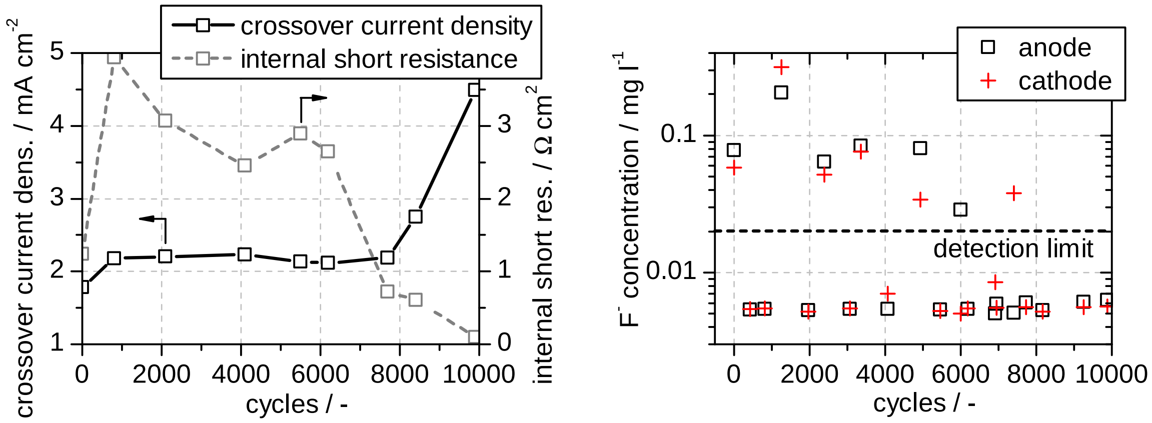

(a) Crossover current density and internal short resistance, measured by LSV.

(b) Fluoride concentration in the product water of anode and cathode.

Figure 7.3: Results from the humidity cycling of a cell with a non-reinforced membrane. Each cycle represents a change of gas inlet humidity from 1.5 to $100\,\%\,\mathrm{RH}$ and vice versa.

general, the fluoride ion concentration oscillated strongly in the first 5000 humidity cycles, indicating a discontinuous release rate from the membrane, while values for anode and cathode mostly showed similar values. In the last 5000 cycles, the concentration generally declined. In most measurement points, the concentration was below the detection limit.

After endplate and BPP were removed from the cathode side, membrane defects were localized by means of an IR camera (Section 4.2.4), while the anode was purged with hydrogen. Figure 7.4 (a) shows the resulting IR image with both GDLs remaining in the assembly. One hot spot with about $190\,°\mathrm{C}$ can be identified in the edge region, outside the GDL area, where the membrane is not sandwiched between GDLs. It indicates a membrane leakage or pinhole. After removing the cathode GDL (Figure 7.4 (b)) this hotspot reached even higher temperatures of $> 200\,°\mathrm{C}$, likely an effect of ongoing membrane deterioration caused by the reaction heat and a subsequent expansion of the pinhole. In addition a second hotspot appears in the cathode outlet region, superimposed to the outer GDL edge.

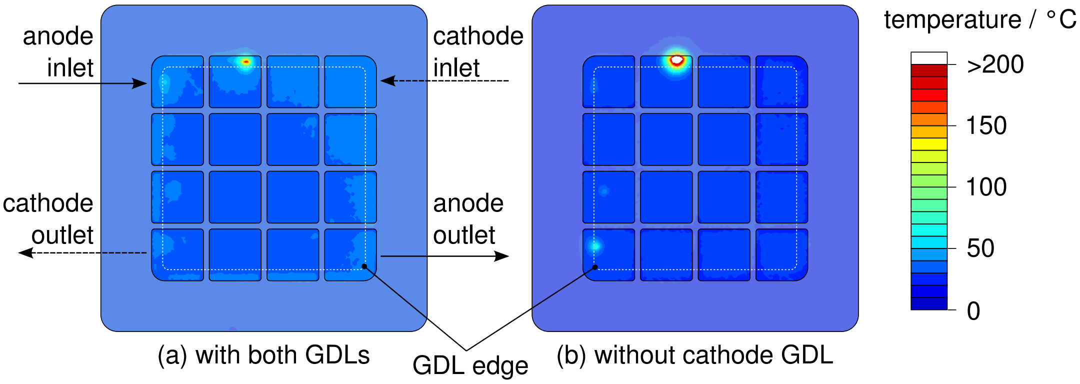

(a) with both GDLs (b) without cathode GDL

Figure 7.4: IR image of the cathode side of the membrane, while the anode was purged with hydrogen. Membrane pinholes were found in the outer perimeter of the cell plane. The dashed line indicates the outer perimeter of both GDLs.

A membrane failure after 10^4 cycles agrees well with the findings of Aindow and O'Neill, where for RH-cycling of a membrane without GDLs over a range of $80\,\%\,\mathrm{RH}$ mechanical failure occurred after about $1.1 \cdot 10^4$ cycles [61].

It was shown that the integration of the CCM in the edge region is crucial in order to avoid cell failure caused by mechanical defects of the membrane. The design of the outer cell perimeter should enable a homogeneous compression of the CCM and reduce in-plane stresses in the membrane. Since the experimental protocol represents harsh operating conditions the effect is expected to become relevant in applications with lifetime requirements of $> 5000\,\mathrm{h}$.

7.2 Component Overlap

So far many different cases of hydrogen starvation on the anode side have been discussed in literature. In most cases, the described mechanisms are triggered by appreciable amounts of oxygen on the anode side, either caused by a hydrogen/oxygen front on the anode at a cell startup or shutdown [220–223] or by a massive hydrogen depletion due to flooding or operating conditions and subsequent oxygen crossover to the anode [51–53]. Oxygen on the anode leads to high electrode potentials and causes a local negative drop of the electrolyte potential since the solid phase potential of the anode is held constant by a high in-plane conductivity of CL and GDL. On the cathode side, the solid potential also exhibits small gradients, so that with the low electrolyte potentials, high cathode electrode potentials can occur. This results in an increased oxidation of the cathode CL carbon support and in a massive impairment of the cell performance.

Transport constants and the width of the starved region can have an essential influence on the intensity of the damaging effects as in-plane transport of gases, ions and electrons equilibrate gradients of the reactant concentrations and of the electrolytic and electrical potentials. Yang et al. [51] investigated the effect of multiple water-clogged channels on the anode side on carbon corrosion, thereby hydrogen transport through the GDL was shown to inhibit carbon corrosion over more than $10\,\mathrm{mm}$ below the clogged channels. Patterson et al. [55] filled the anode GDL pores with an impermeable polymer in a circular region of $20\,\mathrm{mm}$ diameter and verified an increased carbon corrosion of the CL there, beginning at a distance of $4\,\mathrm{mm}$ from the edge of the filled region.

In the outer perimeter of the cell plane both, anode and cathode gas compartment, are spatially limited by a gasket or SG, covering the CCM, as discussed in Section 3.2.2. A lateral offset of these components on both sides of the CCM, as a result of assembling and manufacturing tolerances, can cause an asymmetric supply of the CCM with reactants. In case of an overlapping cathode compartment a fraction of the CCM is supplied with air from one side while the hydrogen supply is inhibited there. Meanwhile the rest of the cell is operated in normal hydrogen/air mode.

In the following part, the effect of component misalignment (SG layers or gaskets) in the outer perimeter of a CCM on local operating conditions and subsequent carbon corrosion of the cathode CL is emphasized with an appropriate experiment and the results are validated by numerical simulation. The model offers the possibility to investigate the sensitivity of the occurring carbon corrosion to a wide range of parameters and operating conditions.

7.2.1 Experimental Setup and Protocol

A standard test cell setup was employed but with the anode being partially covered in its outer perimeter with a $12.5\,\mu\mathrm{m}$ thick Kapton® HN polyimide foil. The foil was shaped as a frame and sandwiched between CCM and GDL as shown in Figure 7.5 and covered the anode CL in its outer perimeter over a width of $6\,\mathrm{mm}$ from the gasket edge.

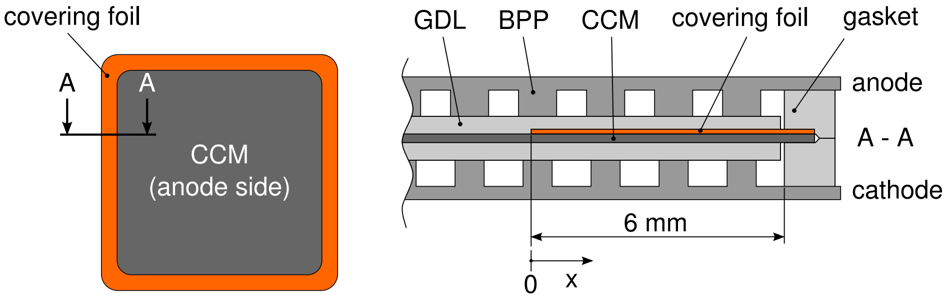

Figure 7.5: Employed cell setup with a covering foil between anode CL and GDL. The foil covers a band of $6\,\mathrm{mm}$ width in the outer CCM perimeter.

After conditioning the cell was operated at standard conditions, but with a stoichiometry of 2.5 and a gas inlet pressure of $300\,\mathrm{mbar}$ on anode and cathode side. Gas humidification was set to $30\,\%\,\mathrm{RH}$. The anode was fed with hydrogen diluted with $30\,\mathrm{vol.}\,\%$ nitrogen. Load was cycled between 10 and $45\,\mathrm{A}$ (0.2 and $0.9\,\mathrm{A\,cm^{-2}}$), with a hold time of $40\,\mathrm{s}$ for each point and current ramps of $0.035\,\mathrm{A\,cm^{-2}\,s^{-1}}$. Every 10 load cycles OCV was held for $30\,\mathrm{s}$. CVs were performed in intervals of about $150\,\mathrm{h}$. The fluoride concentration in product water probes from anode and cathode was analyzed with an ion selective electrode. Thicknesses of membrane and CLs were assessed by SEM analysis of CCM cross section in the CCM edge region as a measure for degradation effects.

7.2.2 Experimental Results

Results from CVs, shown in Figure 7.6 (a), indicate an initially increasing ECA on the anode side from 194 to $222\,\mathrm{cm^2_{Pt}\,mg^{-1}_{Pt}}$ and then a slight decrease to $209\,\mathrm{cm^2_{Pt}\,mg^{-1}_{Pt}}$, while the ECA on the cathode side increases from 256 to $261\,\mathrm{cm^2_{Pt}\,mg^{-1}_{Pt}}$. The smaller ECA on the anode side is probably a result of the covering foil between CL and GDL, so that a substantial part of the CL is not supplied with hydrogen[1]. The crossover current density changes from 2.03 to $1.57\,\mathrm{mA\,cm^{-2}}$ for the anode as a working electrode and from 1.63 to $1.34\,\mathrm{mA\,cm^{-2}}$ for the cathode as a working electrode, respectively. A significant fluoride concentration in the

---

[1] The ECA on the anode side was calculated with the whole geometrical cell area, without respect to the covering foil.

product water could only be detected initially after the conditioning procedure of the cell (Figure 7.6 (b)). Afterwards the concentration dropped below the detection limit of the ion selective electrode. Fluoride concentrations in anode and cathode product water were found to be in good agreement[1].

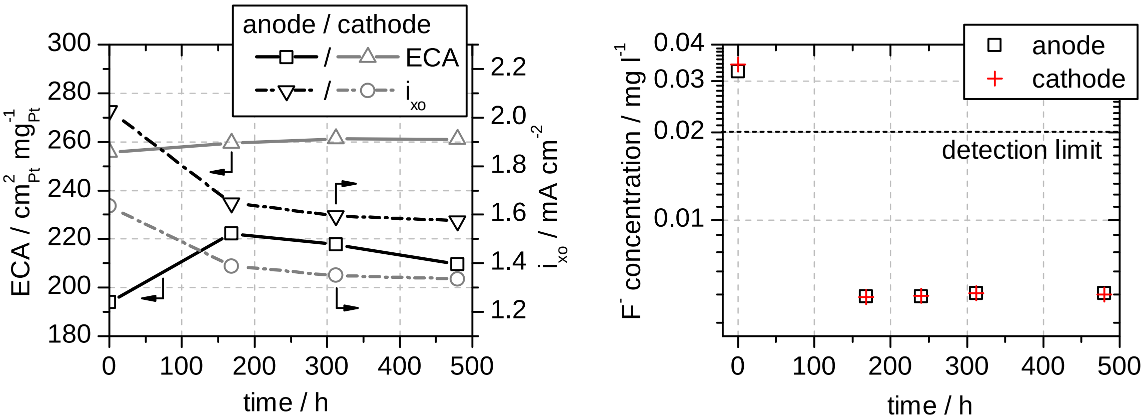

(a) ECA and crossover current density for both anode and cathode as a working electrode, extracted from CV measurement data.

(b) Fluoride concentration in the product water of anode and cathode, measured with an ion selective electrode.

Figure 7.6: Experimental results from the cell operation with a foil covering the anode CL in its outer perimeter.

The thickness change of a CL is a viable indicator for degradation processes, particularly carbon corrosion, as oxidation of the carbon support results in morphology changes and mass loss of the CL. The membrane thickness change can indicate ionomer decomposition. CL and membrane thickness were measured by SEM analysis in cross sections at the outer perimeter of the CCM, summarized in Figure 7.7, whereby the area $x \geq 0$ is covered by the foil. The membrane thickness remained unchanged from the initial value of about $16\,\mu\mathrm{m}$ in all cross sections, differences can be attributed to a measurement error. Also the anode CL does not show significant deviations from a fresh CL with about $8\,\mu\mathrm{m}$ thickness, only four outliers with $5\,\mu\mathrm{m}$ thickness are seen, all other values vary from 6 to $10\,\mu\mathrm{m}$. The cathode CL thickness remains at about $9 - 13\,\mu\mathrm{m}$ in the FF area as well as under the covering foil in the cross sections G and H, which coincides well with the CL thickness in a fresh CCM. Sections G and H are adjacent to the anode inlet distribution channels (cf. Figure 4.1). In all other cross sections A-F, significant thinning of the CL in the hydrogen starved area below the foil is seen

---

[1] Product water samples of anode and cathode are measured separately. It can be excluded that the good agreement between anode and cathode samples is a measurement artifact due to the measurement order.

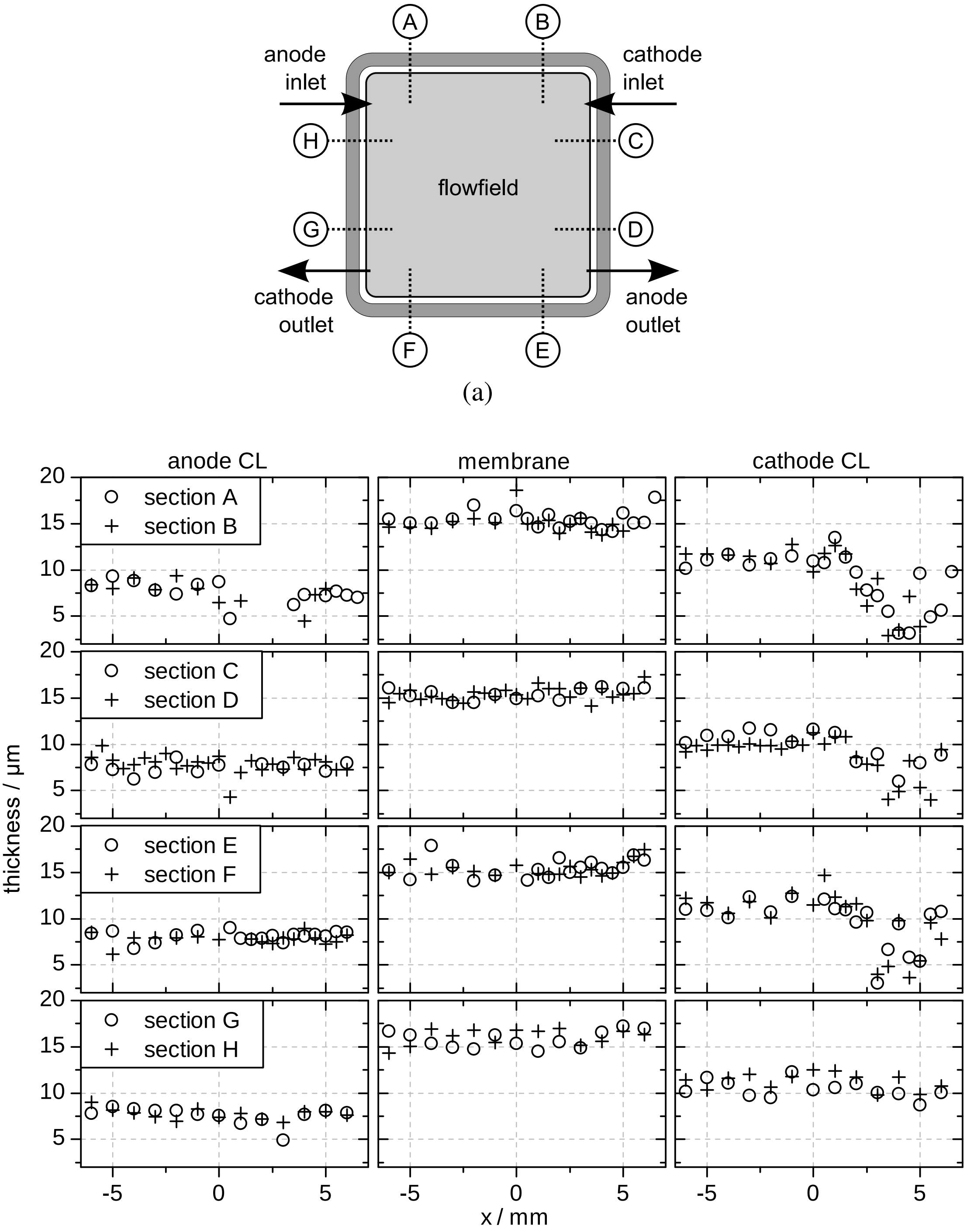

(a)

(b)

Figure 7.7: Results from post-mortem analysis of the CCM, operated with a covering foil on the anode side. (a) Position of analyzed cross sections. (b) Thickness of membrane, anode and cathode CL in the cross sections A-H. The x-axis refers to the relative position to the edge of the covering foil on the anode side.

with minimum values of $3\,\mu\mathrm{m}$. Depending on the cross section, thinning begins approximately between 1 and $2\,\mathrm{mm}$ below the covering foil. A discrete beginning of the CL thinning can hardly be identified. The remaining CL thickness in the starved area is not homogeneous but varies between 3 and $10\,\mu\mathrm{m}$ in the cross sections A-F. Thereby the distance between two maxima/minima lies in the range of the FF pitch ($w_{\mathrm{pitch}} = 1.67\,\mathrm{mm}$), supposing an influence of the channel-land structure on carbon corrosion. However, the regions of more pronounced CL thinning cannot be attributed to the area under the lands or under the channels.

Strong changes of the crossover current density in the first $170\,\mathrm{h}$ and the high fluoride concentration at $0\,\mathrm{h}$ are expected to be an effect of activation and conditioning processes in CL and membrane during the initial phase of operation. Also the initially increasing ECA indicates an activation process of the CLs. Degradation of the cathode CL is not seen in the ECA, likely the covering foil on the anode side inhibits hydrogen crossover to the cathode side in the edge region, so that this area does not contribute to the ECA.

7.2.3 Model Description

In order to investigate the influence of parameter variations on degradation mechanisms, particularly carbon corrosion of the cathode CL, a numerical, isothermal steady-state 2D model is developed. It represents a cross section of the cell, located at its outer perimeter, comprising four FF pitches as depicted in Figure 7.8. The anode is partially covered with an isolating and gas-tight foil as it was the case in the previously described experiment. Anode and cathode compartments both consist out of a porous GDL and a CL. Hydrogen, nitrogen and water vapor are present on the anode and oxygen, nitrogen and water vapor on the cathode side. Multi-component diffusion takes place according to the model of Maxwell-Stefan. Gas crossover over the membrane is modeled, whereas crossed over hydrogen is immediately oxidized on the cathode side and crossed over oxygen is reduced on the anode side. The membrane is equilibrated with water vapor from anode and cathode side. Water located in the membrane is assumed to be liquid and is transported by self-diffusion and electroosmotic drag. Carbon oxidation on the cathode side is modeled but it is not accounted for a carbon loss over the cell lifetime. The following assumptions are made:

- Gas and water transport through the membrane is only diffusive, no convective transport is taken into account.
- Crossover fluxes of hydrogen and oxygen over the membrane completely react on the opposite side CL.

- In porous layers water is only present in gaseous form, in the membrane all water is liquid.
- No water uptake of the ionomer and water diffusion is modeled in the CLs. Its electrolytic conductivity is constant.
- Gas distribution in the FF channels is not modeled, instead the concentration of all gas species is given at the GDL surface.
- The overlap width of the covering foil is only $4\,\mathrm{mm}$ compared to $6\,\mathrm{mm}$ in the experiment in order to reduce computing time, as it was seen that parameters do not change significantly in the outermost $2\,\mathrm{mm}$.
- Gas concentrations at the GDL interface to the FF channel are set to the mean value between cell in- and outlet, so that a position in the middle of a FF channel is represented.

Basic Geometry and Boundary Conditions

The simulation domain comprises four FF pitches as Figure 7.8 schematically depicts. Substantial components are the membrane, CLs, GDLs and BPPs. The covering foil between CL and GDL on the anode side is implemented as a $12.5\,\mathrm{\mu m}$ thick gap with no charge or species transport across it. Gas species concentrations are specified at the GDL interface to the FF channels. No flux conditions are applied on the right and left boundary of the domain. The current density i_{model} is applied on the boundary of the cathode BPP. For parameterization of the model, one FF pitch is abstracted and simulated alone, without the covering foil on the anode side (*calibration model*).

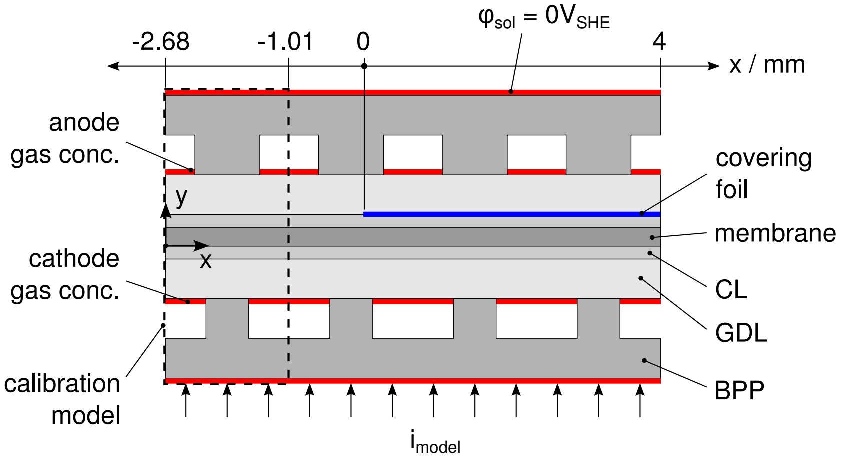

Figure 7.8: Schematic model domain for simulation of hydrogen starvation caused by a covering foil on the anode side and domain for parameterization and calibration of the model.

Charge Transport

In all electrically (CL, GDL, BPP) and electrolytically (membrane, CL) conducting phases, charge conservation according to Ohm's Law is applied with the according current density scalars i_{sol} and i_{ely}, the conductivities σ_{sol} and σ_{ely} and the local potentials φ_{sol} and φ_{ely}, respectively

$$i_{\mathrm{sol}} = \sigma_{\mathrm{sol}} \nabla \varphi_{\mathrm{sol}} \tag{7.1}$$

$$i_{\mathrm{ely}} = \sigma_{\mathrm{ely}} \nabla \varphi_{\mathrm{ely}}. \tag{7.2}$$

At the interfaces GDL-BPP and GDL-CL, the specific contact resistance is set to $r_{\mathrm{gdl,cont}}$. The backside of the anode BPP is set to ground ($\varphi_{\mathrm{sol}} = 0\,\mathrm{V_{SHE}}$), on the cathode side an inward current density i_{model} is set.

Gas Phase Transport

In the CLs and GDLs multicomponent gas diffusion of three species is modeled by the approach of Stefan-Maxwell while for convection driven transport Darcy's Law is employed. On the anode hydrogen, nitrogen and water vapor and on the cathode oxygen, nitrogen and water vapor are present. As Stefan-Maxwell diffusion is not suitable for diluted gases, inlet concentrations of a component cannot be set to zero. Significant concentrations are required to obtain numerical stability. The partial differential equation for species transport in CL and GDL for component i is then [224]

$$\underbrace{\nabla \left[-\rho\omega_i \sum_{\substack{j=1 \\ j\neq i}}^{n} \left(D_{i,j} \left(\nabla\chi_j + (\chi_j - \omega_j) \left(\frac{\nabla p}{p} \right) \right) \right) \right]}_{\text{Stefan-Maxwell Diffusion}} + \underbrace{\nabla \omega_i \rho \frac{\kappa}{\eta_{\mathrm{f}}} \nabla p}_{\text{Darcy's Law}} = \underbrace{\sum_k S_i^k}_{\text{source term}} \quad , \tag{7.3}$$

with the total number of components n. The first term describes the multicomponent diffusion of species i with its mass fraction ω_i and with the mass fractions and molar fractions of all other species ω_j and χ_j, the binary diffusion coefficient of species i and j, $D_{i,j}$ and the local pressure and density p and ρ. The convective transport in the porous layers follows Darcy's Law with the permeability of the structure κ and the dynamic viscosity of the fluid η_{f}. In the CL, species are consumed and generated in chemical reactions and at the membrane interface, water sorption/desorption and crossover of nitrogen, oxygen and hydrogen also act as species sources or sinks, represented with a term S_i^k with a variable k for the different sources/sinks.

In the GDL, the binary diffusion coefficients $D_{i,j}$ are reduced by the porosity ϵ and tortuosity τ of the structure to the effective diffusion coefficient $D_{i,j}^{\text{eff}}$ [225]

$$D_{i,j}^{\text{eff}} = D_{i,j}\frac{\epsilon}{\tau}. \tag{7.4}$$

For the CL, tortuosity values are hardly available. A simple Bruggeman approach is used instead [226]

$$D_{i,j}^{\text{eff}} = D_{i,j}\epsilon^{1.5}. \tag{7.5}$$

Membrane Model

At the interface to the CL the membrane water content λ_{mem} depends on the water vapor activity (relative humidity) of the gas phase $a_{\text{H}_2\text{O}}$. The equilibrium is described by a sorption term developed by Maldonado et al.[1] [227]

$$\lambda_{\text{mem}} = 1.966 + 5.528a_{\text{H}_2\text{O}} + 0.0019\exp\left(8.8045a_{\text{H}_2\text{O}}\right) \qquad [\text{-}]\,. \tag{7.6}$$

Water mass is exchanged with a molar flux $\dot{n}_{\text{H}_2\text{O,sorp}}$ between gas phase and membrane

$$\dot{n}_{\text{H}_2\text{O,sorp}} = v_{\text{sorp}}\left(c_{\text{H}_2\text{O}}^{\text{gas}} - c_{\text{H}_2\text{O}}^{\text{mem}}\right) \tag{7.7}$$

with a sorption rate $v_{\text{sorp}} = 2\cdot 10^{-4}\,\text{m}^3\,\text{m}^{-2}\,\text{s}^{-1}$ and a molar water concentration in the gas phase $c_{\text{H}_2\text{O}}^{\text{gas}}$. Water concentration of the membrane $c_{\text{H}_2\text{O}}^{\text{mem}}$ in $\text{mol}\,\text{m}^{-3}$ and membrane water content λ_{mem} are related by

$$c_{\text{H}_2\text{O}}^{\text{mem}} = \lambda_{\text{mem}}\frac{\rho_{\text{mem}}}{EW} \tag{7.8}$$

with the equivalent weight of the ionomer EW, which is its mass per mole of sulfonic acid. The protonic conductivity of the membrane $\sigma_{\text{ely}}^{\text{mem}}$ depends on the local water content, also by a correlation of Maldonado et al.[2] [227]

$$\sigma_{\text{ely}}^{\text{mem}} = 0.644\cdot\lambda_{\text{mem}}\left[1-\exp\left(-0.606\left(\lambda_{\text{mem}} - 2.947\right)\right)\right] \qquad \left[\text{S}\,\text{m}^{-1}\right]. \tag{7.9}$$

It was not accounted for water vapor in the membrane. The flux of liquid water due to self-diffusion $\dot{n}_{\text{H}_2\text{O,diff}}^{\text{mem}}$ depends on the concentration gradient $\nabla c_{\text{H}_2\text{O}}^{\text{mem}}$

$$\dot{n}_{\text{H2O,diff}}^{\text{mem}} = -D_{\text{H}_2\text{O}}^{\text{mem}}\nabla c_{\text{H}_2\text{O}}^{\text{mem}}. \tag{7.10}$$

---

[1] For a system temperature of 60 °C and a membrane (Nafion 115) pre-dried at 60 °C.

[2] For a system temperature of 60 °C and a membrane (Nafion 115) pre-dried at 60 °C.

The diffusion coefficient $D^{\mathrm{mem}}_{\mathrm{H_2O}}$ is a function of local water content and temperature according to the model of Berg et al. [228]

$$D^{\mathrm{mem}}_{\mathrm{H_2O}} = d^{\mathrm{mem}}_{\mathrm{H_2O}} \exp\left(\frac{-2436\,[\mathrm{K}]}{T}\right) \lambda_{\mathrm{mem}} \tag{7.11}$$

with the diffusion constant $d^{\mathrm{mem}}_{\mathrm{H_2O}} = 2.1 \cdot 10^{-7}\,\mathrm{m^2\,s^{-1}}$. An additional water flux $\dot{n}^{\mathrm{mem}}_{\mathrm{H_2O,eo}}$ through the membrane is induced by electroosmotic drag, proportional to the electrolytic current density i_{ely} and the drag coefficient K_{drag} according to Equation 2.27

$$\dot{n}^{\mathrm{mem}}_{\mathrm{H_2O,eo}} = K_{\mathrm{drag}} \frac{i_{\mathrm{ely}}}{F}. \tag{7.12}$$

Gas Crossover

Crossover of gaseous species over the membrane is possible as the ionomer is not ideally gas-tight. As only diffusive crossover flow is considered the flux $\dot{n}_{i,\mathrm{xo}}$ is determined by the partial pressure difference between the membrane-CL interface on anode (p_i^{an}) and cathode (p_i^{ca}) side for each species i

$$\dot{n}_{i,\mathrm{xo}} = \frac{\psi_i}{t_{\mathrm{mem}}} \left(p_i^{\mathrm{an}} - p_i^{\mathrm{ca}}\right) \tag{7.13}$$

with the membrane thickness t_{mem}. The diffusion coefficients ψ_i for hydrogen and oxygen are implemented according to a model of Weber and Newman [35], the nitrogen crossover according to Ahluwalia and Wang [33] (in $\mathrm{mol\,m^{-1}\,s^{-1}\,Pa^{-1}}$)

$$\psi_{\mathrm{H_2}} = \left(2.2 \cdot 10^{-14} f + 2.9 \cdot 10^{-15}\right) \cdot exp\left[\frac{21000}{\Re}\left(\frac{1}{T_{\mathrm{ref,xo}}} - \frac{1}{T}\right)\right] \tag{7.14}$$

$$\psi_{\mathrm{O_2}} = \left(1.9 \cdot 10^{-14} f + 1.1 \cdot 10^{-15}\right) \cdot exp\left[\frac{22000}{\Re}\left(\frac{1}{T_{\mathrm{ref,xo}}} - \frac{1}{T}\right)\right] \tag{7.15}$$

$$\psi_{\mathrm{N_2}} = \left(0.0295 + 1.21 f - 1.93 f^2\right) \cdot 10^{-14} \cdot exp\left[\frac{24000}{\Re}\left(\frac{1}{T_{\mathrm{ref,xo}}} - \frac{1}{T}\right)\right] \tag{7.16}$$

with the reference temperature $T_{\mathrm{ref,xo}} = 303.15\,\mathrm{K}$. f denotes the water volume fraction in the membrane and is calculated from the membrane water content [35]

$$f = \frac{\lambda_{\mathrm{mem}} V_{\mathrm{H_2O}}}{V_{\mathrm{ion}} + \lambda_{\mathrm{mem}} V_{\mathrm{H_2O}}} \tag{7.17}$$

with the molar volume of the membrane $V_{\mathrm{ion}} = \frac{EW}{\rho_{\mathrm{mem}}}$ and the molar volume of water $V_{\mathrm{H_2O}}$.

Stefan-Maxwell equations are solved for nitrogen on both sides, so that the according source terms in the CLs on anode and cathode side are

$$S^{\mathrm{an}}_{\mathrm{N_2,xo}} = -M_{\mathrm{N_2}}\dot{n}_{\mathrm{N_2,xo}} \qquad S^{\mathrm{ca}}_{\mathrm{N_2,xo}} = M_{\mathrm{N_2}}\dot{n}_{\mathrm{N_2,xo}} \tag{7.18}$$

with the molar mass of nitrogen $M_{\mathrm{N_2}}$. All oxygen crossover flow $\dot{n}_{\mathrm{O_2,xo}}$ is assumed to completely react in an ORR at the anode CL, resulting in an additional current $i^{\mathrm{an}}_{\mathrm{ORR}}$[1]

$$i^{\mathrm{an}}_{\mathrm{ORR}} = 4F\dot{n}_{\mathrm{O_2,xo}}. \tag{7.19}$$

Thereby hydrogen consumption and water production can be expressed by source terms $S^{\mathrm{an}}_{\mathrm{H_2,xo}}$ and $S^{\mathrm{an}}_{\mathrm{H_2O,xo}}$

$$S^{\mathrm{an}}_{\mathrm{H_2,xo}} = \frac{M_{\mathrm{H_2}} i^{\mathrm{an}}_{\mathrm{ORR}}}{2F} \qquad S^{\mathrm{an}}_{\mathrm{H_2O,xo}} = -\frac{M_{\mathrm{H_2O}} i^{\mathrm{an}}_{\mathrm{ORR}}}{2F} \tag{7.20}$$

with the molar masses of hydrogen and water $M_{\mathrm{H_2}}$ and $M_{\mathrm{H_2O}}$. Analogous, all hydrogen crossover flow $\dot{n}_{\mathrm{H_2,xo}}$ reacts in a HOR on the cathode side, leading to an anodic current $i^{\mathrm{ca}}_{\mathrm{HOR}}$

$$i^{\mathrm{ca}}_{\mathrm{HOR}} = 2F\dot{n}_{\mathrm{H_2,xo}}. \tag{7.21}$$

Reaction Kinetics

Reactions are possible in the entire volume of both CLs, HOR and hydrogen evolution reaction (HER) on the anode, ORR, oxygen evolution reaction (OER) and COR on the cathode side. Due to hydrogen and oxygen crossover, HOR is also possible on the cathode side and ORR on the anode side. HOR and HER are implemented with a Butler-Volmer approach, assuming symmetrical characteristics of both reactions. With a transfer coefficient $\alpha_{\mathrm{HOR}} = 1$ it follows from Equation 2.26

$$i^{\mathrm{an}}_{\mathrm{HOR}} = i_{0,\mathrm{HOR}} \left[\frac{c_{\mathrm{H_2}}}{c^{\mathrm{ref}}_{\mathrm{H_2}}} \exp\left(\frac{z_{\mathrm{HOR}} F \eta_{\mathrm{an}}}{\Re T} \right) - 1 \right]. \tag{7.22}$$

Thereby $c_{\mathrm{H_2}}$ and $c^{\mathrm{ref}}_{\mathrm{H_2}}$ are the concentration of hydrogen at the electrode and the reference hydrogen concentration, respectively. $i_{0,\mathrm{HOR}}$ is the HOR/HER exchange current density. The

---

[1] As $\dot{n}_{\mathrm{O_2,xo}}$ is negative for oxygen crossover from cathode to anode side per definition (Equation 7.13), $i^{\mathrm{an}}_{\mathrm{ORR}}$ is negative and hence represents a cathodic current.

resulting source term for hydrogen in the gas phase of the CL $S_{\mathrm{H_2}}^{\mathrm{an}}$ is then

$$S_{\mathrm{H_2,HOR}}^{\mathrm{an}} = -\frac{M_{\mathrm{H_2}} i_{\mathrm{HOR}}^{\mathrm{an}}}{2F}. \tag{7.23}$$

ORR and OER are modeled with a full Butler-Volmer equation. The implementation of ORR and OER as symmetric reactions is considered to be acceptable as the simulation results showed that no OER occurs. The current density $i_{\mathrm{ORR}}^{\mathrm{ca}}$ is then

$$\begin{aligned} i_{\mathrm{ORR}}^{\mathrm{ca}} = i_{0,\mathrm{ORR}} \Bigg[\left(\frac{c_{\mathrm{H_2O}}}{c_{\mathrm{H_2O}}^{\mathrm{ref}}} \right) \exp\left(\frac{\alpha_{\mathrm{ORR}} z_{\mathrm{ORR}} F \eta_{\mathrm{ca}}}{\Re T} \right) \\ - \left(\frac{c_{\mathrm{O_2}}}{c_{\mathrm{O_2}}^{\mathrm{ref}}} \right) \exp\left(\frac{-\left(1-\alpha_{\mathrm{ORR}}\right) z_{\mathrm{ORR}} F \eta_{\mathrm{ca}}}{\Re T} \right) \Bigg], \end{aligned} \tag{7.24}$$

with the transfer coefficient α_{ORR}, the water and oxygen concentrations at the CL $c_{\mathrm{H_2O}}$ and $c_{\mathrm{O_2}}$, the according reference concentrations $c_{\mathrm{H_2O}}^{\mathrm{ref}}$ and $c_{\mathrm{O_2}}^{\mathrm{ref}}$ and the exchange current density $i_{0,\mathrm{ORR}}$. In the ORR oxygen is consumed and water is produced, the according source terms $S_{\mathrm{O_2,ORR}}^{\mathrm{ca}}$ and $S_{\mathrm{H_2O,ORR}}^{\mathrm{ca}}$ are

$$S_{\mathrm{O_2,ORR}}^{\mathrm{ca}} = \frac{M_{\mathrm{O_2}} i_{\mathrm{ORR}}^{\mathrm{ca}}}{4F} \qquad S_{\mathrm{H_2O,ORR}}^{\mathrm{ca}} = -\frac{M_{\mathrm{H_2O}} i_{\mathrm{ORR}}^{\mathrm{ca}}}{2F}. \tag{7.25}$$

Carbon can be oxidized at the cathode electrode with water to carbon dioxide or monoxide (cf. Equations 2.36 and 2.37) [49, 229]. Here only the former case is considered as its effect is dominant

$$\mathrm{C} + 2\,\mathrm{H_2O} \longrightarrow \mathrm{CO_2} + 4\,\mathrm{H^+} + 4\,\mathrm{e^-}. \tag{7.26}$$

For the COR a simple Tafel approach can be employed due to the irreversibility of the reaction. The expression from Takeuchi and Fuller without consideration of the adsorption term is employed [229]

$$i_{\mathrm{COR}}^{\mathrm{ca}} = i_{0,\mathrm{COR}} \left[\frac{c_{\mathrm{H_2O}}}{c_{\mathrm{H_2O}}^{\mathrm{ref}}} \exp\left(\frac{\alpha_{\mathrm{COR}} F \eta_{\mathrm{ca,COR}}}{\Re T} \right) \right]. \tag{7.27}$$

Whereby α_{COR} denotes the transfer coefficient for the COR and $\eta_{\mathrm{ca,COR}}$ the according overpotential. Water is consumed in the COR, described by the source term $S_{\mathrm{H_2O,COR}}^{\mathrm{ca}}$

$$S_{\mathrm{H_2O,COR}}^{\mathrm{ca}} = -\frac{M_{\mathrm{H_2O}} i_{\mathrm{COR}}^{\mathrm{ca}}}{2F}. \tag{7.28}$$

The overpotentials of anode and cathode electrode η_{an} and η_{ca} are determined by the local potential of the electron conducting phases $\varphi_{\mathrm{sol,an}}$ and $\varphi_{\mathrm{sol,ca}}$, the local potential of the electrolyte phases $\varphi_{\mathrm{ely,an}}$ and $\varphi_{\mathrm{ely,ca}}$ and the equilibrium potentials of HOR and ORR, $\Delta\varphi^0_{\mathrm{HOR}}$ and $\Delta\varphi^0_{\mathrm{ORR}}$, respectively

$$\eta_{\mathrm{an}} = \varphi_{\mathrm{sol,an}} - \varphi_{\mathrm{ely,an}} - \Delta\varphi^0_{\mathrm{HOR}} \qquad \eta_{\mathrm{ca}} = \varphi_{\mathrm{sol,ca}} - \varphi_{\mathrm{ely,ca}} - \Delta\varphi^0_{\mathrm{ORR}}. \tag{7.29}$$

For the COR, the overpotential $\eta_{\mathrm{ca,COR}}$ is calculated with the equilibrium potential $\Delta\varphi^0_{\mathrm{COR}}$

$$\eta_{\mathrm{ca,COR}} = \varphi_{\mathrm{sol,ca}} - \varphi_{\mathrm{ely,ca}} - \Delta\varphi^0_{\mathrm{COR}}. \tag{7.30}$$

7.2.4 Parameterization

Boundary conditions are set so that the simulated cross section of the cell is located in the middle of a FF channel. Oxygen concentration on the cathode is set to $17.4\,\mathrm{vol.}\,\%$, which is the mean value between inlet ($21\,\mathrm{vol.}\,\%$ O_2) and outlet ($13.8\,\mathrm{vol.}\,\%$) for a stoichiometry of $\lambda = 2.5$. On the anode side it is accounted for nitrogen crossover and accumulation, therefore a nitrogen fraction of $20\,\mathrm{vol.}\,\%$ is set as listed in Table 7.1. Gas inlet humidity is set to 30 and $80\,\%\,\mathrm{RH}$ on anode and cathode side, respectively. Temperature is set to $65\,°\mathrm{C}$ over all domains as an isothermal case is studied. All other simulation parameters used in the present study are summarized in Table A.1 in the appendix.

Table 7.1: Boundary conditions for the simulation of hydrogen starvation in the outer cell perimeter.

	species	symbol	anode	cathode	unit
system temperature			65		°C
inlet pressure			1.3	1.1	$\mathrm{bar_a}$
relative humidity inlet			30	80	% RH
inlet volume fraction[†]	H_2	$\phi_{\mathrm{H_2}}$	80	-	%
	O_2	$\phi_{\mathrm{O_2}}$	-	17.4	%
	N_2	$\phi_{\mathrm{N_2}}$	20	82.6	%
inlet molar fraction	H_2	$\chi_{\mathrm{H_2}}$	75.4	-	%
	O_2	$\chi_{\mathrm{O_2}}$	-	14.2	%
	N_2	$\chi_{\mathrm{N_2}}$	18.8	67.6	%
	H_2O	$\chi_{\mathrm{H_2O}}$	5.8	18.2	%
inlet mass fraction	H_2	$\omega_{\mathrm{H_2}}$	19.4	-	%
	O_2	$\omega_{\mathrm{O_2}}$	-	17.0	%
	N_2	$\omega_{\mathrm{N_2}}$	67.3	70.7	%
	H_2O	$\omega_{\mathrm{H_2O}}$	13.3	12.3	%

[†] Volumetric gas fractions are noted without consideration of the water vapor content.

7.2.5 Validation and Simulation Results Calibration Model

COMSOL Multiphysics® is used to set up the described model. The geometry is meshed with at least three triangle elements over the thickness of the thin layers with about 20 000 elements in total. Equations are solved with a segregated solver whereby the reactions in the CL and mass and charge transport over the membrane are solved in one step and the species transport in the anode and cathode compartment subsequently in two further steps. The exchange current densities for HOR and ORR on anode and cathode side $i_{0,\mathrm{HOR}}$ and $i_{0,\mathrm{ORR}}$ and the transfer coefficient for the ORR α_{ORR} are fitted to the experimentally measured IV-curve of the cell, shown in Figure 7.9.

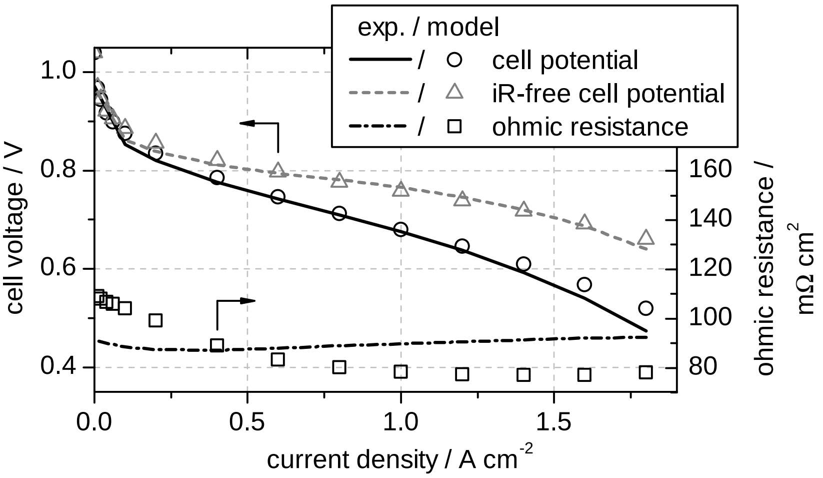

Figure 7.9: Comparison of the experimentally measured IV-curve, the ohmic resistance in the cell (HFR) and the iR-free cell voltage with the model results.

As the measured HFR can be interpreted as the ohmic resistance over the cell ${\sigma_\Omega}^{-1}$, the model can also be fitted to the iR-free cell voltage $\Delta\varphi_{\mathrm{iR-free}}$, calculated from the measured cell voltage $\Delta\varphi_{\mathrm{cell}}$ and the current density i

$$\Delta\varphi_{\mathrm{iR-free}} = \Delta\varphi_{\mathrm{cell}} + \frac{i}{\sigma_\Omega}. \tag{7.31}$$

The model was fitted with few parameters, therefore the cell voltage and iR-free cell voltage could be simulated quite well over a wide load range. In the higher current density region ($> 1\,\mathrm{A\,cm^{-2}}$) the model underestimates ohmic losses. The difference is likely to originate from local membrane dry-out due to in-plane and through-plane temperature gradients, which are not accounted for in the isothermal model. At low current densities, the simulated ohmic resistance is up to $20\,\mathrm{m\Omega\,cm^2}$ higher compared to the experimentally measured value, which could be an effect of residual liquid water in the cell, maintaining a certain membrane humidification. The model does not account for liquid water in the CL and GDL.

Note that in the following graphs, the shown parameters are averaged over the thickness of the according domains, membrane, anode CL or cathode CL.

Species Concentration

Heterogeneities over the channel-land structure of the FF are a characteristic for PEFCs. Recent developments aim to minimize transport losses below the ribs in order to increase the cell performance. The reduction of the FF pitch can mitigate the heterogeneities but is limited by restrictions of the manufacturing processes. Figure 7.10 shows the molar fraction of reactants and water vapor in the CLs. Even under OCV conditions the reactant concentrations drop down slightly below the FF lands on anode and cathode side due to oxygen and nitrogen crossover to the anode and hydrogen crossover to the cathode. With an increasing load, reactant depletion is even more pronounced below the lands due to their consumption in the electrochemical reactions. On the cathode side oxygen fraction falls down to 0 at $1.8\,\mathrm{A\,cm^{-2}}$, emphasizing the cathode as the limiting factor at high current densities due to high mass transport losses. Whereby the hydrogen fraction varies by less than $4\,\%$ at $1.8\,\mathrm{A\,cm^{-2}}$ between channel and land area. Water vapor fraction in turn increases with the current density under the lands on the cathode side due to electrochemically generated water and on the anode as a result of water crossover over the membrane. The anode water fraction remains slightly below the cathode side, emphasizing that water back-diffusion takes place from cathode to anode. Nitrogen represents the remaining molar fraction on anode and cathode side, but is not shown here for clarity.

Reaction Kinetics and Potentials

Amongst others, reaction kinetics of ORR and HOR are controlled by the local reactant concentration. As a result of reactant depletion under the lands at higher current densities, the local current densities of HOR and ORR on anode and cathode, respectively, are significantly reduced there compared to the areas under the channels, as shown in Figure 7.11. At $1.8\,\mathrm{A\,cm^{-2}}$ the current density is about three-fold higher under the channels than under the lands at both anode and cathode side. At $1\,\mathrm{A\,cm^{-2}}$ current production is almost homogeneously distributed, slight peaks are visible at the edges of the ribs, resulting from a good gas supply there combined with low ohmic resistances due to the short electron pathways to the BPP rib. This characteristic is also visible at $1.8\,\mathrm{A\,cm^{-2}}$.

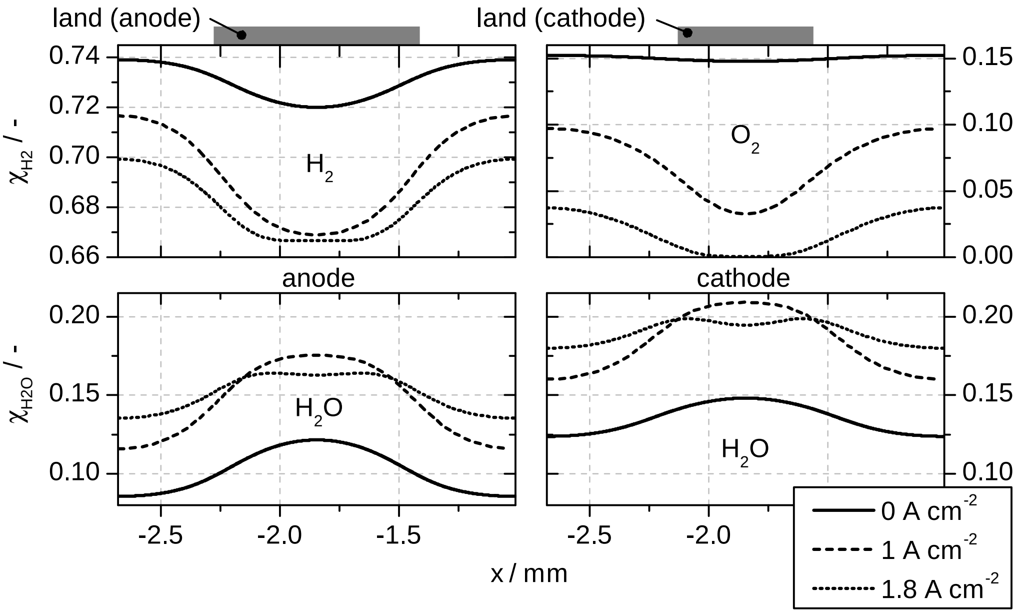

Figure 7.10: Molar fraction of hydrogen and water in the anode CL (left) and of oxygen and water in the cathode CL (right) over the width of one FF pitch for different cell current densities. Values are averaged over the CL thickness. The remaining molar fraction is attributed to nitrogen.

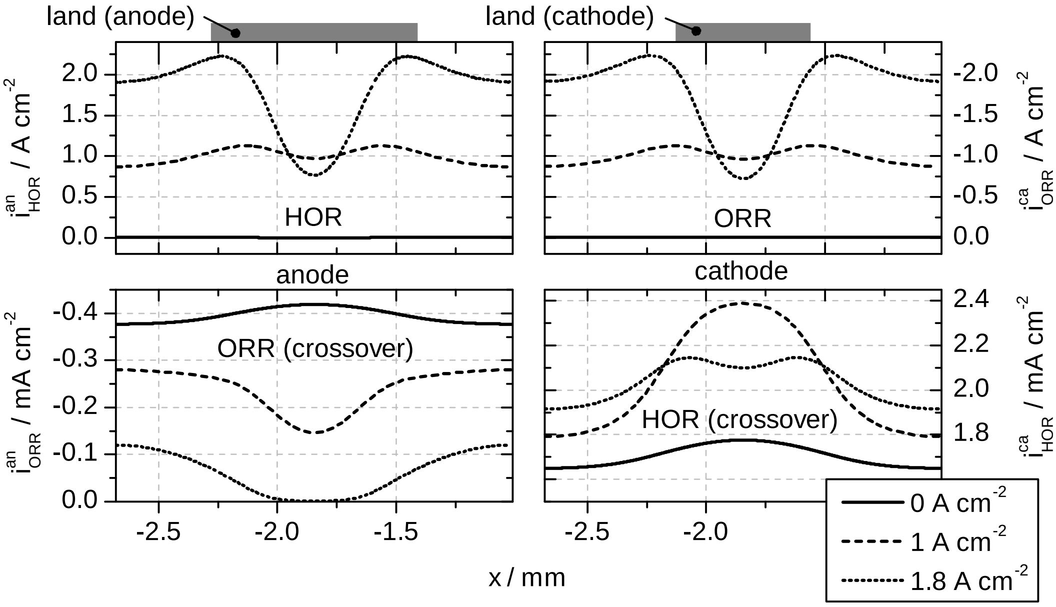

Figure 7.11: Top: Electrode current densities on anode and cathode side for HOR and ORR, respectively. Bottom: Reactions arising from gas crossover flows, ORR on the anode and HOR on the cathode side.

Crossover reactions – ORR on the anode and HOR on the cathode – are shown in the bottom part of Figure 7.11. The ORR on the anode side follows the oxygen concentration on the cathode side, its current density drops down to almost zero at $1.8\,\mathrm{A\,cm^{-2}}$. Whereas the HOR on the cathode side shows entirely inversed characteristics. Over all load points, highest hydrogen crossover and as a result the highest HOR current density is found under the lands. It is a result of the weak heterogeneities in hydrogen concentration on the anode which are superimposed by the inhomogeneous membrane humidification. According to Equation 7.14, a higher humidification of the membrane under the lands leads to a significant increase of hydrogen crossover.

As the CL and GDL are good electrical conductors, in-plane gradients of the solid electrical potential can hardly emerge as shown in Figure 7.12. On the anode side, a maximal gradient of $60\,\mathrm{mV}$ occurs at $1.8\,\mathrm{A\,cm^{-2}}$, with the lowest potential under the channel, indicating electron transport from the channel to the land region. On the cathode the gradient is inverted as electrons are transported in the other direction, but the absolute gradient at $1.8\,\mathrm{A\,cm^{-2}}$ is lower with $5\,\mathrm{mV}$ due to the higher conductivity of the $12\,\mathrm{\mu m}$ thick cathode CL compared to the $8\,\mathrm{\mu m}$ thick anode CL. Electrolytic potentials in both CLs differ slightly from each other under load as the proton flux gives rise to the formation of a negative potential gradient from anode to cathode.

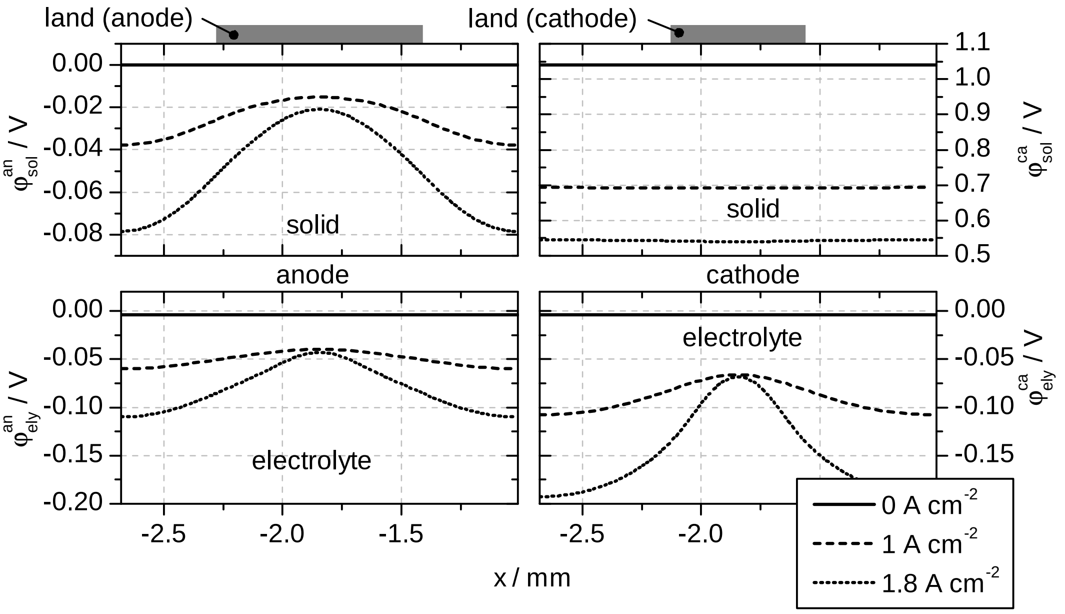

Figure 7.12: Top: Solid electrical potentials in the anode and cathode CL. Bottom: Electrolytic potentials in anode and cathode CL.

7.2.6 Simulation Results Hydrogen Starvation Model

In the following the simulation results of the entire model, comprising four FF pitches and with the anode being partially covered by a foil, are presented. The values on the x-axis refer to the coordinate system in Figure 7.8, the foil on the anode side extends from $x = 0$ to $4\,\mathrm{mm}$. The rectangles on top of the following diagrams indicate the position of the FF lands. In the corresponding experiment (cf. Section 7.2.1), overall cell current densities i_cell were 0, 0.2 and $0.9\,\mathrm{A\,cm^{-2}}$, related to the entire cell area. As the simulation results revealed that the contribution of the area under the foil to current production is marginal, the simulated current densities are reduced by the fraction of the covered region to $i_\mathrm{model} = i_\mathrm{cell} \cdot \frac{2.68}{6.68}$. However, in the following graphs, the noted current density is i_cell for convenience, although i_model is applied on the model domain.

In-Plane Heterogeneities

Self-diffusion of water inside the electrolyte membrane is relatively slow. Distinct water concentration gradients can be established in the in-plane direction of the thin membrane, as Figure 7.13 verifies for different load points. In the normal operated area ($x < 0\,\mathrm{mm}$), the membrane water content increases by about $\lambda_\mathrm{mem} = 1$ between 0 and $0.2\,\mathrm{A\,cm^{-2}}$, but remains constant for a further increase of the current density. Water discharge from the membrane and CLs is generally more pronounced on the anode side, as the gas inlet humidity there is lower with $30\,\%\,\mathrm{RH}$. In the hydrogen starved area water discharge is inhibited on the anode side due to the covering foil, leading to an increased membrane water content of up to $\lambda_\mathrm{mem} = 12$ without respect to the current density.

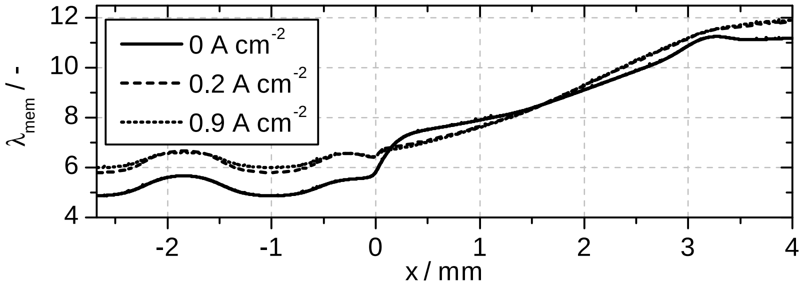

Figure 7.13: Membrane water content λ_mem over the width of the membrane for different load points, exhibiting a clear trend to higher values in the hydrogen starved area.

In Figure 7.14 the molar fractions of hydrogen in the anode and oxygen in the cathode CL are shown for different cell current densities. For $x < 0\,\mathrm{mm}$ the hydrogen fraction decreases under the ribs for a higher current density, coinciding with the results from the calibration

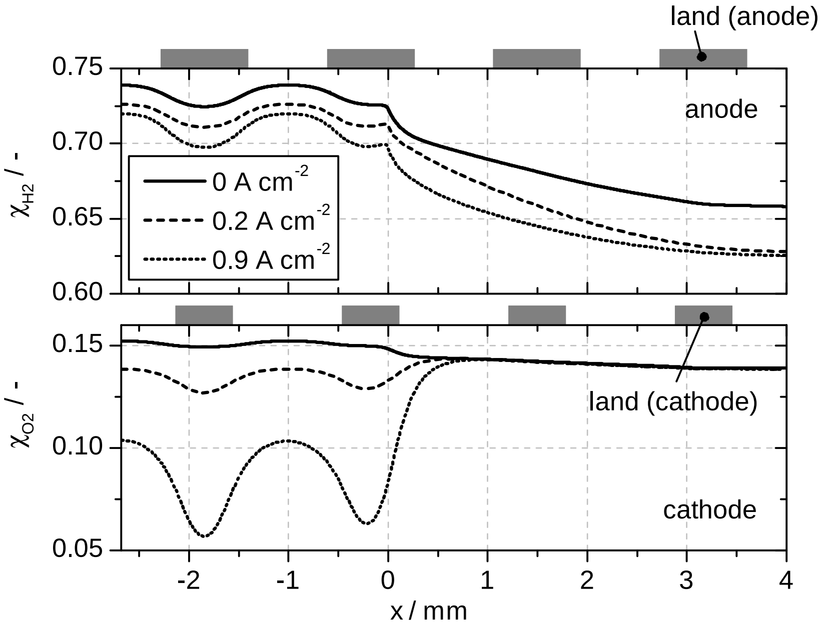

Figure 7.14: Molar concentration of hydrogen in the anode CL and of oxygen in the cathode CL for different overall cell current densities.

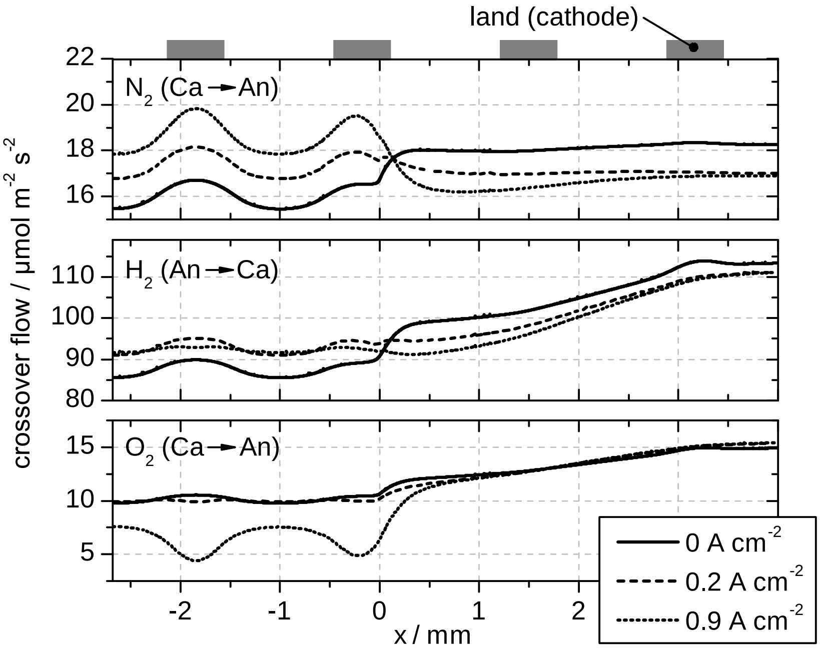

Figure 7.15: Gas crossover fluxes from cathode to anode (nitrogen and oxygen) or vice versa (hydrogen), for different cell current densities.

model. In the area superimposed to the covering foil, hydrogen concentration drops down appreciably to a minimum of $62.5\,\%$ at $0.9\,\mathrm{A\,cm^{-2}}$ as a result of hydrogen consumption in the HOR. Nitrogen crossover from the cathode to the anode side has a major influence on the hydrogen concentration, as the results for $0\,\mathrm{A\,cm^{-2}}$ show, where the hydrogen concentration drops down to $66\,\%$ although the net consumption of hydrogen in the HOR is zero.

On the cathode side, oxygen is diluted with nitrogen and water with a raising current density in the normally operated region ($x < 0\,\mathrm{mm}$), even more pronounced under the lands. In the hydrogen starved area, the oxygen concentration remains above $13\,\%$ due to the low ORR rate there as presented later (Figure 7.16).

Crossover fluxes of hydrogen, oxygen and nitrogen, shown in Figure 7.15, depend on the according partial pressure gradients and the local membrane water content. Nitrogen crossover increases with the current density for $x < 0\,\mathrm{mm}$ due to the increased nitrogen concentration on the cathode side. For $x > 0\,\mathrm{mm}$ the behavior is inverted as on the anode side the nitrogen concentration also increases there with the current density. The influence of the membrane water content on nitrogen crossover is not obvious. In contrast, hydrogen crossover shows a strong dependency from the membrane water content. In the area covered by the foil the characteristic is very similar to λ_{mem}. Hydrogen concentration has a minor impact as it only varies over a small range of less than $5\,\%$ (Figure 7.14). The oxygen crossover flow results from the membrane water content and the partial pressure of oxygen. For $x < 0\,\mathrm{mm}$ the crossover only changes marginal between 0 and $0.2\,\mathrm{A\,cm^{-2}}$ as a decrease in oxygen partial pressure and an increase of membrane water content have a contrary effect. For $x > 0\,\mathrm{mm}$ the crossover does not show a dependency from the current density and increases towards the cell edge.

ORR current density on the cathode side in Figure 7.16 exhibits a similar characteristic for $x < 0\,\mathrm{mm}$ as seen in the calibration model. Heterogeneities increase with the current density, at $0.9\,\mathrm{A\,cm^{-2}}$ the local current density oscillates between absolute values of 0.8 and $0.95\,\mathrm{A\,cm^{-2}}$. ORR current density falls down to zero in the hydrogen starved region for all load points, although the oxygen concentration remains stable there. As later explicated the cathode electrode reaches OCV there and the electrode current density accordingly drops down. The HOR rate on the cathode side, depicted in the bottom part of Figure 7.16, corresponds to the hydrogen crossover flux. It remains below $2.2\,\mathrm{mA\,cm^{-2}}$ for all load points.

On the anode side the ORR occurring due to oxygen crossover from the cathode follows the according crossover flux but never exceeds absolute values of $0.6\,\mathrm{mA\,cm^{-2}}$ (Figure 7.17). As a result of the low hydrogen concentration HOR current density on the anode side and hence proton generation drops down to almost zero in the edge region without respect to

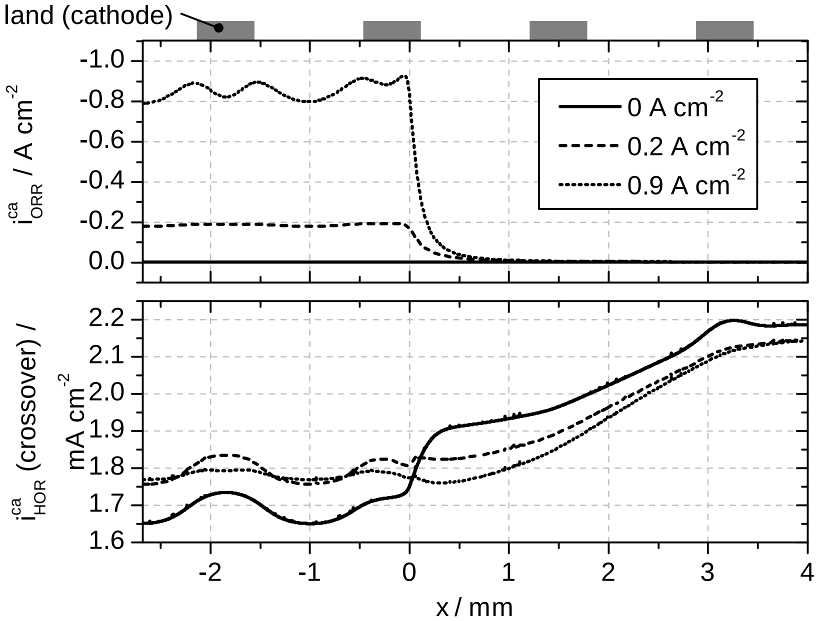

Figure 7.16: Current densities of ORR and HOR in the cathode CL. The latter is caused by hydrogen crossover from the anode.

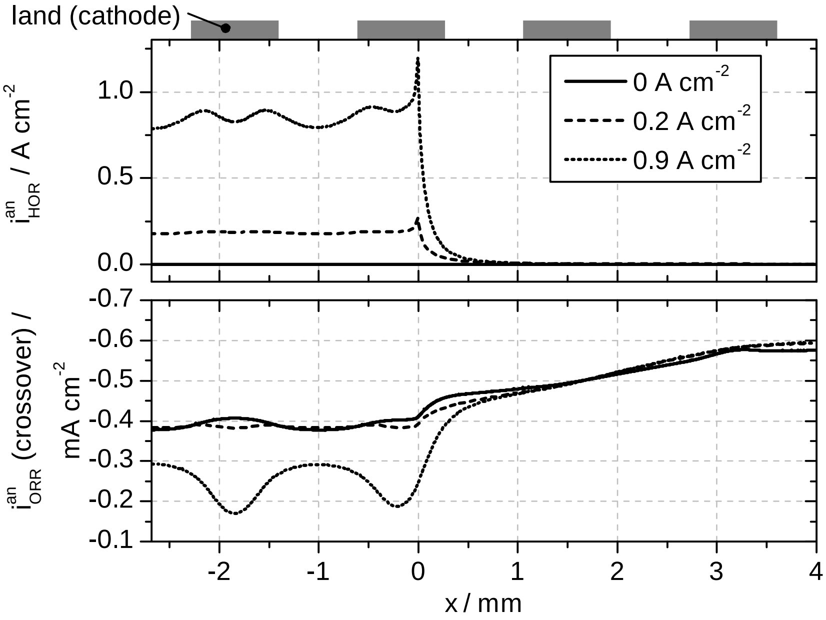

Figure 7.17: HOR and ORR current densities in the anode CL. ORR is caused by oxygen crossover from the cathode side.

the cell current density. The electrolyte potential – equivalent to the proton concentration – drops down to $< -0.3\,\mathrm{V}$ in this area for $i_{\mathrm{cell}} = 0.9\,\mathrm{A\,cm^{-2}}$ as depicted in Figure 7.18, since protons are consumed in the ORR on the cathode side. Both, HOR on the anode and ORR on the cathode side, do not exhibit high current densities, so that the electrodes almost reach their electrochemical equilibrium potentials, $< 10\,\mathrm{mV_{SHE}}$ on the anode and $> 1\,\mathrm{V_{SHE}}$ on the cathode. On the anode side, a significant in-plane gradient of the solid electrode potential can emerge under the covering foil for cell current densities of 0.2 and $0.9\,\mathrm{A\,cm^{-2}}$ due to an electron flux resulting from the remaining marginal HOR current density in the hydrogen starved area. The electrical in-plane conductivity of the anode in the area covered by the foil is relatively low since the thin CL is not electrically contacted by the highly conductive GDL there. Whereby on the cathode side GDL and CL are contacted and potential gradients hardly occur without respect to the cell current density. In general, the electrolyte potential drop in the starved area is more pronounced with a higher overall cell current density as the in-plane electron current in the anode CL is slightly higher and solid and electrolyte phase of the anode are tightly coupled to each other by a low and constant anode overpotential ($< 10\,\mathrm{mV_{SHE}}$)[1]. As a result of the low electrolyte potential and a constantly high solid potential of the cathode CL for $x > 0\,\mathrm{mm}$, the cathode electrode voltage exceeds $1\,\mathrm{V_{SHE}}$ and almost reaches OCV values without respect to the overall cell current density.

Carbon Corrosion

Carbon corrosion rates of the anode CL are negligible as occurring electrode potentials are below the COR equilibrium potential of $0.207\,\mathrm{V_{SHE}}$ [47, 49]. In contrast, the electrode potential of the cathode can exceed $0.8\,\mathrm{V_{SHE}}$ where significant COR rates appear [49]. Figure 7.19 represents the COR rates in the cathode CL for different load points, indicating the general dependence from the electrode potential. For $x < 0\,\mathrm{mm}$, the COR current density decreases with an increasing electrical load, falling below $1\,\mathrm{\mu A\,cm^{-2}}$ at 0.2 and $0.9\,\mathrm{A\,cm^{-2}}$. For $x > 0\,\mathrm{mm}$ the COR current density steadily increases towards the CCM edge and exceeds $4\,\mathrm{\mu A\,cm^{-2}}$ at $x = 2.5\,\mathrm{mm}$ without respect to the cell current density. At OCV, COR remains above $5\,\mathrm{\mu A\,cm^{-2}}$ but slightly decreases towards the outer CCM edge.

The theoretical mass loss rate of carbon $\dot{m}_{\mathrm{C}}$ can be calculated by Faraday's law

$$\dot{m}_{\mathrm{C}} = \frac{M_{\mathrm{C}} i_{\mathrm{COR}}^{\mathrm{ca}}}{z_{\mathrm{COR}} F} \tag{7.32}$$

---

[1] A constant electrode overpotential means the potential of the solid and electrolytic phase of an electrode having a constant offset to each other.

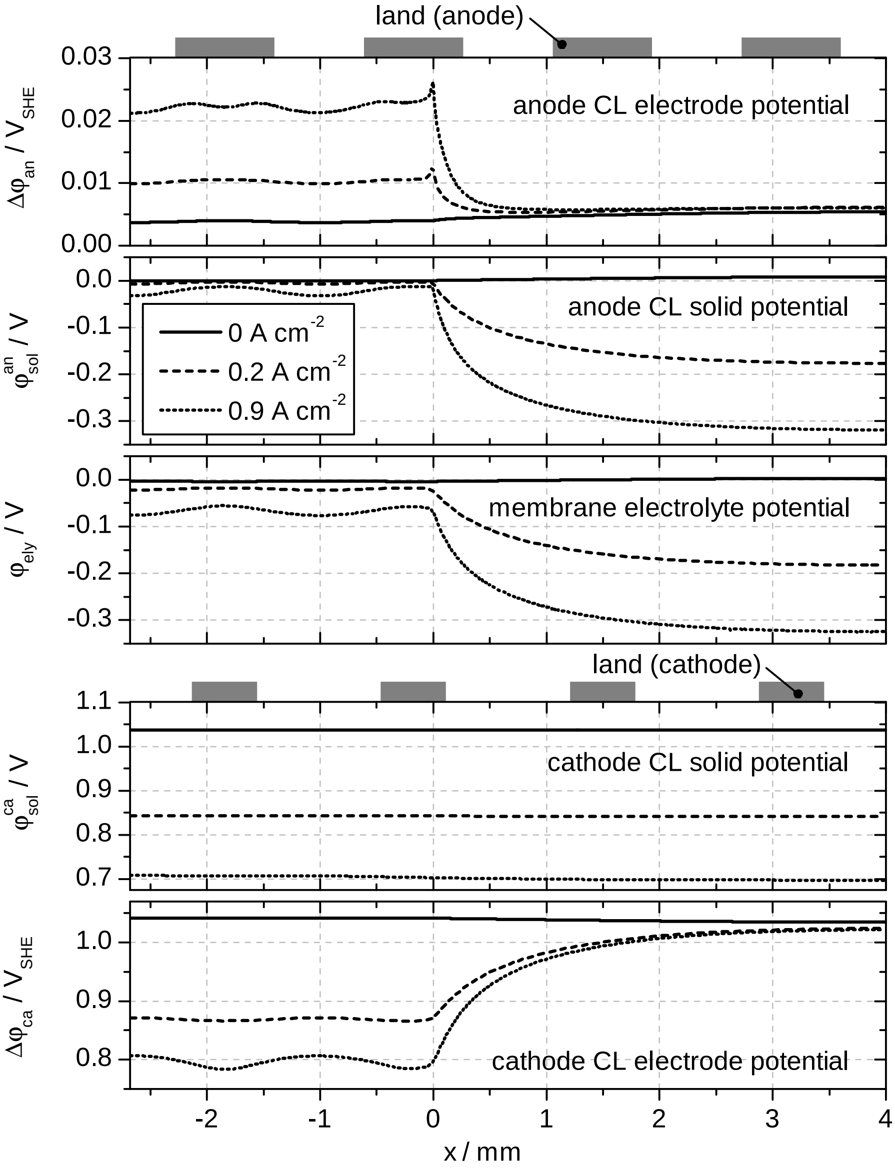

Figure 7.18: In-plane potential distribution in anode and cathode CL solid and in the membrane electrolyte phase for different cell current densities and the resulting electrode potentials on anode and cathode side.

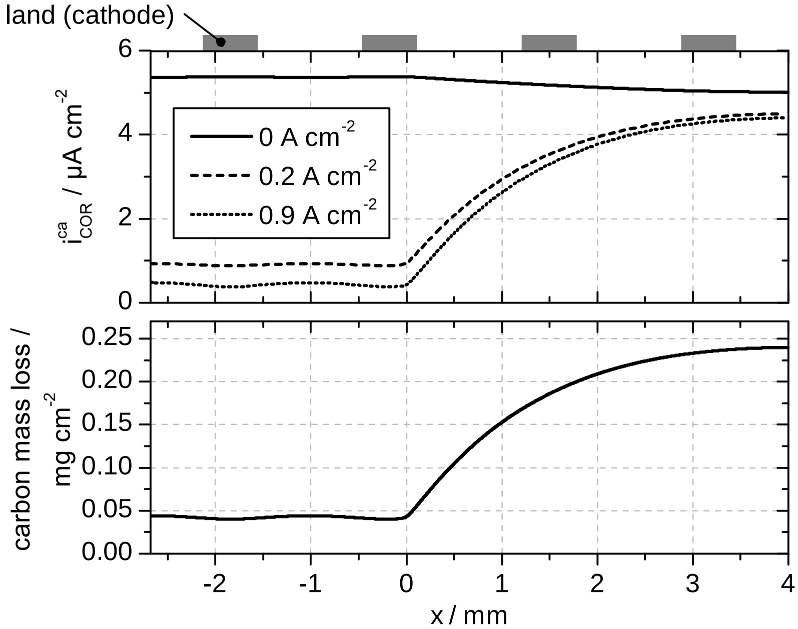

Figure 7.19: Top: COR current densities for different simulated cell current densities over the width of the cathode CL. Bottom: Simulated accumulated carbon mass loss, over a load cycling experiment over $480\,\mathrm{h}$ as described in Section 7.2.1.

with the molar mass of carbon $M_\mathrm{C} = 12.0107\,\mathrm{g\,mol^{-1}}$ and the valency $z_\mathrm{COR} = 4$. In order to reproduce the experimental conditions from Section 7.2.1, the local mass loss of the CL $\Delta m_\mathrm{C}(x)$ is calculated from the mass loss rate $\dot{m}_{\mathrm{C},b}(x)$ for the different load points $b = \{0, 0.2, 0.9\}\,\mathrm{A\,cm^{-2}}$ with the according operation times $t_0 = 11.7\,\mathrm{h}$ and $t_{0.2} = t_{0.9} = 234\,\mathrm{h}$

$$\Delta m_\mathrm{C}(x) = \sum_b \dot{m}_{\mathrm{C},b}(x) \cdot t_b. \tag{7.33}$$

The result is shown in the bottom part of Figure 7.19. Total carbon loss reaches $0.24\,\mathrm{mg\,cm^{-2}}$ in the outer edge of the CCM at most. In the normal operated area, Δm_C remains below $0.05\,\mathrm{mg\,cm^{-2}}$.

Essential for the strong occurrence of the COR is the formation of a potential gradient in the solid phase of the anode CL. As CL and GDL are not electrically contacted in the area superimposed to the covering foil, the potential gradient mainly depends on CL conductivity, apart from HOR current density. The CL conductivity σ_cl is not known for the employed components. $\sigma_\mathrm{cl} = 60\,\mathrm{S\,m^{-1}}$ was taken as a first approach. Literature values vary over a wide range as Table 7.2 shows. Measured values range from 25 to $180\,\mathrm{S\,m^{-1}}$ [234, 235], while for simulations up to $8884\,\mathrm{S\,m^{-1}}$ were assumed [233]. In order to investigate the influence of the CL conductivity, it was varied from 10 to $1000\,\mathrm{S\,m^{-1}}$ in the simulation. The resulting

Table 7.2: Comparison of literature values for the effective electrical conductivity of the CL.

parameter origin	value	unit	Ref.
assumption	30	$\mathrm{S\,m^{-1}}$	Ismail et al. [230]
	90	$\mathrm{S\,m^{-1}}$	Zhou et al. [231]
	1000	$\mathrm{S\,m^{-1}}$	Nam et al. [232]
	2000	$\mathrm{S\,m^{-1}}$	Yang et al. [51]
	8884	$\mathrm{S\,m^{-1}}$	Dobson et al. [233]
measurement	$25 - 180^{\bullet}$	$\mathrm{S\,m^{-1}}$	Du et al. [234]
	$28 - 34^{\dagger}$	$\mathrm{S\,m^{-1}}$	Siroma et al. [235]

$^{\bullet}$ Variation between 25 and 180 $\mathrm{S\,m^{-1}}$ for electrolyte volume ratios in the CL from 0.1 to 0.54.

† Variation between 28 and 34 $\mathrm{S\,m^{-1}}$ for humidification levels from 95 to 25 % RH.

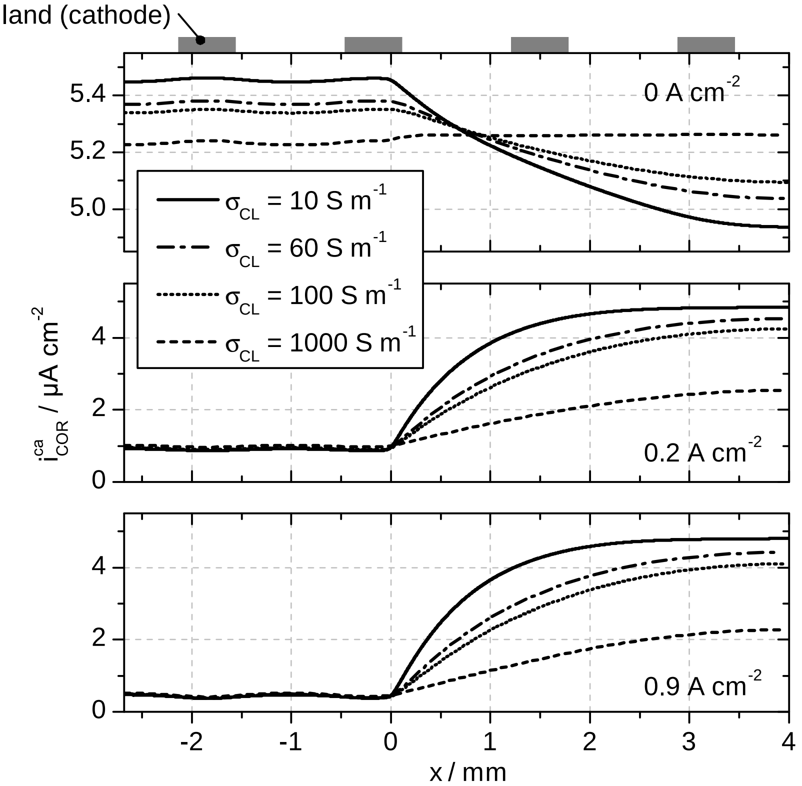

Figure 7.20: COR current density under a variation of the CL conductivity σ_{cl}. High conductivities mitigate potential gradients particularly in the anode CL and the electrolyte, leading to a general reduction of the cathode electrode potential.

COR current densities are depicted in Figure 7.20 for different cell current densities. At $i_{\text{cell}} = 0\,\mathrm{A\,cm^{-2}}$, heterogeneities in the COR decrease with increasing conductivities and almost vanish for $\sigma_{\text{cl}} = 1000\,\mathrm{S\,m^{-1}}$. For cell current densities of 0.2 and $0.9\,\mathrm{A\,cm^{-2}}$, COR is mitigated with the conductivity for $x > 0\,\mathrm{mm}$. For $\sigma_{\text{cl}} = 1000\,\mathrm{S\,m^{-1}}$ only about half of the COR current density compared to $\sigma_{\text{cl}} = 10\,\mathrm{S\,m^{-1}}$ is reached. It can be explained by reduced solid potential gradients and – as the electrolyte potential is tightly coupled to the solid potential on the anode side due to low electrode potentials – due to a low potential gradient in the electrolyte. As a result, the electrode potential on the cathode side and the COR is reduced in the hydrogen starved area.

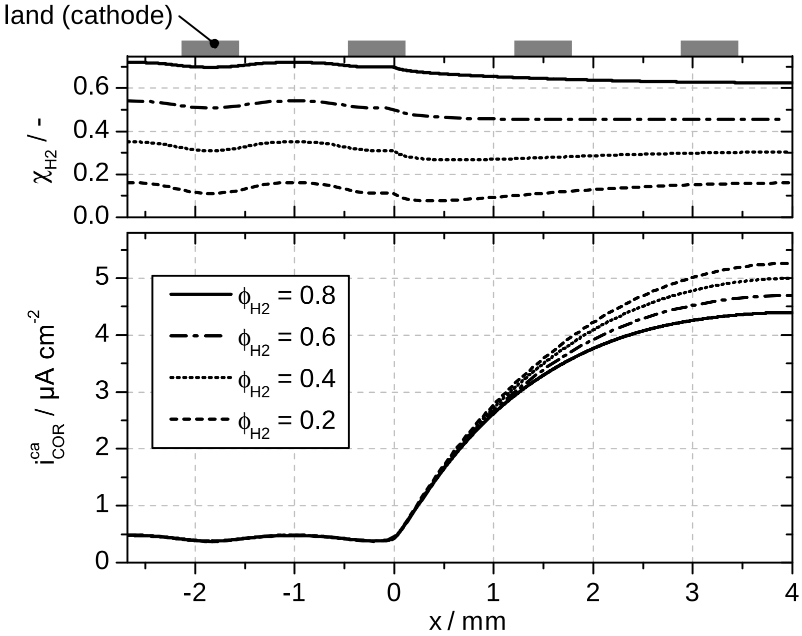

Figure 7.21: Effect of a reduced hydrogen concentration at the anode inlets on carbon corrosion at $i_{\text{cell}} = 0.9\,\mathrm{A\,cm^{-2}}$. Top: Molar fraction of hydrogen in the anode CL. Bottom: Resulting COR current density in the cathode CL.

In the area under the foil on the anode side, the limiting factor for the HOR is the hydrogen concentration. A higher hydrogen concentration is expected to lead to higher HOR current densities towards the outer CCM edge. Figure 7.21 shows the hydrogen concentration in the anode CL and the resulting COR current density in the cathode CL for different hydrogen volume fractions $\phi_{\mathrm{H_2}}$ at the inlets, at a constant cell current density of $0.9\,\mathrm{A\,cm^{-2}}$. For $\phi_{\mathrm{H_2}} = 0.8$ the molar fraction of hydrogen decreases under the covering foil due to hydrogen consumption in the HOR. For $\phi_{\mathrm{H_2}} = 0.4$ and $\phi_{\mathrm{H_2}} = 0.2$, the molar hydrogen fraction increases towards the outer edge of the CCM, as the anode electrode potential falls below the HOR equilibrium potential and hydrogen evolution occurs. The potential gradient in the electrolyte is then slightly negative from cathode to anode side and protons move to the anode. COR current density increases by more than $10\,\%$ when changing the inlet hydrogen fraction $\phi_{\mathrm{H_2}}$ from 0.8 to 0.2, as the anode is shifted from proton generation to proton consumption and hence the cathode potential increases due to a lower electrolyte potential on the cathode side.

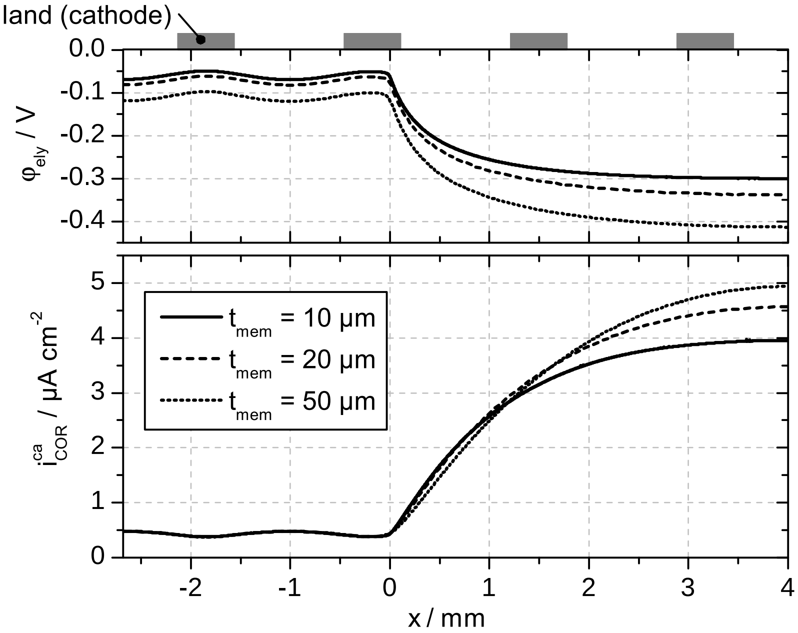

Figure 7.22: Influence of the membrane thickness t_{mem} on the COR at a current density of $i_{\mathrm{cell}} = 0.9\,\mathrm{A\,cm^{-2}}$. Top: Membrane electrolyte potential, averaged over the membrane thickness. Bottom: COR current density in the cathode CL.

In the present case, the formation of an in-plane electrolyte potential gradient is an essential requisite for the occurrence of a high cathode electrode potential and a high carbon corrosion rate, as seen before. The drop of the electrolyte potential in the hydrogen starved area is entailed by the limited electron transport in the solid phase of the anode CL and the constantly low anode overpotential. The in-plane conductivity of the electrolyte can mitigate the COR rate, as it reduces the electrolyte in-plane potential gradient. As this effect is obvious, a further aspect will be discussed here. A main trend for PEFCs is the further reduction of the membrane thickness in order to reduce its ohmic losses. The influence of the membrane thickness on the COR in the present case cannot be concluded straightforward as contradictory effects occur. On the one hand, the in-plane conductivity of the membrane is reduced with a lower thickness, entailing the formation of higher in-plane potential gradients. On the other hand, gas crossover effects are gaining in significance, leading to a reduced electrode potential of the cathode and an increased potential of the anode under OCV conditions, respectively. Figure 7.22 shows the resulting electrolyte potential and the COR current density for different membrane thicknesses. The electrolyte potential drop towards the outer cell edge is mitigated and the COR rate decreases for thinner membranes. Two mechanisms give rise to this effect:

- Oxygen crossover to the anode and its subsequent reduction consumes electrons and leads to a lower net in-plane current in the solid phase of the anode CL and consequently to a lower solid potential gradient. As the electrolyte potential is tightly coupled to the anode CL solid phase, also the electrolyte potential gradient in the hydrogen starved region is reduced.
- The maximum cathode electrode potential is limited by the hydrogen crossover to the cathode[1]. The cathode electrode potential of the calibration model under OCV conditions ($i_{\text{cell}} = 0\,\mathrm{A\,cm^{-2}}$) is reduced from 1.076 to $1.018\,\mathrm{V}$ when changing the membrane thickness from 50 to $10\,\mathrm{\mu m}$ due to a stronger hydrogen crossover. The lower maximum cathode potential entails a reduced carbon corrosion[2].

7.3 Discussion

Mechanical Membrane Deterioration

In the first part of this chapter, the CCM of a cell was mechanically stressed by alternating the gas inlet humidification between 1.5 and $100\,\%\,\mathrm{RH}$. The membrane was directly sealed with flat gaskets in its outer perimeter and sandwiched between two GDLs in the FF area. A significant increase of gas crossover over the membrane was measured by LSV after about 8000 dry/humid cycles. A detailed mapping of the crossover gas flow by IR imaging of the reaction heat of hydrogen crossing over the membrane revealed two local membrane defects. They were located at the outer perimeter of the cell, outside the GDL area and can be attributed to local mechanical membrane faults, such as pinholes, caused by membrane fatigue due to a high local mechanical stress. The internal short resistance of the membrane dropped down concurrently with the increasing membrane leakage, so that the defects are likely to contribute to an internal short over the membrane. The measured fluoride concentration in the product water did not correlate with the high membrane decomposition towards the end of the experiment. At the beginning a somewhat higher release rate was found but decreased to the end of the experiment, indicating that the degradation mechanism does not necessarily lead to

---

[1] No oxygen evolution reaction was observed to occur at the cathode in all simulations, so that the electrode potential always remained below the equilibrium potential of the ORR of $1.175\,\mathrm{V}$.

[2] Without respect to the influence of water concentration, the theoretical COR current density is reduced from 7.7 to $4.2\,\mathrm{\mu A\,cm^{-2}}$ for a cell voltage reduction from 1.076 to $1.018\,\mathrm{V_{SHE}}$, according to Equation 7.27.

an increase of fluoride concentration in the product water, as it was observed for chemical degradation [73].

Although the experimental conditions were harsh and the applied test protocol represents accelerated conditions compared to the real operation in a system, the results exhibit bottlenecks – here in case of mechanical membrane failure – for the operation of a cell over long operating times (e. g. $> 5000\,\mathrm{h}$). It was shown, that a gentle implementation of the CCM in its outer perimeter in order to seal the membrane against the environment, is essential for a long lifetime under alternating humidity conditions. Otherwise a rapid local membrane decomposition is likely to occur and can be crucial for the cell's lifetime. In case of a direct sealing on the CCM, the GDL should be integrally formed with the sealing structure in order to provide an entire coverage of the CCM with GDLs on both sides and hence a favorable mechanical implementation with reduced point loads.

Hydrogen Starvation

In this work, a partial coverage of the CCM on the anode side by a SG or sealing structure – simulating a component misalignment due to manufacturing and assembling tolerances – was experimentally reproduced by introducing a thin foil between anode CL and GDL, covering a width of $6\,\mathrm{mm}$ around the CCM edge. After about $480\,\mathrm{h}$ of load cycling operation, the cross sections of the CCM were analyzed in the outer perimeter. Except in the anode inlet region, a significant thinning of the cathode CL was found while anode CL and membrane thickness remained constant, revealing substantial carbon corrosion of the cathode CL. Thinning in the hydrogen starved area begins about $1 - 2\,\mathrm{mm}$ below the foil edge, and occurred inhomogeneously distributed in the starved area. The CL thickness was locally reduced to $3\,\mu\mathrm{m}$ compared to $12\,\mu\mathrm{m}$ of a fresh CL.

Results from CV measurements did not indicate a ECA loss on the cathode side over the experiment and hence did not confirm the decomposed cathode CL in the starved area. The mass loss of the cathode CL occurred over a width of about $4\,\mathrm{mm}$ on three of four cell edges, where the CL thickness was reduced by an average of about $30\,\%$. This equals a volume loss of about $5\,\%$ of the whole cathode CL. The discrepancy between CV and SEM analysis could arise from the low electrolyte potential in the edge region due to low hydrogen concentration and a low HOR current density on the anode side (for the cathode as a working and the anode as a reference electrode). So that the hydrogen reduction peak in the CV is reduced by the low proton concentration in the electrolyte in the edge region. The fluoride release during the experiment showed an initial peak at the beginning, likely an effect of membrane conditioning, and then dropped down below the detection limit of the ion selective electrode. This confirms the SEM results where the membrane thickness was found unchanged.

Numerical simulation of the present case of hydrogen starvation on the anode revealed a comprehensive image of the relevant processes and influences that lead to a deterioration of the cathode CL in the edge region of the CCM. The central characteristic and origin of the occurring degradation mechanism is a distinct increase of the cathode electrode potential towards the outer CCM edge. Different mechanisms lead to that effect:

- In the hydrogen starved area on the anode side, the low HOR current density due to low hydrogen concentration leads to an interruption of proton generation.
- On the cathode side, oxygen supply is good and as the electrode voltage remains below the equilibrium potential of $1.175\,\mathrm{V_{SHE}}$, protons are consumed in the ORR, thus lowering the electrolyte potential.
- As the anode CL is partially covered by an electrically isolating foil, transport of electrons generated in the HOR can only occur by in-plane transport through the solid phase of the CL, with a relatively low conductivity of $60\,\mathrm{S\,m^{-1}}$ of the $8\,\mathrm{\mu m}$ thick layer. A potential difference of $> 0.3\,\mathrm{V}$ arises over the CL width at the maximum cell current density of $0.9\,\mathrm{A\,cm^{-2}}$ with a minimum at the outer edge of the cell.
- The electrode potential of the anode only varies between 0 and $30\,\mathrm{mV_{SHE}}$, so that solid and electrolyte potential are tightly coupled to each other, provoking a drop of the electrolyte potential in the starved area down to a minimum of $-0.32\,\mathrm{V}$ at maximum cell current density.
- In-plane electron conductivity on the cathode side is high due to the contact to the highly conductive GDL. Emerging potential gradients in the solid electrode phase are negligibly small.
- The combination of a drop of the electrolyte potential in the edge region and a constant and high solid potential of the cathode CL leads to a local increase of the cathode electrode potential up to nearly OCV and to a decrease of the ORR current density to almost zero. The COR increases accordingly.

The cathode electrode potential exceeds $1\,\mathrm{V}$ from about $1.5\,\mathrm{mm}$ below the covering foil at current densities of 0.2 and $0.9\,\mathrm{A\,cm^{-2}}$. The high potential entails a strong oxidation of the carbon support of the cathode CL, COR currents up to $4\,\mathrm{\mu A\,cm^{-2}}$ were calculated, corresponding to a carbon mass loss of about $0.25\,\mathrm{mg\,cm^{-2}}$ over about $480\,\mathrm{h}$ of load cycling. The experimentally determined cathode CL thinning reached more than $50\,\%$. As the initial CL carbon loading is not known, both results cannot be compared directly. However, the model seem to underestimate COR current density as carbon loadings are expected to lie above

$1\,\mathrm{mg\,cm^{-2}}$. Reasons for the discrepancy could be the missing consideration of liquid water in the model, a lower CL electron conductivity than assumed or a lower hydrogen concentration in the experiment than assumed here. The strong dependence of cathode CL support oxidation from the hydrogen concentration is confirmed by the fact that in the anode inlet area of the cell no cathode CL thinning was observed. Another reason for the low calculated COR current density could be the limited validity of the employed kinetic parameters for the COR, taken from the literature, as they can vary significantly with the type of the catalyst system. While the experiments revealed an inhomogeneous cathode CL thinning for $x > 2\,\mathrm{mm}$, the model does not show a similar behavior. The origin of this discrepancy remains unclear, but could also be attributed to an accelerated carbon oxidation due to local accumulation of liquid water under the FF lands.

The key role of the in-plane electron conductivity of the anode CL and of the electrical isolation to the GDL is emphasized by performing the simulation for various CL conductivities. By increasing the conductivity to $1000\,\mathrm{S\,m^{-1}}$, the maximum COR current density at $i_{\mathrm{cell}} = 0.9\,\mathrm{A\,cm^{-2}}$ is halved compared to the standard case with $60\,\mathrm{S\,m^{-1}}$ as potential gradients over the anode CL are mitigated and the drop of the electrolyte potential in the CCM edge is mitigated.

In the inlet region, the cathode CL thinning was not measurable, COR current density is hence expected to be in the same range as in the normal operated region. An explanation is that a higher hydrogen concentration, a lower amount of liquid water and a higher overall pressure in the cell inlet region lead to a higher hydrogen concentration under the covering foil and accordingly to less pronounced effects leading to the strong CL degradation. Reducing the hydrogen concentration in the simulation from 0.8 to $0.2\,\%$ resulted in an increase of the maximum COR current density by about $20\,\%$, supporting this assumption. The two other effects, liquid water and pressure differences over the cell, were not accounted for in the model which could explain a further part of the discrepancy between model and experiment.

Oxygen crossover and reduction on the anode was considered in the model but its influence on carbon corrosion is not obvious. As known from considerations of start-stop mechanisms, local presence of oxygen on the anode pushes the electrode potential towards $1\,\mathrm{V_{SHE}}$ and can cause a significant local break-in of the electrolyte potential as long as the solid potential on the anode is held nearly constant by a high in-plane conductivity of the solid phase. In the present case significant potential gradients of the solid phase can emerge under the covering foil due to the low CL in-plane conductivity. Oxygen crossover from cathode to anode leads to an immediate reduction reaction at the low anode electrode potentials, consuming electrons and mitigating the potential gradient in the solid phase of the anode CL. But as the oxygen crossover flow to the anode does not reach significant values, the anode electrode potential remains low. Even for thinner membranes ($10\,\mu\mathrm{m}$), oxygen crossover is not a dominating effect and the anode electrode potential remains at low values.

Under normal operating conditions, the electrolytic membrane conductivity was at least one order of magnitude below the CL electron conductivity. The accordingly low in-plane proton currents are a prerequisite for the formation of the strong potential gradients in the electrolyte, which in turn enables the described degradation mechanism. Even with a $50\,\mu\mathrm{m}$ thick membrane, the in-plane proton currents are relatively low and cannot mitigate carbon corrosion effects.

In general the degradation of the cathode CL in a limited fraction in the outer perimeter of a cell is not crucial for the overall cell function. In the presented experiments, no membrane degradation or leaks were found. However, according to literature findings it is conceivable that under the OCV conditions on the cathode side, membrane deterioration could be accelerated [8, 236]. After degradation of the cathode CL in the outer cell perimeter, oxygen crossover to the anode could be increased as ORR ceases and oxygen concentration on the cathode is high. Thereby peroxide formation on the anode side, according to Equation 2.38, and a subsequent chemical membrane degradation by radicals could be enhanced [8, 62, 237, 238].

7.4 Conclusions

In this chapter it was shown that an unfavorable mechanical implementation of the CCM in its outer perimeter to the sealing structure can have a negative influence on a cell's lifetime. In particular a case was investigated where the CCM is partially exposed in its outer perimeter, without the coverage of GDLs. Mechanical load, induced by humidity cycling, was shown to lead to a failure after 8000 cycles by forming pinholes in the exposed CCM area, likely due to high mechanical point loads. Although the applied protocol was accelerated compared to regular cell operation, the relevance of an adequate mechanical membrane implementation is illustrated, especially for high lifetime requirements ($> 5000\,\mathrm{h}$). A possible method for a gentle integration of the CCM without the use of a costly SG is a seal-on-GDL concept, where sealing structure and GDL are integrally formed and the CCM is compressed homogeneously. Thereby the seal-on-GDL could also be integrated on the BPP by injection molding, as described in a patent application [239].

A further discussed degradation effect is initiated by the offset of the sealing components (gaskets or the single layers of a SG) on both sides of the CCM in the outer perimeter of the active area. Especially when the anode side of the CCM is partially covered with an isolating layer or foil while the cathode is well supplied with gas, appreciable cathode CL thinning could be observed experimentally from about $1 - 2\,\mathrm{mm}$ below the covering foil. This is also in good accordance with simulation results, where at $1\,\mathrm{mm}$ below the foil already half of the carbon corrosion rate as under OCV conditions was found. The reported literature values for relevant length scales of carbon corrosion are considerably higher [51, 54, 55]. The discrepancy arises from the specific characteristic of the discussed case of hydrogen starvation – the electrical separation of the anode CL from the GDL by an isolating layer[1]. The GDL does not contribute to the in-plane electron conductivity in the covered area. The accordingly formed strong solid potential gradients in the anode CL of up to $0.3\,\mathrm{V}$ pull down the electrolyte potential as the anode electrode potential remains close to $0\,\mathrm{V}_{\mathrm{SHE}}$. As the in-plane solid potential on the cathode side remains nearly constant, the cathode electrode potential almost reaches OCV, resulting in high local COR current densities.

Anode CL and membrane thickness were found to be unchanged in the experiment, so that the overall cell function was not affected. But the discussed literature findings suppose that an overlapping anode CL could initiate strong membrane degradation effects based on peroxide and radical formation. The described aging mechanism by hydrogen starvation can be easily avoided by a nominal offset between SG layers or gaskets, so that the active area on the anode side overlaps the cathode side, even under consideration of the manufacturing and assembling tolerances, as described in a patent application [119]. In addition, a homogeneous hydrogen supply can mitigate the problem as the absence of any CL thinning in the anode inlet region indicates.

---

[1] In the discussed cases of hydrogen starvation in the literature, the in-plane electron conductivities in the starved area are comparatively high, as the CL is electrically connected to the highly conductive GDL. The formation of strong in-plane solid potential gradients is impeded thereby.

Chapter 8

Conclusions

Sealing structures surround the cell plane of PEFCs and restrict the active cell area in its size. Sealants are located in the outer perimeter of the cell, whereby the design of this specific area is mainly determined by the type of the sealing solution and the according manufacturing method. Local conditions such as species distribution, temperature and the mechanical load on the components may differ significantly there from the regular flowfield area. As a result, degradation mechanisms there require a separate consideration. However, this *edge region* has gained little scientific attention with respect to its influence on cell functionality so far. This work aims to close this gap and to comprehensively correlate the design of the edge region to the local operating conditions, degradation mechanisms and to the resulting impact on cell functionality in order to enable the deduction of constructive and operational mitigation strategies.

Neutron radiography helped to extensively study the in-plane water distribution in five $50\,\mathrm{cm}^2$ test cells with different configurations of the edge region under a wide range of operating conditions. It was found that free volumes in the edge region of a cell tend to be flooded with liquid water as long as the area is not supplied with a direct gas feed. Time constants for water transport between flowfield and edge region can then lie in the range of hours, so that removal of the accumulated water can hardly be achieved, even by multiple gas purges. In turn, in cell designs with an edge region which is directly accessible for gas flows, a bypass stream around the flowfield can emerge, leading to a decreased stoichiometry in the flowfield area. It was found that due to the accordingly lower pressure drop, liquid water removal was significantly reduced and the flowfield water content almost doubled compared to a cell without a bypass. Analytical consideration revealed, that the bypass effect is more pronounced in cells with relatively long flowfield channels compared to the bypass channels, such as serpentine flowfields. Neutron images confirmed that as the outer cell perimeter was found to remain relatively dry compared to the flowfield with a water content below $4\,\%$ in all operating points.

Startup capability of PEFCs from freezing conditions is a prerequisite for many applications. Failure of a cold start is believed to go along with freezing of water in the cell and blockage of gas transport pathways. For the first time it could be proven in a $50\,\mathrm{cm}^2$ test cell for an isothermal startup at $-5\,^{\circ}\mathrm{C}$, that freezing can occur over a spatially limited fraction of the cell area while in the rest of the cell liquid water generation continues. The initial freezing event coincided with the start of cell voltage decrease, the final cell failure can be attributed to freezing over the entire cell area. At a moderate startup temperature of $-2.5\,^{\circ}\mathrm{C}$ liquid water droplets emerged into the flowfield. It could be verified by means of a novel dual spectrum neutron radiography method that droplets close to the gas outlets freeze coinciding with the beginning of cell voltage decrease, while the rest of the droplets freeze at the final cell failure. In general, the theory of supercooled water in PEFCs could be confirmed by the verification of liquid water drainage into the flowfield at a moderate cold start temperature of $-2.5\,^{\circ}\mathrm{C}$. Also at temperatures of -5 °C cold starts with about twice the mean value of generated charge could be performed, suggesting the absence of a freezing event and the presence of supercooled water.

Furthermore, it was investigated, how the residual water content in a cell prior to an isothermal cold start can affect cold start capability. The initial water content of the membrane was shown to reduce water uptake capability of the same during a cold start and hence shortens the initial cold start period, which is characterized by membrane humidification. Relevant amounts of liquid water can remain in the outer perimeter of a cell even after appropriate shutdown procedures. Supported by neutron radiography it was proven that residual water in flowfield, GDL or CL generally has a negative influence on cold start capability. Thereby no differentiation between water in the edge region and in the flowfield could be done, as both could not be varied independently. Furthermore it was proven unambiguously by dual spectrum neutron imaging, that residual liquid water in the outer perimeter freezes during cool down of a cell slightly below $0\,^{\circ}\mathrm{C}$.

Failure modes of PEFCs in their outer perimeter are described sporadically in the literature but were not examined comprehensively so far. Two specific degradation mechanisms, inherently coupled to the design of the edge region, were picked out here. In the outer perimeter of the cell, mechanical stress on the membrane was found to be fortified under unfavorable membrane implementation to the sealing structure under cyclic humidification conditions. A gap between GDLs and gaskets led to high local stresses in the membrane and pinhole formation was found from about 8000 dry/humid cycles. The results illustrate the importance of a full faced clamping of the membrane between GDLs and sealing structures without interruptions in order to mitigate stress peaks. This is in particular relevant for applications with high lifetime requirements where no sub-gaskets are employed.

As manufacturing and assembling processes of PEFCs are subject to geometrical tolerances, the components limiting the active area on both sides of a CCM – sealing structures or the single layers of a sub-gasket – can have a lateral offset to each other. It was shown that the case of a locally covered anode, while the cathode is accessible for gas, can lead to strong carbon corrosion of the cathode CL due to electrode potentials in the range of the cathode OCV of about $1\,\mathrm{V}$. The offset of the components was reproduced experimentally as well as by numerical simulation by introducing a thin, gas-impermeable foil in the outer perimeter between CL and GDL on the anode side. In contrast to the cases of hydrogen starvation known from other publications, significant carbon corrosion occurred already at about $1 - 2\,\mathrm{mm}$ from the edge of the starved area. It was intensified particularly by the formation of a high in-plane potential gradient in the solid CL phase of the anode, resulting from the low in-plane conductivity of the anode due to the isolating foil between CL and the highly conductive GDL. As the in-plane electron conductivity on the cathode remained high due to the full face contact between GDL and CL and as the electrolyte potential showed a strong decrease in the hydrogen starved area, high electrode potentials occurred on the cathode side. The effect can easily be avoided by intentionally oversizing the gas supplied area on the anode side over the cathode side [119]. The membrane was not observed to be damaged, so that the overall cell function was not affected. But other publications suggest that a locally missing cathode CL can enhance peroxide formation on the anode side [8, 62, 237, 238]. Also the OCV on the cathode side could generally lead to increased membrane degradation [124].

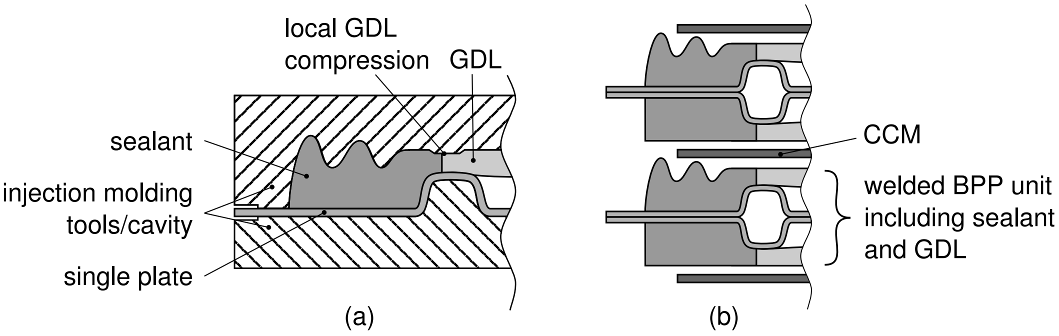

Figure 8.1: (a) Injection molding of a sealant on a single plate of a BPP whereby the GDL is integrally formed with the sealant. (b) Two single plates, each including sealant and GDL, joined to a BPP unit by laser welding, which can be assembled with CCMs to a stack in a subsequent assembly process.

With the results of this work, a novel sealing concept was developed in order to mitigate the described deterioration mechanisms and problems related to cell functionality. The core idea is to integrally form the sealing structure on the BPP in an injection molding process whereby the GDL is integrated simultaneously as schematically depicted in Figure 8.1. An enclosed cavity is required to form the sealing structure and the GDL has to be compressed locally in order to inhibit sealant penetration into the GDL. The GDL compression requires a BPP with a continuously formed edge land around the flowfield in order to mechanically support the GDL compression and to inhibit the intrusion of sealant into the flowfield. The welding process of two single plates including GDL and sealant to a BPP unit also requires the accessibility of relevant cell areas. These restrictions entail extensive modifications of the overall cell design. A possible cell concept is described in a patent application in detail [239]. The basic concept enables a favorable mechanical integration of the membrane as GDL and sealing structure are integrally formed. As the sealant is directly formed onto the edge land of the flowfield, no edge channel is formed and unfavorable water accumulation or flowfield bypasses and the subsequent disadvantages for cell functionality can be avoided. Furthermore, the concept enables the reduction of the required manufacturing and assembling process steps and reduces assembling tolerances.

Appendix A

Simulation Parameters

Table A.1: Basic parameters used for the numeric simulation in Section 7.2.

component	parameter	symbol	value/expression	unit	Ref.
			geometry		
membrane	thickness	t_{mem}	16	µm	own meas.
CL	thickness anode	$t_{\mathrm{cl,an}}$	8	µm	own meas.
CL	thickness cathode	$t_{\mathrm{cl,ca}}$	12	µm	own meas.
GDL	thickness	t_{gdl}	200	µm	own meas.
BPP	geometry taken for graphitic FF, described in Section 4.1.1				
			charge transport		
BPP	electrical conductivity	σ_{bpp}	50 000	$\mathrm{S\,m^{-1}}$	assumed
GDL	electrical conductivity in-plane	$\sigma_{\mathrm{gdl,ip}}$	5434.78	$\mathrm{S\,m^{-1}}$	[241]
	electrical conductivity through-plane	$\sigma_{\mathrm{gdl,tp}}$	250	$\mathrm{S\,m^{-1}}$	[241]
	contact resistance GDL-CL/GDL-BPP	$r_{\mathrm{gdl,cont}}$	$3.37^{\otimes}$	$\mathrm{m\Omega\,cm^2}$	[240]
CL	electrical conductivity	$\sigma_{\mathrm{cl,sol}}$	$60^{\diamondsuit}$	$\mathrm{S\,m^{-1}}$	[234]
	electrolytic conductivity	$\sigma_{\mathrm{cl,ely}}$	$7.5^{\diamondsuit}$	$\mathrm{S\,m^{-1}}$	[234]

component	parameter	symbol	value/expression	unit	Ref.
Gas transport (Stefan-Maxwell-Diffusion and Darcy's Law)					
GDL	tortuosity	τ_{gdl}	4.91	-	[240]
	porosity	ϵ_{gdl}	$0.41^{\star}$	-	[240]
	permeability	κ_{gdl}	$6.25 \cdot 10^{-13}$	m^2	[240]
CL	porosity	ϵ_{cl}	0.5	-	assumption as GDL
	permeability	κ_{cl}	$6.25 \cdot 10^{-13}$	m^2	
CL/GDL	binary diffusion coefficient H_2O-N_2	$D_{\mathrm{H_2O-N_2}}$	$1.87 \cdot 10^{-10} \cdot T^{2.072} \frac{p^{\ominus}}{p}$	$\mathrm{m}^2\,\mathrm{s}^{-1}$	[242]
	binary diffusion coefficient H_2O-O_2	$D_{\mathrm{H_2O-O_2}}$	$1.89 \cdot 10^{-10} \cdot T^{2.072} \frac{p^{\ominus}}{p}$	$\mathrm{m}^2\,\mathrm{s}^{-1}$	[242]
	binary diffusion coefficient H_2O-H_2	$D_{\mathrm{H_2O-H_2}}$	$1.063 \cdot 10^{-4}$	$\mathrm{m}^2\,\mathrm{s}^{-1}$	[243]
	binary diffusion coefficient H_2-N_2	$D_{\mathrm{H_2-N_2}}$	$\frac{1.539 \cdot 10^{-6} \cdot T^{1.548}}{\left(ln\left(\frac{T \cdot 10^7}{3.16}\right)\right)^2 \exp\left(\frac{-2.8}{T}\right) \exp\left(\frac{1067}{T^2}\right)} \cdot \frac{p^{\ominus}}{p}$	$\mathrm{m}^2\,\mathrm{s}^{-1}$	[242]
	binary diffusion coefficient H_2-O_2	$D_{\mathrm{H_2-O_2}}$	$4.17 \cdot 10^{-9} \cdot T^{1.732} \frac{p^{\ominus}}{p}$	$\mathrm{m}^2\,\mathrm{s}^{-1}$	[242]
	binary diffusion coefficient O_2-N_2	$D_{\mathrm{O_2-N_2}}$	$1.13 \cdot 10^{-9} \cdot T^{1.724} \frac{p^{\ominus}}{p}$	$\mathrm{m}^2\,\mathrm{s}^{-1}$	[242]
	molar mass hydrogen	$M_{\mathrm{H_2}}$	$0.002\,016$	$\mathrm{kg}\,\mathrm{mol}^{-1}$	[244]
	molar mass oxygen	$M_{\mathrm{O_2}}$	$0.031\,999$	$\mathrm{kg}\,\mathrm{mol}^{-1}$	[244]
	molar mass nitrogen	$M_{\mathrm{N_2}}$	$0.028\,013$	$\mathrm{kg}\,\mathrm{mol}^{-1}$	[244]
	molar mass water	$M_{\mathrm{H_2O}}$	$0.018\,015$	$\mathrm{kg}\,\mathrm{mol}^{-1}$	[244]
	dynamic fluid viscosity (anode)	$\eta_{\mathrm{f,an}}$	$8.81 \cdot 10^{-6}$	$\mathrm{Pa\,s}$	[52]
	dynamic fluid viscosity (cathode)	$\eta_{\mathrm{f,ca}}$	$1.95 \cdot 10^{-5}$	$\mathrm{Pa\,s}$	[52]

component	parameter	symbol	value/expression	unit	Ref.
			membrane model		
	density (dry)	ρ_{mem}	$2050^{\dagger}$	$\mathrm{kg\,m^{-3}}$	[245]
	equivalent weight	EW	$1.098^{\dagger}$	$\mathrm{kg\,mol^{-1}}$	[245]
	electroosmotic drag coefficient	K_{drag}	1	-	assumed
	self-diffusion constant	$d_{\mathrm{H_2O}}^{\mathrm{mem}}$	$2.1 \cdot 10^{-7}$	$\mathrm{m^2\,s^{-1}}$	[228]
			reaction kinetics		
HOR	equilibrium electrode potential	$\Delta\varphi_{\mathrm{HOR}}^{0}$	0	V	Section 2.2
	transfer coefficient	α_{HOR}	1	-	[53]
	exchange current density	$i_{0,\mathrm{HOR}}$	3500	$\mathrm{A\,m^{-2}}$	fitted
	transferred electrons per H_2	z_{HOR}	2	-	Equation 2.3
	reference hydrogen concentration	$c_{\mathrm{H_2}}^{\mathrm{ref}}$	44.032	$\mathrm{mol\,m^{-3}}$	calc.
ORR	equilibrium electrode potential (65 °C)	$\Delta\varphi_{\mathrm{ORR}}^{0}$	1.175	V	Section 2.2
	transfer coefficient	α_{ORR}	0.8	-	fitted
	exchange current density	$i_{0,\mathrm{ORR}}$	3.5	$\mathrm{A\,m^{-2}}$	fitted
	transferred electrons per O_2	z_{ORR}	4	-	Equation 2.4
	reference oxygen concentration	$c_{\mathrm{O_2}}^{\mathrm{ref}}$	44.032	$\mathrm{mol\,m^{-3}}$	calc.
	reference water concentration	$c_{\mathrm{H_2O}}^{\mathrm{ref}}$	44.032	$\mathrm{mol\,m^{-3}}$	calc.
COR	equilibrium electrode potential	$\Delta\varphi_{\mathrm{COR}}^{0}$	0.207	V	[229]
	transfer coefficient	α_{COR}	0.3	-	[229]
	exchange current density	$i_{0,\mathrm{COR}}$	10^{-5}	$\mathrm{A\,m^{-2}}$	[229]
	transferred electrons per C	z_{COR}	4	-	Equation 7.26
	reference water concentration	$c_{\mathrm{H_2O}}^{\mathrm{ref}}$	44.032	$\mathrm{mol\,m^{-3}}$	calc.

[⊗] Contact resistance was taken for a Freudenberg H23C6 GDL from [240] as only the MPL differs from the employed type H23C8.

[◇] Conductivity values for the CL were taken for $\epsilon_{\mathrm{cl}} = 0.5$ from [234].

[⋆] Porosity in the compressed state, calculated from the value in [240] for the uncompressed GDL (thickness 230 µm) by $\epsilon_{\mathrm{gdl}} = 0.47 \cdot 200/230$.

[†] Values for Nafion 117 H.

List of Abbreviations and Symbols

Latin Symbols

Units are converted according to suitability in this work.

symbol	description	unit
A	area	m^2
a	chemical activity	-
b	load point	-
c	concentration	$\mathrm{mol\,m^{-3}}$
d	depth	m
d_H	hydraulic diameter	m
D	aperture diameter (neutron radiography)	mm
$d^\mathrm{mem}_{\mathrm{H_2O}}$	membrane water self-diffusion constant	$\mathrm{m^2\,s^{-1}}$
$D^\mathrm{mem}_{\mathrm{H_2O}}$	membrane water self-diffusion coefficient	$\mathrm{m^2\,s^{-1}}$
$D_{i,j}$	binary diffusion coefficient of species i and j	$\mathrm{m^2\,s^{-1}}$
ECA	electrochemically active area	$\mathrm{cm^2_{Pt}\,mg^{-1}_{Pt}}$
EW	equivalent weight, membrane mass per mole of sulfonic acid	$\mathrm{kg\,mol^{-1}}$
f	water volume fraction in the membrane	-
Δg_f	molar Gibbs free energy of formation	$\mathrm{kJ\,mol^{-1}}$
Δh_f	molar enthalpy of formation	$\mathrm{kJ\,mol^{-1}}$
i	current density	$\mathrm{A\,m^{-2}}$
I	current	A
i_0	exchange current density	$\mathrm{A\,m^{-2}}$
I_0	intensity of the incident neutron beam from the neutron source	
i_model	current density as boundary condition for numerical model	$\mathrm{A\,m^{-2}}$
I_n	neutron beam intensity behind a sample/measured beam intensity	
k	reaction rate (Arrhenius Equation)	$\mathrm{mol\,s^{-1}\,m^{-2}}$
K	empiric rate constant (Arrhenius Equation)	$\mathrm{m\,s^{-1}}$
k_dp	two phase pressure drop multiplier	-
K_drag	electroosmotic drag coefficient	-
l	length	m
L	distance of sample from aperture (neutron radiography)	mm
L_S	distance between sample and scintillator (neutron radiography)	mm
m	mass	kg
M	molar mass	$\mathrm{kg\,mol^{-1}}$
$\dot{m}_\mathrm{C}$	area specific carbon mass loss rate of catalyst layer	$\mathrm{mg\,h^{-1}\,cm^{-2}}$

symbol	description	unit
Δm_C	area specific accumulated carbon mass loss of catalyst layer	$\mathrm{mg\,cm^{-2}}$
m_Pt	absolute mass of catalyst platinum loading	g
n	number of elements/components	-
$\dot{n}$	specific molar flow	$\mathrm{mol\,s^{-1}\,m^{-2}}$
$\dot{n}_\mathrm{ch}$	molar flow in flowfield channels	$\mathrm{mol\,s^{-1}}$
$n_\mathrm{H_2O}$	amount of substance of water	mol
$n_\mathrm{SO_3^-}$	amount of substance of sulfonic acid	mol
N	atomic density/number density	$\mathrm{m^{-3}}$
p	pressure	bar
Δp	pressure drop	bar
q	accumulated charge current density	$\mathrm{C\,cm^{-2}}$
q_acc	accumulated charge current density from begin of stable cell operation until cell failure	$\mathrm{C\,cm^{-2}}$
q_CS	accumulated charge current density during an entire cold start	$\mathrm{C\,cm^{-2}}$
q_failure	accumulated charge current density between end of a stable voltage plateau until cell failure	$\mathrm{C\,cm^{-2}}$
q_H	transferred charge during hydrogen adsorption/desorption in cyclovoltammetry	$\mathrm{C\,cm^{-2}}$
q_stable	accumulated charge current density during stable cell operation of a cold start	$\mathrm{C\,cm^{-2}}$
q_uptake	accumulated charge current density during membrane water uptake of a cold start	$\mathrm{C\,cm^{-2}}$
r	effective resolution (neutron imaging)	$\mathrm{\mu m}$
R	electrical resistance	Ω
$r_\mathrm{ch,g}$	radius on the flowfield ground	mm
$r_\mathrm{ch,t}$	radius on the flowfield top	mm
$r_\mathrm{gdl,cont}$	specific contact resistance GDL-CL and GDL-BPP	$\mathrm{m\Omega\,cm^2}$
Re	Reynolds number	-
RH	relative humidity	-
s	species variable	-
S	species mass source/sink	$\mathrm{kg\,m^{-2}\,s^{-1}}$
Δs_f	molar entropy of formation	$\mathrm{kJ\,mol^{-1}}$
t	time	s
t_mem	membrane thickness	$\mathrm{\mu m}$
T	temperature	K
u	velocity	$\mathrm{m\,s^{-1}}$
$V_\mathrm{H_2O}$	molar volume of water	$\mathrm{m^3\,mol^{-1}}$
V_ion	molar volume of ionomer	$\mathrm{m^3\,mol^{-1}}$
$\dot{V}$	volume flow	slpm
w	width	m
w_act	width of electrochemically active area per channel	m
x	cartesian coordinate	m
x_bp	molar gas flow fraction through a cell bypass	-

symbol	description	unit
y	cartesian coordinate	m
z	valency/number of elementary charges	-

Greek Symbols

Units are converted according to suitability in this work.

symbol	description	unit
α	transfer coefficient	-
β	regression coefficient /slope of linear regression function	-
γ_{ff}	channel wall slope of a flowfield	deg
γ_{CV}	cyclovoltammetry sweep rate	$\mathrm{mV\,s^{-1}}$
Γ_{Pt}	area specific number of reaction sites of platinum	$\mathrm{\mu C\,cm_{Pt}^{-2}}$
δ	component thickness in parallel direction to the neutron beam	mm
Δ	optical density (neutron radiography)	-
$\Delta\delta$	change of component thickness relative to a reference state	mm
ε	porosity	-
ζ	pressure loss coefficient	-
η	electrode overpotential	V
η_{f}	dynamic fluid viscosity	$\mathrm{Pa\,s}$
Θ	volumetric filling grade/volume fraction	-
$\overline{\Theta}$	averaged volumetric filling grade/volume fraction	-
ι	coefficient for channel geometry (pressure drop calculation)	-
κ	permeability of porous structures	$\mathrm{m^2}$
λ	gas stoichiometry	-
λ_{mem}	membrane water content	-
λ_{n}	neutron wavelength	$\mathrm{\mathring{A}}$
Λ_{H}	geometrical area of hydrogen adsorption/desorption in cyclovoltammogram	$\mathrm{mV\,A\,cm^{-2}}$
μ^*	electrochemical potential	$\mathrm{kJ\,mol^{-1}}$
μ	chemical potential	$\mathrm{kJ\,mol^{-1}}$
ρ	density	$\mathrm{kg\,m^{-3}}$
σ	electrical/electrolytic conductivity	$\mathrm{S\,m^{-1}}$
σ_{n}	microscopic neutron cross section	$\mathrm{m^2}$
σ_{rel}	relative attenuation, relation between microscopic cross section with and without a filter introduced into the neutron beam (dual spectrum neutron radiography)	-

symbol	description	unit
Σ	macroscopic neutron cross section/attenuation coefficient (for water $\Sigma_{\mathrm{H_2O}} = 0.45\,\mathrm{mm}^{-1}$)	mm^{-1}
τ	tortuosity	-
υ	reaction stoichiometry factor	-
υ_{sorp}	rate for water sorption/desorption	$\mathrm{m}^3\,\mathrm{m}^{-2}\,\mathrm{s}^{-1}$
ϕ	volume fraction	-
φ	electrical/electrolytic potential	V
$\Delta\varphi$	cell/electrode potential	V
$\Delta\varphi_{\mathrm{iR-free}}$	cell voltage without ohmic resistances	V
χ	molar fraction	-
ψ	diffusion coefficient, membrane gas crossover	$\mathrm{mol}\,\mathrm{m}^{-1}\,\mathrm{s}^{-1}\,\mathrm{Pa}^{-1}$
Ψ	relative area fraction of the cell area	-
ω	mass fraction	-
Ω_{cl}	surface area of the catalyst layer per geometrical cell area	-

Subscripts

subscript	description
act	activation
ad	adsorbed
an	anode/anodic
b	load point
bpp	bipolar plate
c	component
C	carbon
ca	cathode/cathodic
cell	related to the cell consisting of anode and cathode
ch	channel
cl	catalyst layer
coolant	liquid cell coolant
COR	carbon oxidation reaction
COR,CO_2	carbon oxidation reaction to CO_2
COR,CO	carbon oxidation reaction to CO
cs	cold start
diff	diffusive
e^-	electron
ec	edge channel
ely	electrolyte/electrolytic/electrolytical conducting phase
eo	electroosmotic drag
ESF	edge spread function
ff	flowfield

subscript	description
filter	with a filter introduced into the neutron beam
FWHM	full width at half maximum
gdl	gas diffusion layer
H_2	hydrogen
H_2O	water
H_2O_2	hydrogen peroxide
H_3O^+	oxonium
HER	hydrogen evolution reaction
HOR	hydrogen oxidation reaction
i	species variable
in	inlet
ip	in-plane
j	species variable
l	flowfield land/rib
max	maximum
mem	membrane
min	minimum
N_2	nitrogen
nofilter	without a filter introduced into the neutron beam
O_2	oxygen
OER	oxidation evolution reaction
ORR	oxidation reduction reaction
ox	oxidized/oxidation/oxidant
pitch	periodicity of parallel flowfield channels or of the bipolar plates of a stack
react	reactant
rec	recirculation
red	reduced/reduction/reducing agent
ref	reference
seg	segment
sol	solid phase/electron conducting phase
sorp	sorption
stoich	stoichiometric
th	theoretical
tp	through-plane
trans	species transport
xo	membrane crossover
Ω	ohmic resistance/loss

Superscripts

superscript	description
0	electrochemical equilibrium
an	anode
ca	cathode
eff	effective
gas	gas phase
k	component variable
mem	membrane
OCV	open circuit voltage
ref	under reference conditions
$\ominus$	standard conditions $T^{\ominus} = 298.15\,\mathrm{K}$ and $p^{\ominus} = 101\,325\,\mathrm{Pa}$
‡	activated state

Constants

symbol	description	value	unit	Ref.
e	elementary charge	$1.602\,176 \cdot 10^{-19}$	C	[246]
F	Faraday constant	$96\,485.39$	$\mathrm{C\,mol^{-1}}$	[246]
$\Re$	molar gas constant	$8.314\,471$	$\mathrm{J\,mol^{-1}\,K^{-1}}$	[246]
$T^{\ominus}$	standard temperature	298.15	K	
$p^{\ominus}$	standard pressure	$101\,325$	Pa	

Acronyms

acronym	description
ATP	adenosine triphosphate
BPP	bipolar plate
CCM	catalyst coated membrane
CIP	cured-in-place
CL	catalyst layer
CMOS	complementary metal-oxide-semiconductor/active pixel sensor
COR	carbon oxidation reaction
CV	cyclovoltammetry
EPDM	ethylene propylene diene monomer rubber
ESF	edge spread function
FF	flowfield
FOV	field of view

acronym	description
FWHM	full width at half maximum
GDL	gas diffusion layer
HER	hydrogen evolution reaction
HFR	high frequency resistance
HOR	hydrogen oxidation reaction
ICON	Imaging with COld Neutrons, neutron beamline at SINQ
IM	injection molding
IR	infrared
LSF	line spread function
LSR	liquid silicone rubber
LSV	linear sweep voltammetry
MPL	micro porous layer
NR	neutron radiography
OCV	open circuit voltage
OER	oxygen evolution reaction
ORR	oxygen reduction reaction
PEFC	polymer electrolyte fuel cell
PEN	polyethylene naphthalate
PET	polyethylene terephthalate
PFSA	perfluorinated sulfonic acid
PTFE	polytetrafluoroethylene
RH	relative humidity
SEM	scanning electron microscope
SG	sub-gasket
SHE	standard hydrogen electrode
SINQ	Swiss Spallation Neutron Source at Paul Scherrer Institute, Switzerland
TISAB	total ionic strength adjustment buffer
UV	ultra-violet

Bibliography

[1] P. Atkins and J. de Paula, *Physical Chemistry*, 8th ed., W. H. Freeman and Company, New York, 2006

[2] J. W. Rohen and E. Lütjen-Drecoll, *Funktionelle Histologie: kurzgefaßtes Lehrbuch der Zytologie, Histologie und mikroskopischen Anatomie des Menschen nach funktionellen Gesichtspunkten*, vol. 4, Schattauer Verlag, 2000

[3] B. Moosmann and C. Behl, *Mitochondrially encoded cysteine predicts animal lifespan*, Aging Cell 7 (1), 2008, 32–46

[4] C. H. Hamann and W. Vielstich, *Elektrochemie*, 4th ed., Wiley-VCH, 2005

[5] T. J. Peckham, Y. Yang and S. Holdcroft, *Proton Exchange Membranes*, in: D. P. Wilkinson, J. Zhang, R. Hui, J. Fergus and X. Li, eds., Proton Exchange Membrane Fuel Cells, Materials Properties and Performance, Taylor and Francis Group, LLC, 2010, chap. 3, 107–189

[6] K.-D. Kreuer, S. J. Paddison, E. Spohr and M. Schuster, *Transport in Proton Conductors for Fuel-Cell Applications: Simulations, Elementary Reactions, and Phenomenology*, Chemical Reviews 104 (10), 2004, 4637–4678

[7] Y. Yang, A. Siu, T. J. Peckham and S. Holdcroft, *Structural and Morphological Features of Acid-Bearing Polymers for PEM Fuel Cells*, in: G. G. Scherer, ed., Advances in Polymer Science, Fuel Cells I, Springer-Verlag Berlin Heidelberg, 2008, 55–126

[8] M. Inaba, *Chemical Degradation of Perfluorinated Sulfonic Acid Membranes*, in: F. N. Büchi, M. Inaba and T. J. Schmidt, eds., Polymer Electrolyte Fuel Cell Durability, Springer Science+Business Media, 2009, chap. 3, 57–69

[9] M. Odgaard, *The use of Nafion® as electrolyte in fuel cells*, in: T. Nakajima, ed., *Fluorinated Materials for Energy Conversion*, 1st ed., Tsuyoshi Nakajima and Henri Groult, 2005, chap. 20, 439–468

[10] M. Eikerling, A. A. Kornyshev and E. Spohr, *Proton-Conducting Polymer Electrolyte Membranes: Water and Structure in Charge*, in: G. G. Scherer, ed., Advances in Polymer Science, Fuel Cells I, Springer-Verlag Berlin Heidelberg, 2008, 15–54

[11] E. M. Lee, R. K. Thomas, A. N. Burgess, D. J. Barnes, A. K. Soper and A. R. Rennie, *Local and long-range structure of water in a perfluorinated ionomer membrane*, Macromolecules 25 (12), 1992, 3106–3109

[12] T. D. Gierke, G. E. Munn and F. C. Wilson, *The Morphology in Nafion Perfluorinated Membrane Products, as Determined by Wide- and Small-Angle X-Ray Studies*, Journal of Polymer Science: Polymer Physics Edition 19 (11), 1981, 1687–1704

[13] E. J. Roche, M. Pineri, R. Duplessix and A. M. Levelut, *Small-Angle Scattering Studies of Nafion Membranes*, Journal of Polymer Science: Polymer Physics Edition 19 (1), 1981, 1–11

[14] L. M. Onishi, J. M. Prausnitz and J. Newman, *Water-Nafion Equilibria. Absence of Schroeder's Paradox*, The Journal of Physical Chemistry B 111 (34), 2007, 10166–10173

[15] R. O'Hayre, S.-W. Cha, W. Colella and F. B. Prinz, *Fuel Cell Fundamentals*, 2nd ed., Wiley, 2009

[16] S. U. M. Khan, R. C. Kainthla and J. O. M. Bockris, *The redox potential and the Fermi level in solution*, The Journal of Physical Chemistry 91 (23), 1987, 5974–5977

[17] G. Job and F. Herrmann, *Chemical potential—a quantity in search of recognition*, European Journal of Physics 27 (2), 2006, 353–371

[18] H. Lohninger, *Standard Enthalpies, Free Energies of Formation, Standard Entropies*, access date: 15.01.2016, 2015, URL: `http://www.vias.org/genchem/standard_enthalpies_table.html`

[19] J. X. Wang, T. E. Springer, P. Liu, M. Shao and R. R. Adzic, *Hydrogen Oxidation Reaction on Pt in Acidic Media: Adsorption Isotherm and Activation Free Energies*, Journal of Physical Chemistry C 111 (33), 2007, 12425–12433

[20] T. Erdey-Gruz and M. Volmer, *Zur Theorie der Wasserstoffüberspannung*, Zeitschrift für physikalische Chemie 150, 1930, 203–213

[21] K. Elbert, J. Hu, Z. Ma, Y. Zhang, G. Chen, W. An, P. Liu, H. S. Isaacs, R. R. Adzic and J. X. Wang, *Elucidating Hydrogen Oxidation/Evolution Kinetics in Base and Acid by Enhanced Activities at the Optimized Pt Shell Thickness on the Ru Core*, ACS Catalysis, 2015, 6764–6772

[22] J. R. Murdoch, *What is the rate-limiting step of a multistep reaction?*, Journal of Chemical Education 58 (1), 1981, 32–36

[23] A. D. McNaught and A. Wilkinson, eds., *Compendium of chemical terminology : IUPAC recommendations*, 2nd ed., IUPAC Chemical Data, Oxford England Malden, MA, USA: Blackwell Science, 1997

[24] S. Park, J.-W. Lee and B. N. Popov, *A review of gas diffusion layer in PEM fuel cells: Materials and designs*, International Journal of Hydrogen Energy 37 (7), 2012, 5850–5865

[25] Y. Aoyama, K. Suzuki, Y. Tabe and T. Chikahisa, *Observation of water transport in the micro-porous layer of a polymer electrolyte fuel cell with a freezing method and cryo-scanning electron microscope*, Electrochemistry Communications 41, 2014, 72–75

[26] P. Oberholzer, P. Boillat, R. Siegrist, A. Kästner, E. H. Lehmann, G. G. Scherer and A. Wokaun, *Simultaneous neutron imaging of six operating PEFCs: Experimental set-up and study of the MPL effect*, Electrochemistry Communications 20, 2012, 67–70

[27] S. Karimi, N. Fraser, B. Roberts and F. R. Foulkes, *A Review of Metallic Bipolar Plates for Proton Exchange Membrane Fuel Cells: Materials and Fabrication Methods*, Advances in Materials Science and Engineering 2012, 2012, 1–22

[28] H. Wang and J. A. Turner, *Reviewing Metallic PEMFC Bipolar Plates*, Fuel Cells 10 (4), 2010, 510–519

[29] X. Ren and S. Gottesfeld, *Electro-osmotic Drag of Water in Poly(perfluorosulfonic acid) Membranes*, Journal of The Electrochemical Society 148 (1), 2001, A87–A93

[30] Z. Luo, Z. Chang, Y. Zhang, Z. Liu and J. Li, *Electro-osmotic drag coefficient and proton conductivity in Nafion® membrane for PEMFC*, International Journal of Hydrogen Energy 35 (7), 2010, 3120–3124

[31] M. Ise, K. D. Kreuer and J. Maier, *Electroosmotic drag in polymer electrolyte membranes: an electrophoretic NMR study*, Solid State Ionics 125 (1-4), 1999, 213–223

[32] T. A. Zawodzinski, J. Davey, J. Valerio and S. Gottesfeld, *The water content dependence of electro-osmotic drag in proton-conducting polymer electrolytes*, Electrochimica Acta 40 (3), 1995, 297–302

[33] R. K. Ahluwalia and X. Wang, *Buildup of nitrogen in direct hydrogen polymer-electrolyte fuel cell stacks*, Journal of Power Sources 171 (1), 2007, 63–71

[34] S. S. Kocha, J. Deliang Yang and J. S. Yi, *Characterization of gas crossover and its implications in PEM fuel cells*, AIChE Journal 52 (5), 2006, 1916–1925

[35] A. Z. Weber and J. Newman, *Transport in Polymer-Electrolyte Membranes*, Journal of The Electrochemical Society 151 (2), 2004, A311–A325

[36] E. Truckenbrodt, *Fluidmechanik*, 4th ed., Springer Science + Business Media, 2008

[37] J. Eller, *X-Ray Tomographic Microscopy of Polymer Electrolyte Fuel Cells*, PhD thesis, ETH Zürich, 2013

[38] J. Kim, J. Je, T. Kim, M. Kaviany, S. Y. Son and M. Kim, *Breakthrough/drainage pressures and X-ray water visualization in gas diffusion layer of PEMFC*, Current Applied Physics 12 (1), 2012, 105–108

[39] H. Markötter, K. Dittmann, J. Haußmann, R. Alink, D. Gerteisen, H. Riesemeier, J. Scholta, J. Banhart and I. Manke, *Influence of local carbon fibre orientation on the water transport in the gas diffusion layer of polymer electrolyte membrane fuel cells*, Electrochemistry Communications 51, 2015, 133–136

[40] S. Litster, D. Sinton and N. Djilali, *Ex situ visualization of liquid water transport in PEM fuel cell gas diffusion layers*, Journal of Power Sources 154 (1), 2006, 95–105

[41] A. Forner-Cuenca, V. Manzi-Orezzoli, J. Biesdorf, M. E. Kazzi, D. Streich, L. Gubler, T. J. Schmidt and P. Boillat, *Advanced Water Management in PEFCs: Diffusion Layers with Patterned Wettability*, Journal of The Electrochemical Society 163 (8), 2016, F788–F801

[42] D. Gerteisen and C. Sadeler, *Stability and performance improvement of a polymer electrolyte membrane fuel cell stack by laser perforation of gas diffusion layers*, Journal of Power Sources 195 (16), 2010, 5252–5257

[43] D. Gerteisen, N. Zamel, C. Sadeler, F. Geiger, V. Ludwig and C. Hebling, *Effect of operating conditions on current density distribution and high frequency resistance in a segmented PEM fuel cell*, International Journal of Hydrogen Energy 37 (9), 2012, 7736–7744

[44] O. E. Herrera, D. P. Wilkinson and W. Mérida, *Anode and cathode overpotentials and temperature profiles in a PEMFC*, Journal of Power Sources 198, 2012, 132–142

[45] A. Siu, J. Schmeisser and S. Holdcroft, *Effect of Water on the Low Temperature Conductivity of Polymer Electrolytes*, The Journal of Physical Chemistry 110 (12), 2006, 6072–6080

[46] E. L. Thompson, T. W. Capehart, T. J. Fuller and J. Jorne, *Investigation of Low-Temperature Proton Transport in Nafion Using Direct Current Conductivity and Differential Scanning Calorimetry*, Journal of The Electrochemical Society 153 (12), 2006, A2351–A2362

[47] K. Sasaki, M. Shao and R. Adzic, *Dissolution and Stabilization of Platinum in Oxygen Cathodes*, in: F. N. Büchi, M. Inaba and T. J. Schmidt, eds., Polymer Electrolyte Fuel Cell Durability, Springer Science + Business Media, 2009, chap. 1, 7–27

[48] R. Borup, J. Meyers, B. Pivovar, Y. S. Kim, R. Mukundan, N. Garland, D. Myers, M. Wilson, F. Garzon, D. Wood, et al., *Scientific Aspects of Polymer Electrolyte Fuel Cell Durability and Degradation*, Chemical Reviews 107 (10), 2007, 3904–3951

[49] S. Maass, F. Finsterwalder, G. Frank, R. Hartmann and C. Merten, *Carbon support oxidation in PEM fuel cell cathodes*, Journal of Power Sources 176 (2), 2008, 444–451

[50] L. M. Roen, C. H. Paik and T. D. Jarvi, *Electrocatalytic Corrosion of Carbon Support in PEMFC Cathodes*, Electrochemical and Solid-State Letters 7 (1), 2004, A19–A22

[51] X.-G. Yang, Q. Ye and P. Cheng, *In-plane transport effects on hydrogen depletion and carbon corrosion induced by anode flooding in proton exchange membrane fuel cells*, International Journal of Heat and Mass Transfer 55 (17-18), 2012, 4754–4765

[52] J. H. Ohs, U. Sauter, S. Maass and D. Stolten, *Modeling hydrogen starvation conditions in proton-exchange membrane fuel cells*, Journal of Power Sources 196 (1), 2011, 255–263

[53] C. A. Reiser, L. Bregoli, T. W. Patterson, J. S. Yi, J. D. Yang, M. L. Perry and T. D. Jarvi, *A Reverse-Current Decay Mechanism for Fuel Cells*, Electrochemical and Solid-State Letters 8 (6), 2005, A273–A276

[54] J. Chen, J. B. Siegel, T. Matsuura and A. G. Stefanopoulou, *Carbon Corrosion in PEM Fuel Cell Dead-Ended Anode Operations*, Journal of The Electrochemical Society 158 (9), 2011, B1164–B1174

[55] T. W. Patterson and R. M. Darling, *Damage to the Cathode Catalyst of a PEM Fuel Cell Caused by Localized Fuel Starvation*, Electrochemical and Solid-State Letters 9 (4), 2006, A183–A185

[56] W. R. Baumgartner, P. Parz, S. D. Fraser, E. Wallnöfer and V. Hacker, *Polarization study of a PEMFC with four reference electrodes at hydrogen starvation conditions*, Journal of Power Sources 182 (2), 2008, 413–421

[57] H. Tang, Z. Qi, M. Ramani and J. F. Elter, *PEM fuel cell cathode carbon corrosion due to the formation of air/fuel boundary at the anode*, Journal of Power Sources 158 (2), 2006, 1306–1312

[58] X. Huang, R. Solasi, Y. Zou, M. Feshler, K. Reifsnider, D. Condit, S. Burlatsky and T. Madden, *Mechanical endurance of polymer electrolyte membrane and PEM fuel cell durability*, Journal of Polymer Science Part B: Polymer Physics 44 (16), 2006, 2346–2357

[59] B. Wu, M. Zhao, W. Shi, W. Liu, J. Liu, D. Xing, Y. Yao, Z. Hou, P. Ming, J. Gu, et al., *The degradation study of Nafion/PTFE composite membrane in PEM fuel cell under accelerated stress tests*, International Journal of Hydrogen Energy 39 (26), 2014, 14381–14390

[60] A. Laconti, H. Liu, C. Mittelsteadt and R. McDonald, *Polymer Electrolyte Membrane Degradation Mechanisms in Fuel Cells - Findings Over the Past 30 Years and Comparison with Electrolyzers*, ECS Transactions 1 (8), 2006, 199–219

[61] T. T. Aindow and J. O'Neill, *Use of mechanical tests to predict durability of polymer fuel cell membranes under humidity cycling*, Journal of Power Sources 196 (8), 2011, 3851–3854

[62] V. O. Mittal, H. R. Kunz and J. M. Fenton, *Is H_2O_2 Involved in the Membrane Degradation Mechanism in PEMFC?*, Electrochemical and Solid-State Letters 9 (6), 2006, A299–A302

[63] V. A. Sethuraman, J. W. Weidner, A. T. Haug, S. Motupally and L. V. Protsailo, *Hydrogen Peroxide Formation Rates in a PEMFC Anode and Cathode*, Journal of The Electrochemical Society 155 (1), 2008, B50–B57

[64] B. Vogel, *Zersetzungsmechanismen von Polymerelektrolytmembranen für Brennstoffzellenanwendungen*, PhD thesis, Universität Stuttgart, 2010

[65] J. P. Meyers and R. M. Darling, *Model of Carbon Corrosion in PEM Fuel Cells*, Journal of The Electrochemical Society 153 (8), 2006, A1432–A1442

[66] J. Zhang, R. N. Carter, P. T. Yu, W. Gu, F. T. Wagner and H. A. Gasteiger, *Fuel Cells - Proton-Exchange Membrane Fuel Cells – Catalysts: Life-Limiting Considerations*, Encyclopedia of Electrochemical Power Sources, 2009, 626–638

[67] P. T. Yu, Z. Liu and R. Makharia, *Investigation of Carbon Corrosion Behavior and Kinetics in Proton Exchange Membrane Fuel Cell Cathode Electrodes*, Journal of The Electrochemical Society 160 (6), 2013, F645–F650

[68] V. A. Sethuraman, J. W. Weidner, A. T. Haug, M. Pemberton and L. V. Protsailo, *Importance of catalyst stability vis-à-vis hydrogen peroxide formation rates in PEM fuel cell electrodes*, Electrochimica Acta 54 (23), 2009, 5571–5582

[69] S. R. Dhanushkodi, M. Schwager, D. Todd and W. Mérida, *PEMFC Durability: Spatially Resolved Pt Dissolution in a Single Cell*, Journal of The Electrochemical Society 161 (14), 2014, F1315–F1322

[70] P. J. Ferreira, G. J. la O´, Y. Shao-Horn, D. Morgan, R. Makharia, S. Kocha and H. A. Gasteiger, *Instability of Pt/C Electrocatalysts in Proton Exchange Membrane Fuel Cells*, Journal of The Electrochemical Society 152 (11), 2005, A2256–A2271

[71] M. Crum and W. Liu, *Effective Testing Matrix for Studying Membrane Durability in PEM Fuel Cells: Part 2. Mechanical Durability and Combined Mechanical and Chemical Durability*, ECS Transactions 3 (1), 2006, 541–550

[72] W. Liu and M. Crum, *Effective Testing Matrix for Studying Membrane Durability in PEM Fuel Cells: Part I. Chemical Durability*, ECS Transactions 3 (1), 2006, 531–540

[73] X.-Z. Yuan, S. Zhang, S. Ban, C. Huang, H. Wang, V. Singara, M. Fowler, M. Schulze, A. Haug, K. A. Friedrich, et al., *Degradation of a PEM fuel cell stack with Nafion® membranes of different thicknesses. Part II: Ex situ diagnosis*, Journal of Power Sources 205, 2012, 324–334

[74] H. Tang, S. Peikang, S. P. Jiang, F. Wang and M. Pan, *A degradation study of Nafion proton exchange membrane of PEM fuel cells*, Journal of Power Sources 170 (1), 2007, 85–92

[75] L. Guétaz, S. Escribano and O. Sicardy, *Study by electron microscopy of proton exchange membrane fuel cell membrane-electrode assembly degradation mechanisms: Influence of local conditions*, Journal of Power Sources 212, 2012, 169–178

[76] N. Linse, G. G. Scherer, A. Wokaun and L. Gubler, *Quantitative analysis of carbon corrosion during fuel cell start-up and shut-down by anode purging*, Journal of Power Sources 219, 2012, 240–248

[77] A. Lamibrac, G. Maranzana, J. Dillet, O. Lottin, S. Didierjean, J. Durst, L. Dubau, F. Maillard and M. Chatenet, *Local Degradations Resulting from Repeated Start-ups and Shut-downs in Proton Exchange Membrane Fuel Cell (PEMFC)*, Energy Procedia 29, 2012, 318–324

[78] A. Taniguchi, T. Akita, K. Yasuda and Y. Miyazaki, *Analysis of degradation in PEMFC caused by cell reversal during air starvation*, International Journal of Hydrogen Energy 33 (9), 2008, 2323–2329

[79] A. Bose, P. Babburi, R. Kumar, D. Myers, J. Mawdsley and J. Milhuff, *Performance of individual cells in polymer electrolyte membrane fuel cell stack under-load cycling conditions*, Journal of Power Sources 243, 2013, 964–972

[80] Y. Ishigami, K. Takada, H. Yano, J. Inukai, M. Uchida, Y. Nagumo, T. Hyakutake, H. Nishide and M. Watanabe, *Corrosion of carbon supports at cathode during hydrogen/air replacement at anode studied by visualization of oxygen partial pressures in a PEFC—Start-up/shut-down simulation*, Journal of Power Sources 196 (6), 2011, 3003–3008

[81] P. Ferreira-Aparicio, A. M. Chaparro, B. Gallardo, M. A. Folgado and L. Daza, *Anode Degradation Effects in PEMFC Stacks by Localized Fuel Starvation*, ECS Transactions 26 (1), 2010, 257–265

[82] J. Kraft, P. Stahl, M. Götz and M. Morcos, *Elektrochemische Vorrichtung*, German Pat. App. 102014104017, 2014

[83] J. A. Rock, H. Schlag and K. R. Griffith, *Geprägte bipolare Platte für Brennstoffzellen*, German Pat. 10394231T5, 2006

[84] X. Zhao, Y. Fu, W. Li and A. Manthiram, *Effect of non-active area on the performance of subgasketed MEAs in PEMFC*, International Journal of Hydrogen Energy 38 (18), 2013, 7400–7406

[85] R. Zuber, K. Schaack, S. Wittpahl, A. Kabza and M. Maier, *Catalyst-coated ionomer membrane with protective film layer and membrane-electrode-assembly made thereof*, European Pat. 1403949B1, 2008

[86] R. L. James, S. D. Valentine and J. Leistra, *Manufacture or Membrane Electrode Assembly with Edge Protection for PEM Fuel Cells*, US Pat. App. 20080105354A1, 2008

[87] C. Wulff and M. Keuerleber, *Haltevorrichtung mit einer Membran einer Membran-Elektroden-Einheit für eine Brennstoffzelle und Verfahren zu deren Herstellung*, German Pat. 102011105072B3, 2012

[88] B. Sompalli, H. A. Gasteiger and B. A. Litteer, *Catalyst Layer Edge Protection for Enhanced MEA Durability in PEM Fuel Cells*, US Pat. 6861173B2, 2005

[89] B. Sompalli, B. A. Litteer, J. P. Healy, S. G. Yan, H. A. Gasteiger, W. Gu and G. W. Fly, *Edge-Protected Catalyst-Coated Membrane Electrode Assemblies*, US Pat. App. 20050271929A1, 2005

[90] R. Ströbel, B. Gaugler, A. Sailer, C. Kunz, J. Scherer, C. Schleier and J. Waldvogel, *Electrochemical System with Fluid Passage Integrated within a Sealing Bead*, US Pat. 7718293B2, 2010

[91] M. W. Keyser and G. W. Fly, *Interlockable Bead Seal*, US Pat. App. 20120164560A1, 2012

[92] G. W. Fly, J. A. Rock and S. C. Ofslager, *Metal Bead Seal for Fuel Cell Plate*, US Pat. App. 20090197147A1, 2009

[93] B. Gaugler, A. Sailer, C. Kunz, J. Scherer, R. Ströbel, C. Schleier and J. Waldvogel, *Brennstoffzellensystem sowie Verfahren zur Herstellung einer in dem Brennstoffzellensystem enthaltenen Bipolarplatte*, German Pat. 10248531B4, 2005

[94] M. A. Belchuk, S. Wagener and J. Zabold, *Sealing PEM Fuel Cells*, access date: 05.06.2013, Freudenberg-NOK, Freudenberg FCCT KG, 2010, URL: `http://fuelcellseminar.com/wp-content/uploads/a293_1.pdf`

[95] B. Tripathy and E. Szele, *LEM-Dichtungstechnik für Brennstoffzellen*, MTZ Motortechnische Zeitschrift 72 (3), 2011, 210–213

[96] D. Miller, S. J. Spencer, R. Thompson, M. Beutel and S. Xu, *Verstärkter Umfang einer Brennstoffzellen-Metallplatte*, German Pat. App. 102011117095A1, 2012

[97] V. Gnielinski, S. Kabelac, M. Kind, H. Martin, D. Mewes, K. Schaber and P. Stephan, eds., *VDI-Wärmeatlas*, 10th ed., Springer-Verlag Berlin Heidelberg, 2006

[98] B. Gaugler, C. Schleier, R. Glück, C. Kunz and J. Scherer, *Elektrochemisches System und Biopolarplatte*, German Pat. 102007048184B3, 2009

[99] Y. Tang, M. H. Santare, A. M. Karlsson, S. Cleghorn and W. B. Johnson, *Stresses in Proton Exchange Membranes Due to Hygro-Thermal Loading*, Journal of Fuel Cell Science and Technology 3 (2), 2006, 119–124

[100] Z. Lu, M. H. Santare, A. M. Karlsson, F. C. Busby and P. Walsh, *Time-dependent mechanical behavior of proton exchange membrane fuel cell electrodes*, Journal of Power Sources 245, 2014, 543–552

[101] J. Kraft, *PEM fuel cell technologies at ElringKlinger*, f-cell conference, Stuttgart, Germany, 2013

[102] J. Tan, Y. J. Chao, J. W. Van Zee, X. Li, X. Wang and M. Yang, *Assessment of mechanical properties of fluoroelastomer and EPDM in a simulated PEM fuel cell environment by microindentation test*, Materials Science and Engineering: A 496 (1-2), 2008, 464–470

[103] C.-W. Lin, C.-H. Chien, J. Tan, Y. J. Chao and J. W. Van Zee, *Chemical degradation of five elastomeric seal materials in a simulated and an accelerated PEM fuel cell environment*, Journal of Power Sources 196 (4), 2011, 1955–1966

[104] U. Basuli, J. Jose, R. H. Lee, Y. H. Yoo, K.-U. Jeong, J.-H. Ahn and C. Nah, *Properties and Degradation of the Gasket Component of a Proton Exchange Membrane Fuel Cell - A Review*, Journal of Nanoscience and Nanotechnology 12 (10), 2012, 7641–7657

[105] J. Tan, Y. J. Chao, J. W. Van Zee and W. K. Lee, *Degradation of elastomeric gasket materials in PEM fuel cells*, Materials Science and Engineering: A 445-446, 2007, 669–675

[106] J. Tan, Y. J. Chao, H. Wang, J. Gong and J. W. Van Zee, *Chemical and mechanical stability of EPDM in a PEM fuel cell environment*, Polymer Degradation and Stability 94 (11), 2009, 2072–2078

[107] T. Cui, C.-W. Lin, C. H. Chien, Y. J. Chao and J. W. Van Zee, *Service life estimation of liquid silicone rubber seals in polymer electrolyte membrane fuel cell environment*, Journal of Power Sources 196 (3), 2011, 1216–1221

[108] J. Tan, Y. J. Chao, M. Yang, W.-K. Lee and J. W. Van Zee, *Chemical and mechanical stability of a Silicone gasket material exposed to PEM fuel cell environment*, International Journal of Hydrogen Energy 36 (2), 2011, 1846–1852

[109] S. J. C. Cleghorn, D. K. Mayfield, D. A. Moore, J. C. Moore, G. Rusch, T. W. Sherman, N. T. Sisofo and U. Beuscher, *A polymer electrolyte fuel cell life test: 3 years of continuous operation*, Journal of Power Sources 158 (1), 2006, 446–454

[110] M. Schulze, T. Knöri, A. Schneider and E. Gülzow, *Degradation of sealings for PEFC test cells during fuel cell operation*, Journal of Power Sources 127 (1-2), 2004, 222–229

[111] M. Zachary, S. Camara, A. C. Whitwood, B. C. Gilbert, M. van Duin, R. J. Meier and V. Chechik, *EPR study of persistent free radicals in cross-linked EPDM rubbers*, European Polymer Journal 44 (7), 2008, 2099–2107

[112] S. A. Freunberger, M. Reum, J. Evertz, A. Wokaun and F. N. Büchi, *Measuring the Current Distribution in PEFCs with Sub-Millimeter Resolution*, Journal of The Electrochemical Society 153 (11), 2006, A2158–A2165

[113] S. A. Freunberger, *Mass and Charge Transfer on Various Relevant Scales in Polymer Electrolyte Fuel Cells*, PhD thesis, ETH Zürich, 2006

[114] J. Li, C.-Y. Wang and A. Su, *Prediction and Experimental Validation of In-Plane Current Distribution Between Channel and Land in a PEFC*, Journal of The Electrochemical Society 155 (1), 2008, B64–B69

[115] C.-Y. Lee and M. Lee, *In-situ diagnosis of local fuel cell performance using novel micro sensors*, International Journal of Hydrogen Energy 37 (5), 2012, 4448–4456

[116] B. Li, Y. S. Kim, R. Mukundan, M. S. Wilson, C. Welch, J. Fenton and R. L. Borup, *Mixed Hydrocarbon/Fluoropolymer Membrane/Ionomer MEAs for Durablity Studies*, ECS Transactions 33 (1), 2010, 913–924

[117] H. Wang, *Behavior of Raipore Radiation-Grafted Polymer Membranes in H_2/O_2 Fuel Cells*, Journal of The Electrochemical Society 145 (3), 1998, 780–784

[118] Y. Luan and Y. Zhang, *Membrane Degradation*, in: H. Wang, H. Li and X.-Z. Yuan, eds., PEM Fuel Cell Failure Mode Analysis, CRC Press LLC, 2012, chap. 4, 73–108

[119] P. Stahl, J. Kraft and M. Götz, *Elektrochemische Einheit für einen Brennstoffzellenstapel*, German Pat. App. 102015100740A1, 2015

[120] Z. Liu, J. S. Wainright, W. Huang and R. F. Savinell, *Positioning the reference electrode in proton exchange membrane fuel cells: calculations of primary and secondary current distribution*, Electrochimica Acta 49 (6), 2004, 923–935

[121] W. He and T. V. Nguyen, *Edge Effects on Reference Electrode Measurements in PEM Fuel Cells*, Journal of The Electrochemical Society 151 (2), 2004, A185–A195

[122] S. B. Adler, B. T. Henderson, W. M. A., D. M. Taylor and R. E. Richards, *Reference electrode placement and seals in electrochemical oxygen generators*, Solid State Ionics 134 (1-2), 2000, 35–42

[123] J. Winkler, P. V. Hendriksen, N. Bonanos and M. Mogensen, *Geometric Requirements of Solid Electrolyte Cells with a Reference Electrode*, Journal of The Electrochemical Society 145 (4), 1998, 1184–1192

[124] B. Sompalli, B. A. Litteer, W. Gu and H. A. Gasteiger, *Membrane Degradation at Catalyst Layer Edges in PEMFC MEAs*, Journal of The Electrochemical Society 154 (12), 2007, B1349–B1357

[125] J. Kawaji, S. Suzuki, T. Mizukami and K. Yamaga, *Membrane Degradation at cathode edges in MEA for direct methanol fuel cell*, 63th Annual Meeting of the International Society of Electrochemistry, Prague, Czech Republic, 2012

[126] P. Stahl, J. Biesdorf, P. Boillat, J. Kraft and K. A. Friedrich, *Water Distribution Analysis in the Outer Perimeter Region of Technical PEFC Based on Neutron Radiography*, Journal of The Electrochemical Society 162 (7), 2015, F677–F685

[127] P. Stahl, J. Biesdorf, P. Boillat and K. A. Friedrich, *An Investigation of PEFC Sub-Zero Startup: Evidence of Local Freezing Effects*, Journal of The Electrochemical Society 163 (14), 2016, F1535–F1542

[128] P. Stahl, J. Biesdorf, P. Boillat and K. A. Friedrich, *An Investigation of PEFC Sub-Zero Startup: Influence of Initial Conditions and Residual Water*, Fuel Cells 17 (6), 2017, 778–785

[129] L. Josic, E. H. Lehmann, D. Mannes, N. Kardjilov and A. Hilger, *Investigation of phase transfer properties of light and heavy water by means of energy selective neutron imaging*, Nuclear Instruments and Methods in Physics Research Section A: Accelerators, Spectrometers, Detectors and Associated Equipment 670, 2012, 68–72

[130] V. F. Sears, *Neutron scattering length and cross sections*, Neutron News 3, 1992, 26–37

[131] P. Boillat, *Advanced Characterization of Polymer Electrolyte Fuel Cells using High Resolution Neutron Imaging*, PhD thesis, ETH Zürich, 2009

[132] M. Inaba, T. Kinumoto, M. Kiriake, R. Umebayashi, A. Tasaka and Z. Ogumi, *Gas crossover and membrane degradation in polymer electrolyte fuel cells*, Electrochimica Acta 51 (26), 2006, 5746–5753

[133] S. Kreitmeier, M. Michiardi, A. Wokaun and F. N. Büchi, *Factors determining the gas crossover through pinholes in polymer electrolyte fuel cell membranes*, Electrochimica Acta 80, 2012, 240–247

[134] J. Heinze, *Cyclovoltammetrie — die „Spektroskopie" des Elektrochemikers*, Angewandte Chemie 96 (11), 1984, 823–840

[135] D. A. Stevens and J. R. Dahn, *Electrochemical Characterization of the Active Surface in Carbon-Supported Platinum Electrocatalysts for PEM Fuel Cells*, Journal of The Electrochemical Society 150 (6), 2003, A770–A775

[136] S. Gottesfeld, *Electrocatalysis of Oxygen Reduction in Polymer Electrolyte Fuel Cells: A Brief History and a Critical Examination of Present Theory and Diagnostics*, in: M. T. M. Koper, ed., Fuel Cell Catalysis - A Surface Science Approach, John Wiley & Sons, Inc., 2009, chap. 1, 1–30

[137] S. Liao, B. Li and Y. Li, *Physical Characterization of Electrocatalysts*, in: J. Zhang, ed., PEM Fuel Cell Electrocatalysts and Catalyst Layers, Springer Verlag London, 2008, chap. 10, 487–546

[138] B. V. Tilak, B. E. Conway and H. Angerstein-Kozlowska, *The real condition of oxidized pt electrodes: Part III. Kinetic theory of formation and reduction of surface oxides*, Journal of Electroanalytical Chemistry and Interfacial Electrochemistry 48 (1), 1973, 1–23

[139] T. R. Ralph, G. A. Hards and J. E. Keating, *Low Cost Electrodes for Proton Exchange Membrane Fuel Cells*, Journal of The Electrochemical Society 144 (11), 1997, 3845–3857

[140] J. Wang, *Analytical Electrochemistry*, 2nd ed., Wiley-VCH, 2001

[141] M. S. Frant and J. W. Ross, *Use of a total ionic strength adjustment buffer for electrode determination of fluoride in water supplies*, Analytical Chemistry 40 (7), 1968, 1169–1171

[142] *perfectION™ Guidebook - Successful Ion Measurement*, access date: 04.03.2016, Mettler Toledo, 2011, URL: `http://www.mt.com/us/en/home/library/operating-instructions/lab-analytical-instruments/GB_Fluoride/jcr:content/download/file/file.res/perfectION_Guidebook_Fluoride.pdf`

[143] S. Kundu, K. Karan, M. Fowler, L. C. Simon, B. Peppley and E. Halliop, *Influence of micro-porous layer and operating conditions on the fluoride release rate and degradation of PEMFC membrane electrode assemblies*, Journal of Power Sources 179 (2), 2008, 693–699

[144] K. Tüber, *Analyse des Betriebsverhaltens von Polymer-Elektrolyt-Membran-Brennstoffzellen für portable Systeme*, PhD thesis, Universität Duisburg-Essen, 2004

[145] F.-B. Weng, A. Su, C.-Y. Hsu and C.-Y. Lee, *Study of water-flooding behaviour in cathode channel of a transparent proton-exchange membrane fuel cell*, Journal of Power Sources 157 (2), 2006, 674–680

[146] X. Liu, H. Guo, F. Ye and C. F. Ma, *Water flooding and pressure drop characteristics in flow channels of proton exchange membrane fuel cells*, Electrochimica Acta 52 (11), 2007, 3607–3614

[147] J. Li, S. Lee and J. Roberts, *Ice formation and distribution in the catalyst layer during freeze-start process - CRYO-SEM investigation*, Electrochimica Acta 53 (16), 2008, 5391–5396

[148] Z. Zhang, J. Martin, J. Wu, H. Wang, K. Promislow and B. J. Balcom, *Magnetic resonance imaging of water content across the Nafion membrane in an operational PEM fuel cell*, Journal of Magnetic Resonance 193 (2), 2008, 259–266

[149] K. R. Minard, V. V. Viswanathan, P. D. Majors, Q. Wang and P. C. Rieke, *Magnetic resonance imaging (MRI) of PEM dehydration and gas manifold flooding during continuous fuel cell operation*, Journal of Power Sources 161 (2), 2006, 856–863

[150] I. Manke, C. Hartnig, M. Grünerbel, W. Lehnert, N. Kardjilov, A. Haibel, A. Hilger, J. Banhart and H. Riesemeier, *Investigation of water evolution and transport in fuel cells with high resolution synchrotron x-ray radiography*, Applied Physics Letters 90 (17), 2007, 174105

[151] J. Eller, T. Rosén, F. Marone, M. Stampanoni, A. Wokaun and F. N. Büchi, *Progress in In Situ X-Ray Tomographic Microscopy of Liquid Water in Gas Diffusion Layers of PEFC*, Journal of The Electrochemical Society 158 (8), 2011, B963–B970

[152] J. Roth, M. R. Zurbrugg, S. Irvine, F. Marone, M. Stampanoni and F. N. Buchi, *Investigation of PEFC Freeze Start by X-ray Tomographic Microscopy*, ECS Transactions 58 (1), 2013, 453–462

[153] J. P. Owejan, T. A. Trabold, D. L. Jacobson, M. Arif and S. G. Kandlikar, *Effects of flow field and diffusion layer properties on water accumulation in a PEM fuel cell*, International Journal of Hydrogen Energy 32 (17), 2007, 4489–4502

[154] J. P. Owejan, J. J. Gagliardo, J. M. Sergi, S. G. Kandlikar and T. A. Trabold, *Water management studies in PEM fuel cells, Part I: Fuel cell design and in situ water distributions*, International Journal of Hydrogen Energy 34 (8), 2009, 3436–3444

[155] R. Satija, D. L. Jacobson, M. Arif and S. A. Werner, *In situ neutron imaging technique for evaluation of water management systems in operating PEM fuel cells*, Journal of Power Sources 129 (2), 2004, 238–245

[156] D. Kramer, J. Zhang, R. Shimoi, E. Lehmann, A. Wokaun, K. Shinohara and G. G. Scherer, *In situ diagnostic of two-phase flow phenomena in polymer electrolyte fuel cells by neutron imaging*, Electrochimica Acta 50 (13), 2005, 2603–2614

[157] I. A. Schneider, D. Kramer, A. Wokaun and G. G. Scherer, *Spatially resolved characterization of PEFCs using simultaneously neutron radiography and locally resolved impedance spectroscopy*, Electrochemistry Communications 7 (12), 2005, 1393–1397

[158] N. Pekula, K. Heller, P. A. Chuang, A. Turhan, M. M. Mench, J. S. Brenizer and K. Ünlü, *Study of water distribution and transport in a polymer electrolyte fuel cell using neutron imaging*, Nuclear Instruments and Methods in Physics Research Section A: Accelerators, Spectrometers, Detectors and Associated Equipment 542 (1-3), 2005, 134–141

[159] C. Hartnig, I. Manke, N. Kardjilov, A. Hilger, M. Grünerbel, J. Kaczerowski, J. Banhart and W. Lehnert, *Combined neutron radiography and locally resolved current density measurements of operating PEM fuel cells*, Journal of Power Sources 176 (2), 2008, 452–459

[160] P. Boillat, J. Biesdorf and P. Oberholzer, *Accuracy of water quantification in fuel cells by neutron imaging*, Annual Report of Electrochemistry Laboratory (LEC), Paul Scherrer Institute, 2013

[161] P. Boillat, G. G. Scherer, A. Wokaun, G. Frei and E. H. Lehmann, *Transient observation of ^{2}H labeled species in an operating PEFC using neutron radiography*, Electrochemistry Communications 10 (9), 2008, 1311–1314

[162] J. Biesdorf, P. Oberholzer, F. Bernauer, A. Kaestner, P. Vontobel, E. H. Lehmann, T. J. Schmidt and P. Boillat, *Dual Spectrum Neutron Radiography: Identification of Phase Transitions between Frozen and Liquid Water*, Physical Review Letters 112 (24), 2014, 248301

[163] P. Oberholzer and P. Boillat, *Local Characterization of PEFCs by Differential Cells: Systematic Variations of Current and Asymmetric Relative Humidity*, Journal of The Electrochemical Society 161 (1), 2013, F139–F152

[164] P. Oberholzer, P. Boillat, R. Siegrist, R. Perego, A. Kästner, E. Lehmann, G. G. Scherer and A. Wokaun, *Cold-Start of a PEFC Visualized with High Resolution Dynamic In-Plane Neutron Imaging*, Journal of The Electrochemical Society 159 (2), 2012, B235–B245

[165] P. Boillat, A. Iranzo and J. Biesdorf, *Layer by Layer Segmentation of Water Distribution from Neutron Imaging of Large Scale Cells*, Journal of the Electrochemical Society 162 (6), 2015, F531–F536

[166] J. P. Owejan, J. J. Gagliardo, R. C. Reid and T. A. Trabold, *Proton transport resistance correlated to liquid water content of gas diffusion layers*, Journal of Power Sources 209, 2012, 147–151

[167] J. Spendelow, R. Mukundan, J. Davey, T. Rockward, D. S. Hussey, D. Jacobson, M. Arif and R. L. Borup, *High Resolution Neutron Radiography Imaging of Operating PEM Fuel Cells: Effect of Flow Configuration and Gravity on Water Distribution*, ECS Transactions 16 (2), 2008, 1345–1355

[168] J. Eller, J. Roth, F. Marone, M. Stampanoni, A. Wokaun and F. N. Büchi, *Implications of polymer electrolyte fuel cell exposure to synchrotron radiation on gas diffusion layer water distribution*, Journal of Power Sources 245, 2014, 796–800

[169] W. J. Moore, G. Trafara and K. Holland-Moritz, *Physikalische Chemie*, ed. by D. O. Hummel, 4th ed., Walter de Gruyter, 1986

[170] A. P. Kaestner, S. Hartmann, G. Kühne, G. Frei, C. Grünzweig, L. Josic, F. Schmid and E. H. Lehmann, *The ICON beamline – A facility for cold neutron imaging at SINQ*, Nuclear Instruments and Methods in Physics Research Section A: Accelerators, Spectrometers, Detectors and Associated Equipment 659 (1), 2011, 387–393

[171] G. Kühne, G. Frei, E. Lehmann, P. Vontobel, A. Bollhalder, U. Filges and M. Schild, *ICON - The New Facility for Cold Neutron Imaging at the Swiss Spallation Neutron Source SINQ*, Swiss Neutron News 28, 2005, 20–29

[172] C. Grünzweig, F. Pfeiffer, O. Bunk, T. Donath, G. Kühne, G. Frei, M. Dierolf and C. David, *Design, fabrication, and characterization of diffraction gratings for neutron phase contrast imaging*, Review of Scientific Instruments 79 (5), 2008, 053703

[173] L. Torres, J. R. Granada and J. J. Blostein, *Total cross sections of benzene at 90 K and light water ice at 115 K*, Nuclear Instruments and Methods in Physics Research Section B: Beam Interactions with Materials and Atoms 251 (1), 2006, 304–305

[174] F. N. Büchi and G. G. Scherer, *In-situ resistance measurements of Nafion® 117 membranes in polymer electrolyte fuel cells*, Journal of Electroanalytical Chemistry 404 (1), 1996, 37–43

[175] P. Dimitrova, K. A. Friedrich, B. Vogt and U. Stimming, *Transport properties of ionomer composite membranes for direct methanol fuel cells*, Journal of Electroanalytical Chemistry 532 (1-2), 2002, 75–83

[176] I. Alaefour, *Current and Temperature Distribution in Proton Exchange Membrane Fuel Cell*, PhD thesis, University of Waterloo, 2012

[177] N. Y. Steiner, D. Candusso, D. Hissel and P. Moçoteguy, *Model-based diagnosis for proton exchange membrane fuel cells*, Mathematics and Computers in Simulation 81 (2), 2010, 158–170

[178] R. Banerjee, D. Howe, V. Mejia and S. G. Kandlikar, *Experimental validation of two-phase pressure drop multiplier as a diagnostic tool for characterizing PEM fuel cell performance*, International Journal of Hydrogen Energy 39 (31), 2014, 17791–17801

[179] F. Barbir, H. Gorgun and X. Wang, *Relationship between pressure drop and cell resistance as a diagnostic tool for PEM fuel cells*, Journal of Power Sources 141 (1), 2005, 96–101

[180] R. Mukundan, Y. S. Kim, T. Rockward, J. R. Davey, B. Pivovar, D. S. Hussey, D. L. Jacobson, M. Arif and R. Borup, *Performance of PEM Fuel Cells at Sub-Freezing Temperatures*, ECS Transactions 11 (1), 2007, 543–552

[181] R. Mukundan, J. R. Davey, R. W. Lujan, J. S. Spendelow, Y. S. Kim, D. S. Hussey, D. L. Jacobson, M. Arif and R. L. Borup, *Performance and Durability of PEM Fuel Cells Operated at Sub-Freezing Temperatures*, ECS Transactions 16 (2), 2008, 1939–1950

[182] R. Mukundan, R. Lujan, J. R. Davey, J. S. Spendelow, D. S. Hussey, D. L. Jacobson, M. Arif and R. Borup, *Ice Formation in PEM Fuel Cells Operated Isothermally at Sub-Freezing Temperatures*, ECS Transactions 25 (1), 2009, 345–355

[183] S. Ge and C.-Y. Wang, *Characteristics of subzero startup and water/ice formation on the catalyst layer in a polymer electrolyte fuel cell*, Electrochimica Acta 52 (14), 2007, 4825–4835

[184] J. Mishler, Y. Wang, P. P. Mukherjee, R. Mukundan and R. L. Borup, *Subfreezing operation of polymer electrolyte fuel cells: Ice formation and cell performance loss*, Electrochimica Acta 65, 2012, 127–133

[185] A. Santamaria, H.-Y. Tang, J. W. Park, G. Park and Y.-J. Sohn, *3D neutron tomography of a polymer electrolyte membrane fuel cell under sub-zero conditions*, International Journal of Hydrogen Energy 37 (14), 2012, 10836–10843

[186] K. Tajiri, Y. Tabuchi and C.-Y. Wang, *Isothermal Cold Start of Polymer Electrolyte Fuel Cells*, Journal of The Electrochemical Society 154 (2), 2007, B147–B152

[187] E. L. Thompson, J. Jorne, W. Gu and H. A. Gasteiger, *PEM Fuel Cell Operation at -20°C. I. Electrode and Membrane Water (Charge) Storage*, Journal of The Electrochemical Society 155 (6), 2008, B625–B634

[188] E. L. Thompson, J. Jorne, W. Gu and H. A. Gasteiger, *PEM Fuel Cell Operation at -20°C. II. Ice Formation Dynamics, Current Distribution, and Voltage Losses within Electrodes*, Journal of The Electrochemical Society 155 (9), 2008, B887–B896

[189] C. Chacko, R. Ramasamy, S. Kim, M. Khandelwal and M. Mench, *Characteristic Behavior of Polymer Electrolyte Fuel Cell Resistance during Cold Start*, Journal of The Electrochemical Society 155 (11), 2008, B1145–B1154

[190] K. Tajiri, Y. Tabuchi, F. Kagami, S. Takahashi, K. Yoshizawa and C.-Y. Wang, *Effects of operating and design parameters on PEFC cold start*, Journal of Power Sources 165 (1), 2007, 279–286

[191] M. Oszcipok, D. Riemann, U. Kronenwett, M. Kreideweis and M. Zedda, *Statistic analysis of operational influences on the cold start behaviour of PEM fuel cells*, Journal of Power Sources 145 (2), 2005, 407–415

[192] Y. Ishikawa, H. Hamada, M. Uehara and M. Shiozawa, *Super-cooled water behavior inside polymer electrolyte fuel cell cross-section below freezing temperature*, Journal of Power Sources 179 (2), 2008, 547–552

[193] Y. Tabe, M. Saito, K. Fukui and T. Chikahisa, *Cold start characteristics and freezing mechanism dependence on start-up temperature in a polymer electrolyte membrane fuel cell*, Journal of Power Sources 208, 2012, 366–373

[194] Y. Hishinuma, T. Chikahisa, F. Kagami and T. Ogawa, *The Design and Performance of a PEFC at a Temperature Below Freezing*, JSME International Journal, Series B 47 (2), 2004, 235–241

[195] J. Hou, B. Yi, H. Yu, L. Hao, W. Song, Y. Fu and Z. Shao, *Investigation of resided water effects on PEM fuel cell after cold start*, International Journal of Hydrogen Energy 32 (17), 2007, 4503–4509

[196] J. Biesdorf, P. Stahl, M. Siegwart, T. J. Schmidt and P. Boillat, *When Size Matters: Active Area Dependence of PEFC Cold Start Capability*, Journal of The Electrochemical Society 162 (10), 2015, F1231–F1235

[197] E. Schießwohl, T. von Unwerth, F. Seyfried and D. Brüggemann, *Experimental investigation of parameters influencing the freeze start ability of a fuel cell system*, Journal of Power Sources 193 (1), 2009, 107–115

[198] S. Ge and C.-Y. Wang, *In Situ Imaging of Liquid Water and Ice Formation in an Operating PEFC during Cold Start*, Electrochemical Solid-State Letters 9 (11), 2006, A499–A503

[199] T. Colinart and F. N. Büchi, *Sub-Millimeter Current Density Distribution in PEFC at sub-Zero Temperatures*, 216th ECS Meeting, Vienna, Austria, 2009

[200] R. K. Ahluwalia and X. Wang, *Rapid self-start of polymer electrolyte fuel cell stacks from subfreezing temperatures*, Journal of Power Sources 162 (1), 2006, 502–512

[201] S. Ge and C.-Y. Wang, *Cyclic Voltammetry Study of Ice Formation in the PEFC Catalyst Layer during Cold Start*, Journal of The Electrochemical Society 154 (12), 2007, B1399–B1406

[202] R. Lin, Y. Weng, Y. Li, X. Lin, S. Xu and J. Ma, *Internal behavior of segmented fuel cell during cold start*, International Journal of Hydrogen Energy 39 (28), 2014, 16025–16035

[203] K. Jiao, I. E. Alaefour, G. Karimi and X. Li, *Simultaneous measurement of current and temperature distributions in a proton exchange membrane fuel cell during cold start processes*, Electrochimica Acta 56 (8), 2011, 2967–2982

[204] Y. Tabe, R. Ichikawa and T. Chikahisa, *Analysis of Ice Formation Process in Cathode Catalyst Layer of PEFC at Cold Start*, Energy Procedia 28, 2012, 20–27

[205] K. Jiao, I. E. Alaefour, G. Karimi and X. Li, *Cold start characteristics of proton exchange membrane fuel cells*, International Journal of Hydrogen Energy 36 (18), 2011, 11832–11845

[206] Y. Ishikawa, T. Morita, K. Nakata, K. Yoshida and M. Shiozawa, *Behavior of water below the freezing point in PEFCs*, Journal of Power Sources 163 (2), 2007, 708–712

[207] H. Mendil-Jakani, R. J. Davies, E. Dubard, A. Guillermo and G. Gebel, *Water crystallization inside fuel cell membranes probed by X-ray scattering*, Journal of Membrane Science 369 (1-2), 2011, 148–154

[208] Y. Ishikawa, M. Shiozawa, M. Kondo and K. Ito, *Theoretical analysis of supercooled states of water generated below the freezing point in a PEFC*, International Journal of Heat and Mass Transfer 74, 2014, 215–227

[209] T. J. Dursch, M. A. Ciontea, C. J. Radke and A. Z. Weber, *Isothermal Ice Crystallization Kinetics in the Gas-Diffusion Layer of a Proton-Exchange-Membrane Fuel Cell*, Langmuir 28 (2), 2012, 1222–1234

[210] M. V. Santis Alvarez, *Investigations of Current Density Inhomogeneities in Polymer Electrolyte Fuel Cells*, PhD thesis, ETH Zürich, 2006

[211] A. Morin, Z. Peng, J. Jestin, M. Detrez and G. Gebel, *Water management in proton exchange membrane fuel cell at sub-zero temperatures: An in operando SANS-EIS coupled study*, Solid State Ionics 252, 2013, 56–61

[212] A. L. Buck, *New Equations for Computing Vapor Pressure and Enhancement Factor*, Journal of Applied Meteorology 20 (12), 1981, 1527–1532

[213] F. Jiang, W. Fang and C.-Y. Wang, *Non-isothermal cold start of polymer electrolyte fuel cells*, Electrochimica Acta 53 (2), 2007, 610–621

[214] A. M. J. Bazylak, *Liquid water transport in fuel cell gas diffusion layers*, PhD thesis, University of Victoria, 2008

[215] Q. Du, B. Jia, Y. Luo, J. Chen, Y. Zhou and K. Jiao, *Maximum power cold start mode of proton exchange membrane fuel cell*, International Journal of Hydrogen Energy 39 (16), 2014, 8390–8400

[216] Y. Zhou, Y. Luo, S. Yu and K. Jiao, *Modeling of cold start processes and performance optimization for proton exchange membrane fuel cell stacks*, Journal of Power Sources 247, 2014, 738–748

[217] Y. Luo, K. Jiao and B. Jia, *Elucidating the constant power, current and voltage cold start modes of proton exchange membrane fuel cell*, International Journal of Heat and Mass Transfer 77, 2014, 489–500

[218] M. F. Mathias, R. Makharia, H. A. Gasteiger, J. J. Conley, T. J. Fuller, C. J. Gittleman, S. S. Kocha, D. P. Miller, C. K. Mittelsteadt, T. Xie, et al., *Two Fuel Cell Cars In Every Garage*, The Electrochemical Society Interface 14 (3), 2005, 24–35

[219] X.-Z. Yuan, S. Zhang, H. Wang, J. Wu, J. C. Sun, R. Hiesgen, K. A. Friedrich, M. Schulze and A. Haug, *Degradation of a polymer exchange membrane fuel cell stack with Nafion® membranes of different thicknesses: Part I. In situ diagnosis*, Journal of Power Sources 195 (22), 2010, 7594–7599

[220] G. Maranzana, A. Lamibrac, J. Dillet, S. Abbou, S. Didierjean and O. Lottin, *Startup (and Shutdown) Model for Polymer Electrolyte Membrane Fuel Cells*, Journal of The Electrochemical Society 162 (7), 2015, F694–F706

[221] J. Kim, J. Lee and Y. Tak, *Relationship between carbon corrosion and positive electrode potential in a proton-exchange membrane fuel cell during start/stop operation*, Journal of Power Sources 192 (2), 2009, 674–678

[222] I. A. Schneider and S. von Dahlen, *Start-Stop Phenomena in Channel and Land Areas of a Polymer Electrolyte Fuel Cell*, Electrochemical and Solid-State Letters 14 (2), 2011, B30–B33

[223] N. Linse, *Start/stop phenomena in polymer electrolyte fuel cells*, PhD thesis, ETH Zürich, 2012

[224] *Proton Exchange Membrane Fuel Cell*, Manual, Comsol Multiphysics®, 2008

[225] Y. Fu, Y. Jiang, S. Poizeau, A. Dutta, A. Mohanram, J. D. Pietras and M. Z. Bazant, *Multicomponent Gas Diffusion in Porous Electrodes*, Journal of The Electrochemical Society 162 (6), 2015, F613–F621

[226] P. K. Das, X. Li and Z.-S. Liu, *Effective transport coefficients in PEM fuel cell catalyst and gas diffusion layers: Beyond Bruggeman approximation*, Applied Energy 87 (9), 2010, 2785–2796

[227] L. Maldonado, J.-C. Perrin, J. Dillet and O. Lottin, *Characterization of polymer electrolyte Nafion membranes: Influence of temperature, heat treatment and drying protocol on sorption and transport properties*, Journal of Membrane Science 389, 2012, 43–56

[228] P. Berg, K. Promislow, J. St. Pierre, J. Stumper and B. Wetton, *Water Management in PEM Fuel Cells*, Journal of The Electrochemical Society 151 (3), 2004, A341–A353

[229] N. Takeuchi and T. F. Fuller, *Modeling and Investigation of Carbon Loss on the Cathode Electrode during PEMFC Operation*, Journal of The Electrochemical Society 157 (1), 2010, B135–B140

[230] M. S. Ismail, D. B. Ingham, K. J. Hughes, L. Ma and M. Pourkashanian, *Effective diffusivity of polymer electrolyte fuel cell gas diffusion layers: An overview and numerical study*, International Journal of Hydrogen Energy 40 (34), 2015, 10994–11010

[231] T. Zhou and H. Liu, *Effects of the electrical resistances of the GDL in a PEM fuel cell*, Journal of Power Sources 161 (1), 2006, 444–453

[232] J. Nam, P. Chippar, W. Kim and H. Ju, *Numerical analysis of gas crossover effects in polymer electrolyte fuel cells (PEFCs)*, Applied Energy 87 (12), 2010, 3699–3709

[233] P. Dobson, C. Lei, T. Navessin and M. Secanell, *Characterization of the PEM Fuel Cell Catalyst Layer Microstructure by Nonlinear Least-Squares Parameter Estimation*, Journal of The Electrochemical Society 159 (5), 2012, B514–B523

[234] C. Y. Du, P. F. Shi, X. Q. Cheng and G. P. Yin, *Effective protonic and electronic conductivity of the catalyst layers in proton exchange membrane fuel cells*, Electrochemistry Communications 6 (5), 2004, 435–440

[235] Z. Siroma, J. Hagiwara, K. Yasuda, M. Inaba and A. Tasaka, *Simultaneous measurement of the effective ionic conductivity and effective electronic conductivity in a porous electrode film impregnated with electrolyte*, Journal of Electroanalytical Chemistry 648 (2), 2010, 92–97

[236] S. Zhang, X.-Z. Yuan, J. N. C. Hin, H. Wang, J. Wu, K. A. Friedrich and M. Schulze, *Effects of open-circuit operation on membrane and catalyst layer degradation in proton exchange membrane fuel cells*, Journal of Power Sources 195 (4), 2010, 1142–1148

[237] V. O. Mittal, H. R. Kunz and J. M. Fenton, *Membrane Degradation Mechanisms in PEMFCs*, Journal of The Electrochemical Society 154 (7), 2007, B652–B656

[238] V. O. Mittal, H. R. Kunz and J. M. Fenton, *Effect of Catalyst Properties on Membrane Degradation Rate and the Underlying Degradation Mechanism in PEMFCs*, Journal of The Electrochemical Society 153 (9), 2006, A1755–A1759

[239] P. Stahl, J. Kraft and M. Götz, *Elektrochemische Vorrichtung und Verfahren zum Herstellen einer elektrochemischen Einheit für eine elektrochemische Vorrichtung*, German Pat. App. 102015109393A1, 2015

[240] A. El-kharouf, T. J. Mason, D. J. L. Brett and B. G. Pollet, *Ex-situ characterisation of gas diffusion layers for proton exchange membrane fuel cells*, Journal of Power Sources 218, 2012, 393–404

[241] *Freudenberg Gas Diffusion Layers for PEMFC and DMFC, Datasheet*, access date: 02.02.2016, Freudenberg Performance Materials SE & Co. KG (former name Freudenberg FCCT SE & Co. KG), 2014, URL: `http://www.freudenbergfuelcellproducts.com/sites/default/files/2014-12-15_technical_data_sheet_gdl.pdf`

[242] T. R. Marrero and E. A. Mason, *Gaseous Diffusion Coefficients*, Journal of Physical and Chemical Reference Data 1 (1), 1972, 3–118

[243] R. L. McMurtrie and F. G. Keyes, *A Measurement of the Diffusion Coefficient of Hydrogen Peroxide Vapor into Air*, Journal of the American Chemical Society 70 (11), 1948, 3755–3758

[244] *NIST Standard Reference Database Number 69*, access date: 02.02.2016, NIST, 2015, URL: `http://webbook.nist.gov/chemistry/`

[245] D. R. Morris and X. Sun, *Water-sorption and transport properties of Nafion 117 H*, Journal of Applied Polymer Science 50 (8), 1993, 1445–1452

[246] P. J. Mohr, B. N. Taylor and D. B. Newell, *CODATA recommended values of the fundamental physical constants: 2006*, Reviews of Modern Physics 80 (2), 2008, 633–730

Author's Remarks

This work contains self-citations. Instead of a detailed indication of the relating contents, the chapter headings are marked accordingly for a better readability. An overview over the citations is given subsequently.

Parts of Chapter 4 were published in:

> [126] P. Stahl, J. Biesdorf, P. Boillat, J. Kraft and K. A. Friedrich, *Water Distribution Analysis in the Outer Perimeter of Technical PEFC Based on Neutron Radiography*, Journal of The Electrochemical Society 162 (7), 2015, F677-F685,
>
> [127] P. Stahl, J. Biesdorf, P. Boillat and K. A. Friedrich, *An Investigation of PEFC Sub-Zero Startup: Evidence of Local Freezing Effects*, Journal of The Electrochemical Society 163 (14), 2016, F1535-F1542 and
>
> [128] P. Stahl, J. Biesdorf, P. Boillat and K. A. Friedrich, *An Investigation of PEFC Sub-Zero Startup: Influence of Initial Conditions and Residual Water*, Fuel Cells 17 (6), 2017, 778-785.

Parts of Chapter 5 were published in:

> [126] P. Stahl, J. Biesdorf, P. Boillat, J. Kraft and K. A. Friedrich, *Water Distribution Analysis in the Outer Perimeter of Technical PEFC Based on Neutron Radiography*, Journal of The Electrochemical Society 162 (7), 2015, F677-F685.

Parts of Chapter 6 were published in:

> [127] P. Stahl, J. Biesdorf, P. Boillat and K. A. Friedrich, *An Investigation of PEFC Sub-Zero Startup: Evidence of Local Freezing Effects*, Journal of The Electrochemical Society 163 (14), 2016, F1535-F1542 and
>
> [128] P. Stahl, J. Biesdorf, P. Boillat and K. A. Friedrich, *An Investigation of PEFC Sub-Zero Startup: Influence of Initial Conditions and Residual Water*, Fuel Cells 17 (6), 2017, 778-785.

Some figures and tables are reproduced with or without modifications from further publications. For a better readability it was resigned from references in the according figure or table captions. The following figures and tables are reprinted with permission from Journal of the Electrochemical Society, 162 (7), 2015, F677-F685. Copyright 2015, The Electrochemical Society:

Figures 4.1, 4.2, 5.1, 5.3 to 5.16 and 7.1 and Tables 4.2 and 5.1.

The following figures and tables are reprinted with permission from Journal of the Electrochemical Society, 163 (14), 2016, F1535-F1542. Copyright 2016, The Electrochemical Society:

Figures 6.2 to 6.7 and 6.13 and Tables 6.1 to 6.3.

The following figures and tables are reprinted with permission from Fuel Cells 17 (6), 2017, 778-785. Copyright 2017, John Wiley & Sons, Inc.:

Figures 6.1, 6.2 and 6.8 to 6.12 and Table 6.1.

Acknowledgment

A part of this work was carried out with the support of the European Community. The author appreciates the support of the European Research Infrastructure H2FC European Infrastructure (funded under the FP7 specific program Capacities, grant Agreement Number 284522) and its partner the Paul Scherrer Institute.

Own Publications

Peer-Reviewed Papers

P. Stahl, J. Biesdorf, P. Boillat, J. Kraft and K. A. Friedrich, *Water Distribution Analysis in the Outer Perimeter Region of Technical PEFC Based on Neutron Radiography*, Journal of The Electrochemical Society 162 (7), 2015, F677–F685

J. Biesdorf, P. Stahl, M. Siegwart, T. J. Schmidt and P. Boillat, *When Size Matters: Active Area Dependence of PEFC Cold Start Capability*, Journal of The Electrochemical Society 162 (10), 2015, F1231–F1235

P. Stahl, J. Biesdorf, P. Boillat and K. A. Friedrich, *An Investigation of PEFC Sub-Zero Startup: Evidence of Local Freezing Effects*, Journal of The Electrochemical Society 163 (14), 2016, F1535–F1542

P. Stahl, J. Biesdorf, P. Boillat and K. A. Friedrich, *An Investigation of PEFC Sub-Zero Startup: Influence of Initial Conditions and Residual Water*, Fuel Cells 17 (6), 2017, 778–785

Patent Applications

J. Kraft, P. Stahl, M. Götz and M. Morcos, *Elektrochemische Vorrichtung*, German Pat. App. 102014104017, 2014

P. Stahl, J. Kraft and M. Götz, *Elektrochemische Einheit für eine elektrochemische Vorrichtung und Verfahren zum Herstellen einer solchen*, German Pat. App. 102015100737, 2015

P. Stahl, J. Kraft and M. Götz, *Elektrochemische Einheit für einen Brennstoffzellenstapel*, German Pat. App. 102015100740, 2015

P. Stahl, J. Kraft and M. Götz, *Elektrochemische Vorrichtung und Verfahren zum Herstellen einer elektrochemischen Einheit für eine elektrochemische Vorrichtung*, German Pat. App. 102015109393, 2015

S. Hemmer, J. Kraft and P. Stahl, *Brennstoffzellenvorrichtung und Verfahren zum Betreiben einer Brennstoffzellenvorrichtung*, German Pat. App. 102017115871, 2017

J. Kraft, A. Bayer and P. Stahl, *Bipolarplatte für eine elektrochemische Vorrichtung*, German Pat. App. 102017115873, 2017

A. Wiechert, J. Kraft, P. Stahl and C. Jung, *Dichtungsanordnung für eine elektrochemische Vorrichtung*, German Pat. App. 102017115884, 2017

P. Stahl, K. Dahl, A. Gröh, J. Kraft and O. Fink, *Elektrochemisch aktive Einheit für eine elektrochemische Vorrichtung*, German Pat. App. 102017117146, 2017

Conferences/Talks

P. Stahl, J. Biesdorf, P. Boillat, J. Kraft and K. A. Friedrich, *Water Distribution Analysis in the Outer Perimeter of Technical PEFC Based on Neutron Radiography*, 12th Symposium for Fuel Cell and Battery Modeling and Experimental Validation (Modval), Freiburg, Germany, 2015

P. Stahl, *Brennstoffzellen - Herausforderungen und Wege zur Kommerzialisierung*, Kolloquium Das neue Auto - elektrisch, automatisiert, vernetzt, Technische Akademie Esslingen, Ostfildern, Germany, 2016